THE EFFECTS OF FIBER ORIENTATION STATE OF EXTRUSION DEPOSITION ADDITIVE MANUFACTURED FIBER-FILLED THERMOPLASTIC POLYMERS

by

Pasita Pibulchinda

A Thesis

Submitted to the Faculty of Purdue University

In Partial Fulfillment of the Requirements for the degree of

Master of Science in Aeronautics and Astronautics

School of Aeronautics and Astronautics

West Lafayette, Indiana

August 2020

THE PURDUE UNIVERSITY GRADUATE SCHOOL
STATEMENT OF COMMITTEE APPROVAL

Dr. R. Byron Pipes, Chair

Department of Aeronautics and Astronautics

Dr. Tyler Tallman

Department of Aeronautics and Astronautics

Dr. Wenbin Yu

Department of Aeronautics and Astronautics

Dr. Johnathan Goodsell

Department of Aeronautics and Astronautics

Approved by:

Dr. Gregory Blaisdell

To Mama, Papa, and Eng

ACKNOWLEDGMENTS

My master's thesis journey is only possible because of the opportunity my advisor, Prof. R. Byron Pipes has given me. I would like to express my most sincere gratitude to Prof. Pipes for providing valuable advice throughout the journey as well as for his unconditional encouragement and support. I will never forget the truly amazing time I had at the Composite Manufacturing and Simulation Center, a Purdue University Center of Excellence.

I would also like to express my gratitude to Eduardo Barocio for his friendship, mentorship, and trust. I am always grateful to Eduardo who not only provided countless invaluable academic discussions, but also for being kindhearted, understanding, and encouraging. I thank Miguel Ramirez, Sushrut Karmarkar, and Garam Kim for always willing to teach and help me with countless experiments. I would also like to thank them along with my additive manufacturing teammates who I truly enjoy being with: Vasudha Kapre, Jorge Ramirez, Akshay Thomas, Alfredo Ocegueda, and Logan Greenlee for all their support and their friendship. I would like to express my appreciation to my trusted friends Vasudha Kapre, Neha Shakelly, and Yuwei He for a great time together and for their continuous emotional and mental support. I would like to thank everyone at the composite manufacturing & simulation center including the undergraduate research assistants for creating a positive and healthy work environment.

I would also like to thank the Institute for Advanced Composites Manufacturing Innovation (IACMI) for funding part of this research. For making the project valuable and enjoyable, I am thankful to those involved in this project: Eduardo Barocio, Mike Bogdanor, Alan Wedgewood, and Charles Hill.

Finally, I want to express my deepest gratitude to my parents and my sister for their continuous encouragement, understanding, and support throughout my life and my future.

TABLE OF CONTENTS

LIST OF TABLES

LIST OF FIGURES

ABSTRACT

Extrusion Deposition Additive Manufacturing (EDAM) is a process in which fiber-filled thermoplastic polymers are mixed and melted in an extruder and deposited onto a build plate in a layer-by-layer basis. Anisotropy caused by flow-induced orientation of discontinuous fibers along with the non-isothermal cooling process gives rise to internal stresses in printed parts which results in part deformation. The deformation and residual stresses can be abated by modifying the fiber orientation in the extrudate to best suit the print geometry. To that end, the focus of this research is on understanding the effect of fiber orientation state and fiber properties on effective properties of the printed bead and the final deformation of a part. The properties of three different orientation tensors of glass fiber-filled polyamide and carbon fiber-filled polyamide were experimentally and virtually characterized via micromechanics. A thermo-mechanical simulation framework developed in ABAQUS© was used to understand the effects of the varying fiber orientation tensor and fiber properties on the final deformation of printed parts. In particular, a medium-size geometry that is prone to high deformation was simulated and compared among the three orientation tensors and two material systems. This serves to be a good preliminary study to understand microscopic properties induced deformations in EDAM.

1. INTRODUCTION

This chapter begins by introducing the Extrusion Deposition Additive Manufacturing (EDAM) process used for fabricating three-dimensional geometries in a layer-by-layer basis. Including the current applications and examples of tooling applications for EDAM technology. A brief overview of the phenomena involved in the manufacturing process is presented after. In addition, some technical challenges of the EDAM process are presented along with previous efforts in solving the challenges. Following the literature review is the overview of the micromechanics method and overview of EDAM process simulation which is utilized in this study. Lastly, the motivation for this work is stated.

1.1 Overview of Extrusion Deposition Additive Manufacturing

EDAM is one of the many methods of additive manufacturing (AM). AM is a process of adding materials to fabricate objects in successive layers to form three-dimensional (3D) parts. In earlier years, AM was limited to single material printing. Currently, material with fiber-reinforced composites can be manufactured/printed by stereolithography (SL), laminated object manufacturing (LOM), fused deposition modeling (FDM), selective laser sintering (SLS), and extrusion (EDAM). Despite mentioning multiple methods, the focus of this study is only on the EDAM process.

Description of the steps in the EDAM process

The process of the EDAM starts with drying a feedstock material, which is in a pellet form, to a certain humidity level. The dried material is melted in the printing equipment and extruded through a printing nozzle in the form of beads. The bead exiting the nozzle turns 90 degrees and deposited the first layer on a substrate which can be heated to a predefined temperature or maintained at room temperature. A sequence of layers is deposited one after another until a 3D part is formed. The deposition pattern is predefined following a machine code that provides time, position, etc.

Applications for the EDAM process

One advantage of EDAM is utilizing pelletized feedstock material which has a wide range of commercially available materials. Moreover, EDAM has high deposition rates, so parts are printed near the final shape and, if needed, surface finished in a separate operation. Examples of the commercially available large-scale EDAM printers are Big Area Additive Manufacturing (BAAM) developed by Cincinnati Incorporated in collaboration with Oak Ridge National Laboratories (ORNL) [1], Large Scale Additive Manufacturing (LSAM) developed by Thermwood, Wide and High Additive Manufacturing (WHAM) developed by ORNL and Ingersoll Machine Tools, Inc, etc. At Purdue University, an EDAM based 3D printer was also developed called the Composite Additive Manufacturing Research Instrument (CAMRI) capable of depositing 6 kilograms per hour of high temperature and highly reinforced polymer composites [2]. Big and massive parts can be manufactured the large-scale printers. To put in perspective, the deposition rate of LSAM ranges from 90 to 230 kilograms per hour [3], and WHAM has the targeted deposition rate of 450 kilograms per hour [4]. Figure 1.1-1 shows three parts that were printed at Local Motors.

(a) Olli, Local Motors

(b) Strati, Local Motors

(c) LM3D Swim , Local Motors

Figure 1.1-1: Examples of EDAM applications

Phenomena involved in the EDAM process

This section summarized the key phenomena involved in the EDAM process which may be different for each printer. In other words, the bead's properties are printer dependent. A detailed discussion can be found in the dissertation by Barocio [2]. First, the pelletized material enters the single-screw extruder and is heated along the barrel of the extruder. While in the extruder, the degradation of fiber length in single-screw extrusion occurs during the extrusion process due to pellet-to-pellet and pellet-to-extruder interactions[5], [6]. The amount of fiber attrition depends on the screw design. Upon exiting extruder through the print nozzle, the material is fully melted. The material flowing out of fiber suspensions off the nozzle is highly anisotropic due to the local orientation of the fiber which has been reorientated in the steps discussed before. Depending on the nozzle design, features like converging zones in printing nozzles and shear flow developed inside the printing nozzle can give rise to rapid collimation of fibers along the extrusion direction [7]. The local fiber orientation is also dependent on the size and length of the nozzle.

Once the material leaves the extrusion nozzle fiber suspension is called an extrudate or a printed bead. Because the nozzle is held vertically, the extrudate rotates 90 degrees to lay down on a horizontal build plate. During the 90-degree turn, the fiber suspension experiences shear deformation, thereby promoting further orientation of the fibers along the printing direction. The factors that may affect fiber orientation is the nozzle size and the height between the nozzle and the deposition plane. Lastly, compaction of the extrudate with either a roller (LSAM) or a tamping mechanism (CAMRI) occurs right after this 90-degree turn. Depending on the compaction conditions, changes in fiber orientation inside the extrudate can be introduced. Now it is understandable that the fiber orientation is dependent on both the printer and the processing condition.

It is an advantage of the EDAM process that the processing conditions can be altered to optimize the properties of the printed bead. It is known that the properties of a fiber-reinforced polymer are highly dependent on fiber orientation. The elastic, thermomechanical, thermophysical, and thermoelastic properties are all dependent on the fiber orientation. In fact, the motivation of this study is to understand the effect of fiber orientation tensor in the residual stress and deformation of the final part.

1.2 Technical challenges of the EDAM process

Composite materials are anisotropic by nature which is both helpful in some applications but can also be a challenge of AM. In an anisotropic material, the properties vary with direction. The fiber reinforcement is oriented in the optimal direction to carry the load and the matrix will protect and support the reinforcement. It also comes with the drawback of having different behaviors in all directions, therefore, posing a new challenge for geometry assurance.

First, since the reinforcing fibers generally align during the extrusion process, the thermal expansion of the composite along the deposition direction is restrained by fibers, whereas the thermal expansion perpendicular to the bead is largely unconstrained. This leads to an anisotropic expansion of the material that is dependent upon the local deposition path, which can be complex. Multiple studies discuss in this section found that the deposition of the material leads to asymmetrical thermal gradients that caused residual stress and then distortion.

Temperature gradient

The temperature gradient in the part during material deposition is unavoidable in the EDAM process because the hot extruded bead of each layer is laid down at a different time. Temperature gradient leads to a mismatch in thermal strain among layers which results in residual stress [8] [9]. Upscaling the size of printed objects from the centimeters scale to the meters scale aggravated the difference in thermal strain [9]. There have been studies to improve the thermal conductivity in order to lessen the temperature gradient. Some studies add thermal conductive fillers such as aluminum nitride, silicon nitride, alumina, boron nitrite, graphite, and carbon nanotubes [10]. However, adding some particle worsen the mechanical properties. A study by Minghui et al. [10] reinforced the polyamide filled with thermally conductive fillers, with glass fiber and carbon fiber reinforced fibers separately to improve the mechanical properties of the composites. Despite the improvement of the thermal properties of the material, the thermal gradient in EDAM print will still exist.

Residual stress

The distortion of the part during and after the print is one of the most important issues in the EDAM process. The non-isothermal cooling process of the printed part and the anisotropy of the printed

material give rise to internal stresses in printed parts [11] [12] [13]. This residual stress could lead to distortion and de-layering problems [9], which affect the shape and the final dimensions of the parts. In some cases, it could prevent the completion of the objects due to detachment of the part from the bed. A common technique to attach the part to the bed is to use a heated bed with some type of adhesive, or a substrate with the ability to adhere to the bottom layer surface. Although such procedures help reduce distortions, they can increase the residual stresses in the final part. Residual stress not only give rise to part distortion and dimensional inaccuracy but also has a detrimental influence on mechanical performance [14][15][16]. Efforts have been made by researchers in understanding the residual stresses in additively manufactured parts. For example, Kantaros et al. [11] studied the residual strains in ABS parts fabricated by FDM using fiber Bragg grating method. Zhang et al. [16] studied the effects of raster angle and printing speed on neat and reinforced ABS. These research efforts have contributed to the understanding of residual stresses in additively manufactured parts. However, more studies on short fiber reinforced thermoplastic and the EDAM processing parameters are still needed to be conducted to understand and to minimize the detrimental effects of residual stress.

Deformation

One type of dimensional change is the warpage which happens in the out of plane direction (the stacking direction). The main cause of the warpage is the mismatch in thermal strain which is caused by thermal gradient in the AM process, as discussed earlier. Another dimensional distortion is called “spring-forward’, or “sping-in” which is an in-plane deformation. The main cause of spring- in deformation is the mismatch in thermal expansion along and the print direction and the transverse direction which accumulates as residual stress. According to Radford and Rennick [15], there are two components contributing to the distortion, thermoelastic and non-thermoelastic components. Thermoelsatic distortion refers to shape changes related to the thermal expansion coefficient (CTE). Non-thermoelastic distortion refers to stress introduced isothermally during the irreversible cure process such as crystallization shrinkage.

Adding carbon fibers reduces the overall thermal expansion of the thermoplastic because carbon fiber is an order of magnitude smaller than that of polymers [8]. On the other hand, having fibers in the polymer during the extrusion process leads to anisotropic behavior because fibers are

generally aligned in the deposition direction. Therefore, understanding the thermal and mechanical performance becomes more challenging.

1.3 Overview of Micromechanics and methods for calculating composite effective properties

The main advantage of micromechanics is to perform virtual testing to reduce the cost of an experimental characterization. The experimental characterization of composite materials is laborious and expensive. In the context of EDAM, where processing conditions can be varied and tailored to a specific need. To understand the mechanical properties change due to different printers, or even changes made in the same system (e.g., nozzle sizes, bead compaction levels, or processing speeds), it would require a perpetual number of tests.

Virtual characterization can be done once the properties of the constituent are known. There are several ways to obtain constituent material properties. To mention a few; experimental testing for each constituent, and by reverse-engineering the constituent properties through some experimental testing of the heterogeneous material. For this study, some limited constituent properties were provided by the manufacturer. For the properties not provided, reverse engineering was performed.

During the past years, there have been several approaches formulated to evaluate the effective elastic properties of a unidirectional short fiber composite. These are Voigt and Reuss approximations, Eshelby [17] inclusion approximation, self-consistent scheme [18], Mori- Tanaka scheme [19], and the Halpin-Tsai model.

The objective of the homogenization models is to predict the effective properties of heterogeneous materials using the underlying microstructural information, such as shape, orientation, volume fraction, etc. Homogenization techniques can be classified into analytical and numerical computational based approaches. Methods based on finite element analysis (FEA), Generalized method of cells (GMC), Fast Fourier Transforms (FFT), and Mean-Field Homogenization (MFH) are some of the examples of the homogenization techniques. The focus of this study is on MFH because it can compute approximate but accurate estimates at a reasonable computational cost.

However, the limitation is the MFH is unable to predict any strain or stress localization, and cannot take into account clustering, percolation, and size effects [20].

Mean-Field Homogenization

The purpose of mean-field homogenization (MFH) is to compute approximate but accurate estimates of the volume averages of the stress and strain fields. Some examples of the MFH model are the Voigt model, the Reuss model, Hashin-Shtrikman bounds, Self-consistent schemes, Eshelby model, and the Mori-Tanaka model. Voigt model assumes that the strain field is uniform inside the RVE. In the Reuss model, the stress field is assumed to be uniform in the RVE. Both Voigt and Reuss models generalize the simple 1D models of bars in parallel, and in series, respectively. Both models are too simplistic but can be used as upper and lower bounds solution. The method selected for this study is the Mori-Tanaka Model because it has been often the primary choice among engineers to provide quick estimates of the macroscopic response of generally random composites.

Eshelby [17] model is discussed first here as it enables to solve the single inclusion problem. Eshelby model a single-inclusion problem described as an ellipsoid is cut out of an infinite matrix, undergoes a stress-free eigenstrain, and is inserted back into the matrix as shown in Figure 1.3-1 obtained from Digimat user manual. Starting from the stress-free state, the inclusion undergoes a stress-free transformation strain, fitting the inclusion and matrix back together, and produces the strain state in both the inclusion and the matrix.

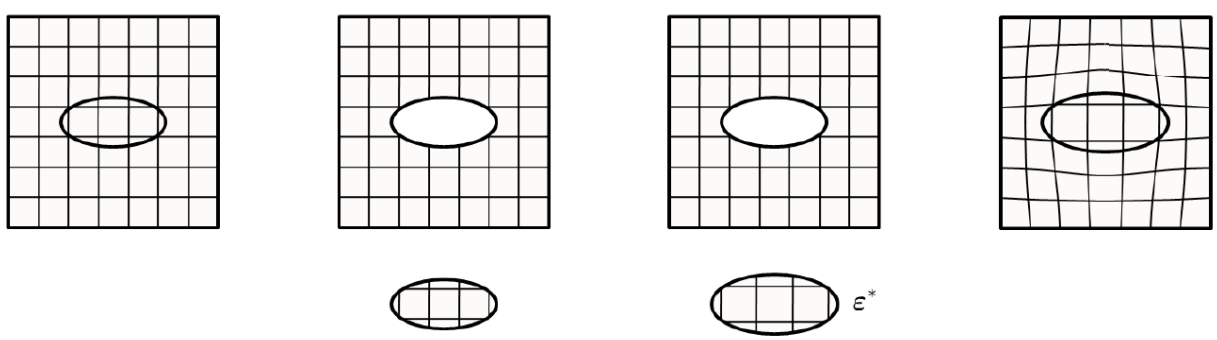

Figure 1.3-1: Illustration of Eshelby's problem. Figure from Digimat user manual [21]

The key result of Eshelby was to show that the strain inside the ellipsoidal inclusion volume is uniform and related to the eigenstrain as

$$\varepsilon(x) = \zeta(I, C_0): \varepsilon^*, \forall x \in (I)$$

Where $\zeta(I, C_0)$ is Eshelby's tensor, and it depends only on the inclusion aspect ratio and the matrix elastic constants C_0. More information can be found in Mura's work [22].

Eshelby's model is for a single inclusion problem, but composites have several inclusions in the matrix. Let's now look at the Mori-Tanaka [19] model which was developed for a two-phase composite. The derivation is based on an approximate use of Eshelby's solution. The Mori-Tanaka model assumes that each inclusion behaves like an isolated inclusion and the strain in the matrix is considered as the far-field strain. That is, each inclusion views a far-field strain equal to the average strain in the matrix. Benveniste [23] assumed perfect bonding is between the constituents which can have general elastic anisotropic behavior. Benveniste's derivation is limited to two-phase composites, which can be anisotropic elastic constituents, with an inclusion phase consisting of ellipsoidal particles. Benveniste then proposed the constitutive equations of a fiber-reinforced composite expressed in terms of the average strain and stress based on the Mori–Tanaka model by,

$$\langle\sigma\rangle = C\langle\varepsilon\rangle$$

Where C is the effective average elastic moduli given by

$$C = \left(V_m C_m + V_f C_f A\right)\left(V_m I + V_f \langle A\rangle\right)^{-1}$$

Where I is the fourth-order tensor identity tensor, C_f is the fourth-order elasticity tensor of the fiber, C_m is the fourth-order elasticity tensor of the matrix, V_f is the volume fractions of the fibers, V_m is the volume fractions of the matrix, and A is the Eshelby strain-concentration tensor which relates the average strain ε_f and ε_m through the expression

$$\varepsilon_f = A\varepsilon_m$$

Where A is given by

$$A = \left[I + \zeta (C_m)^{-1} \left(C_f - C^m\right)\right]^{-1}$$

Where ζ denotes fourth-order Eshelby's tensor. The components of ζ for several cases of anisotropic matrix and isotropic matrix can be found in the study by Mura [24].

Figure 1.3-2 illustrates the Mori-Tanaka model. The Mori-Tanaka model is very successful in predicting the effective properties of two-phase composites. In theory, it is restricted to moderate volume fractions of inclusions of less than 25% , but in practice, it can give good predictions well beyond this range [21].

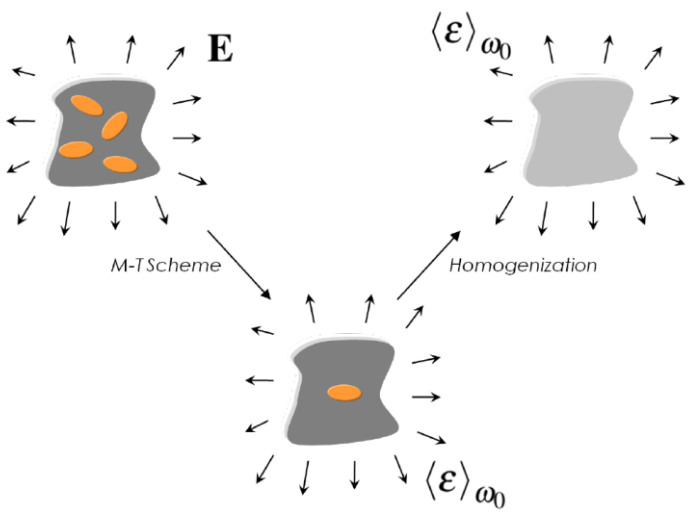

Figure 1.3-2: Illustration of the Mori-Tanaka (M-T) model. Figure from Digimat user's manual [21]

Multi-step homogenization

Generally, the matrix material is reinforced with inclusion, which is not necessarily aligned in the same direction, and not necessarily the same size. A multi-step homogenization procedure introduced by Camacho et al. [21], Lielens [21], and Friebel [25] was developed for RVE containing a matrix and inclusions of different orientations. For this study, this refers to composites with non-aligned inclusions. The homogenization programmed in Digimat-MF is carried out in two steps which are illustrated in Figure 1.3-3. The composite is decomposed into an aggregate

called pseudo-grains, with each grain containing one inclusion family and the matrix. The inclusions in each family have the same material properties, aspect ratio, and orientation. The homogenization of the model RVE is performed in two steps. In the first step, homogenization is performed in each grain using the user-specified formulation. Digimat MF has two options; Mori-Tanaka or interpolative Double inclusion. In the second step, the Voigt formulation is used to compute the properties of the overall composite by homogenizing the pseudo-grains. Mori-Tanaka model wasn't used here because it might lead to physically unacceptable macro predictions, according to Benveniste et al. [26], Pierard et al. [25], and Digimat user's manual [21].

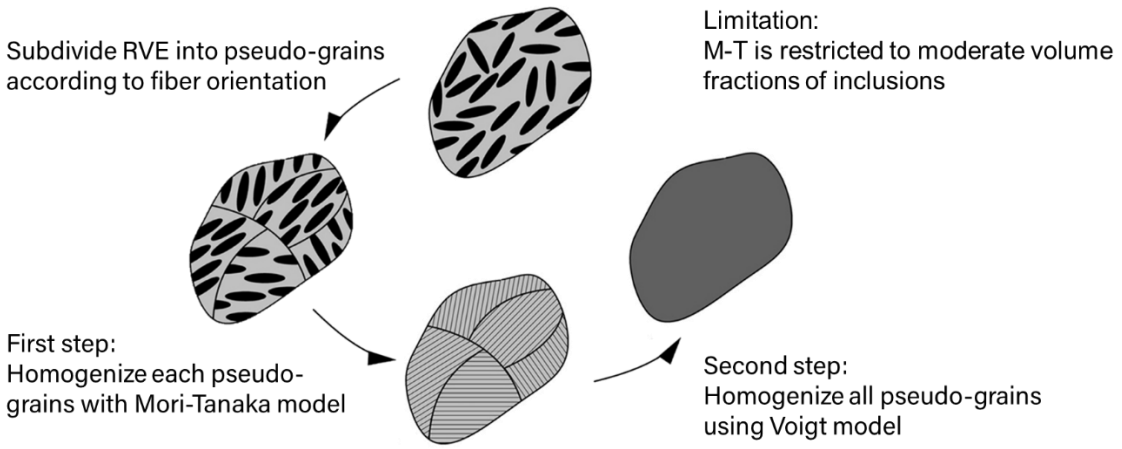

Figure 1.3-3: The RVE is decomposed into a set of pseudo-grains, which are individually homogenized in the first step. The second step is homogenization over all the pseudo-grains

1.4 Overview of EDAM process simulation with Additive3D

EDAM process simulation, called Additive 3D, is a thermo-mechanical simulation framework utilizing Abaqus© developed by Barocio, Brenken, and Favaloro[2], [27], [28]. The simulation captures the actual process of depositing beads of molten material in a layer by layer basis is replicated by activating elements in a finite element mesh. This section only provides an overview, the description of the simulation framework is discussed in detail in the dissertation by Brenken [27], and Barocio [2].

Figure 1.4-1 shows the Process simulation Additive3D inputs and outputs. Machine code refers to the geometry definition including slicing parameters such as infill percentage, number of outer perimeters, angle of the infill, number of solid layers, etc. Upon slicing of the geometry, the machine code that contains the printing trajectories is generated in the language of G-code containing only position

commands. The event series is generated from G-code contains printing history, namely time, the spatial position of the extruder, extrusion status, and type of feature printed. Next, the AM system card contains information about the environment of the printer such as the type and temperature of the print bed, the compaction system, etc. The last input is the digital material card, this includes all the properties characterize in the section 2.EXPERIMENTAL CHARACTERIZATION OF ADDITIVELY MANUFACTURED FIBER REINFORCED THERMOPLASTIC. Some of the material properties are printer dependent, namely, crystallization kinetics, glass transition temperature, and melting behavior. Some properties are printer dependent and have to be experimentally or virtually characterize for each printer.

The EDAM process simulation performs heat transfer analysis first by utilizing multiple user subroutines, namely UFIELD©, the UMATHT©, and the UMDFLUX©. The heat transfer analysis captures phenomena like convection, radiation, tamper heat losses, orthotropic heat transfer, latent heat of crystallization, etc. The key information obtained from the heat transfer analysis are the prediction of temperature, degree of crystallinity, and the degree of bonding between adjacent layers. The temperature history output by the heat transfer analysis is then used in a mechanical analysis along with the other subroutines, namely UMAT© and UEXPAND©. By doing so, the material shrinkage and the stress evolution in the printed part is coupled with the temperature evolution precomputed in the heat transfer analysis. The thermoviscoelastic behavior and the orthotropic material shrinkage of the printed CF reinforced PPS was analyzed in the mechanical analysis. The results of the stress analysis are the residual stresses and residual deformation of the printed part.

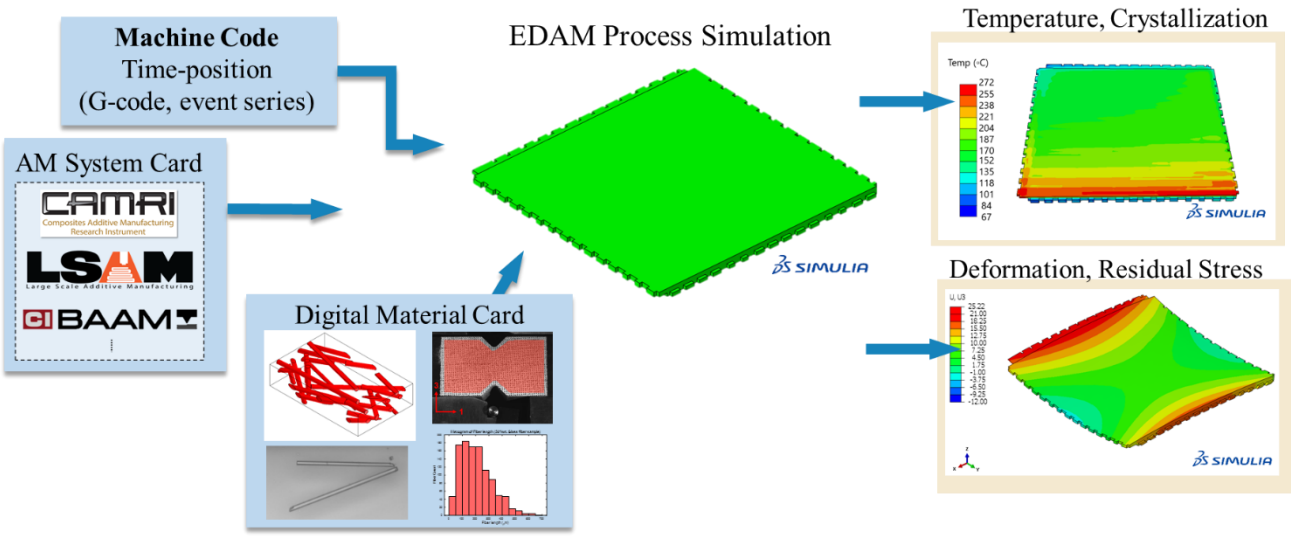

Figure 1.4-1: Overview of the process simulation Additive3D for the EDAM method

1.5 Motivation for this work

One of the EDAM process's challenges is part distortion such as warpage, spring in, and delamination. Compare to neat polymer, the fiber reinforcement makes the thermomechanical performance of the printed part more complex. Meanwhile, it also improves the thermal performance and strength of the part. Moreover, because of the complexity, it also provides the opportunity to tweak the system to the user's advantage. In order to use the fibers to the maximum advantage, this thesis aims to study the relationship between the fiber orientation tensor to the properties of the composite and the residual stress and deformation of the final part. By doing so will provide better knowledge to optimize the fiber direction to best suit for a specific use of the part. The fiber alignment can be altered in several ways such as changing the shape and size of the nozzle, compaction system, print speed, bead dimension, etc.

The importance of mitigating stress is highlighted in the medium to large scale prints. The deformation may not seem significant in a small scale print, but for a large scale print with dimensions in the scale of meters, the residual stress accumulates and the deformation becomes noticeable. In some cases, internal stress lead to interlayer crack and failed prints. Even though the part can be printed with excess geometry and machined down to the final shape, those internal stress still exists.

The reason behind studying fiber orientation state is because it is the prime factor that governs the properties of the additive manufactured bead. When aligned in a particular direction, performance in that direction immediately improves. It can be helpful in some applications in terms of strength and geometry accuracy in that direction. However, high fiber collimation also leads to a high degree of anisotropy. The effect of fiber types, such as isotropic fiber, like glass fiber, and transversely isotropic fiber, such as carbon fiber, are also expected to influence the effective properties of the composites. Thus, the first question to be addressed in this study is: How do microstructural properties of short fiber composite affect the macroscopic effective properties?

In a related topic, the EDAM parts are also expected to be influenced by the macroscopic effective properties of the composites. Anisotropic cooling and anisotropic shrinkage, and directional strength of the composites are some factors that influence the residual stress and deformation of the printed parts. Therefore, another interesting question that this study aims to address is: how does fiber orientation tensor affect the deformation and residual stress of an EDAM part? This serves to be a good preliminary study to understand process-induced deformations in EDAM.

2. EXPERIMENTAL CHARACTERIZATION OF ADDITIVELY MANUFACTURED FIBER REINFORCED THERMOPLASTIC

The material characterization was carried out with the panels printed with a bead aspect ratio of 4 and bead dimensions of 0.8” x 0.2” (width x thickness) which is the condition used predominantly in the LSAM system. The goal is to characterize mechanical, thermomechanical, thermoviscoelastic, and thermophysical properties in all three-principal direction. Given that the GF-PA is a semi-crystalline polymer, the melting and crystallization kinetics also need to be characterized. All of the printing was done at Local Motors.

2.1 Specimen Preparation

To perform the characterization that is dependent on the bead orientation, two types of panels were printed. Panels for characterizing properties in the 1-3 plane were extracted from hollow rectangles printed with one bead walls, whereas panels for characterizing properties in the 1-2 plane were extracted from rectangular panels printed horizontally on the build plate.

Table 2.1-1 lists the extrusion condition such as temperature profiles for the extruder and print speeds used for processing the GF-PA in the LSAM.

Table 2.1-1: Extrusion conditions used in the LSAM

Extrusion Conditions	Values (°C)
Extruder hopper	250
Extruder zone 1	260
Extruder zone 2	282
Extruder zone 3	296
Melt Pump connector	261
Melt Pump	296
Extrusion Nozzle	343
Deposition Speed (mm/min)	2540
Build plate temperature	Room

2.1.1 1 - 3 Plane

Figure 2.1-1 illustrates the preparation process of the panel in the 1-3 plane. First, a one bead hollow rectangular box was printed with the LSAM system at Local Motors. The width of the printed bead and therefore the width of the single-bead walls is 20.32 mm (0.8”). Similarly, the height is 25 beads which correspond to around 127 mm (5”). Notice that the side of the wall is not smooth due to the curvature of the bead. Once the wall cooled to room temperature, the surface of the panels was machined for removing the scalloped surface. A wood planner equipped with carbide tips was used for machining the panels. By removing equal amounts of material from each side, a 12 mm wide panel was obtained. Based on the measured sample dimensions, 40% of the original printed bead width was removed or about 20% from each side. Additionally, the two bottom-most layers of the wall were discarded.

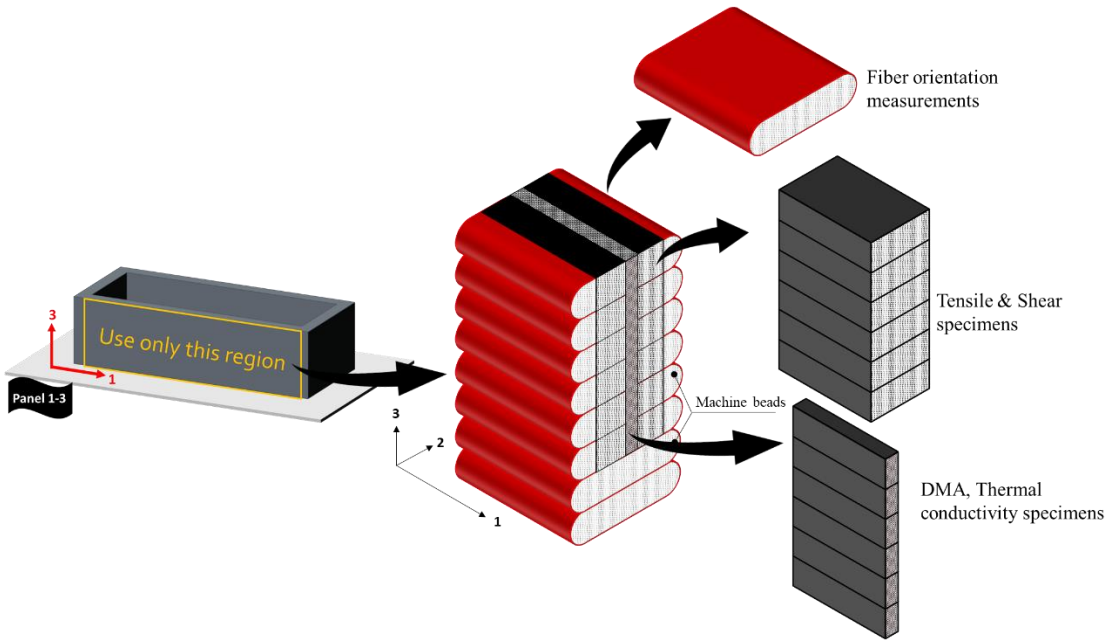

Figure 2.1-1: Steps for preparing panels in the 1-3 plane

Next, as depicted in Figure 2.1-1 above, the long rectangular pieces were machined in the print direction from the long side of the printed box. These tensile coupons were six printed bead layers wide (3 direction) and 165 mm long (1 direction). The gage width is designed to be the nearest integer of bead height closest to 20 mm. From these rectangular pieces, taper shouldered tensile bars were machined having a gauge width that was four beads wide (3 direction). As a result, the

tab width is six beads wide or 1.5 times the gauge width. Resulting in a cross-sectional area of approximately 255 mm^2. The dimensions of the tensile specimen can be found in the APPENDIX Figure A 1. All coupons were manufactured according to the ASTM D638 guidelines [29]. Note that specimens were extracted from panels instead of being printed to their final shape with no post-machining operations because the goal is to characterize the tensile properties of the material, not the properties of the mesostructure of the printed tensile structure.

2.1.2 1 - 2 Plane

The preparation process of the panels in the 1-2 plane starts with printing a horizontal panel with five layers in the stacking direction. The height of one layer is 0.2 in (5.08 mm) which makes the height of the panel approximately 25.4 mm. Then, using the wood planar, two layers from the bottom and one layer from the top were removed. The final height of the part is approximately 10 mm. Figure 2.1-2 shows the specimen extraction location for characterizing the material properties in the 1-2 plane.

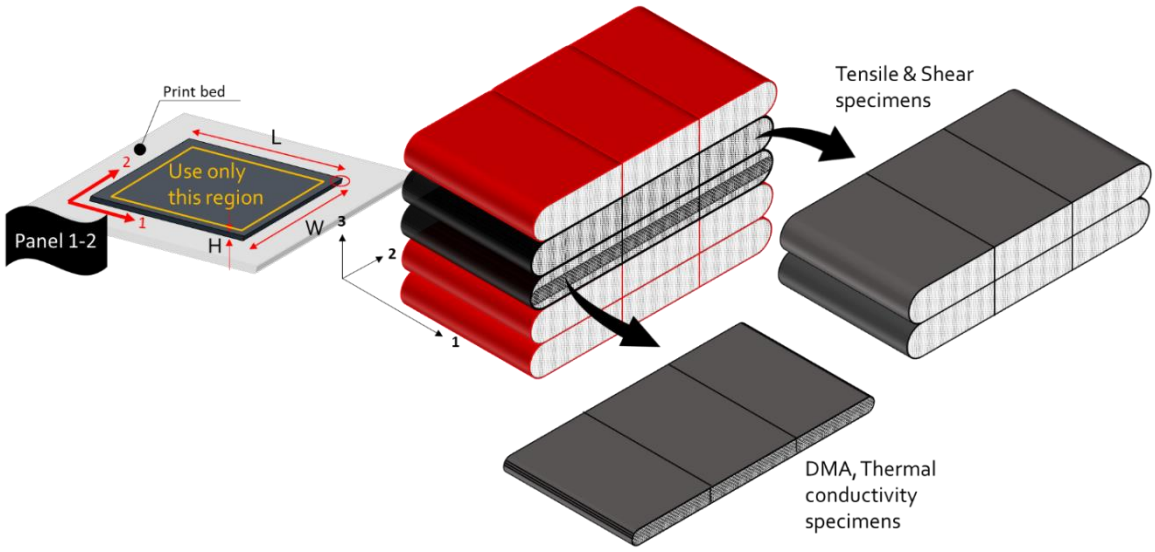

Figure 2.1-2: Steps for preparing panels in the 1-2 plane

All the panels were heat-treated at 170 °C for two hours in a forced convection oven. This step is required to achieve the maximum possible crystallinity in the material and to relieve thermal stresses developed during the printing process of the panels. Following the waterjet cut, the

specimens were dried in an industrial material dryer for 12 hours at 50 °C to remove the moisture from the specimens.

2.2 Microstructure of Printed Material

Most properties characterized in this program are dependent on the microstructure of the printed bead, namely fiber length distribution, fiber orientation distribution, and void content. For example, the coefficient of thermal expansion (CTE) and the elastic properties are strongly dependent on the fiber orientation distribution [30].

The GF-PA used in this program is made through a compounding process that yields a composite material with relatively short average fiber length. Furthermore, additional attrition of the fibers can occur during the melting process of the pellets in the single-screw extrusion process [31]. Therefore, the distribution of fiber lengths was characterized for material processed in the LSAM system.

2.2.1 Fiber Orientation

The microstructure measurement sample is shown in Figure 2.2-1. A single bead was sectioned using the precision sectioning saw for fiber orientation measurements from the 1-3 panel.

Figure 2.2-1: Fiber orientation measurement sample

The fiber orientation was obtained by using micro-Computerized Tomography (CT) technique scan-generated three-dimensional image of fibers. The raw CT-Scan data were collected using a Zeiss Xradia 510 Versa Micro CT instrument with a voxel size of 3.24um. The reconstructed data was a vertical stitch of 4 separate scans (each scan setting: 2001 frames, 20s exposure time, source

voltage 80kV, and source power 7W). The reconstructed data was imported as 8-bit unsigned tiffs into Volume Graphics VGStudio Max 3.2 and filtered with a non-local means filter with a smoothing factor of 1. The fiber orientation was calculated using the Fiber Composite Material Analysis Add-in with an integration mesh defined by six cells in the thickness direction, 4 cells in the width direction, and 1 cell in the length.

The micro-CT scans were broken into finite rectangular sections as shown in the red sectioning lines in Figure 2.2-2. The average fiber orientation in the three-principal directions was calculated in each section. A11 is the orientation tensor in the 1 direction which is the print direction. Because the figure shows the bead's cross-sectional area, 1 direction is the direction pointing out of the page. A22 is the orientation tensor along the transverse direction which is to the left and right of the page. A33 is the orientation tensor along the stacking direction pointing up. Table 2.1 2 listed the average fiber orientation in the 1-direction of the corresponding section in Figure 2.2-2. The table of the average fiber orientation of the 2-direction and 3-direction can be found in APPENDIX Figure A 2. The bolded numbers mean the section is completely filled with material, which is mainly in the middle of the bead. The regular unbolded numbers mean the section is not filled with material, therefore, they will need further calculation to obtain the actual area-weighted average.

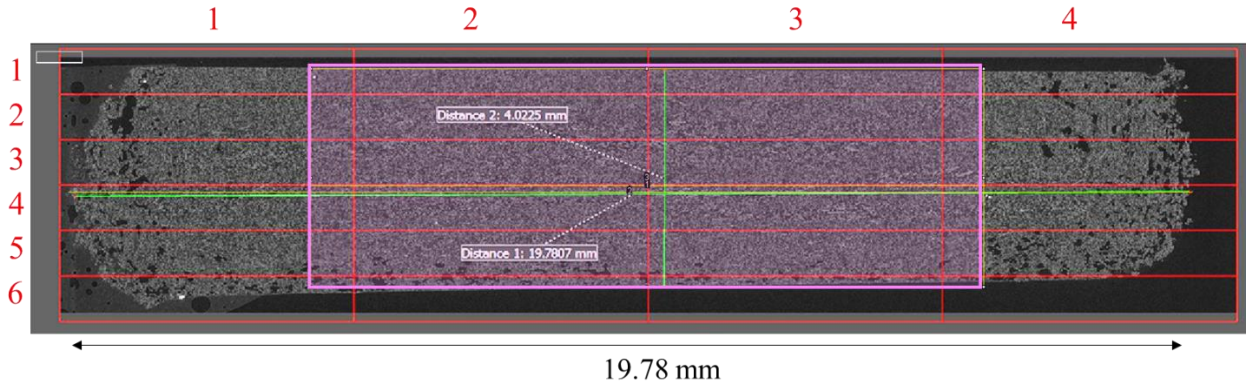

Figure 2.2-2: Micro CT scan of LSAM- AR 4

Table 2.2-1: Fiber Orientation of LSAM- AR 4 in the 1-direction of each section of the bead

A11 = 0.58	**1**	**2**	**3**	**4**
1	0.68	0.57	0.58	0.63
2	0.66	**0.47**	**0.51**	0.61
3	0.62	**0.44**	**0.43**	0.61
4	0.62	**0.49**	**0.45**	0.62
5	0.67	**0.62**	**0.6**	0.68
6	0.64	0.64	0.6	0.54

As shown in, the average fiber orientation in the outer region of the bead has higher A11 than in the middle region highlighted in blue. The final fiber orientation is a weighted area average of these sections. The weighted area average is preferred over the number average because the bead is an ellipse, therefore, the outer edge section is not completely filled with material. Therefore, the contribution of those outer edge sections should be less than the middle section which is completely filled with material. Area fraction is the area of the material in each subsection divided by the area of the CT scan rectangular divided subsection. For example, the section completely filled with material such as in the middle of the bead has an area fraction of 1. The section with only half of the area occupied with the material has an area fraction of 0.5. The ImageJ software was used to measure the area of the material filled in each subsection of the bead. The area-weighted average fiber orientation of each subsection can be found in the APPENDIX Table A 2.

For the mechanical testing purpose, the outer part of the bead or the curvature part of the bead was removed by a wood planer. The outer part of the bead, in other words, the curvature part of the bead was machined away. It is inappropriate to assume the fiber orientation of the mechanical specimens, namely shear, and tensile specimens to have the same fiber orientation as the whole bead's fiber orientation. Thus, another step is required. Figure 2.1 2 shows the region of the shear and tensile specimens in pink. ImageJ was again used to measure the area of the sections in pink. Therefore, the tensile specimen bead was only the area in pink shown in Figure 2.2-2. The area-weighted fiber orientation of the pink region was calculated and shown in in the APPENDIX.

Table 2.2-2 summarizes the fiber orientation tensor of the area weight whole bead and area-weighted planed bead which will be utilized in the characterization section.

Table 2.2-2: Summary of the number average, area-weighted average fiber orientation Tensor A_{ij} of LSAM- AR4 whole bead and machined bead

Sample	Number Average Whole Bead	Area Weighted Whole bead	Machined bead
LSAM – AR 4	$A_{ij} = \begin{bmatrix} 0.58 & 0 & 0 \\ 0 & 0.32 & 0 \\ 0 & 0 & 0.10 \end{bmatrix}$	$A_{ij} = \begin{bmatrix} 0.57 & 0 & 0 \\ 0 & 0.34 & 0 \\ 0 & 0 & 0.09 \end{bmatrix}$	$A_{ij} = \begin{bmatrix} 0.53 & 0 & 0 \\ 0 & 0.39 & 0 \\ 0 & 0 & 0.08 \end{bmatrix}$

2.2.2 Fiber Length

To isolate fibers from the matrix, a small section of the LSAM printed part with AR of 4 was burnt off in a small furnace. The samples were heated to 700°C and kept in the furnace for a total of two hours before turning off the furnace. This process burnt off the polyamide in the composite, leaving the glass fibers accompanied with some residues. Figure 2.2-3 shows the printed material before and after the matrix burnt off. The LSAM printed GF-PA is indicated by the red circle.

Figure 2.2-3: Printed GF-PA before and after burning off the matrix

Following the burn off of the matrix, the white glass fiber was transferred into a microscope glass slide and dispersed with silicone oil. A thin microscope cover glass was placed on top of the fiber which also helps further dispersed the fibers. A mosaic of images was captured with a LEICA DMI 5000 M optical microscope. The image constructed with the mosaic of images was then used for measuring the length of the fibers. Figure 2.2-4 shows a section of the image used for measuring

fibers. The software ImageJ [32] was utilized for manually measuring 1000 fibers. To measure the fiber length, line segments were drawn manually for each fiber ignoring fragments and residues such as the one highlighted in Figure 2.2-4.

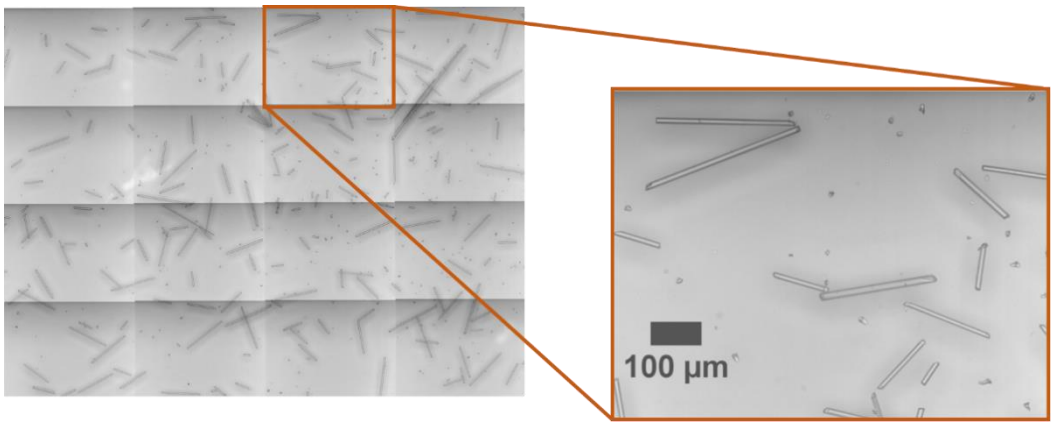

Figure 2.2-4: Fibers dispersed on a glass slide

A histogram was constructed with the 1000 measurements to display the distribution of fiber length (Figure 2.2-5). While the longest fiber measured was 638.83 µm, the shortest fiber measured was 22.09 µm. There are two methods of averaging fiber length, the number average, and the weighted average. The number average method, L_n, can be computed using the equation 2.2.1, where n_i is the number of fibers of length L_i. Number average is the common way to determine the average quantity of interest.

$$L_n = \frac{\sum_i n_i L_i}{\sum_i n_i} \tag{2.2.1}$$

On the other hand, the weighted average method, L_w, is better in capturing the presence of longer fibers as it is believed to influence the mechanical properties more than the short fibers [33]. Weight average fiber length can be calculated using equation 2.2.2.

$$L_w = \frac{\sum_i n_i L_i^2}{\sum_i n_i L_i} \tag{2.2.2}$$

The number average fiber length computed is 205.83 µm and the weight average fiber length computed is 272.41 µm. The weighted average fiber length is used in the micromechanics virtual characterization and reverse engineering in a later section.

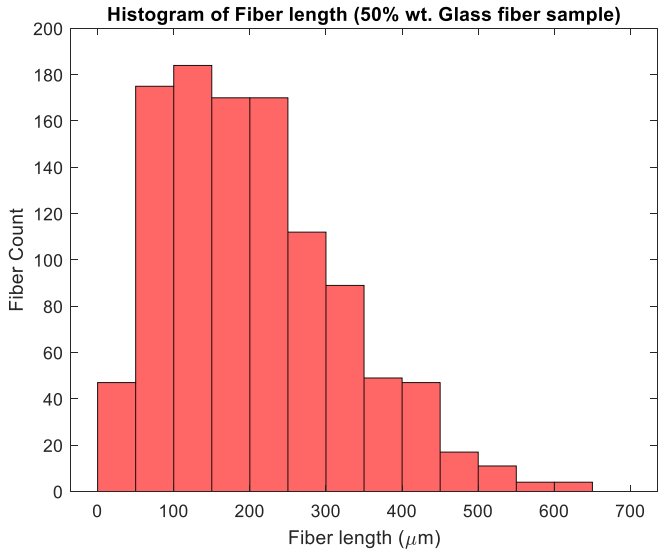

Figure 2.2-5: Fiber length distribution

2.3 Elastic properties

To characterize an orthotropic material, 9 constants are required to complete the compliance or stiffness matrix. The constants are reduced from 21 to 9 due to the three mutually orthogonal planes of symmetry. Those constants are E_1, E_2, E_3, G_{12}, G_{13}, G_{23}, v_{12}, v_{13}, and v_{23} as shown in the compliance matrix used in Equation 2.3. Some of which can be calculated by the relationship of

$\frac{v_{21}}{E2} = \frac{v_{12}}{E1}$, $\frac{v_{31}}{E3} = \frac{v_{13}}{E1}$, $\frac{v_{32}}{E3} = \frac{v_{23}}{E2}$.

$$\begin{Bmatrix} \varepsilon_{11} \\ \varepsilon_{22} \\ \varepsilon_{33} \\ 2\varepsilon_{23} \\ 2\varepsilon_{13} \\ 2\varepsilon_{12} \end{Bmatrix} = \begin{bmatrix} \frac{1}{E_1} & -\frac{v_{21}}{E_2} & -\frac{v_{31}}{E_3} & 0 & 0 & 0 \\ -\frac{v_{12}}{E_1} & \frac{1}{E_2} & -\frac{v_{23}}{E_3} & 0 & 0 & 0 \\ -\frac{v_{13}}{E_1} & -\frac{v_{23}}{E_2} & \frac{1}{E_3} & 0 & 0 & 0 \\ 0 & 0 & 0 & \frac{1}{G_{23}} & 0 & 0 \\ 0 & 0 & 0 & 0 & \frac{1}{G_{13}} & 0 \\ 0 & 0 & 0 & 0 & 0 & \frac{1}{G_{12}} \end{bmatrix} \begin{Bmatrix} \sigma_{11} \\ \sigma_{22} \\ \sigma_{33} \\ \sigma_{23} \\ \sigma_{13} \\ \sigma_{12} \end{Bmatrix} \tag{2.3}$$

However, in this study only E_1, E_2, E_3, G_{13}, v_{13} were physically measured. The other properties were obtained via micromechanics. Tensile test, and shear (Iosipescu) test procedures and results will be discussed.

2.3.1 Tensile Properties (E_1, E_2, E_3)

The sample preparation includes printing, machining, heat treating, water jetting, drying, and applying speckle patterns. Printing and machining were covered in the subsection. The tensile test in the print direction and data reduction was performed at DuPont and the test in the transverse and stacking direction were performed at Purdue University.

Tensile Properties in the Print direction

Tensile testing in the 1-direction was performed using a 100,000 lbf Servo Hydraulic Test Frame. The sample was held with hydraulic wedge grips with textured grip faces and the force was measured with a 100,000 lbf load cell. The test speed was 2 mm/minute and data was collected at 20 Hz. A clip-on extensometer was used to measure the strain over a 2-inch gauge length. Figure 2.3-1 shows the test set-up including the servo hydraulic test frame, the load cell, and the extensometer.

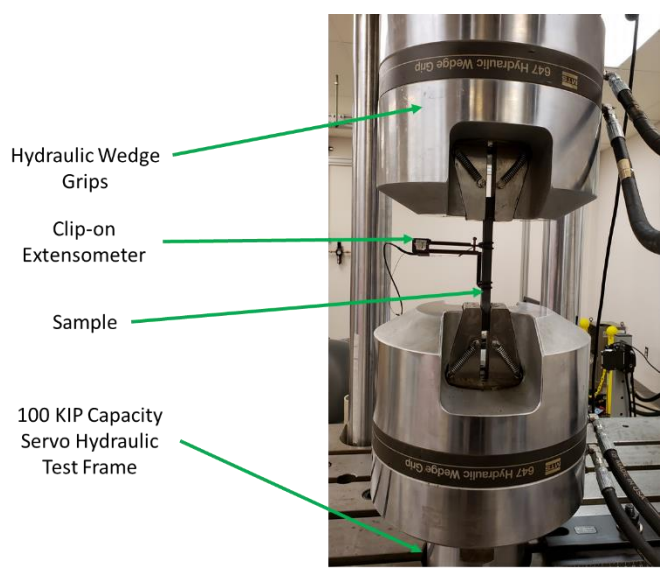

Figure 2.3-1: Illustration of servo hydraulic test set-up

Tensile properties were measured in the print direction for the three different print conditions to assess the effect of the bead aspect ratio on the tensile modulus and strength. Figure 2.3-2 shows all sample failures initiated in the shoulder region at the interface between the continuous and interrupted print layers.

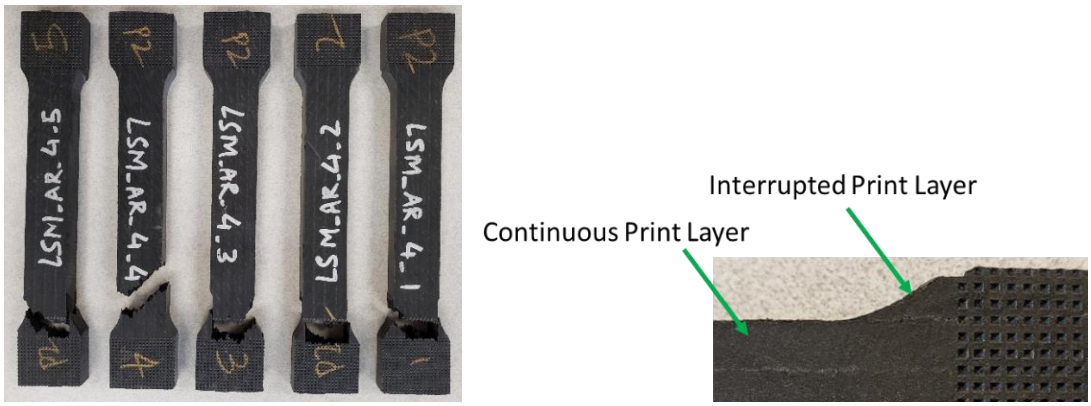

Figure 2.3-2: Failed LSAM -AR 4 sample, illustrating the initiation of failure in the shoulder region, between the continuous and interrupted print layers

It is possible that failures occurred in this region due to additional shear stresses being generated due to uneven tensile load sharing between the interrupted print layer and the continuous print layer. Figure 2.3-2 shows the shear angle distribution along the tensile specimen. Regions with higher shear angle indicate areas where additional shear stresses are being generated. It is possible that failure may be initiated in shear and not tensile failure. These samples may have increased strength if this effect can be minimized.

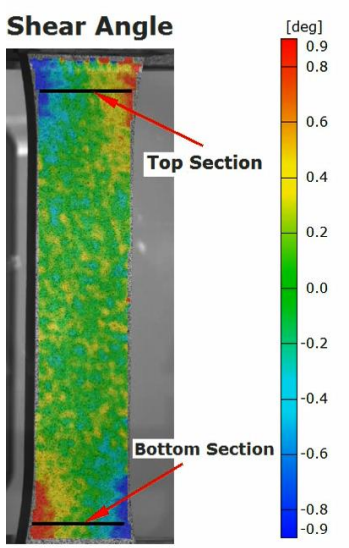

Figure 2.3-3: Digital Image Correlation image illustrating the high shear stress that develops in the shoulder region near the interface between the continuous and interrupted print layers

Figure 2.3-4 shows the stress vs strain plot of all the 1-direction tensile samples. The green lines represent the aspect ratio of 4 samples. Table 2.3-1 summarizes the tensile test results as a function of the bead aspect ratio.

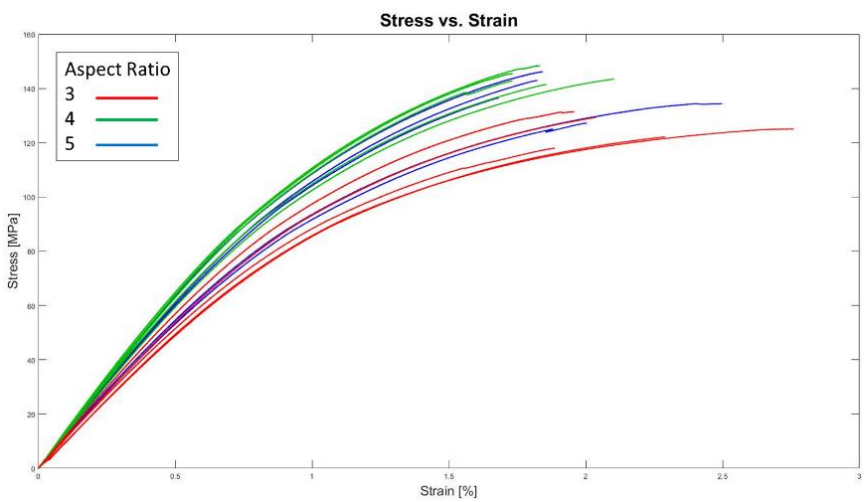

Figure 2.3-4: Stress-strain curves as a function of aspect ratio for the first five of seven tested samples

Table 2.3-1: Modulus of Elasticity of Print Direction Specimens

Sample	E_x (GPa)	X_x^T(MPa)
1	13.23	142.9
2	13.5	145.6
3	12.88	141.6
4	12.55	143.5
5	13.65	148.5
Average	13.16	144.4
SD	0.45	2.7
Variance	0.16	5.83

The Poisson ratio was determined using Digital Image Correlation (DIC) to measure the axial and transverse strain in the gauge length. The samples were tested at a rate of 2mm/minute and images of the sample were taken at a rate of 4 Hz during testing. A rectangular area was selected in the gauge section and an average value of the axial and transverse strains was calculated for each image. A plot of the transverse strain versus the axial strain was made and the slope of the resulting line between 0.05% and 0.25% axial strain was calculated to determine the Poisson Ratio. Figure 2.3-5 shows an example of the transverse versus the axial strain measured for one of the samples using the DIC.

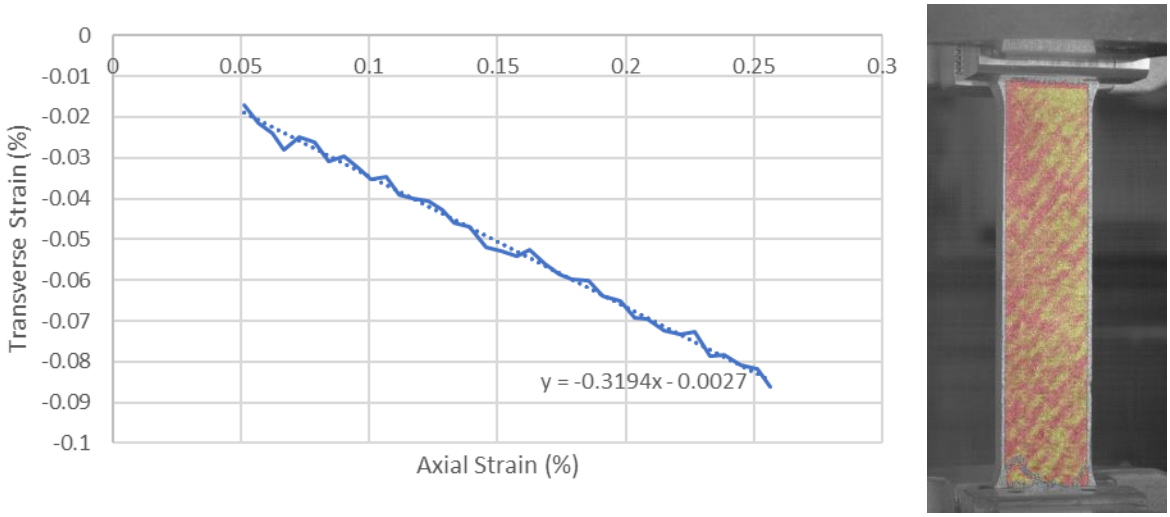

Figure 2.3-5: Example plot of the transverse versus axial strain measured by Digital Image Correlation used to determine the Poisson Ratio

Table 2.3-2: Summary of tensile properties measured for aspect ratio of 4 printed in the LSAM

AR	Avg E1 (GPa)	SD	Avg Ult. Strength (MPa)	SD	Avg. Failure Strain (%)	SD	Poison Ratio
4	13	0.9	141.2	7.1	1.86	0.14	0.336

Tensile Properties in the Transverse Direction

The specimen in the 2-direction or the transverse direction is simpler to extract than the 1-direction specimen. The gage length of the specimen is approximately 60 mm and the bead width is 20.32 mm. Therefore, there are 3 beads in the gage section. Dimensions of the 2-direction tensile specimen can be found in the APPENDIX Figure A 2.

A mechanical test system (MTS) load frame with 22-kip capacity was used for load transfer. The full-field strain field was acquired from the Digital Image Correlation (DIC) system which includes light sources and two 5-megapixel cameras one looking down to the specimen from the top and one looking up from the bottom which simultaneously capturing images as shown in Figure 2.3-6.

Figure 2.3-6: Tensile test setup for the tensile test in the 2 and 3-direction

Eleven specimens were tested and fractured specimens are shown in Figure 2.3-7. Every sample failed laterally with some of the fracture failing at the grip and some failing in the gage section.

According to ASTM D638[29], the failure code of the samples are LAT- lateral failure at the grip region located at the top, LGM – lateral failure at the gage section in the middle, and Sample #3 failed LIT – lateral inside grip/tab region at the top.

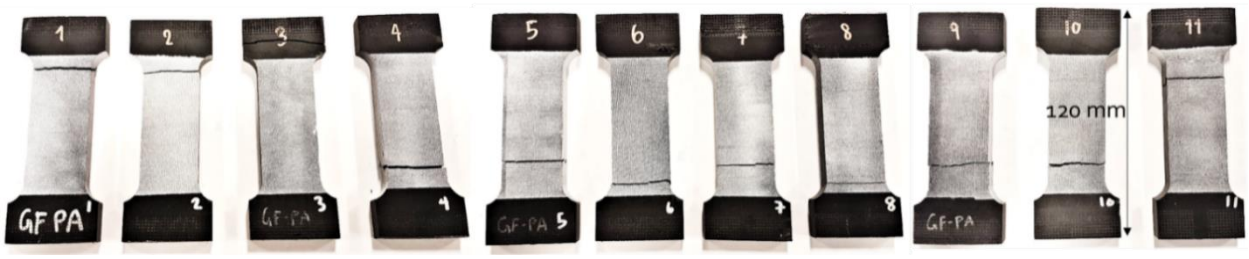

Figure 2.3-7: Fractured transverse direction tensile specimens

The strain snapshot of the transverse direction is shown in Figure 2.3-8. There are some 'hot spots' shown in the strain field which corresponds to the interface region because there is no fiber crossing the adjacent bead interface. The only contribution to strength in the interface region is the matrix which is more compliant than the region within the beads.

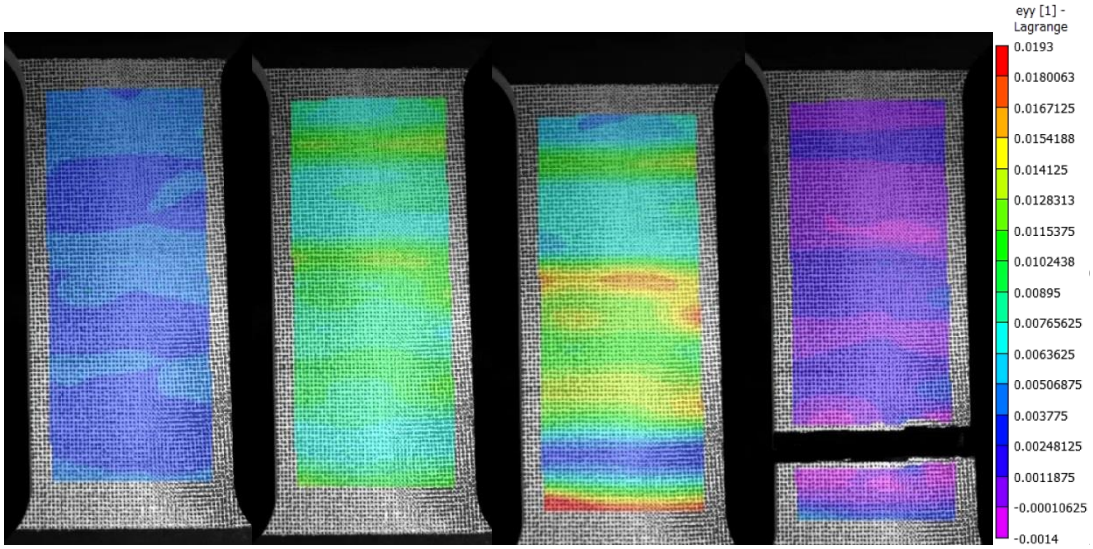

Figure 2.3-8: Strain field of tensile coupons in the transverse direction

Figure 2.3-9 is the stress vs strain plot of every sample. There is some variation among samples in both modulus and strength. Table 2.3-3 shows the modulus and ultimate strength measured for each sample.

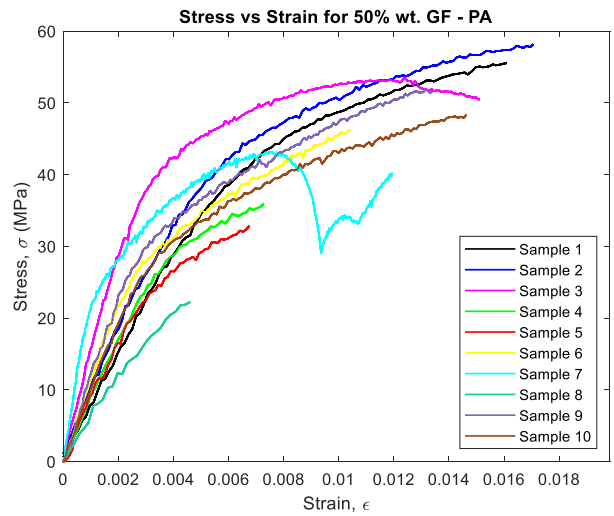

Figure 2.3-9: Stress-strain plots of transverse direction specimens

Table 2.3-3: Modulus of elasticity of transverse direction specimens

Sample	E_2 (GPa)	Ultimate Strength (Mpa)
1	7.35	55.59
2	7.93	58.2
3	10.81	53.55
4	7.45	35.98
5	6.85	32.89
6	8.18	46.21
7	5.32	43.22
8	5.33	22.26
9	8.91	51.92
10	8.07	49.17
11	5.52	48.38
AVG	7.43	45.22
STDEV	1.66	10.89
VAR	2.77	118.54

Tensile Properties in the Stacking Direction

The specimen in the 3 direction or the stacking direction has a gage length of the specimen of approximately 48 mm and the bead height is 5.08 mm. Therefore, there are approximately 9

layers in the gage section. Dimensions of the 2-direction tensile specimen can also be found in Figure 2.4 3 in the APPENDIX Figure A 3.

Regarding the tensile test in the stacking direction, ten specimens were tested and the fractured specimens are shown in Figure 2.3-10. Every sample had lateral failure type with some of the fracture failed at the grip some failed in the gage section. According to ASTM 3039 [34] failure code, is LAT- lateral failure at the grip region located at the top, and LGM – lateral failure at the gage section in the middle.

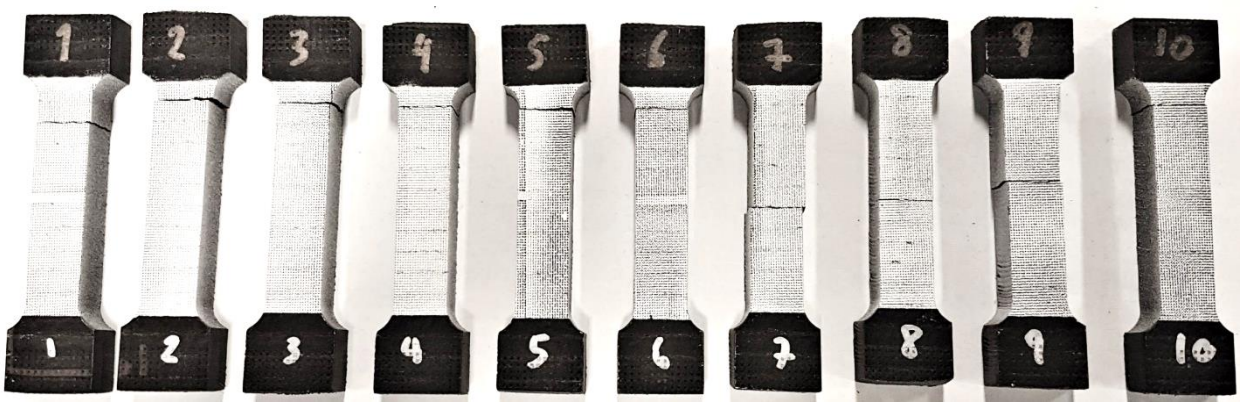

Figure 2.3-10: Fractured stacking direction tensile specimens.

The strain snapshot of the transverse direction is shown in Figure 2.3-11. The hotspots of the specimens correspond to the interface region between layers which is more compliant than the rest because it is governed by only the matrix properties. Figure 2.3-12 is the stress vs strain plot of every sample.

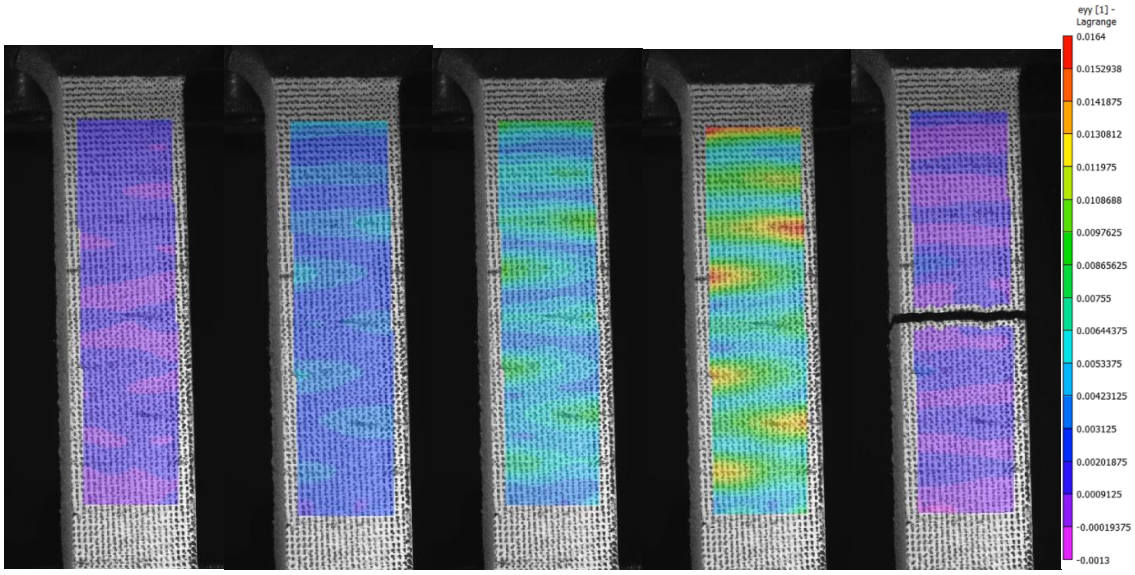

Figure 2.3-11: Strain field of tensile coupons in the stacking direction

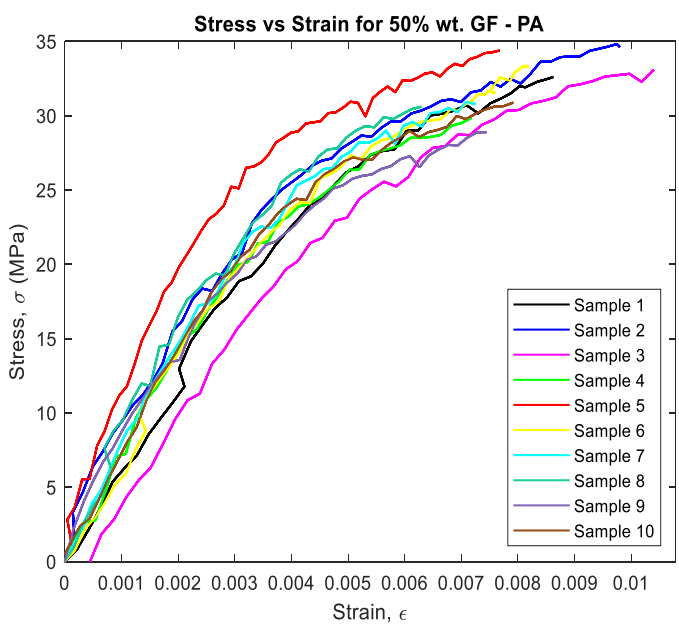

Figure 2.3-12: Stress-strain plots of stacking direction specimens

Table 2.3-4 shows the modulus and ultimate strength measured for each sample.

Table 2.3-4: Modulus of elasticity of specimens in stacking (3) direction

Sample	Modulus of Elasticity (Gpa)	Ultimate Strength (Mpa)
1	6.73	32.64
2	5.63	34.84
3	5.87	33.6
4	5.98	31.69
5	6.66	34.51
6	6.47	33.37
7	5.92	31.68
8	5.64	30.76
9	5.3	29.93
10	6.23	30.97
AVG	6.04	32.4
STDEV	0.47	1.66
Var	0.22	2.74

2.3.2 Shear properties (G_{13})

The orientation investigated was on edge (1-3 plane). The test in the 1-3 direction characterizes shear modulus and strength, shear properties describing the response resulting from a shear force or deformation applied to the 1-3 material planes. The shear specimen geometry followed specifications outlined in ASTM D-5379 [35] which are illustrated in Figure 2.3-13. The sample preparation steps are identical to tensile specimens' preparation, except for the specimen's geometry. As mentioned earlier the bead width of the printed wall is 0.8" (20.32 mm), therefore the width of the wall is approximately 20.32 mm. In this experiment, the side of the wall was smoothened using the wood planar, and the center region of the bead results in a width of 12 mm. The two bottom-most layers of the wall were also discarded.

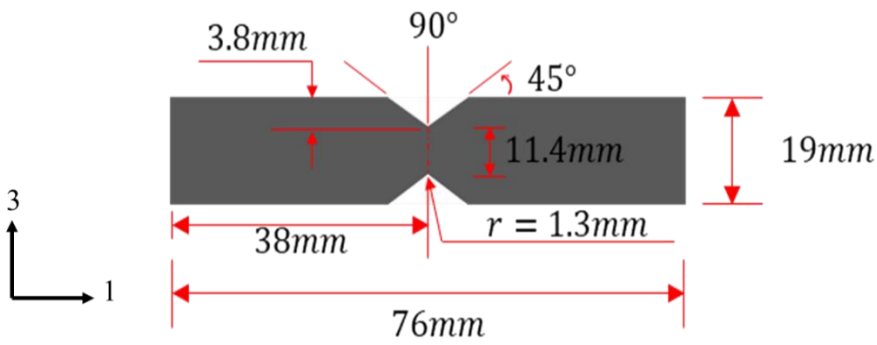

Figure 2.3-13: Dimension of a shear coupon

There are two types of shear specimen alignment with respect to the bead as shown in Figure 2.3-14. Group A) consists of four layers total having two full layers between the notches and two almost full layers on the edges. Group B) consists of three full layers total, and two partial layers on the top and bottom. Between the notches, there is one full bead and two partial beads. Since the geometry of the Iosipescu fixture is fixed, there is no variation of the specimen geometry for this specific bead dimension. The samples were dried with the tensile specimens. Note that specimens were extracted from panels instead of being printed to their final shape with no post-machining operations because the goal is to characterize the shear properties of the material, not the properties of the mesostructure of the printed shear structure.

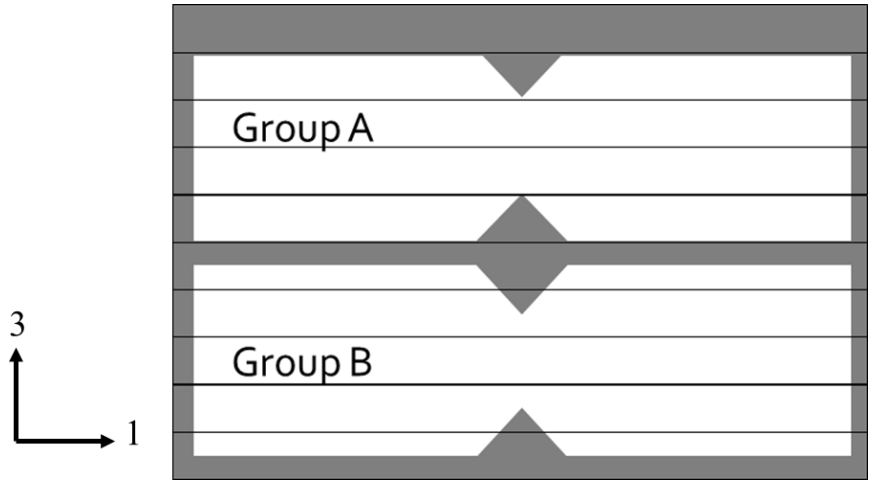

Figure 2.3-14: Group A) and Group B) specimen alignment with respect to the bead height

Identically to tensile specimens preparation, once the shear specimens have been appropriately dried, they were sprayed paint with three thin coats of white enamel paint to the region around the notch, then a speckle pattern was applied. Figure 2.3-15 shows a specimen with a speckle pattern.

Figure 2.3-15: Shear specimen with a speckle pattern

The experiment was performed using the MTS universal testing machine equipped with a 5 kN load cell. The illustration of the Iosipescu fixture from Wyoming Test Fixture Inc is shown in Figure 2.3-16. The complete DIC testing setup as shown in Figure 2.3-17 which includes two 5-megapixel cameras facing one side of the specimen, one looking down to the specimen from the top and one looking up from the bottom while simultaneously capturing images. Once the DIC is calibrated and the setup is done, the specimen was inserted into the fixture with the notch located along the line of action of loading by means of an alignment tool that references the fixture. The specimens were loaded at a rate of 2 mm/min and load values were recorded at a rate of 5 Hz.

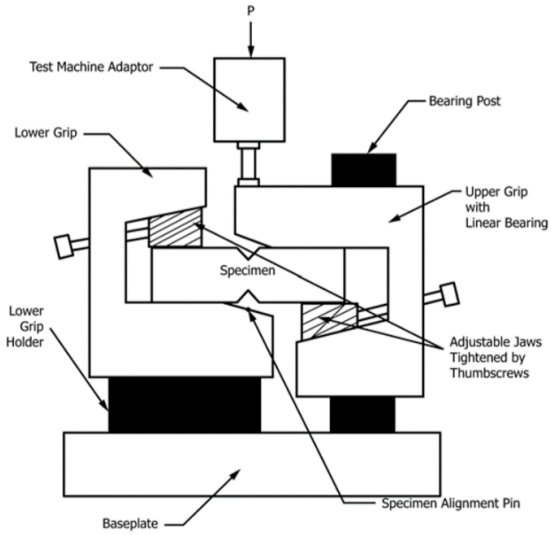

Figure 2.3-16: V-Notched beam test fixture schematic

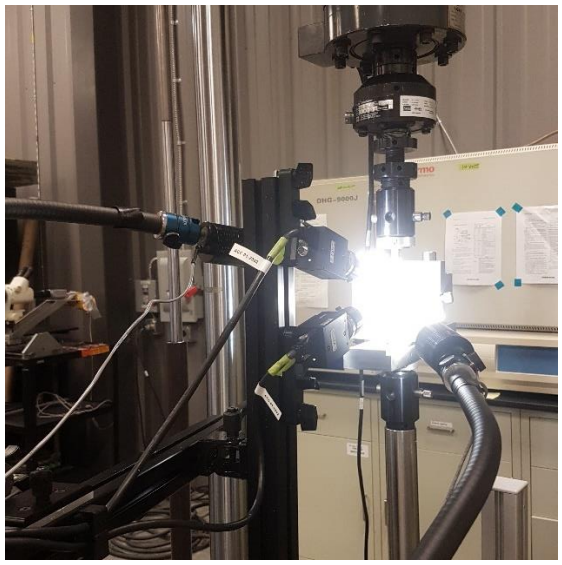

Figure 2.3-17: Shear test setup

Figure 2.3-18 shows the fractured samples after the shear test. The failure of the samples is very consistent and repeatable. The failure mode according to ASTM 5379 [35] for this category is HGN - horizontal cracking (H) in the gage section (G) and between notches (N).

Figure 2.3-18: Fractured shear specimens

Figure 2.3-19 shows six snapshots of the strain in the x-y direction (ϵ_{xy}) at the beginning, just before crack, after a crack was observed, while cracking, just before fracture, and after the specimen completely fractured. The strain shown in the figure is Lagrange strain tensor which

defines gradients in terms of the original configuration. As expected, the high strain region is around the middle of the specimen. The crack starts at the interface between layers in the central region. Again, because there is no fiber crossing between the layers, the interface region is governed by only the matrix.

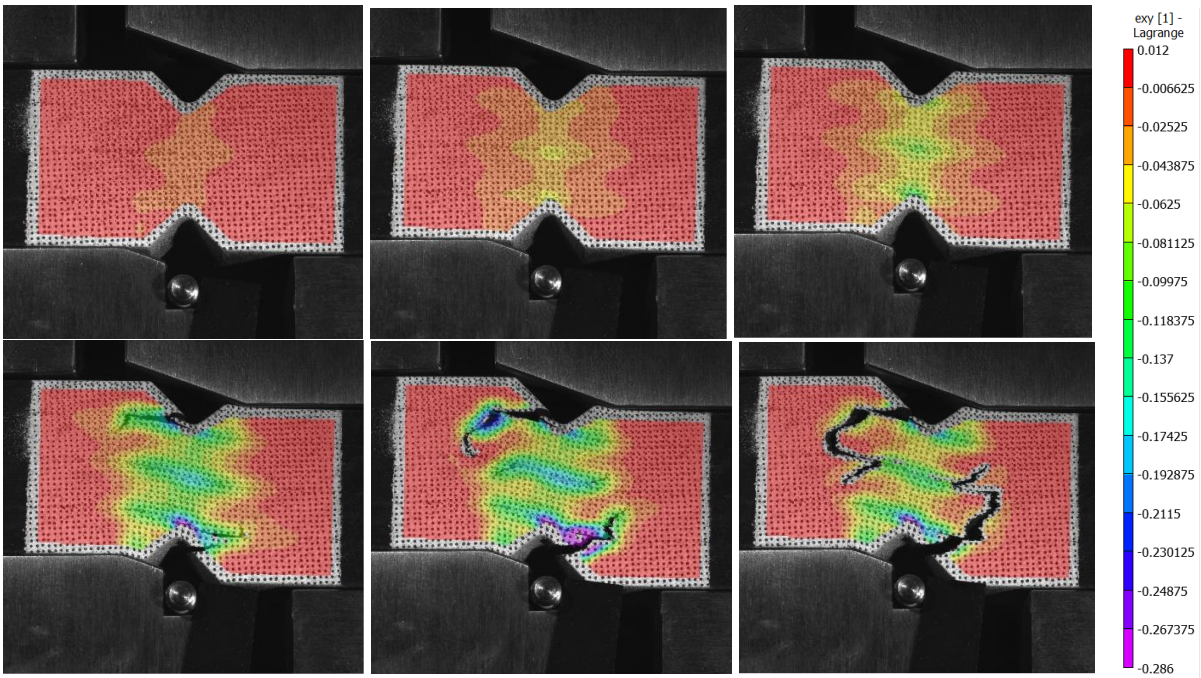

Figure 2.3-19: Snapshots of a shear specimen with ε_{xy} color gradient

The DIC images were analyzed to extract the average strain over the region of interests (ROI), which in this study, is a rectangular area at the center of the specimen measuring 11 mm wide by 11 mm as shown in Figure 2.3-20. Again, the strain exported from DIC is Lagrange strain tensor which defines gradients in terms of the original configuration. The average stress which is the force applied by the crosshead divided by the cross-sectional area between the notches and strain behavior were imported and analyzed in Matlab©.

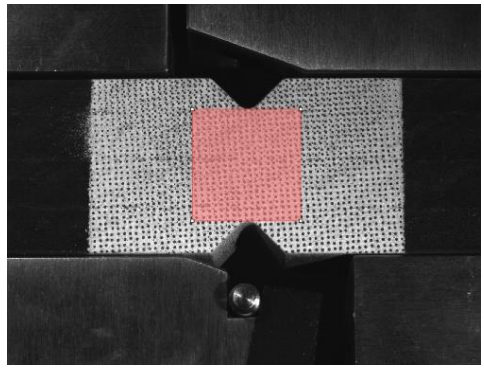

Figure 2.3-20: Region of interests for DIC analysis.

Figure 2.3-20 shows the graphs of shear stress vs engineering shear strain. Shear stress (y-axis) data were obtained from the load applied to the fixture by the initial cross-sectional area of the v-notch section. The engineering shear strain (x-axis) was obtained by twice the Lagrange strain (ϵ_{xy}) in the x-y direction obtained from the DIC. The ϵ_{xy} data is the average strain over the entire ROI. Only the linear section of the stress vs strain plot was used to calculate for shear modulus. Specifically, the strain ranging from 3000 με to 9000 με were used in the linear fit which was determined from the most linear part of the graphs. The shear modulus (G_{13}) and ultimate shear strength (τ_{13}^{max}) are shown in Table 2.3-5 below. Lastly, Table 2.3-6 summarizes the shear modulus of elasticity and average ultimate shear strength in all three principal directions.

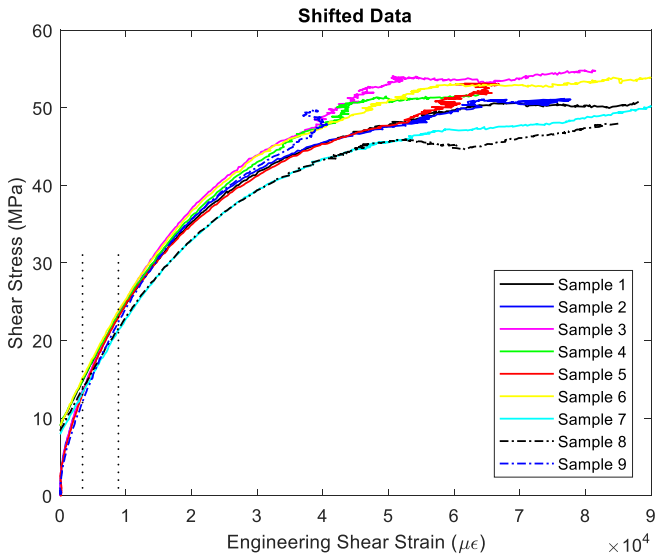

Figure 2.3-21: Shear stress vs engineering shear strain of all the samples

Table 2.3-5: Ultimate shear strength, shear modulus, and 0.2% offset shear strength

Sample	Ultimate Shear Strength (MPa)	Shear Modulus (GPa)	0.2 % Offset shear strength (MPa)
1	50.77	1.52	32.63
2	51.15	1.80	30.62
3	54.84	1.83	32.82
4	51.92	1.54	34.11
5	53.11	1.81	29.76
6	54.19	1.59	33.63
7	50.74	1.47	30.80
8	47.96	1.43	30.72
9	49.70	1.88	30.90
Average	51.60	1.65	31.78
STDEV	2.18	0.17	1.54
Variance	4.75	0.03	2.36

Table 2.3-6: Modulus of elasticity and the average ultimate strength of the three principal directions

	Modulus (GPa)				Average Ultimate Strength (MPa)			
	E_1	E_2	E_3	G_{13}	σ_1^{ult}	σ_2^{ult}	σ_3^{ult}	τ_{13}^{max}
AVG	13.16	7.43	6.04	1.65	144	7.43	32.4	51.60
SD	0.45	1.66	0.47	0.03	2.7	10.89	1.66	2.18

2.3.3 Micromechanics: virtual characterization for full LSAM bead's elastic properties

EDAM short fiber composite bead is a heterogeneous material whose microstructure consists of a matrix material and short fibers and voids which in these microstructures are on the order of micrometers. The objective of micromechanical modeling is to predict the interaction between the microstructure and the macroscopic/ overall properties. In other words, to take constituent properties obtained from the microstructure and predict the composite's mechanical performance. The process is homogenization in linear elasticity. The simplified explanation of the process is to find an equivalent homogeneous material that has the same effective macro stiffness as the real heterogeneous composite, under the same boundary conditions.

The mean-field homogenization model used in this study is the Mori-Tanaka model [21]. It assumes that each inclusion, i.e. fibers, behaves as if it were isolated in the matrix. That there is no interaction between inclusions and that the stress and strain in one inclusion does not affect any other inclusion. Therefore, the Mori-Tanaka model, in theory, is restricted to moderate volume fractions of inclusions. The Mori-Tanaka model is illustrated in Figure 2.3-22 taken from the Digimat user's manual [21].

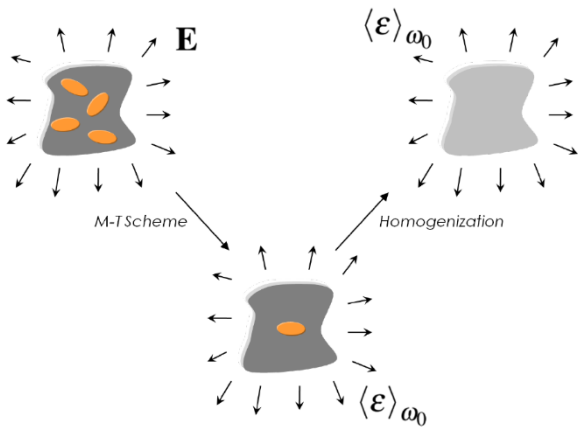

Figure 2.3-22: Illustration of the Mori-Tanaka (M-T) model [21]

The goal of this section is to obtain the material properties at the bead level which is equivalent to the elastic properties obtained from the experiment earlier. The reason being, the differences in fiber orientation due to the outer edge of the part being shaved with the wood planar to ease the specimen preparation and testing. The homogenization method in Digimat is designed to predict the effective properties by specifying the constitutive properties. However, the constituent properties, i.e. fiber and matrix properties are currently unknown. For glass fiber and Polyamide, the values obtained from the manufacturer, experiment, and literature are shown in Table 2.3-7. Because there are multiple blends of Polyamide, the modulus found in the literature couldn't be used. Therefore, the unknown here is Young's modulus of the Polyamide. Thus, a reverse engineering method was used to obtain the Polyamide's modulus given the modulus in three principal directions and fiber orientation of the tensile coupons. The process is illustrated in Figure 2.3-23. After several reverse engineering repetitions, the modulus of Polyamide was found to be 3.1 GPa.

Table 2.3-7: Fiber and matrix properties

Properties	Glass Fiber (E-glass)	Nylon (polyamide)
Symmetry	Isotropic	Isotropic
Density $\frac{kg}{m^3}$	2540	1090
Young's Modulus (GPa)	72	3.1
Poisson ratio	0.22	0.35
Fiber aspect ratio	27.2	-
Fiber Diameter	10 microns	-

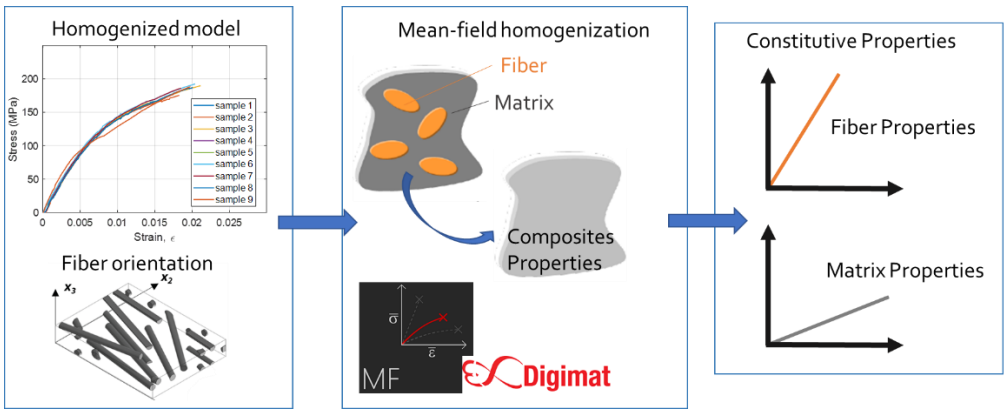

Figure 2.3-23: Reverse engineering method

Utilizing the area-weighted fiber orientation of the whole bead along with the constitutive properties, the nine elastic properties at the bead level are listed in Table 2.3-8 below.

Table 2.3-8: Elastic properties at the bead level

Properties	**Values**
E1 (GPa)	13.16
E2 (GPa)	7.43
E3 (GPa)	6.04
G12 (GPa)	3.45
G13 (GPa)	2.40
G23 (GPa)	2.21
v12	0.37
v21	0.21
v13	0.32
v31	0.15
v23	0.40
v32	0.32

2.4 Thermophysical Properties

2.4.1 Heat Capacity

The heat capacity characterization was outsourced to the Thermophysical Properties Research laboratory Inc, West Lafayette, IN. Heat capacity was characterized as a function of temperature according to the ASTM E1269 [36] standard. The heat capacity and density of the material are required for calculating the thermal conductivity from the diffusivity measurements. Circular specimens with dimensions of $5.8\ mm$ (0.23") in diameter and $1.5\ mm$ in thickness or square specimens with dimensions of $3.8\ mm$ in length and $1.5\ mm$ in thickness are required. Further, the heat capacity measurements are independent of the material orientation, and therefore specimens can be prepared from any plane in the material. Figure 2.4-1 shows the plot of the heat capacity as a function of temperature. The exothermic peak shown in the heat flow signal, dash-dot blue line in the figure is the result of the crystallization process occurring while the sample is cooled down. The heat capacity values are tabulated in Table A.4 in the APPENDIX.

Further, the sensitive heat associated with the reduction in the temperature of the sample needs to be removed from the heat flow signal before integrating the heat flow to estimate the energy released during crystallization. Assuming the heat capacity of the material does not change significantly as it crystallizes, a straight baseline can be drawn connecting the inflection point in the heat flow signal at the onset of crystallization with the last inflection point in the heat flow signal corresponding to the end of the crystallization.

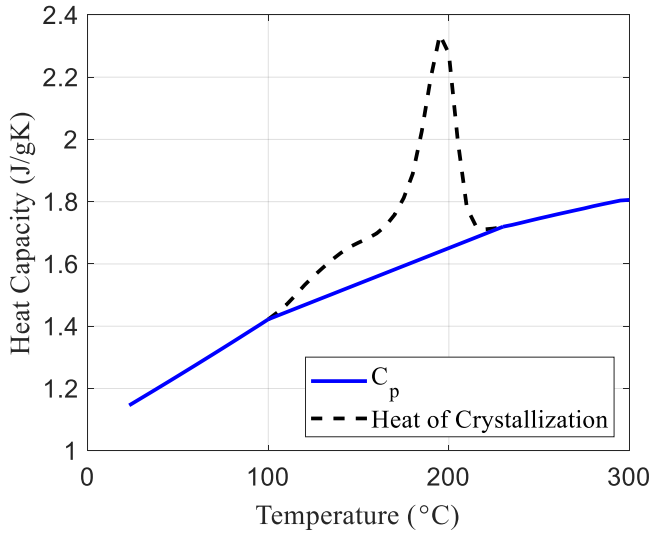

Figure 2.4-1: Heat capacity as a function of temperature

2.4.2 Thermal Conductivity

The thermal conductivity of a material is a measure of its ability to conduct heat. It determines the quantity of heat which flows in unit time through unit area of a layer of the substance of unit thickness with unit difference of temperature between its faces. The characterization was also outsourced to Thermophysical Properties Research laboratory Inc which utilized the ASTM E1461 [37] laser flash method.

The specimens for the laser flash method is circular specimens with a diameter, D, of 12.7 mm (1/2") and a thickness, h of 3 mm (0.12"). The specimens require to be completely solid and with the two faces parallel. Thermal conductivity in the three principal directions were required namely with the parallel faces oriented normal to the print direction (1-direction), the transverse to the print direction, (2-direction), and the stacking direction (3-direction). The thermal diffusivity was characterized at the level of the bead, and thus specimens represent the bead-level printed microstructure. Figure 2.4-2 shows schematically specimens with beads oriented in the three principal directions. However, the bead dimensions may exceed the dimensions allowed for the specimen. In this case, the region from which the specimens were extracted were specified. This will allow predicting the effective thermal diffusivity at the bead level.

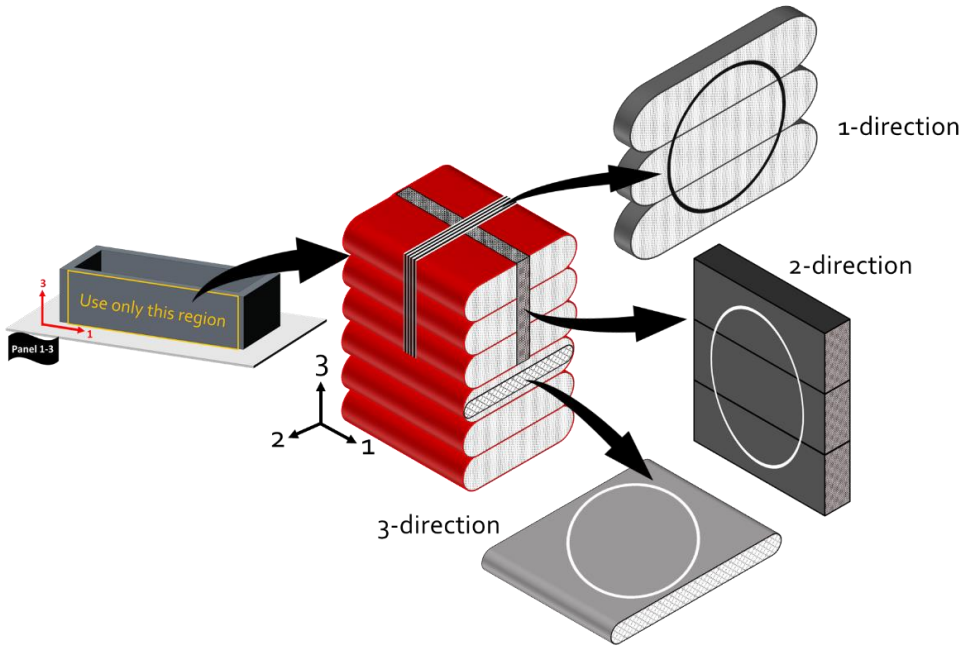

Figure 2.4-2: Schematic representation of bead distribution within specimens for thermal diffusivity

Figure 2.4-3 shows the plot of the thermal conductivity of the specimens as a function of temperature in the three principal directions. The thermal conductivity in the 1, 2, and 3-direction is indicated as K_{11}, K_{22}, and K_{33} consecutively. The values are tabulated in Table A.5 in the APPENDIX.

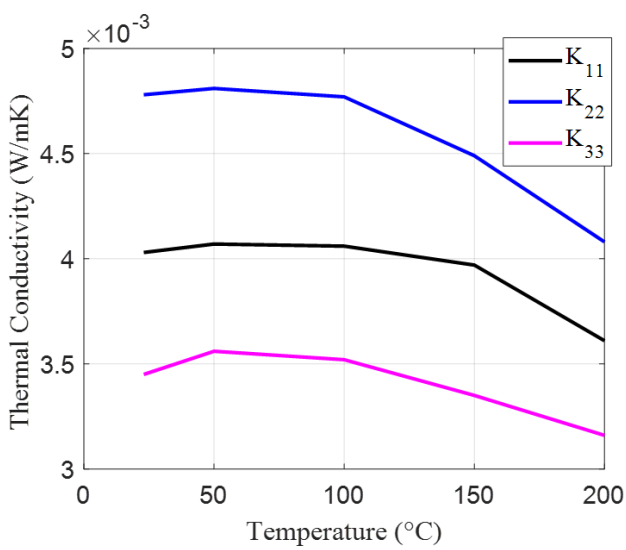

Figure 2.4-3: Thermal conductivity of 50% wt. GF-PA in the three principal direction

Note that the properties shown in the figure were obtained from the sample which is not at the bead level. In other words, the fiber orientation of the thermal conductivity sample is different from the whole bead fiber orientation. The thermal conductivity sample has a dimension requirement of 3 mm maximum in the thickness. However, one LSAM bead is 5.08 mm thick. Section 2.4.3 discusses the method to obtain the thermal conductivity at the LSAM bead level.

2.4.3 Micromechanics: Virtual Characterization for Full LSAM Bead's Thermophysical Properties

As stated in the sample preparation step at the beginning of section 2.4, the dimensions of the sample do not represent the whole bead. Therefore, a virtual characterization is needed to obtain the thermal conductivity at the bead level. As mention in the section 2.3.3 mechanical properties section, the objective of micromechanical modeling is to predict the interaction between the microstructure and the macroscopic/ overall properties. Figure 2.4-4 illustrates the process of virtual characterization starting with fiber orientation of the thermal conductivity samples and the thermal conductivity in the three-principal direction. Next, using the mean-field homogenization to reverse engineering to obtain the constitutive properties following the same concept as in section 2.3.3.

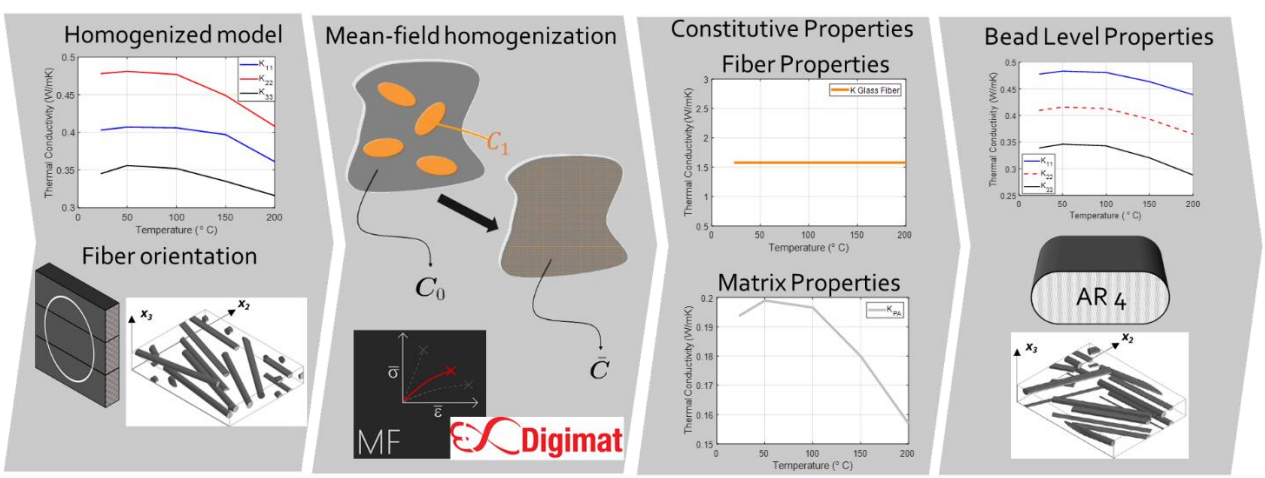

Figure 2.4-4: Virtual characterization for the bead level properties

The thermal conductivity of glass fiber is assumed to be constant at 1.56 W/mK. The thermal conductivity of Polyamide was reverse-engineered at 25, 50, 100, 150, and 200 ◦C. Lastly, utilize

the constitutive properties to obtain the thermal conductivity of the 50% wt. GF-PA (30% vol. GF-PA) with the fiber orientation of the whole bead with an aspect ratio (AR) of 4. The thermal conductivity of the three principal directions is plotted as a function of time in Figure 2.4-5 and tabulated in Table 2.4-1 along with Polyamide's properties.

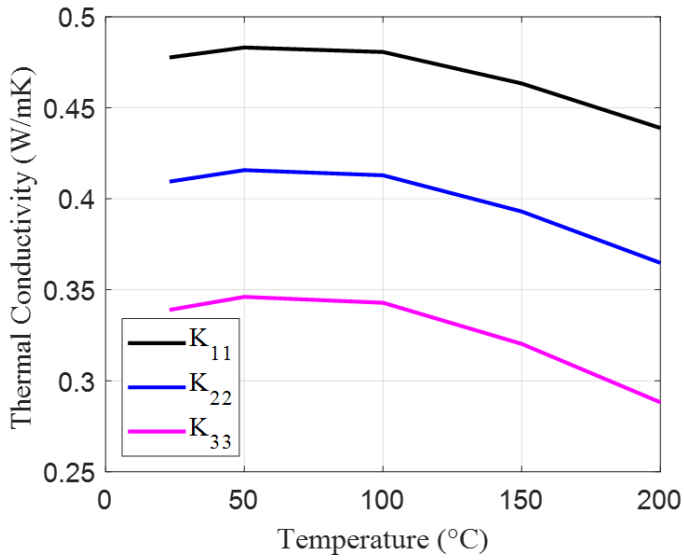

Figure 2.4-5: Thermal conductivity in the three principal direction

Table 2.4-1: Thermal conductivity in the three principal direction and polyamide constitutive properties

Temp (C)	1 -direction	2 -direction	3 -direction	Polyamide
23	**0.478**	**0.409**	**0.339**	**0.194**
50	0.483	0.416	0.346	0.199
100	0.481	0.413	0.343	0.197
150	0.463	0.393	0.320	0.180
200	0.439	0.365	0.288	0.157
250	0.319	0.229	0.136	0.057
300	0.299	0.208	0.114	0.044

2.5 Melting and Crystallization Kinetics

In the EDAM process, a solid filament is drawn into an extruder, heated to a temperature where the polymer flows readily, then deposited layer-by-layer onto a build plate. After deposition, the extrudate layers bond with the previous layer and solidifies. Depending on the polymer, the solidification process will either occur via a glass transition or crystallization, and the type of process will have a significant impact on the mechanism of strength enhancement of the bonding between polymer layers.

2.5.1 Polymer Crystallization

Polyamide is a semi-crystalline polymer that partly crystallizes when they are cooled from the melt. Polymer crystallization is an exothermic process in which polymer chains locally fold in dense arrangements, called crystals, which cause shrinkage of the material. In order to capture the polymer crystallization process in an EDAM process simulation, it needs to be described with an appropriate model definition. Two sets of experiments, isothermal and non-isothermal experiments, were performed to provide data sets to fit a phenomenological model capturing the crystallization kinetics.

A first set consists of isothermal crystallization experiments where the sample is heated and held for several minutes at the recommended material processing temperature to melt all the polymer crystals. Subsequently, the material is quenched to a constant temperature and maintained at the same temperature until the polymer starts to crystallize. Since the heat flow due to the kinetics (crystallization) can overlap with the heat flow due to the sensitive heat, a baseline DSC experiment is performed to decouple these two mechanisms. One approach is to repeat the same isothermal DSC experiment but with a sample that has a similar thermal mass as the sample with polymer but that does not undergo any exothermic or endothermic reaction. Inert materials with a constant heat capacity in the range of temperature under consideration are recommended for the baseline measurement. As an additional recommendation for the DSC experiments, the weight used for preparing the DSC samples should be consistent within $6 \pm 0.5\ mg$. Also, the material should be dried according to the recommendation provided by the manufacturer.

An example of an isothermal DSC experiment conducted on a 50 wt. GF-PA is provided as a reference in Figure 2.5-1. The blue plot indicates the temperature profile, and the green plot shows the heat flow of the sample due to the change in temperature where positive value means exothermic heat transfer. The little peak indicated with the red circle in Figure 2.5-1 is the crystallization peak.

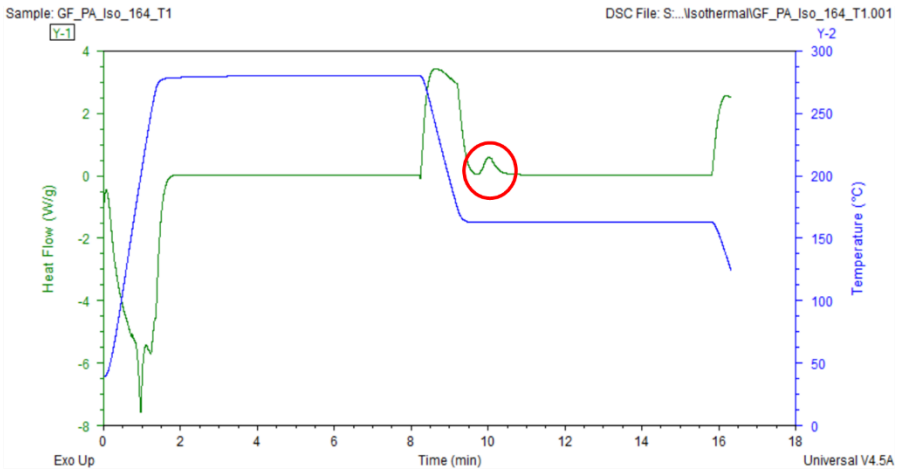

Figure 2.5-1: Example of isothermal DSC experiment of a semi-crystalline polymer

A general recipe for the isothermal experiments of the GF/PA is provided in Table 2.5-1. It should be noted that the cooling rate highlighted in red in Table 2.5-1 corresponds to the maximum cooling rate that can be achieved with the DSC.

Table 2.5-1: Steps required for the isothermal DSC experiments of GF/PA

Step	Description
1	Equilibrate temperature at 30 $°C$
2	Ramp temperature at 200 $°C/min$ to 280 $°C$
3	Dwell for 7 min
4	Ramp temperature at 280 $°C/min$ to X$°C$
5	Dwell for 7 min
6	Ramp temperature at 200 $°C/min$ to 30 $°C$

The isothermal temperature (X) at which the experiments will be conducted is highlighted in yellow in Table 2.5-1. The same recipe will be carried out twice with the material under investigation and once with an inert material which is glass. Clearly, both samples should have

similar thermal mass. The temperature range to perform the isothermal experiments was already determined from a non-isothermal DSC experiment and is defined between $155\ °C$ and $167\ °C$. During crystallization, the material releases heat which can be seen by the area of the crystallinity peak as shown in Figure 2.5-2. H_c^{∞} is the total energy released by the completed crystallization, and $\Delta H_c(t)$ is the energy released by partial crystallization. H_f is the latent heat of crystallization of a perfect crystal for which 100% of the material crystallizes. A value for H_f of 98 J/g was assumed based on Wang et. al. [38] for 50% wt. of Polyamide matrix material. For 100% Polyamide H_f would be twice, because 50% of the material weight was glass fiber, which does not undergo a crystallization phase transition. Therefore, computed crystallinities were the crystal fractions of the matrix material only, not of the overall composite material. The crystal volume fraction or crystallinity X_{vc} is defined as Equation 2.5.1 below.

$$X_{vc}(t) = \left(\frac{\Delta H_c(t)}{\Delta H_c^{\infty}}\right) \cdot \frac{1}{H_f} \tag{2.5.1}$$

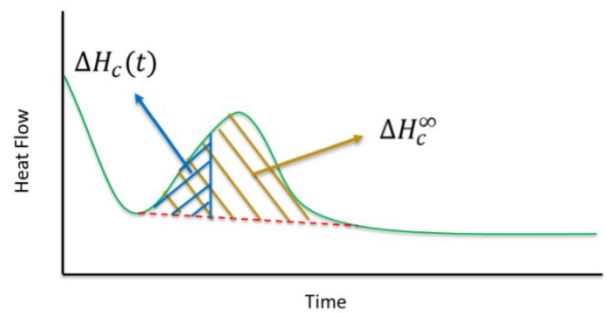

Figure 2.5-2: Heat flow during crystallization

The isothermal crystallization data was required for generating an Avrami plot to find the Avrami exponents. This is a common way of analyzing isothermal crystallization kinetics data [39]. The Avrami equation in Equation 2. can be rewritten to get

$$\log\left(-log\left(1-\frac{X}{X_{\infty}}\right)\right) = \log k(T) + nlogt \tag{2.5.1}$$

Figure 2.5-3 is a diagram of $\log\left(-\log\left(1-\frac{X}{X_\infty}\right)\right)$ vs. logt, the Avrami exponents n can be read out as the slope of the resulting graphs. In order to generate the data, the relative crystallinity $\frac{X}{X_\infty}$ was computed for each isothermal temperature by dividing the crystallinity vector X by its maximum value X_∞. There are two different slopes that can be identified for all of the isothermal temperatures as shown in Figure 2.5-3. This indicates that two dominant crystallization mechanisms are governing the overall crystallization behavior, each represented by a corresponding Avrami exponent. In order to determine the Avrami exponents, linear functions were fitted to the different portions of the data for each temperature. The resulting Avrami exponents for the five different temperatures are tabulated in Table 2.5-2.

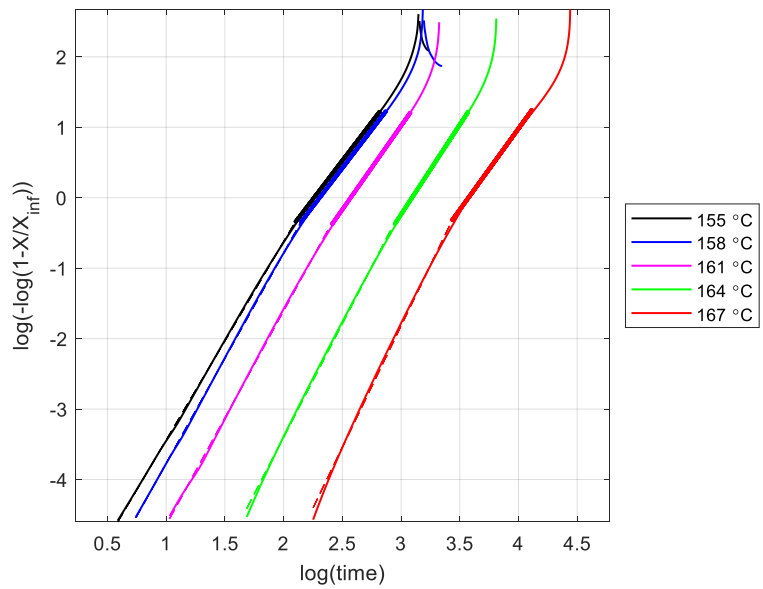

Figure 2.5-3: Avrami plot for the characterized GF-PA material

Table 2.5-2: Summary of the extracted Avrami exponents

Temperature	Avrami exponent 1	Avrami exponent 2
155 ◦C	2.82	2.18
158 ◦C	2.98	2.18
161 ◦C	3.04	2.38
164 ◦C	3.22	2.55
167 ◦C	3.45	2.30
average	3.10	2.32
Selected value	3.1	2.3

The EDAM printing process is a highly non-isothermal process, i.e. material cools down after material deposition. During a non-isothermal experiment, the material is exposed to varying temperature conditions, so the nucleation rate and the growth rate vary, resulting in a different degree of crystallinity. Thus, the second set of experiments to characterize crystallization kinetics of non-isothermal DSC experiments is needed. In this type of experiment, the material is heated at a constant rate to the recommended material processing temperature at 285 ℃ and held for several minutes until all the polymer crystals are molten. Then, the sample is cooled at a constant rate to room temperature. Utilizing the cooling rates and heating rates of the same magnitude is recommended to also characterize the melting behavior. To extract more information on the melting behavior after crystallizing under controlled non-isothermal conditions, a second heating and cooling cycle should be performed. Again, the weight used for preparing the DSC samples was consistent within 6 $\pm 0.5\ mg$. One of the non-isothermal DSC experiments conducted on a glass fiber reinforced Polyamide is provided as a reference Figure 2.5-4. The red circled peak is the exothermic crystallization peak.

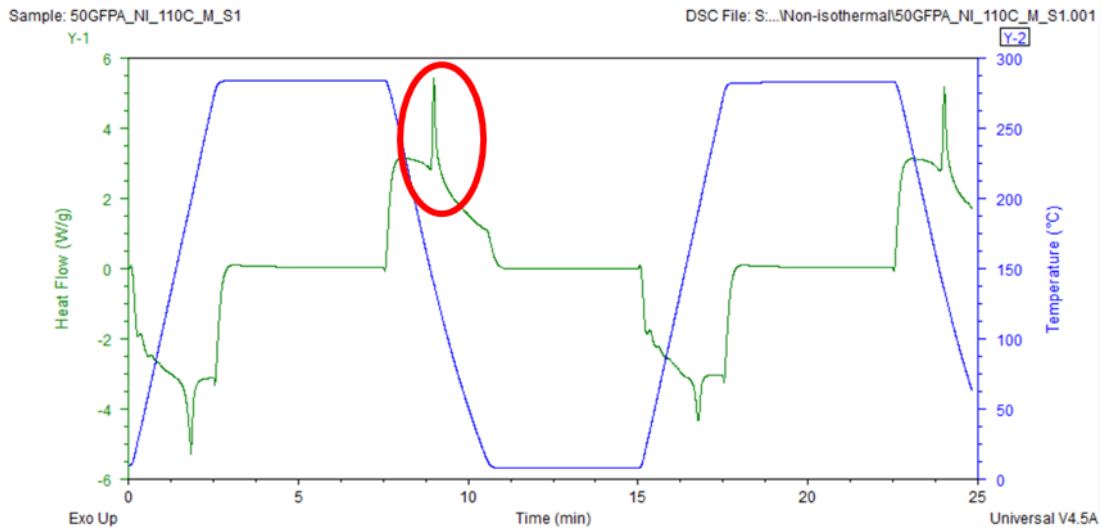

Figure 2.5-4: Non-isothermal DSC experiment of a GF-PA

A general recipe for the non-isothermal experiments of the GF-PA is provided in Table 2.5-3. The variables in non-isothermal experiments are heating rate and cooling rate ranges from 10 $°C/min$ to 150 $°C/min$ with an increment of 10 $°C$. Clearly, the heating rate should be the same as the cooling rate for any experiment.

Table 2.5-3: Steps required for the non-isothermal DSC experiments of GF-PA

Step	Description
1	Equilibrate temperature at 30 $°C$
2	Ramp temperature at ____ $°C/min$ to 280 $°C$
3	Dwell for 5 min
4	Ramp temperature at ____ $°C/min$ to 30 $°C$
5	Repeat step 1-4

Similar to the analysis procedure of the isothermal experiments, the experimental exothermic crystallization data was exported from the DSC analysis software TA Universal Analysis© and stored in Excel© files. This data was imported with a Matlab© script to compute the evolution of crystallinity for the non-isothermal experiments. The crystallinity calculation procedure to compute was the same as for the isothermal experiments. The resulting mass fraction crystallinities for the different cooling rates are illustrated in Figure 2.5-5.

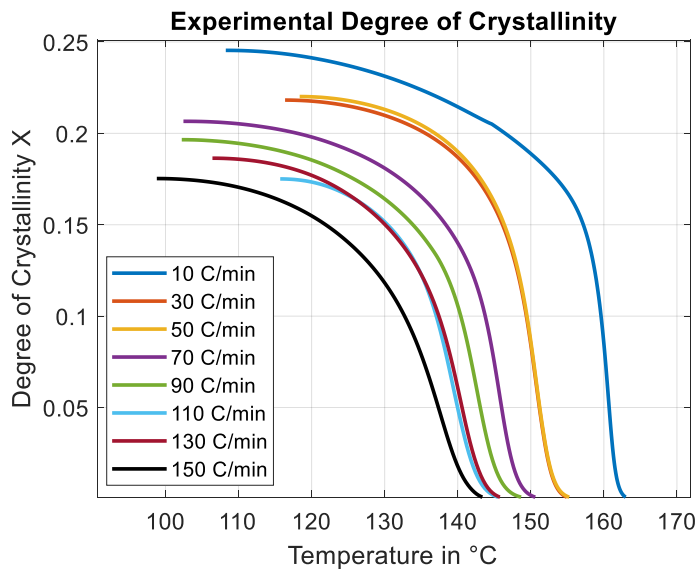

Figure 2.5-5: Resulting degrees of crystallinity for the different cooling rates

Crystallization Kinetics Model Fitting

From studying the isothermal experiment indicates that two dominant crystallization mechanisms are governing the overall crystallization behavior, each represented by a corresponding Avrami exponent. Therefore, the Velisaris and Seferis [40] non-isothermal dual kinetics model was selected for modeling the non-isothermal due to its capability of describing two crystallization

mechanisms. The slightly modified version of the Velisaris and Seferis model is shown in Equation 2.5.1 and Equation 2.5.2 below.

$$X_{vc}(T,t) = X_{vc\infty}(w_1 F_{vc_1} + w_2 F_{vc_2}) \tag{2.5.1}$$

$$F_{vc_i} = 1 - \exp[-C_{1_i} \int_0^t T \cdot exp\left[\frac{-C_{2_i}}{(T - T_g + T_{c_i})} - \frac{C_{3_i}}{\left(T\left(T_{m_i} - T\right)^2\right)}\right] n_i \tau^{n_i - 1} d\tau \tag{2.8}$$

Where X_{vc} is the crystallinity volume fraction, w_1 and w_2 are weight factors, C_{1_i} are pre-exponential factors capturing the temperature dependence, C_{2_i} are empirical parameters associated with the temperature dependence of diffusion, C_{3_i} are empirical parameters associated with the free enthalpy of nucleation, n_i are the Avrami coefficients for each crystallization mechanism. The known parameters and their values are listed in Table 2.5-4. Leaving 11 parameters to be determined based on the experimental data: C_{1_i}, C_{2_i}, C_{3_i}, w_1, $T_{\mathrm{m,i}}$,and $T_{\mathrm{add,i}}$ where i = 1, 2.

Table 2.5-4: Known parameter for the fitting process of the crystallization kinetics model.

Parameter	Value
Avrami exponent n_1	3.1
Avrami exponent n_2	2.3
Glass transition temperature T_g	70 °C
w_2	(1 - w_1)
x_∞	0.25

Table 2.5-5 provides the final parameters that describe the GF-PA material. Figure 2.5-6 illustrates the comparison of the model predictions, utilizing the model parameter from Table 2.5-5, with the experimental crystallization curves for several different cooling rates.

Table 2.5-5: Obtained best-fit parameters for the Velisaris and Seferis [40] model CF reinforced PA

Parameters	Mechanism 1 ($\boldsymbol{i = 1}$)	Mechanism 2 ($\boldsymbol{i = 2}$)
$\boldsymbol{w_i}$	0.877	0.123
$\boldsymbol{n_i}$	3	2
$\boldsymbol{C_{1i}}$ $(\boldsymbol{s^{-n}K^{-1}})$	$8.131 \cdot 10^5$	$5.631 \cdot 10^8$
$\boldsymbol{C_{2i}}$ $(\boldsymbol{K})$	$2.605 \cdot 10^3$	$1.701 \cdot 10^6$
$\boldsymbol{C_{3i}}$ $(\boldsymbol{K^3})$	$6.467 \cdot 10^7$	$5.507 \cdot 10^{10}$
$\boldsymbol{T_{ci}}$ $(\boldsymbol{K})$	70.58	66.73
$\boldsymbol{T_{mi}}$ $(\boldsymbol{K})$	511.55	235.03

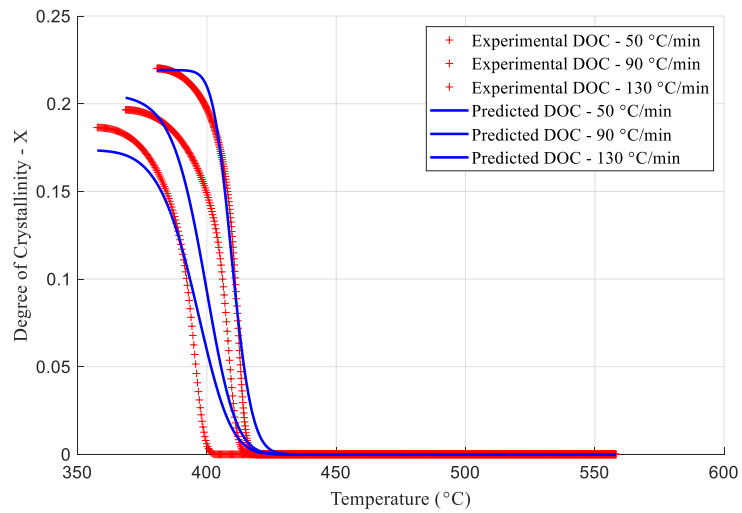

Figure 2.5-6: Comparison of the model prediction for crystallinity with the experimental data for various different cooling rates.

2.5.2 Polymer Melting

In EDAM, re-melting occurs at the regions when a newly deposited material is in contact with the partially crystallized previously deposited bead. The melting material was characterized using DSC experiments similar to the crystallization kinetics characterization experiments. In fact, the same non-isothermal data was utilized, but focusing on the heating cycle.

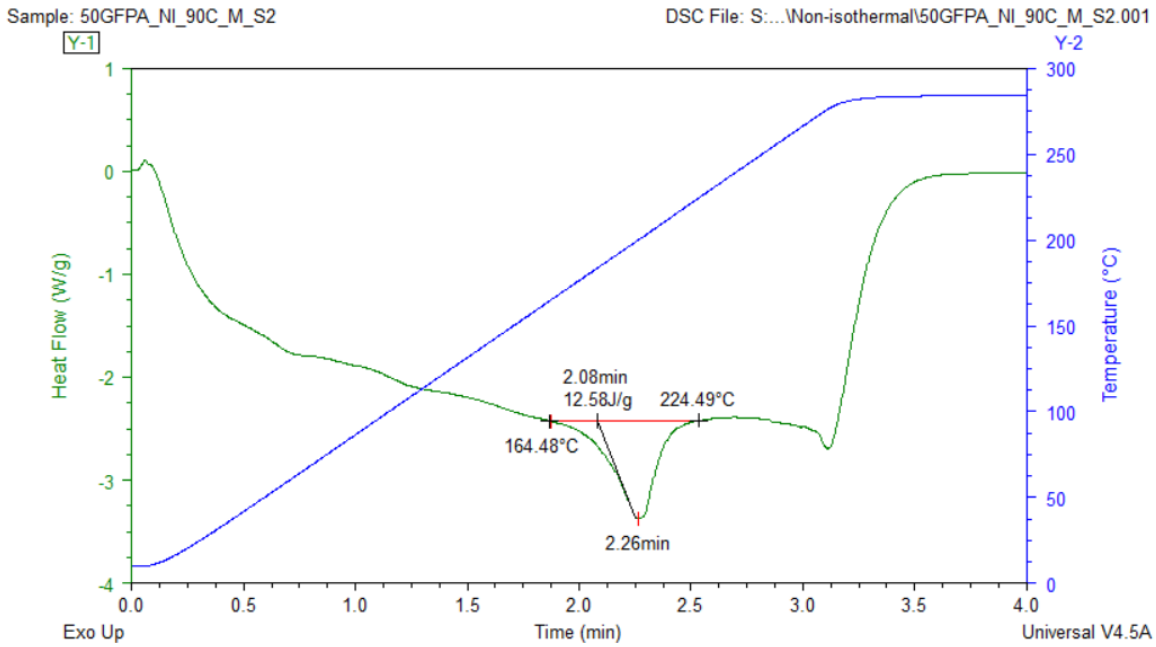

Figure 2.5-7: Illustration of the endothermic melting peaks in the heat flow signal for the heating rates 90°C/min.

The heating rates are in the range of 10°C/min – 150°C/min and the melting kinetics behavior was investigated by analyzing the endothermic melting peak in the heat flow signal. Figure 2.5-7 shows the melting peaks for the heating rates of 90°C/min. A statistical temperature dependent melting model proposed by Greco and Maffezzoli [41] was utilized to describe the melting process of the material as shown in Equation (2.9).

$$X_m(T,p) = \left\{1 + (d-1)e^{-k_{mb}(T-T_c)}\right\}^{\frac{1}{1-d}} \tag{2.9}$$

Where $X_m(T,p)$ is the relative degree of melting, and T_C is average maximum melting peak temperature which is the average maximum temperature of the peaks from the experimental data. Leaving, d, shape parameter, and k_{mb}, the intensity factor the only two fitting parameters. The resulting values for the optimized parameters are provided in

Table 2.5-6. A comparison of the model prediction with the temperature dependent degrees of melting for the different melting rates from the experiments is illustrated in Figure 2.5-8.

Table 2.5-6: Optimized parameters for the melting model.

Parameter	Value
T_C (K)	464.27
k_{mb}	0.1532
d	1.7575

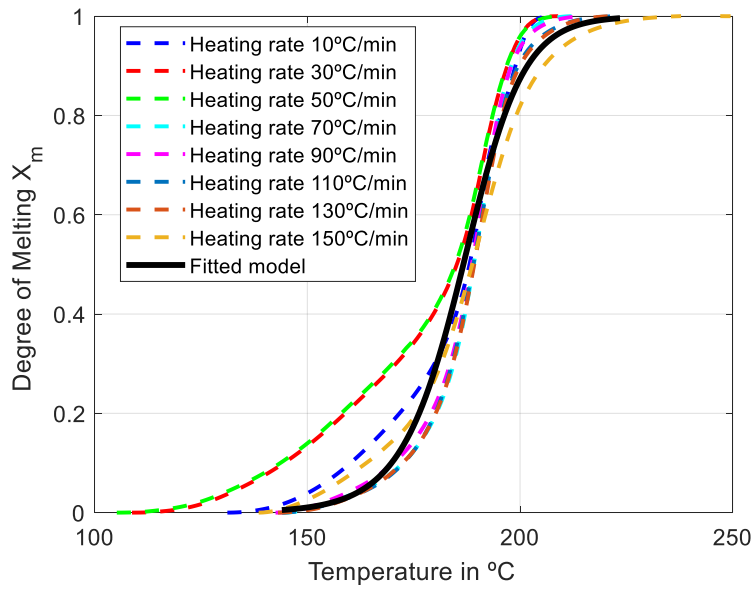

Figure 2.5-8: Comparison between the experimental results and the prediction by the fitted melting model for the temperature dependent evolution of the degree of melting.

2.6 Thermomechanical Properties

2.6.1 Glass Transition Temperature

The glass transition is a property of only the amorphous portion of a semi-crystalline solid. The crystalline portion remains crystalline during the glass transition. At a low temperature, the amorphous regions of a polymer are in the glassy state in which the molecules are frozen on place. When a semi-crystalline polymer is heated, the temperature at which the polymer structure turns from solid to rubbery is called the Glass Transition Temperature, T_g [42]. At this temperature polymer now is in its rubbery state and portions of the molecules can start to move around.

In this study, the dynamic mechanical analysis (DMA) was utilized to measure T_g. DMA measures the viscoelastic moduli, storage and loss modulus, damping properties, and tan delta, of materials

as they are deformed under a periodic (sinusoidal) deformation (stress or strain). DMA experiments were carried out in a TA InstrumentsQ800. The double cantilever fixture used in this experiment is shown in Figure 2.6-1, the middle fixture oscillates with a frequency of 1Hz, with the strain amplitude of 60 με.

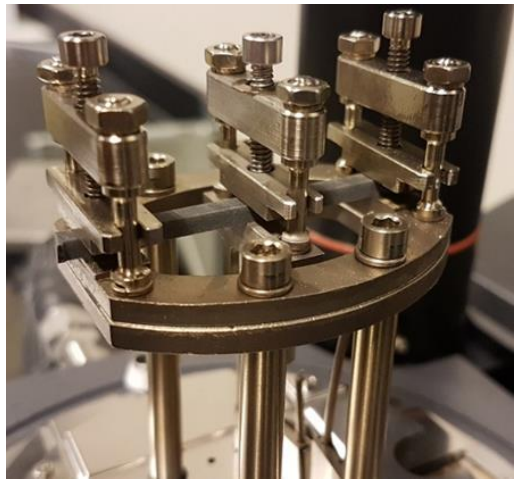

Figure 2.6-1: DMA double cantilever fixture

The temperature of the furnace ramped to 250℃ by 5℃ /min. Since, T_g is independent on the direction, a sample of any direction can be tested. The length of the sample was 60 mm, width is approximately 3.78 mm, and a thickness of 2.75 mm.

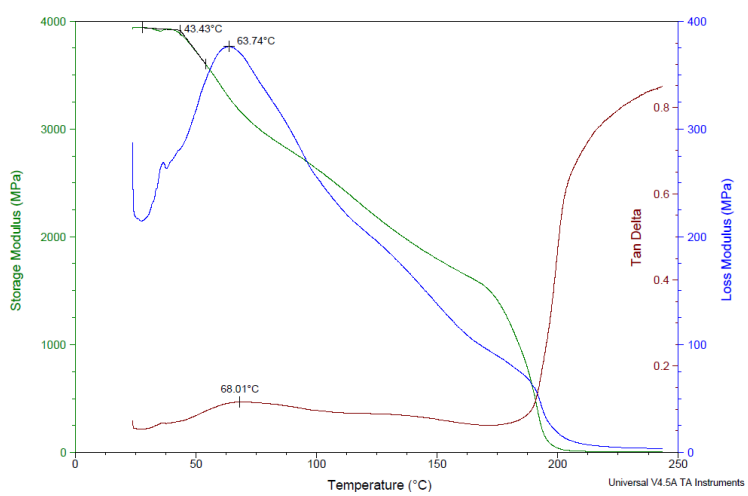

Figure 2.6-2: Tg from Storage modulus, loss modulus, and tan delta vs temperature of 50% GF-PA

The glass transition temperature can be obtained from three methods: from storage modulus, loss modulus, and tan delta. The graph of the storage modulus, loss modulus vs temperature and the T_g obtained from the three methods is depicted in Figure 2.6-2. The T_g obtained from the DMA and DSC is listed in Table 2.6-1. The T_g obtained from the onset decrease in of the storage modulus is 43.43 ℃ which occurs at the lowest temperature and relates to mechanical failure. The T_g obtained from the peak of loss modulus is 63.74 ℃ which occurs at the middle temperature and is more closely related to the physical property changes attributed to the glass transition in plastics. It reflects molecular processes and agrees with the idea of T_g as the temperature at the onset of segmental motion. Lastly, T_g from the Tan Delta Peak is 68.01 ℃ occurs at the highest temperature which is physically midpoint between the glassy and rubbery states of a polymer [42].

Table 2.6-1: Tg from the storage modulus, the loss modulus, and the tan delta.

T_g		
Storage Modulus	**Loss Modulus**	**Tan Delta**
43.43 ℃	63.74 ℃	68.01 ℃

2.6.2 Coefficient of Thermal Expansion and Crystallization Shrinkage

In the EDAM process, after a melted material is deposited on a surface, it cools down and shrinkage occurs. The total shrinkage of a semi-crystalline thermoplastic polymer is composed of both the thermomechanical shrinkage, governed by the coefficients of thermal expansion (CTE) and the crystallization shrinkage that is imposed when the material crystallizes. The coefficient of thermal expansion is a parameter used to express the dimensional change (volume, length, etc.) of a material in response to temperature change. Thermal expansion is defined as the change of dimensions of a body or material as a result of a temperature change. The material property constant describing this phenomenon is the coefficient of thermal expansion (CTE), indicated by the symbol α and defined as shown in Equation (2.6.1).

$$\alpha = \frac{\Delta\varepsilon}{\Delta T} \tag{2.6.1}$$

Where $\Delta\ \varepsilon$ is the increment of strain measured for an unconstrained material subject to a temperature change ΔT. A different constant can be used CTE to express thermomechanical strains for the temperature ranges above and below the glass transition temperature.

To ease the data reduction process, the material used in this section is 50% wt. GF-PA printed with the Composite Additive Manufacturing Research Instrument (CAMRI) system. The CAMRI system prints a much smaller bead. Keeping the aspect ratio of 4, the print bead has a bead height of 1.6 mm and a bead width of 6.4 mm. The CTE sample is a square with a width of 25.4 mm and a thickness of approximately 3 mm. The sample preparation steps are identical to the tensile and shear samples described in section 3.2.2 Mechanical Characterization. The order of the process is: print, heat treat, waterjet, dry, and speckle. Because GF-PA has fiber oriented in such a way that the printed material is anisotropic, the CTE is dependent on the directions. Therefore, samples have to be prepared for all three-principal directions. The samples tested were in the 1-2 plane (perpendicular to the stacking direction) and 2-3 plane (perpendicular to the printing direction). The 1-direction CTE was obtained from the 1-2 plane, and the 3-direction CTE was obtained from the 2-3 plane. The 2-direction CTE can be obtained from both of the samples in both planes. However, the 1-2 plane results in smoother and linear CTE while the crystallization shrinkage is more observable in the 2-3 plane. Therefore, the CTE in the 2-direction was obtained from 1-2 plane, while crystallization shrinkage was obtained from the 2-3 plane.

It is preferred to use panels printed in the CAMRI system because the bead size is smaller. Therefore, multiple CAMRI system's full beads can be captured within the 25.4 mm x 25.4 mm square. This eases the virtual characterization step because the fiber orientation of the whole CAMRI bead can be utilized directly, instead of taking more micrographs of a machined shaved LSAM beads.

For the experimental setup, a Digital Image Correlation (DIC) system with a camera was utilized in combination with an INSTEC heating stage and a thermocouple to determine the temperature-dependent CTE of the printed composite material and the crystallization strains. The digital camera was leveled with the plane of the sample and placed over it. The distance between the sample and the camera was adjusted to capture the full sample area covered with the speckle pattern. The test

set up is shown in Figure 2.6-3, the sample was placed on the Kapton film in the middle of the heating stage, with both lights shining on it. The purpose of the Kapton film is to prevent melted material from sticking to the heated stage plate. Next, the sample was subjected to the prescribed thermal cycle during which the digital camera made photographs every 15 seconds. The heated stage ramps the temperature up to 285 ℃ at the rate of 3 ℃/min, then isothermal for 15 minutes, then cools down at the rate of 2 ℃/min.

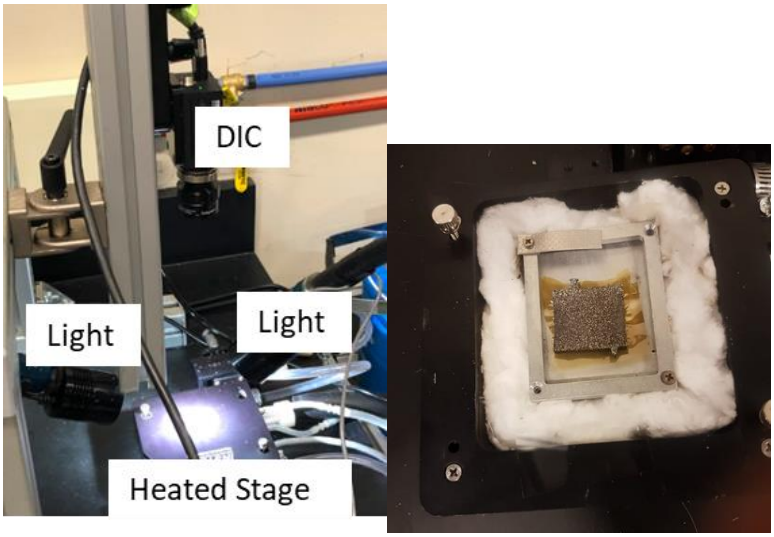

Figure 2.6-3: (Left) Digital image correlation setup for CTE test, (Right) sample on the Kapton film in the heated stage

The snapshot of the sample in the 2-3 plane is shown Figure 2.6-4. The snapshots were taken when the temperature of the heated stage is 88 ℃, 150℃, 200℃, and 230℃ as labeled. In the CAMRI prints, the fibers are mainly aligned in the 1-direction or the print direction which fibers constrain the expansion/shrinkage of the part while temperature changes. Therefore, the sample in the 1-2 plane doesn’t expand nor shrink significant enough to notice in snapshots.

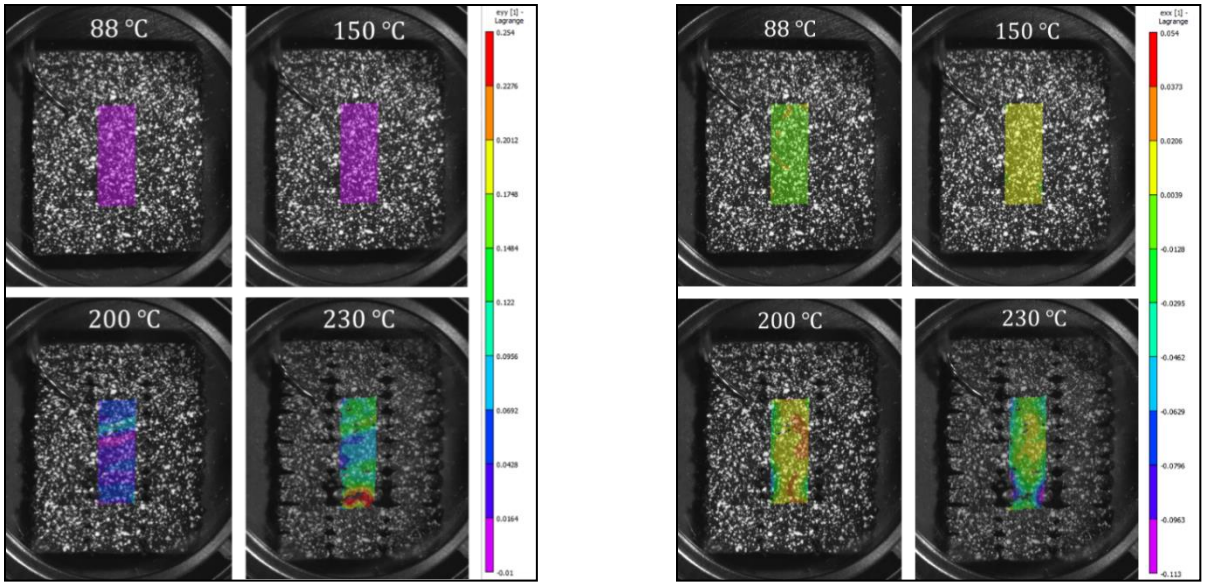

Figure 2.6-4: (Left) Strain in the 3-direction, (Right) strain the 2-direction.

The strain in the three principal directions were exported from the DIC and imported into Matlab© for CTE calculation. Figure 2.6-5 illustrates the computed strain histories for each of the investigated directions. The 2-direction strain shown in the figure was from the 2-3 plane. Figure 2.6-5 has three different colors, each separating the three material transitions. The temperature in the blue section is below the glass transition temperature, green is between T_g and melting temperature (T_m), and red is above T_m.

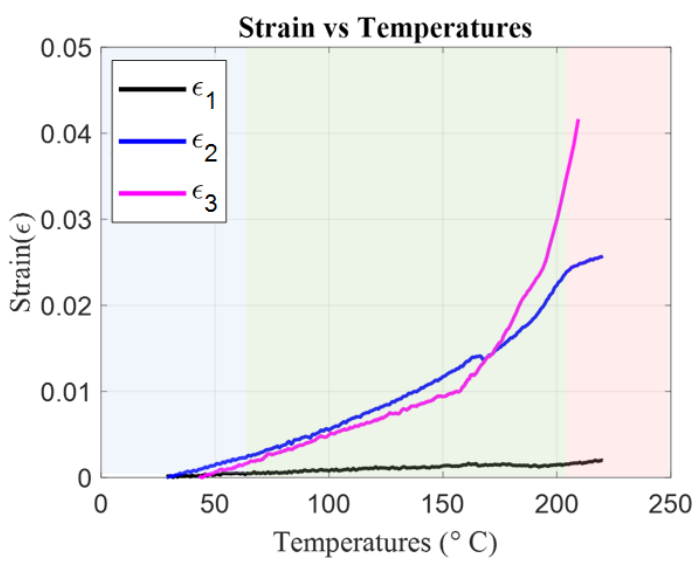

Figure 2.6-5: Computed strain histories from the recorded DIC data

The CTE was obtained by linear fitting the strain at room temperature up to $T_g = 63$ ℃ and another linear fitting the strain from T_g up to 150 ℃, as illustrated in Figure 2.6-6. The strain the 2-direction was obtained from the 1-2 plane.

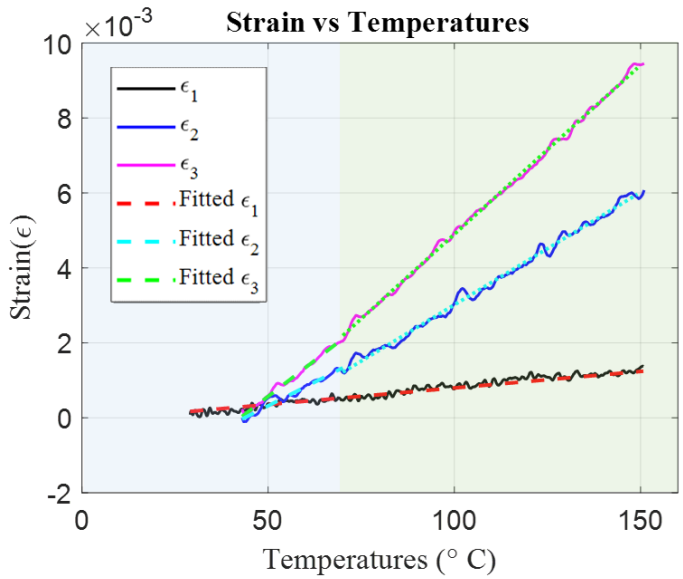

Figure 2.6-6: Experimental and fitted strain vs temperature

The CTE is taken as the derivative of the fitted strain function. Therefore, the CTE will be a single value because the fitted strain is a linear function. Figure 2.6-7 shows the calculated CTE as a function of temperature for all the three principal directions. Those CTE as a function of temperature is also listed in Table 2.6-2.

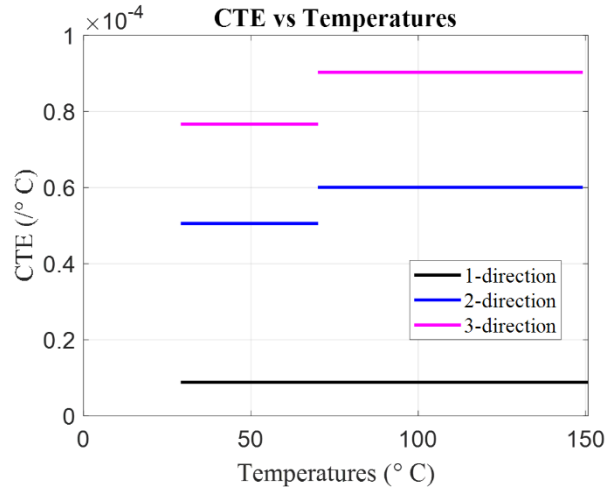

Figure 2.6-7: CTE as a function of the temperature of the CAMRI printed parts

Table 2.6-2: CTE as functions of Temperature in all three principal directions

CTE ($°C^{-1}$)	1-direction	2-direction	3- direction
Below $\boldsymbol{T_g}$	$8.851 \cdot 10^{-6}$	$5.055 \cdot 10^{-5}$	$7.662 \cdot 10^{-5}$
Above $\boldsymbol{T_g}$	$8.851 \cdot 10^{-6}$	$6.004 \cdot 10^{-5}$	$9.027 \cdot 10^{-5}$

It is worthy to note that the CTE listed in Table 2.6-2 is the properties of the sample printed in the CAMRI system. A virtual characterization involving micromechanics is needed to obtain properties of LSAM AR 4 full bead. The fiber orientation of a CAMRI and LSAM full bead is shown in Table 2.6-3.

Table 2.6-3: Fiber orientation of LSAMAR 4 and CAMRI AR4

LSAM AR4	CAMRI AR4
$\mathbf{A_{ij}} = \begin{bmatrix} \mathbf{0.57} & \mathbf{0} & \mathbf{0} \\ \mathbf{0} & \mathbf{0.34} & \mathbf{0} \\ \mathbf{0} & \mathbf{0} & \mathbf{0.09} \end{bmatrix}$	$A_{ij} = \begin{bmatrix} 0.73 & 0 & 0 \\ 0 & 0.20 & 0 \\ 0 & 0 & 0.07 \end{bmatrix}$

Digimat Mean-field homogenization was the tool used for this purpose. Because the GF-PA pellets are the same type from the same supplier, the fiber volume fraction of both CAMRI and LSAM bead is 30%. The constitutive properties of both fiber and matrix are needed for virtual micromechanics calibration as shown in Table 2.6-4. The fiber properties are from manufacturer

and literature. The matrix properties are calibrated from CAMRI experimental data except for the Poisson ratio which is obtained from the manufacturer. The temperature was broken down to two range; below T_g and above T_g. The matrix's properties are different at each temperature range due to its viscoelastic nature.

Table 2.6-4: Fiber and Matrix Properties required for CTE virtual characterization.

Properties	Glass Fiber	Nylon (Polyamide)
Youngs modulus at 25 ℃	72 GPa	1.9 GPa
Youngs above T_g	72 GPa	1.3 GPa
Poisson Ratio	0.21	0.35
CTE below T_g	$2.5 \cdot 10^{-6}$	$8.8 \cdot 10^{-5}$
CTE above T_g	$2.5 \cdot 10^{-6}$	$1.10 \cdot 10^{-4}$
Fiber aspect ratio	27.2	-

CTE at the LSAM bead level was found utilizing the properties in Table 2.6-4 with the LSAM fiber orientation. One virtual characterization was done to predict the CTE below T_g and another for CTE above T_g. Finally, the CTE in the three principal directions calibrated for a full bead of LSAM with an aspect ratio of 4 is shown in Figure 2.6-8 and listed in Table 2.6-5.

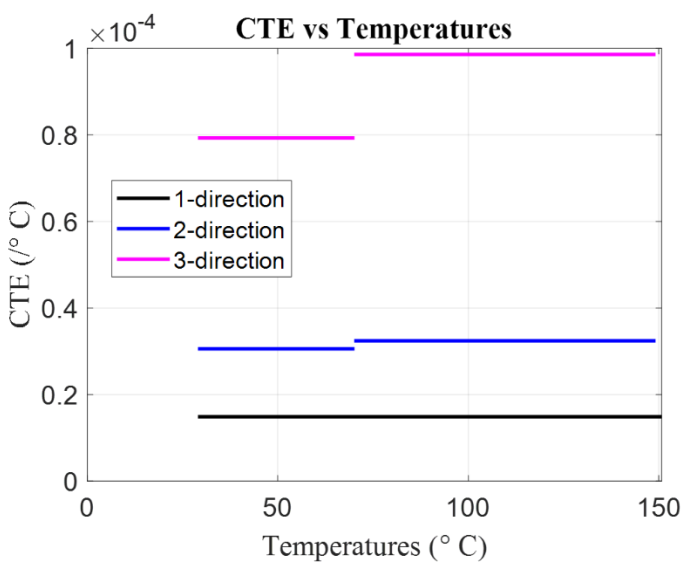

Figure 2.6-8: CTE as a function of temperature for the full bead printed in the LSAM

Table 2.6-5: CTE as a function of the temperature of the LSAM full beads

CTE ($°C^{-1}$)	1-direction	2-direction	3- direction
Below T_g	$1.487 \cdot 10^{-5}$	$3.057 \cdot 10^{-5}$	$7.93 \cdot 10^{-5}$
Above T_g	$1.487 \cdot 10^{-5}$	$3.241 \cdot 10^{-5}$	$9.861 \cdot 10^{-5}$

The CTE in the 1-direction of the LSAM's bead is significantly higher than that of CAMRI because the fibers are more collimated in the CAMRI's bead ($A_{11}^{LSAM} = 0.57, A_{11}^{CAMRI} = 0.73$). More fibers alignment helps restrain the bead from matrix expansion, while also helps restrain the bead while matrix shrinks. CTE in the 2-direction is higher for CAMRI bead because there is less fiber alignment in the 2-direction in CAMRI than in LSAM bead ($A_{22}^{LSAM} = 0.34, A_{22}^{CAMRI} = 0.2$). The 3-direction always has very few fibers alignment, therefore, the properties are dominated by the matrix. Because of this, the CTE in the 3-direction is almost identical for LSAM and CAMRI beads.

In the stacking direction (3-direction), the measured shrinkage strains of the material are the largest since almost no fibers are aligned in this direction. In the transverse in-plane direction (2-direction) the final material shrinkage is a little more than 5 times of this value, based on the much higher amount of fibers aligning in the 2-direction, compared to the stacking direction. Finally, the total crystallization shrinkage in the printing direction (1-direction) is almost negligible due to the highly collimated fiber orientation in this direction. Crystallization occurs in the green section, as well as crystallization shrinkage.

2.6.3 Crystallization Shrinkage

Figure 2.6-9 is the strain from the 1-2 plane sample, and the focus of this paragraph is on the 2-direction strain. As illustrated in the figure for the shown example, the shrinkage strain curves were approximated with a linear fit for the strain at room temperature up to T_g (in green dashed line), and quadratic fits between T_g to the beginning of the crystallization temperature and extrapolated to the end of the crystallization temperature (in red dashed line).

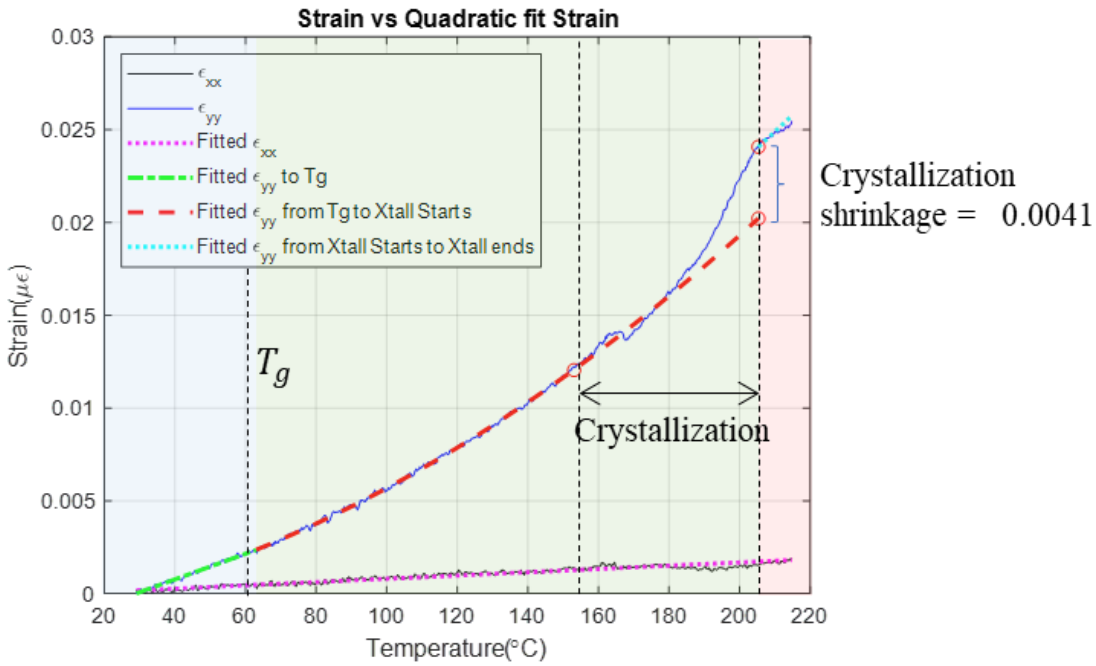

Figure 2.6-9: Experimental and fitted strain vs temperature of the 1- and 2-direction

The crystallization shrinkage is the difference between the experimental strain and fitted strain at the end of the crystallization temperature. The strain above the end of the crystallization temperature was extrapolated utilizing the same quadratic fitting coefficient (in blue dotted line). Figure 2.6-9 shows the fitted strain as a function of temperature for all the three-principal direction.

2.7 Thermoviscoelastic Properties

In contrast to elastic materials, polymers show viscoelastic mechanical material behavior. This means that they exhibit both the solid characteristics of elastic materials and store elastic energy when loaded, but also dissipate a part of the energy and flow on the microscale showing behavior similar to fluids.

In order to characterize the thermoviscoelastic material behavior of a printed fiber-reinforced material that can be assumed orthotropic, temperature-dependent relaxation experiments need to be conducted for each of the nine independent components C_{ij} of the stiffness matrix as discussed in the 2.3 Elastic properties section. A fiber- and matrix dominated relaxation behavior can be

experimentally determined and applied to the corresponding other matrix components such as off-axis components of the stiffness matrix which are difficult to characterize.

Material is investigated experimentally using stress relaxation time-temperature superposition TTS experiments with a Dynamic Mechanical Analyzer (DMA) where material samples are automatically tested in relaxation experiments at different temperatures. The DMA sample has the dimension of 60 mm $\times$ 12 $mm \times 3$ mm $(length \times width \times thickness)$. Both the 1-direction and the 2-direction samples were extracted from the 1-2 plane. Figure 2.7-1 shows the location with respect to the bead of the DMA samples.

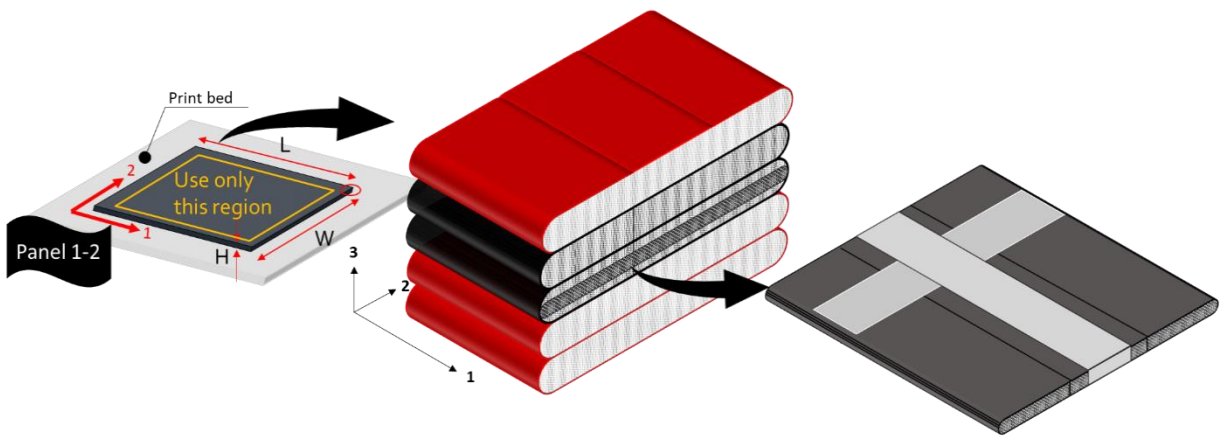

Figure 2.7-1: DMA samples extracted from the bead

Four types of samples were prepared, the 1-direction sample in the 1-2 plane, 2-direction sample in the 1-2 plane, 1-direction sample in the 1-3 plane, and 3-direction sample in the 1-3 plane. Two samples for each type were tested in stress relaxation time-temperature superposition (TTS) experiments utilizing a Q800 DMA (Dynamic Mechanical Analyzer) from TA Instruments©. The samples were tested with the three-point bending clamp. In this mode, the sample is supported at both ends, and force is applied in the middle. Since clamping effects are eliminated, a three-point bend is considered a "pure" mode of deformation. The temperature increase in an incremental manner with 15 °C increments from 35°C to 185°C. 5-minute soak time was held at the desired temperature before each stress relaxation test which lasts for 30 min. A strain of 0.05% was imposed on the sample throughout each temperature increment. A static load of 0.1 N was also applied to the sample to ensure proper contact with the support. Figure 2.7-2 shows the relaxation modulus of a 1-direction sample in the 1-2 plane.

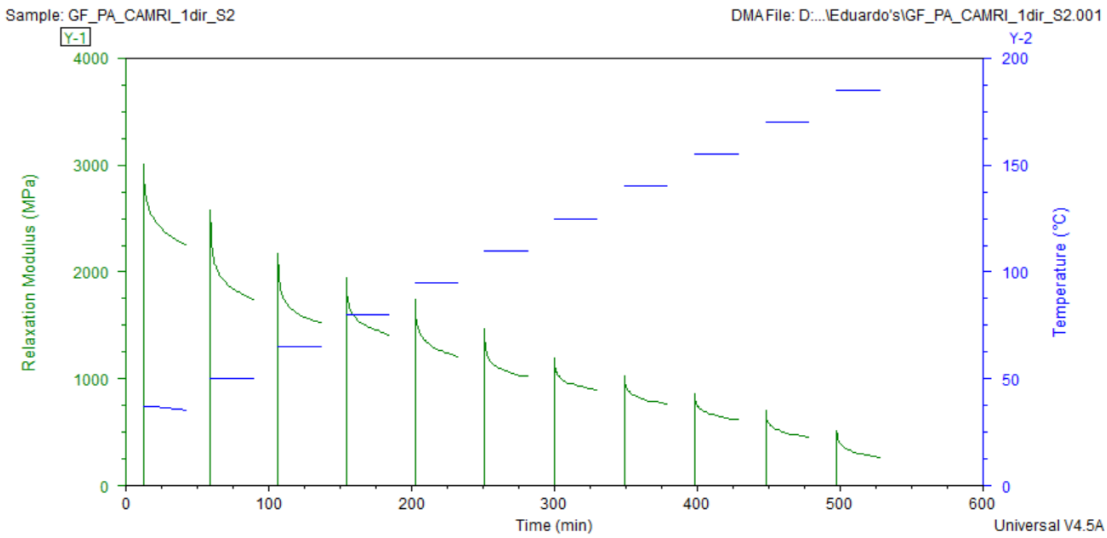

Figure 2.7-2: Time and temperature dependent relaxation modulus during the TTS

The TTS data was exported from the TA analysis© software and was imported into Rheology Advantage Data Analysis© from TA Instruments© to calculate for the horizontal TTS shifts with built-in functionality. The TTS data and horizontal shifts were imported into Matlab©. Figure 2.7-3 shows the results from different relaxation experiments at various temperatures for a relaxation modulus of the 1-direction (a) and the 2-direction (b) of a printed glass fiber reinforced PA material.

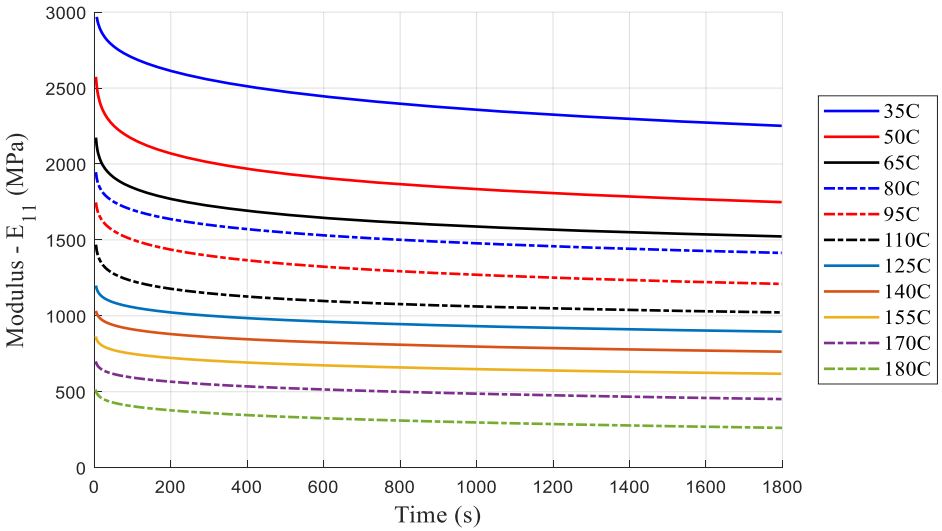

a) Relaxation modulus of the 1-direction at various temperatures

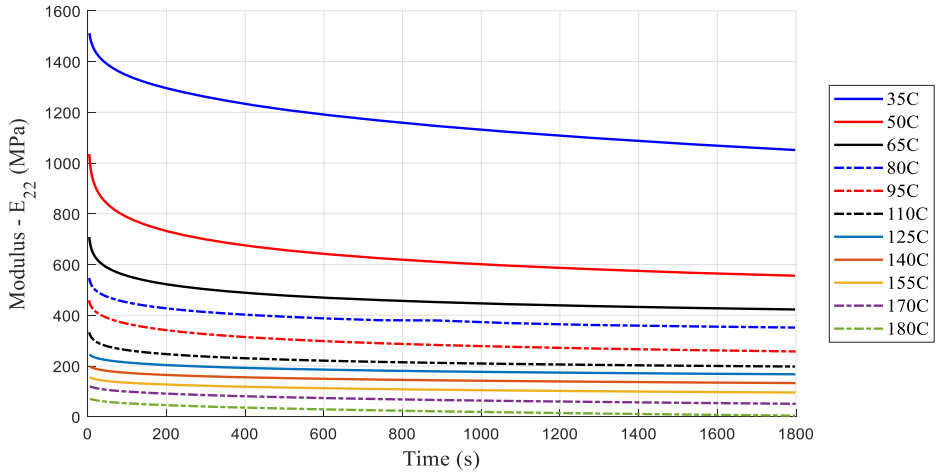

b) Relaxation modulus of the 2-direction at various temperatures

Figure 2.7-3: Stress relaxation experiments at various temperature

The experimental results obtained from relaxation experiments must be shifted horizontally to form master curves at a reference temperature of 65°C. The shift factor for the horizontal TTS shifts was obtained via the built-in functionality for the shifting process in the software Rheology Advantage Data Analysis© from TA Instruments. A good fitting procedure is described by Brinson and Brinson [43]. Both the relaxation experiments data and the shift factor were read into Matlab©. Figure 2.7-4 illustrates the resulting master curves in the 1-direction and 2- direction.

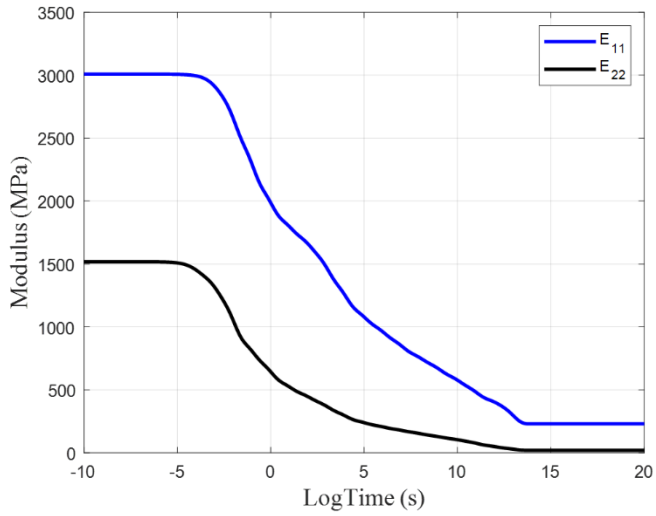

Figure 2.7-4: Master curves in the 1-direction and 2- direction

A generalized Maxwell model was used to describe the relaxation behavior of a realistic polymer. It is a series of parallel single Maxwell models to provide better mathematical representation of the overall stress response in a viscoelastic material [44][27]. Utilizing the Prony series representation, the stiffness matrix components C_{ij} can be expressed with Prony series type models fitted to master curves for a reference temperature T_0 as shown in Equation (2.7.1) [44].

$$C_{ij}(T_0, t) = C_{ij0} + \sum_{w=1}^{N} C_{ijw} \exp\left(-\frac{t}{\lambda_{ijw}}\right) \tag{2.7.1}$$

In the Equation (2.7.1), C_{ij0} are the relaxed and C_{ijw} the instantaneous parts of the stiffness matrix components. λ_{ijw} are the relaxation times of the respective Maxwell elements describing the viscoelastic behavior of the material. The accuracy of the material description is dependent on the number N of Maxwell elements used to model the material behavior. In this study 21 Maxwell elements were utilized, therefore there are 21 λ_{ijw} and 21 C_{ijw} values listed in

Table A 6 in the APPENDIX. More information is contained in the thesis by Brenken [27].

The master curve obtained above describes the E_{11} and E_{22} of the DMA sample with a certain fiber orientation. To create a master curve for the properties at the bead level, micromechanics analyses are utilized as an addition to the experiments to get the full orthotropic material description. The micromechanics estimate values for all the elastic properties at the bead level can be found in Table 2.3-8 in section 2.3.3. The elastic properties were multiplied to normalized master curves to estimate the full TTS behavior [27]. Figure 2.7-5 depicted resulting master curves for the stiffness matrix components at the reference temperature of 65 ℃.

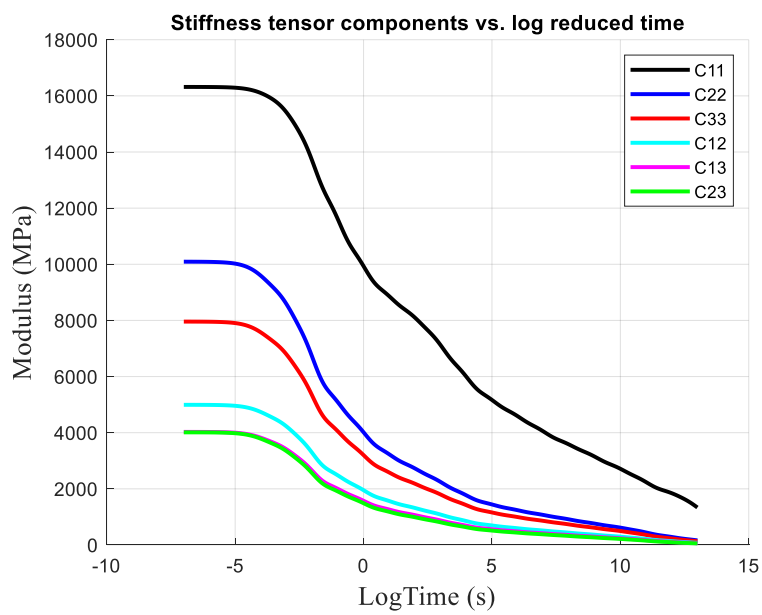

Figure 2.7-5: Master curves for the stiffness components.

3. VALIDATION OF EDAM PROCESS SIMULATION

Predicting residual stresses and deformation developed during the printing process of a geometry is of paramount importance for mitigating expensive print trials. Printing a geometry successfully can involve multiple iterations with the current empirical approaches. Hence, predictive simulation tools are essential for assisting engineers in the design for additive manufacturing as well as for continuing to expand the applications for this technology.

A digital material card required for simulating the EDAM process with GF-PA was developed from the extensive characterization carried out for this material. The EDAM process is simulated using ADDITIVE3D, a physics-based simulation workflow developed at Purdue University [45], [46].

3.1 ADDITIVE3D©

ADDITIVE3D© is a comprehensive simulation workflow that captures the multiple phenomena occurring as beads of molten material are deposited and gradually cooled during the EDAM process. Phenomena such as anisotropic heat transfer, material shrinkage, polymer crystallization, interlayer bonding, stress relaxation, and creep are captured in ADDITIVE3D©. This workflow utilizes the implicit solver (Abaqus©/Standard) of the commercial finite element software Abaqus©. Utilizing the trajectory of the print head provided in the machine code, the process of depositing material in a bead-by-bead basis is simulated by activating elements in a finite element mesh. Additionally, local orientations of the fiber-reinforced polymer are mapped to each material point in the finite elements based on the trajectory of the print head [28].

The simulation of the EDAM process consists of a sequentially coupled thermomechanical analysis since the temperature field does not depend strongly on the stress and deformation fields. Figure 3.1-1. shows the steps involved in the simulation of the EDAM process. The first and second steps, namely geometry and slicing, are relatively standard steps in the preparation for additive manufacturing of a geometry. In the slicing process, the 3D geometry is discretized into a set of layers wherein each layer can have a unique printing pattern. The slicing outputs the

machine code (G-code) that contains the trajectory for the print head. At this point in the simulation workflow, the G-code is used for generating the event series which is a discrete representation of the trajectory of the print head in time. The event series is used in both the heat transfer and mechanical analysis to coordinate the activation of the finite elements and to assign local material orientations.

The transient heat transfer analysis provides the temperature time history that governs the evolution of crystallinity in the case of semi-crystalline polymers, the thermomechanical shrinkage, and the thermoviscoelastic behavior of the printed material. Figure 3.1-2 summarizes the heat transfer mechanisms captured in ADDITIVE3D©. As depicted in Figure 3.1-2., the deposition process starts with the delivery of the extrudate of molten material at the exit of the extrusion nozzle. The material is then deposited on the top of the substrate corresponding to either the build plate or the previously deposited material. The temperature difference between a newly deposited bead and the substrate leads to heat conduction governed by the thermal conductivity that depends on the orientation of the fibers within the bead. Temperature-dependent orthotropic heat conduction is considered in ADDITIVE3D©.

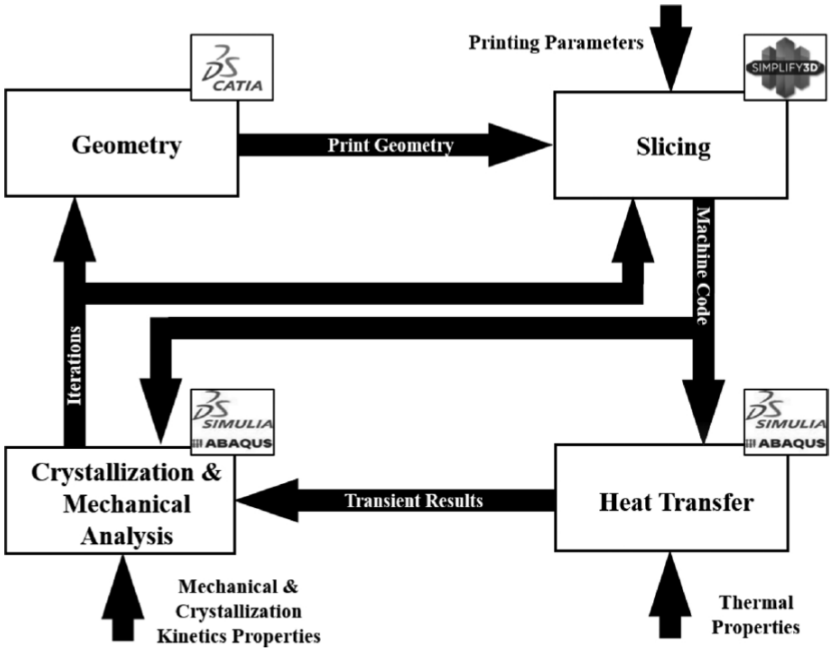

Figure 3.1-1. – Flowchart of process simulation in ADDITIVE3D©

The extrudate is compacted with a roller in the LSAM to aid wetting the substrate with molten material and to close the gaps between adjacent beads. The surface of the roller is actively cooled to prevent the adhesion of the molten polymer to the surface of the roller. The temperature difference between the roller and the extrudate results in heat losses through conduction. The heat removed during compaction is captured in ADDITIVE3D© by representing the roller with an in-plane ellipsoidal heat flow distribution that moves with the deposition nozzle. Further, the total heat removed with the roller can be estimated from the heat carried with the fluid used for cooling the compacter.

The crystallization process of the polyamide used in this work releases thermal energy (exothermic process), which affects the temperature history. Further, the inverse process of melting crystallized material absorbs thermal energy. Melting and crystallization kinetics are strongly coupled with temperature in ADDITIVE3D©. As a result, changes in the temperature history affect crystallization history and vice versa.

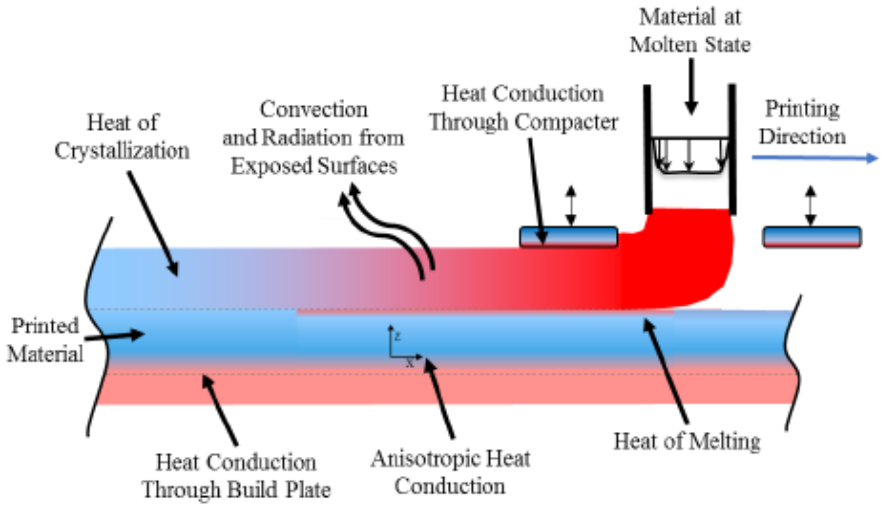

Figure 3.1-2. – Heat transfer mechanisms captured in ADDITIVE3D©

Thermal losses also occur by convection and radiation at the continuously changing exposed surfaces of the printed geometry. Convection arises due to heat conduction from the hot surface of the printed material to the air surrounding the part, which in turn gives rise to local changes in air density. Buoyancy driven flow arises from changes in density, thereby giving rise to a hydrodynamic and a thermal boundary layer that acts together to convey thermal energy away from the surface through the movement of air. Since the convection heat transfer is highly geometry dependent, ADDITIVE3D© treats different geometric features conditions by using a set of correlation equations. Similarly, heat losses through radiation are important particularly at elevated temperatures since its contribution scales with the fourth power of the temperature at the surface. A more detailed description of the heat transfer analysis carried out in ADDITIVE3D© can be found in the dissertation by Eduardo Barocio [47].

The stress and deformation analysis utilize the temperature and crystallinity predicted in the heat transfer analysis. Internal stresses arise primarily from restraining the anisotropic shrinkage of the printed material. As a new layer is deposited, the substrate, which is already at a relatively lower temperature is wetted with the molten material of the newly deposited bead. At that point, the shrinkage at the bottom of the newly deposited bead is practically restrained by the substrate. The difference in shrinkage developed as the layers cool down and the development of stiffness with temperature gives rise to internal stresses.

The total shrinkage of a semi-crystalline thermoplastic polymer is composed of both the thermomechanical shrinkage and the crystallization shrinkage. The thermomechanical shrinkage is governed by the coefficients of thermal expansion, which is dependent on temperature and anisotropic due to the orientation of fibers within the bead. The crystallization shrinkage depends on the degree of crystallinity that forms during the cooling process and the related densification of the matrix material. Thermomechanical and crystallization shrinkage are captured in ADDITIVE3D©.

The mechanical behavior of the printed material is also anisotropic and evolves as a function of temperature and time. As the material cools down from the deposition temperature, the material stiffness undergoes multiple transitions wherein significant changes occur. For instance, fiber-reinforced semi-crystalline polymers transition from a viscoelastic-fluid like behavior to a viscoelastic-solid like behavior upon crystallization. An additional change in the stress relaxation behavior occurs at the glass transition temperature of the polymer. Including the thermoviscoelastic behavior of the fiber-reinforced polymer is paramount to predict residual stresses and deformation. ADDITIVE3D© utilizes an orthotropic thermoviscoelastic material formulation for computing the evolution of internal stresses with temperature and time. Further details on the mechanical analysis can be found in the dissertation by Bastian Brenken [27].
Predictions for temperature-time history and deformation have been validated with a material card generated previously for 50% by weight of carbon fiber reinforced polyphenylene sulfide (PPS) [27], [45], [47].

3.2 Printing Experiment

Two geometries were designed and printed in the LSAM for validating predictions of the temperature-time history and deformation made with ADDITIVE3D© and with the material card developed for the GF-PA. The geometries were designed with the following considerations. One of the geometries was designed to develop significant out-of-plane deformation due to stresses induced by the anisotropy of the printed material and by the temperature gradients developed during the printing process. Further, geometries with flat surfaces are preferred since these are less susceptible to error in the measurement of deformation. In other words, the scalloped surface introduced with the rounded ends of the printed beads can obscure the measurements of

deformation. A second geometry was designed with a vertical wall to facilitate monitoring the temperature-time history with a thermal camera throughout and posterior to the printing process. Further, this geometry was of similar scale as the vehicle components that are relevant to the project partners. Following these considerations, a flat plate and a curved wedge were designed and investigated in ADDITIVE3D© to confirm the expected outcome before conducting the printing experiments.

The flat plate and the curved wedge were printed with GF-PA in the LSAM printer at Local Motors. A build sheet made from Acrylonitrile Butadiene Styrene (ABS) was used as a printing substrate. The build sheets were secured with electrical tape along the edges to a vacuum table which held the build sheets throughout the prints. A thermal camera FLIR® A655SC was used for monitoring the temperature evolution during the print. The thermal camera is calibrated for two different ranges of temperature, namely from $-40\ °C$ to $150\ °C$ and from $150\ °C$ to $650\ °C$. Thus, the temperature calibration was changed as the printed geometries cooled to below $150\ °C$. Portable cameras (GoPro®) were used for monitoring the out-of-plane deformation at specific locations in the parts during the printing process. A metric scale attached to squares placed in the field of view of the portable cameras provided a reference to estimate the out-of-plane displacement. An extra camera was used for recording a video of the printing process.

3.2.1 Flat Plate

The first geometry is a flat plate with a layup (layer stack) consisting of two layers oriented at 0° followed by two layers oriented at 90°, $[0_2 90_2]$. The unsymmetrical and unbalanced configuration of this layup leads to bending-twisting coupling in the response of the plate to deformation. The chosen layup produces an anticlastic curvature that depends strongly on the mismatch in CTE of the printed material along the directions parallel and transverse to the print. Further, thermal stresses resulting from temperature gradients developed in the plane of printing also affect the anticlastic curvature developed in the plate. Hence, the flat plate is a suitable geometry for validating the predictions for deformation since deformation occurs on flat surfaces that can be readily measured with a laser scanner.

Figure 3.2-1 shows the CAD geometry of the flat plate printed with four layers. The plate geometry was sliced with bead dimensions of 20.32 mm by 5.08 (aspect ratio of 4). The printing speed was set to 3810 mm/min (150 in/min), thereby resulting in a print time of around 18 minutes.

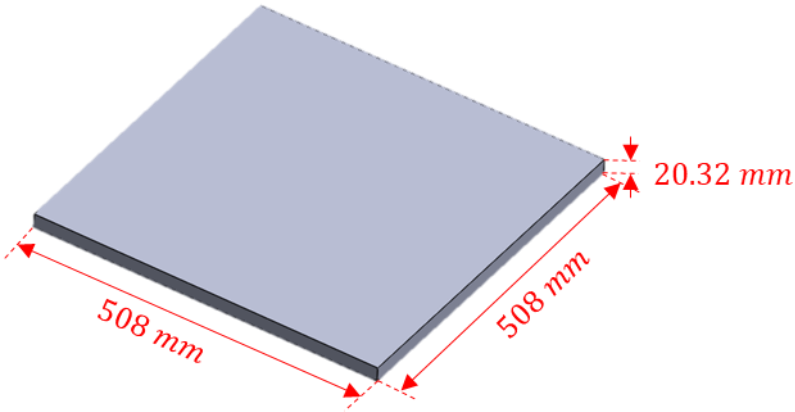

Figure 3.2-1: CAD geometry of the four-layer plate

Figure 3.2-2 shows the second and third layers generated after slicing the plate with the commercial slicer Simplify3D©. The first two layers share the same starting point whereas the last two layers share a starting point that is different from the first two layers. This slicing strategy was replicated in the slicer used for the LSAM.

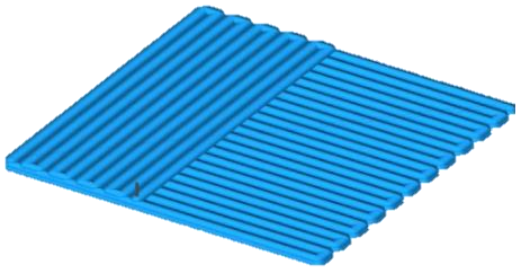

Figure 3.2-2: Flat plate slicing of layer 3 with Simplify 3D

Two print trials were carried out for calibrating the flow rate of the extrusion system and thereby determining the flow rate to speed ratio necessary to close the gap between adjacent beads. Table 3.2-1 summarizes the process conditions used in the LSAM.

Table 3.2-1: Process conditions used for printing plate in LSAM

Process Conditions	**Value**
Print Speed ($\boldsymbol{mm/min}$)	3810
Extrusion Temperature ($°\boldsymbol{C}$)	290
Melt Pump Temperature ($°\boldsymbol{C}$)	269
Nozzle Temperature ($°\boldsymbol{C}$)	343
Vacuum ($\boldsymbol{mBar}$)	715
Time for cooling after printing part ($\boldsymbol{min}$)	> 15

Figure 3.2-3 shows the experimental setup in the LSAM which includes a thermal camera, a video camera, two portable cameras, and scales placed in the field of view of the portable cameras (not shown in this figure). The thermal camera was configured to record the temperature of the part at 15 Hz and was located at approximately $2.5\ m$ from the plate. The first portable camera labeled as "GoPro 1" captured time-lapse photos every 10 seconds of the print and was focused on the corner labeled as 4. Similarly, the portable camera labeled as "GoPro 2" was focused at the edge of the plate in the corner labeled as 3. Finally, the video camera recorded the entire printing process of the part.

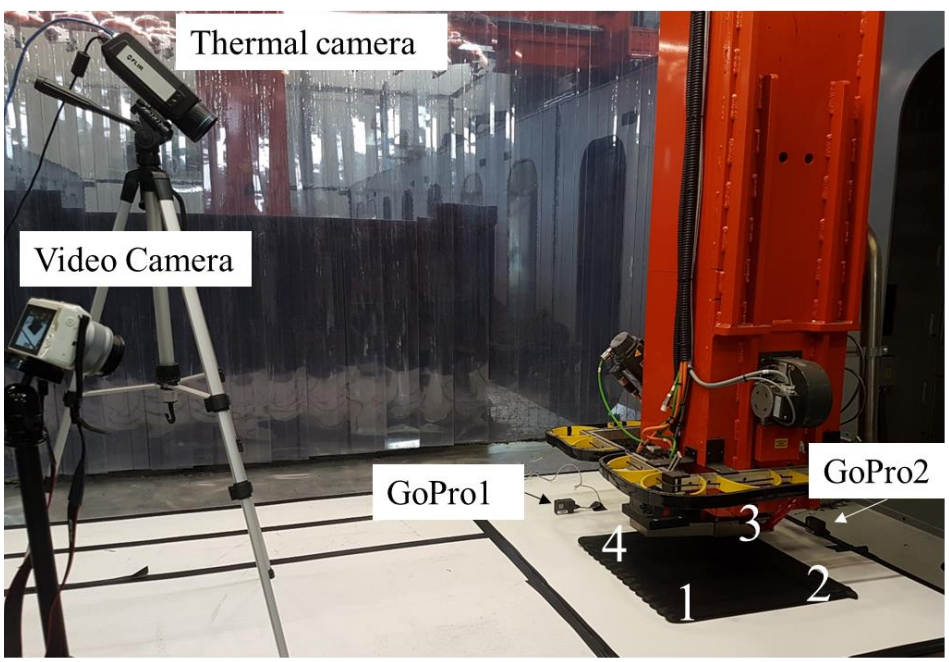

Figure 3.2-3: Experimental set-up used in the printing experiment of the plate

As the plate was printed, residual stresses developed due to temperature gradients developed across the plate and to the anisotropy of the printed material, thereby giving rise to gradually debonding of the printed plate from the build sheet. The removal of the constraint imposed by the build sheet allowed the deformation of the printed plate. The time-lapse photos captured the evolution of the deformation at the corners labeled as 3 and 4. Figure 3.2-4 shows the deformation at corner 4 at different instants of time during the print.

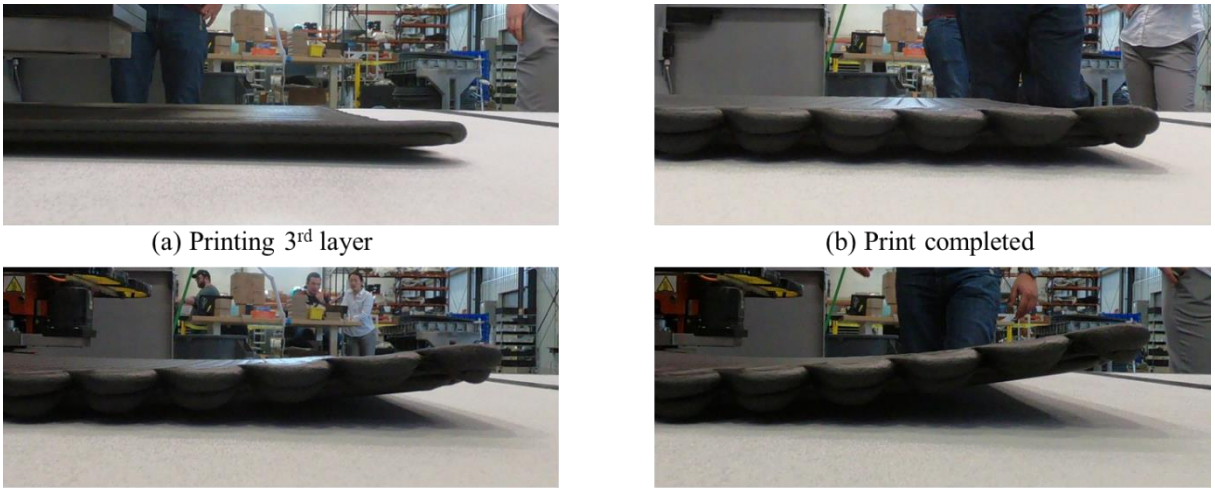

(a) Printing 3rd layer (b) Print completed

(c) 5 min cooling (d) 15 min cooling

Figure 3.2-4: Evolution of deformation at corner 4 in the printed plate captured in time-lapse photos

The bottom surface of the printed plate was scanned using a laser Faro® arm after the part was cooled to the room temperature and the maximum deformation was developed. The bottom surface was chosen since it preserved the smoothness and continuity of the surface of the build sheet. Otherwise, the measurements would be affected by the scalloped surface created with the beads at the top of the plate. Figure 3.2-5 shows the point cloud scanned from the bottom surface of the printed plate.

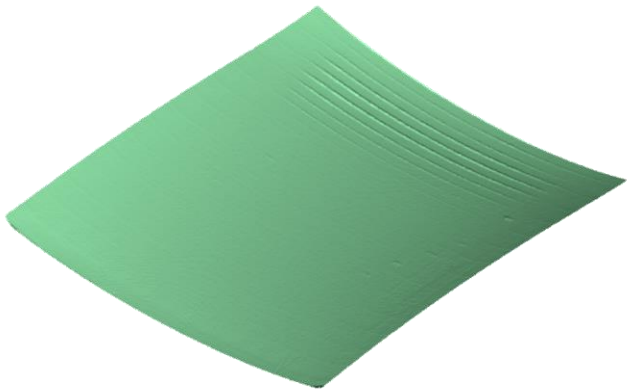

Figure 3.2-5: Point cloud scanned from the bottom surface of the printed plate

3.2.2 Curved Wedge

The second geometry is referred to as “Curved Wedge” and is in the scale of components relevant to the automotive industry. Figure 3.2-6 shows the CAD geometry of the curved wedge. This geometry was designed with a double purpose. First, the curved section was designed to introduce stresses in the radial and hoop direction that can lead to spring-in deformation. Stresses develop due to the difference in CTE in the radial and hoop direction and thus the larger the mismatch in CTE the higher the stresses developed. Second, the tapered regions were designed to promote warpage at the ends of the part. The warpage introduced at the ends results from the competing effect of stresses developed as layers of molten material are deposited on top of previously deposited layers that are at a relatively lower temperature and the development of out-of-plane bending stiffness with the addition of new layers (bending stiffness scales with the cube of the height). Therefore, one of the ends is tapered to promote the warpage by reducing the bending stiffness in the region.

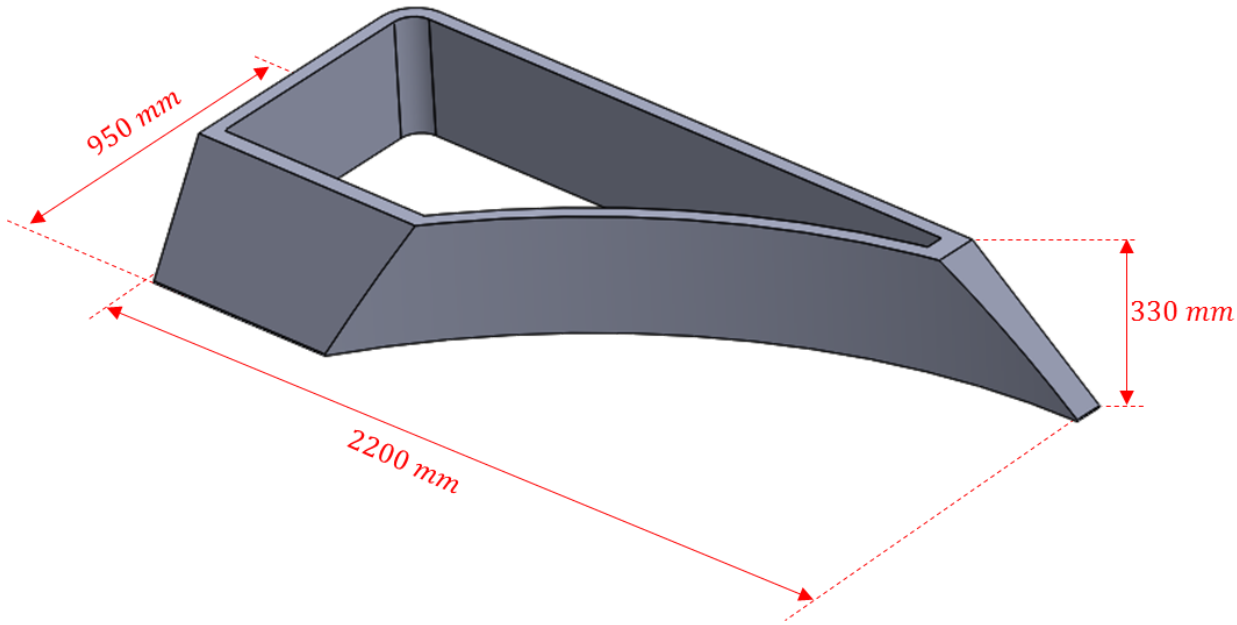

Figure 3.2-6: CAD geometry of the curved wedge

The curved wedge was sliced with two beads across the width of the wall as illustrated in Figure 3.2-7. The beads were deposited from the inside to the outside and transitioned between layers at the front left corner as indicated in Figure 3.2-7. The printing speed was constant throughout the print which led to layer times decreasing from 3 min 43 sec at the bottom of the part to 3 min 4 sec at the top of the part. Printing the 65 layers in the curved wedge took around 4 hours at a rate of 3175 mm/min (125 in/min). Once the printing process was completed, the curved wedge was left in the LSAM printer overnight for cooling with the build sheet held with a vacuum. Table 3.2-2 summarizes the process conditions used for printing the curved wedge in the LSAM.

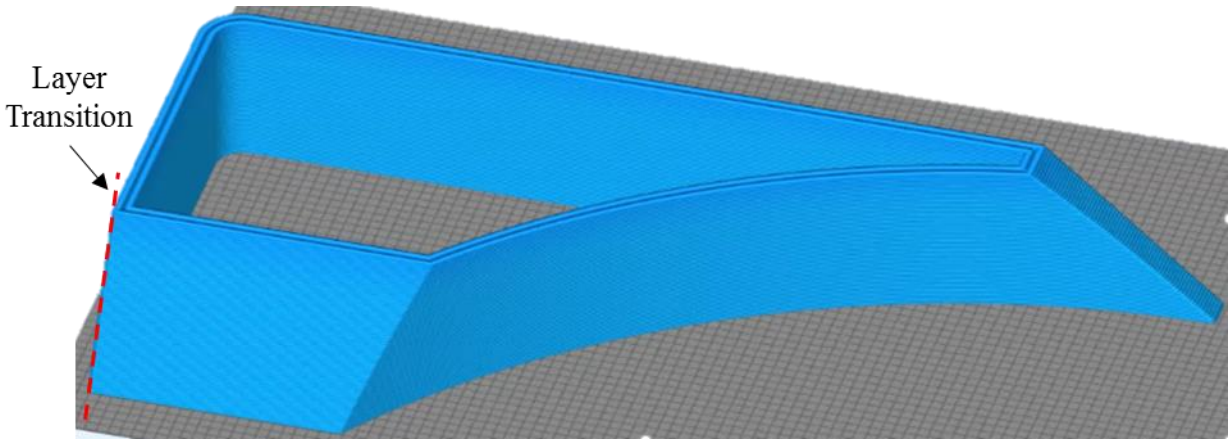

Figure 3.2-7: Slicing of the curved wedge geometry

The time-temperature history was recorded at the exterior surface of the longest straight wall in the curved wedge. Further, the cooling process of the part after the printing process was recorded for about 30 minutes. Portable cameras were also employed to monitor the warpage of the curved wedge at three different corners. Figure 3.2-8 shows the experimental set-up used which includes a thermal camera, a video camera, three portable cameras labeled as GoPro1, 2 and 3, and three scales placed in the field of view of the portable cameras. The thermal camera was located approximately 3 m from the vertical wall in the curved wedge and recorded at 15 frames per second. The portable cameras captured time-lapse photos of the print at a rate of 1 photo per 10 seconds and were focused at the corners labeled from 1 through 3 in Figure 3.2-8. Finally, the video camera recorded the overall printing to confirm the layer time and the start point of a new layer.

Table 3.2-2: Process conditions used for printing the curved wedge in the LSAM.

Curved Wedge	
Print Speed ($\boldsymbol{mm/min}$)	3175
Extrusion Temperature ($°\boldsymbol{C}$)	290
Melt Pump Temperature ($°\boldsymbol{C}$)	296
Nozzle Temperature ($°\boldsymbol{C}$)	343
Vacuum ($\boldsymbol{mBar}$)	715
Time for cooling after printing part ($\boldsymbol{min}$)	>30

The curved wedge was printed over two pieces of build sheet connected with electrical tape at the middle. The surface appearance of the build sheets was similar despite that one section had been reused multiple times and the other section was completely new. However, differences in the

adhesion of the printing material to the build sheet were noticed later between the two sections of the build sheet. Such a difference was observed while removing printing trials made for the plates. Therefore, the section of the curved wedge printed on each type of build sheet was recorded. The first 75 cm of the wide portion in the curved wedge was printed on the new build sheet (right section shown in Figure 3.2-8) whereas the rest of the curved wedge was printed on the reused build sheet.

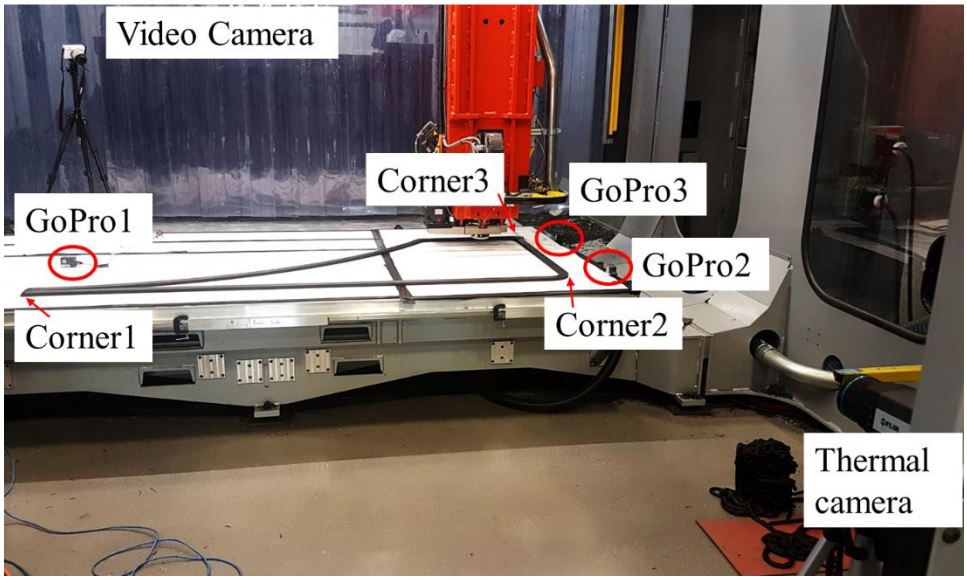

Figure 3.2-8: Experimental set-up used in the printing experiment of the curved wedge

The experimental temperature was recorded with the FLIR thermal camera. The temperature extraction was done using FLIR® ResearchIR Max software. The frequency of the thermal camera was set to 15 Hz. Table 3.2-3 listed the parameters set for the thermal camera calibration.

Table 3.2-3: Calibration parameters used in FLIR® ResearchIR Max.

Parameters	**Values**
Emissivity	0.92
Distance (m)	3
Reflected temp (℃)	30
Atmospheric Temp (℃)	20
Relative Humidity	50%
External optic temperature (℃)	20
Transmission	1

The curved wedge detached from the build sheet and warped up as intended at corner 1 during the print and it also warped but to a lesser extent at corners 2 and 3. Figure 3.2-9 shows the evolution of the deformation occurring at corner 1 as the curved wedge was printed and after cooling in the LSAM system.

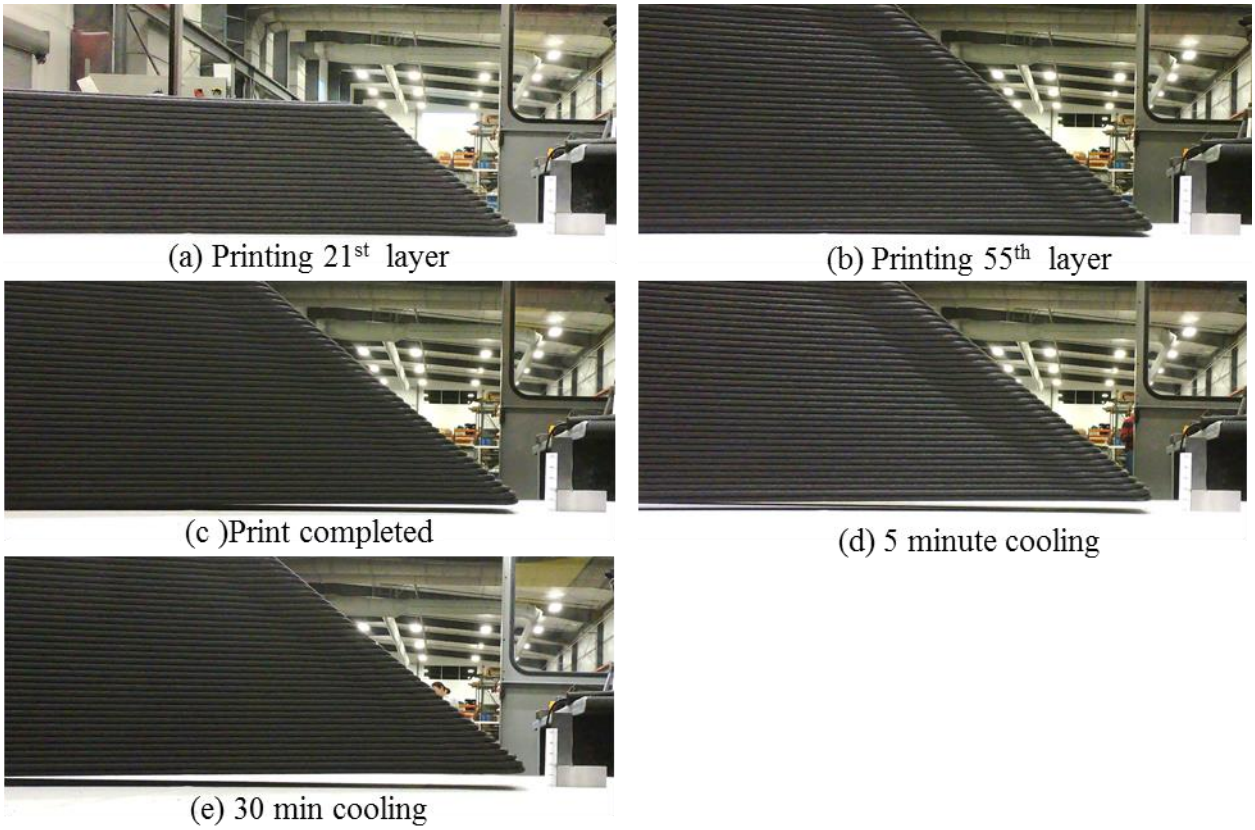

Figure 3.2-9: Go Pro time laps of the deformation at corner 1 of the curved wedge

Similarly, the vertical deflection was measured at the bottom of each corner after cooling the curved wedge overnight. Table 3.2-4 reports the vertical deformation measured at the bottom of each corner after cooling the curved wedge to room temperature.

Table 3.2-4: Vertical deformation measured at the bottom of each corner after cooling the curved wedge to the room temperature

Location	Maximum deformation (mm)
Curved wedge, corner 1	16
Curved wedge, corner 2	13
Curved wedge, corner 3	13

After cooling the curved wedge overnight, the part was laser scanned with the Faro® laser scanner in three different sections. This was necessary since the reach of the scanner was not sufficient for scanning the part with a single setup. The three scans included overlap to allow aligning the three different scans in the software Geomagic Wrap©. Figure 3.2-10 shows the point cloud generated with the three laser scans of the curved wedge.

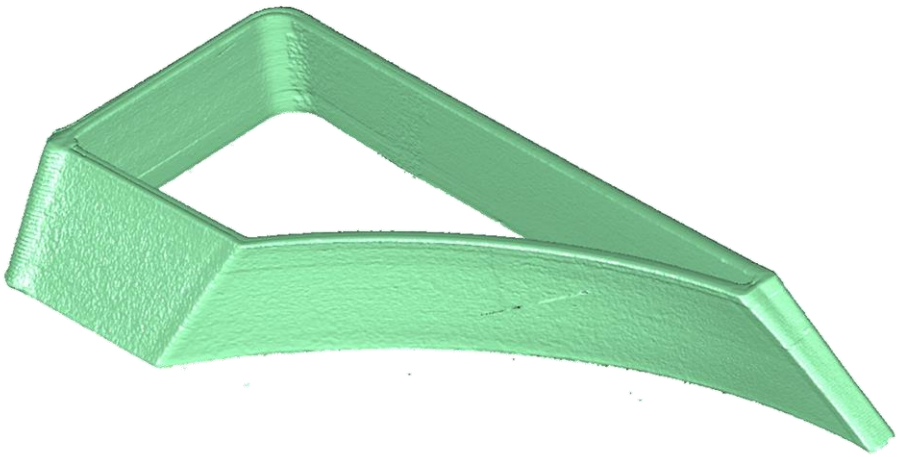

Figure 3.2-10: Point cloud scanned from the curved wedge printed in the LSAM.

3.3 Simulation of Printing Experiment

The printing process of the two geometries used for the printing experiments was simulated using ADDITIVE3D©. The first step required for simulating the printing process of a sliced geometry is to generate an event series, a spatial and temporal description of the print head motion. Utilizing the event series, the times for activating elements as well as the local orientation of the material within the part are determined [28]. The event series was generated based on the machine code (G-code) output from the slicer. A voxel finite element (FE) mesh was generated for each of the geometries using the event series. The next subsections provide the process conditions used in the simulations of the two printing experiments.

3.3.1 Flat Plate

A voxel FE mesh was generated based on the event series of the flat plate. Thus, elements are only present where the print head deposits material. Beads were discretized with two elements in the width and two in the height which lead to elements with dimensions of 10.16 mm in width and

2.54 mm in height. Linear brick elements type DC3D8 and C3D8 were used in the heat transfer and mechanical analysis, respectively [48]. A total of 50,045 finite elements were used to represent the geometry of the plate. To capture the process of debonding of the plate from the build sheet, a cohesive contact was defined between the bottom surface of the printed part and a substrate. The substrate was included only in the mechanical analysis and was modeled as an analytical rigid surface. This approach only considers debonding of the part from the build sheet since it was the only failure mechanisms occurring during the printing experiments. Figure 3.3-1 shows the FE mesh generated for the plate and the substrate that represents the build sheet.

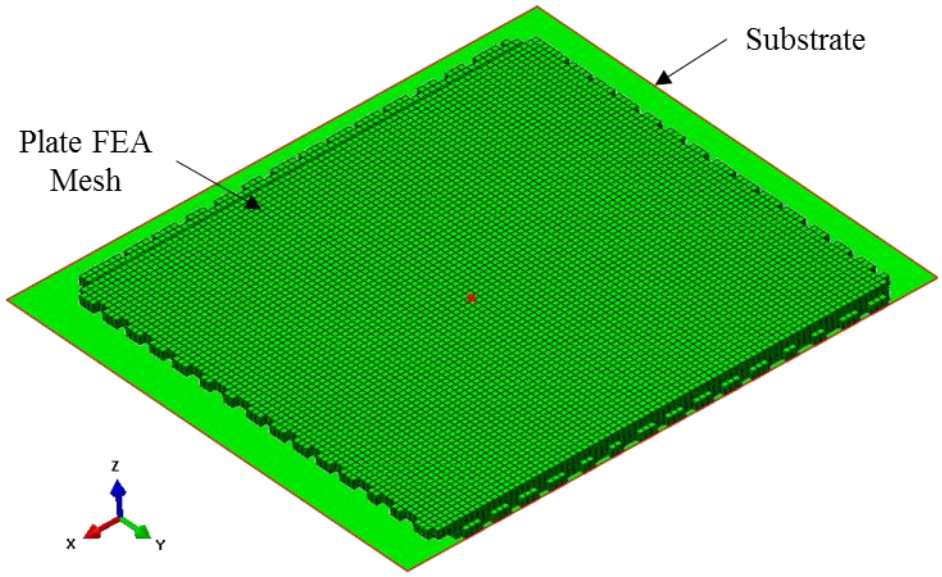

Figure 3.3-1: Voxel FEA mesh generated for the plate

The material properties reported in the section 0 One of the EDAM process's challenges is part distortion such as warpage, spring in, and delamination. Compare to neat polymer, the fiber reinforcement makes the thermomechanical performance of the printed part more complex. Meanwhile, it also improves the thermal performance and strength of the part. Moreover, because of the complexity, it also provides the opportunity to tweak the system to the user's advantage. In order to use the fibers to the maximum advantage, this thesis aims to study the relationship between the fiber orientation tensor to the properties of the composite and the residual stress and deformation of the final part. By doing so will provide better knowledge to optimize the fiber direction to best suit for a specific use of the part. The fiber alignment can be altered in several

ways such as changing the shape and size of the nozzle, compaction system, print speed, bead dimension, etc.

The importance of mitigating stress is highlighted in the medium to large scale prints. The deformation may not seem significant in a small scale print, but for a large scale print with dimensions in the scale of meters, the residual stress accumulates and the deformation becomes noticeable. In some cases, internal stress lead to interlayer crack and failed prints. Even though the part can be printed with excess geometry and machined down to the final shape, those internal stress still exists.

The reason behind studying fiber orientation state is because it is the prime factor that governs the properties of the additive manufactured bead. When aligned in a particular direction, performance in that direction immediately improves. It can be helpful in some applications in terms of strength and geometry accuracy in that direction. However, high fiber collimation also leads to a high degree of anisotropy. The effect of fiber types, such as isotropic fiber, like glass fiber, and transversely isotropic fiber, such as carbon fiber, are also expected to influence the effective properties of the composites. Thus, the first question to be addressed in this study is: How do microstructural properties of short fiber composite affect the macroscopic effective properties?

In a related topic, the EDAM parts are also expected to be influenced by the macroscopic effective properties of the composites. Anisotropic cooling and anisotropic shrinkage, and directional strength of the composites are some factors that influence the residual stress and deformation of the printed parts. Therefore, another interesting question that this study aims to address is: how does fiber orientation tensor affect the deformation and residual stress of an EDAM part? This serves to be a good preliminary study to understand process-induced deformations in EDAM.

EXPERIMENTAL CHARACTERIZATION OF ADDITIVELY MANUFACTURED FIBER REINFORCED THERMOPLASTIC were used in the simulation of the EDAM process. To simulate the material in the molten state prior to deposition, the temperature of the nodes in the FEA mesh were initialized to the melt temperature. The bottom surface of the plate was assumed adiabatic due to the low thermal conductivity of the material used for the build sheet (ABS). The convection conditions developed at the surface of the plate were governed by a correlation equation that provides a local convection coefficient [47]. The heat removed with the compression wheel, the emissivity, and the ambient temperature for radiation are calibrated based on the printing experiments. The addition of instrumentation such as a flow rate meter and thermocouples at the inlet and outlet of the flow lines in the compression wheel would allow characterizing the heat removed with the compression wheel [47]. Similarly, the emissivity of the material can be determined using a black body cavity printed with the same material [47]. The constitutive behavior of the cohesive contact defined between the bottom surface of the printed part and the substrate was also calibrated based on the printing experiments. The substrate was assumed to only fail under mode-I loading. Thus, a maximum stress failure initiation criterion and a displacement-based damage evolution law were used to describe the initiation and evolution of the debonding process, respectively. The cohesive stiffness, cohesive strength, and separation to failure were calibrated with the plate print experiment. Table 3.3-1 lists the parameters related to the process and to the material used in the simulation of the EDAM process of the plate.

Table 3.3-1: Parameters of the process and material used in the simulation of the printing process of the plate

Parameter	**Value**
Extrusion Temperature ($°\boldsymbol{C}$)	300
Deposition speed ($\boldsymbol{mm}/\mathbf{min}$)	3810
Ambient Temperature Convection ($°\boldsymbol{C}$)	35
Ambient Temperature Radiation ($°\boldsymbol{C}$)	35
Heat Removed with Compression Wheel ($\boldsymbol{W}$)	35
Emissivity - $\boldsymbol{\varepsilon}$	0.92
Cohesive Stiffness ($\boldsymbol{MPa}/\boldsymbol{mm}$)	0.125
Cohesive Strength ($\boldsymbol{KPa}$)	25
Separation to Failure ($\boldsymbol{mm}$)	5

3.3.2 Curved Wedge

A voxel FE mesh was generated based on the event series of the curved wedge. Thus, elements are only present where the print head deposits material. Unlike the plate, a coarser mesh was used to discretize the geometry of the curved wedge. Beads were discretized with two elements in the width and one in the height which lead to elements with dimensions of 10.16 mm in width and 5.08 mm in height. Linear brick elements type DC3D8 and C3D8 were used in the heat transfer and mechanical analysis, respectively [48]. A total of 124,208 finite elements were used to discretize the geometry of the curved wedge. To capture the process of debonding of the curved wedge from the build sheet, a cohesive contact was defined between the bottom surface of the printed part and a substrate. The substrate was included only in the mechanical analysis and was modeled as an analytical rigid surface. This approach only considers the debonding of the part from the build sheet since it was the only failure mechanisms occurring during the printing experiments. Figure 3.3-2 shows the FE mesh generated for the plate and the substrate that represents the build sheet.

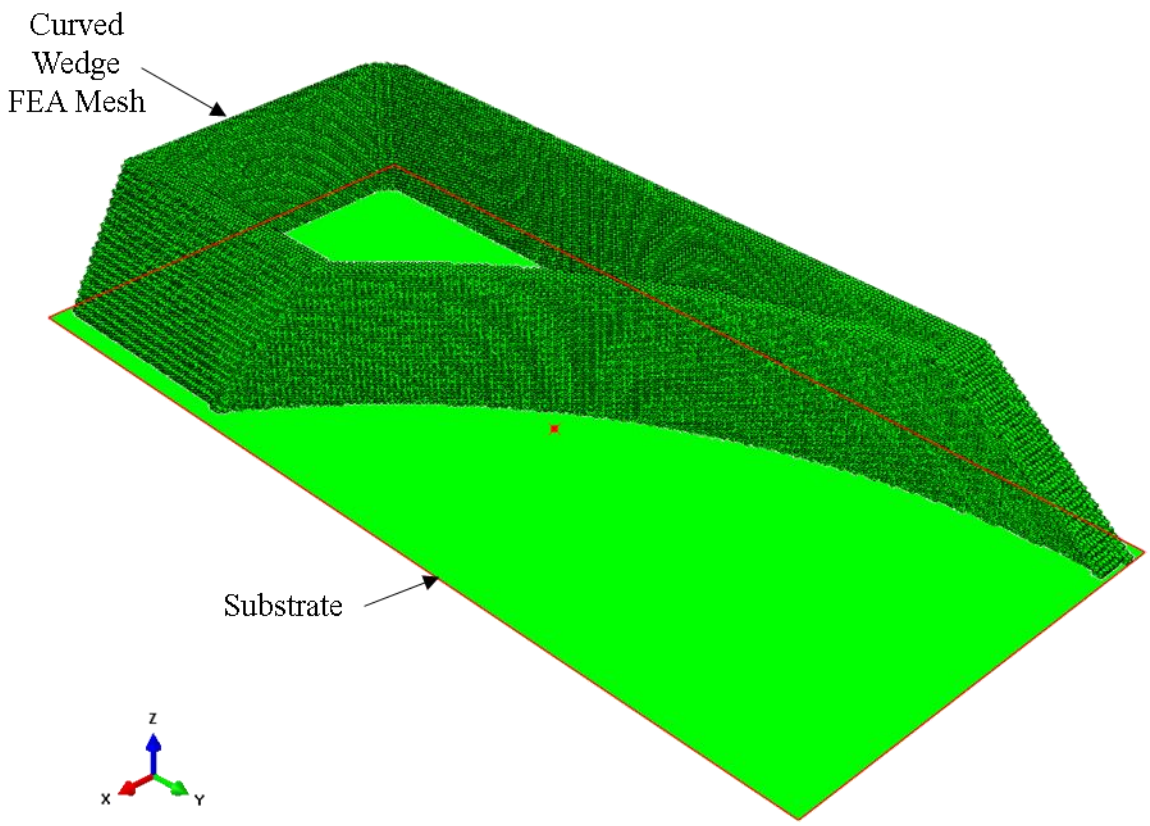

Figure 3.3-2: Voxel FEA mesh generated for the curved wedge

The material properties reported in the chapter 2 were used in the simulation of the EDAM process. To simulate the material in the molten state prior to deposition, the temperature of the nodes in the FEA mesh was initialized to the melt temperature. The bottom surface of the plate was assumed adiabatic due to the low thermal conductivity of the material used for the build sheet (ABS). The convection conditions developed at the surface of the curved wedge were governed by a correlation equation that provides a local convection coefficient [47]. The heat removed with the compression wheel, the emissivity, and the ambient temperature for radiation are calibrated based on the printing experiments. The constitutive behavior of the cohesive contact defined between the bottom surface of the printed part and the substrate was also calibrated based on the printing experiments. The substrate was assumed to only fail under mode-I loading. Thus, a maximum stress failure initiation criterion and a displacement-based damage evolution law were used to describe the initiation and evolution of the debonding process, respectively. The cohesive stiffness, cohesive strength, and displacement to failure were calibrated with the print experiments. Table 3.3-2 lists the parameters related to the process and to the material used in the simulation of the EDAM process of the curved wedge.

Table 3.3-2: Parameters of the process and material used in the simulation of the printing process of the curved wedge.

Parameter	**Value**
Extrusion Temperature ($°\boldsymbol{C}$)	300
Deposition speed ($\boldsymbol{mm/\mathrm{min}}$)	3175
Ambient Temperature Convection ($°\boldsymbol{C}$)	35
Ambient Temperature Radiation ($°\boldsymbol{C}$)	35
Heat Removed with Compression Wheel ($\boldsymbol{W}$)	35
Emissivity - $\boldsymbol{\varepsilon}$	0.8
Cohesive Stiffness ($\boldsymbol{MPa/mm}$)	0.125
Cohesive Strength ($\boldsymbol{KPa}$)	60
Displacement to Failure ($\boldsymbol{mm}$)	5

3.4 Results

3.4.1 Flat Plate

An extensive material characterization program was conducted in this program to determine the material properties required for simulating the EDAM process with GF-PA. The results of the material characterization were reported in section 2. EXPERIMENTAL CHARACTERIZATION OF ADDITIVELY MANUFACTURED FIBER REINFORCED THERMOPLASTIC.

A digital material card was generated for the GF-PA with the bead-level effective properties measured experimentally and computed with micromechanics. ADDITIVE3D© was used for simulating the printing process of two printing experiments conducted in the LSAM at Local Motors. The printing experiments consisted of a flat plate printed with two layers in one direction followed by two layers at ninety degrees, thereby giving rise to an anticlastic deformation of the plate. A second geometry called curved wedge consisted of a double-bead wall geometry with curved and linear segments in the scale of the components that are of interest to the partners related to the automotive industry. The curved wedge was designed also to warp during and after the printing process. Results of the process simulation are presented in this section and validated against experimental measurements.

Predicting the temperature history is of paramount importance in the EDAM process since temperature controls the evolution of the viscoelastic behavior, crystallization, and shrinkage of the printed material. Figure 3.4-5 shows a qualitative comparison between the temperature fields captured with the thermal camera (left) and the temperature field predicted in the process simulations (right) after printing the second, the third, and the fourth layer. The temperature gradient in both temperature fields is on the same scale. Overall, temperature fields characterized experimentally and predicted through the EDAM process simulations are in good agreement. The predicted temperature field is slightly colder than the one observed experimentally.

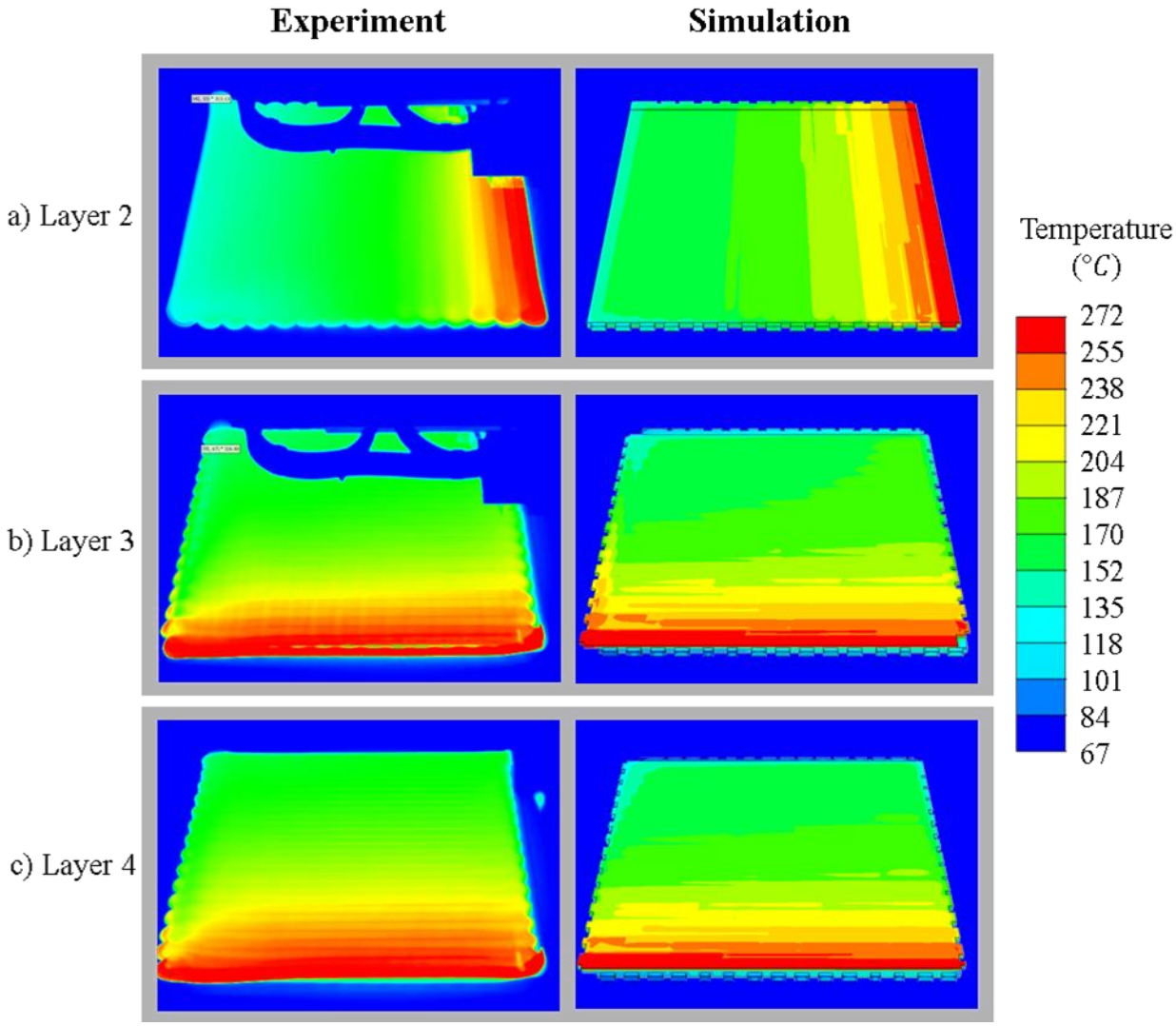

Figure 3.4-1: Comparison of temperature fields measured experimentally and predicted with process simulation at different instants of the printing process of the plate

The development of temperature gradients during the printing process of the plate drove the evolution of crystallinity in the same direction as the temperature gradients. Figure 3.4-2 shows the evolution of the degree of crystallinity as the plate was printed. The crystallinity in the plate started to develop around the end of the second layer and developed from the edge that was deposited first and moved towards the side that was deposited last (Figure 3.4-2-a). The crystallization of the polymer was not completely developed at the end of the printing process and required about six minutes to reach the maximum crystallinity level of 25% (Figure 3.4-2-e and d). It should be noted that the temperature fields shown in Figure 3.4-1 are displayed from a different perspective than the crystallinity fields shown in Figure 3.4-2.

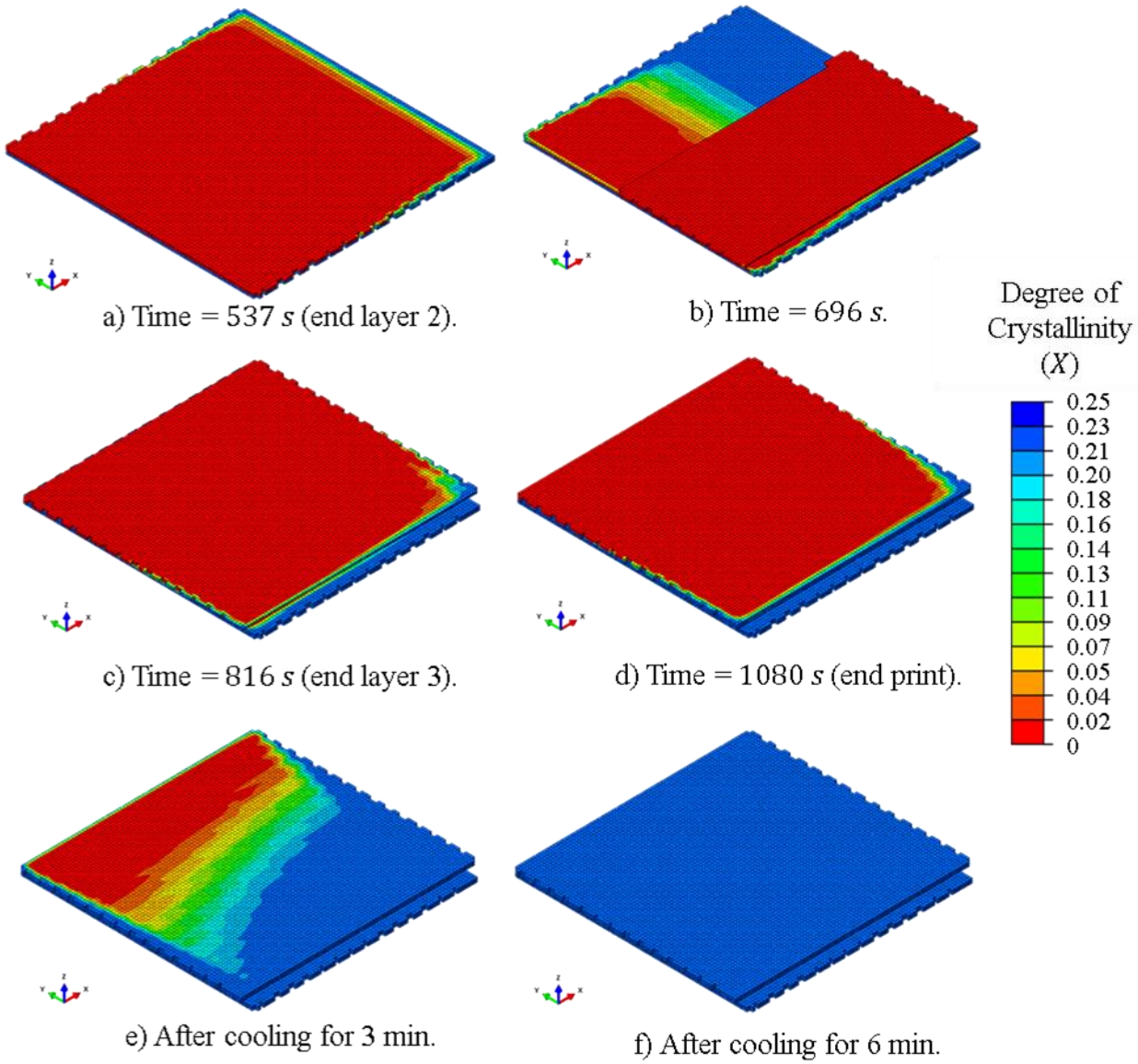

Figure 3.4-2: Predictions of the degree of crystallinity at different instants of time during the printing process of the plate

In order to validate the degree of crystallinity, a DSC test was performed. A small sample was extracted at the surface of the plate and heated at a heating rate of 30 $℃/min$ to 280 ℃. The goal is to observe the cold crystallization peak. The cold crystallinity peak appears when the material was quenched cool and didn't allow enough time for the polymer chain to crystallize [49]. However, if the material had achieved maximum crystallinity during the cool-down process, the cold crystallization peak should not be observed in the heat flow curve. Figure 3.4-3 shows the heat flow, in green, and temperature, in blue, from the DSC experiment. On the left is the data

from the raw GF-PA pellet from the manufacturer. The cold crystallization peak, labeled T_{cc} , exists because the raw pellet is not fully crystallized. The data on the right graphs was obtained from a piece extracted from the printed plate. No cold crystallization peak was observed in the heat flow curve which confirms that the plate has achieved the maximum degree of crystallinity of 25% as predicted.

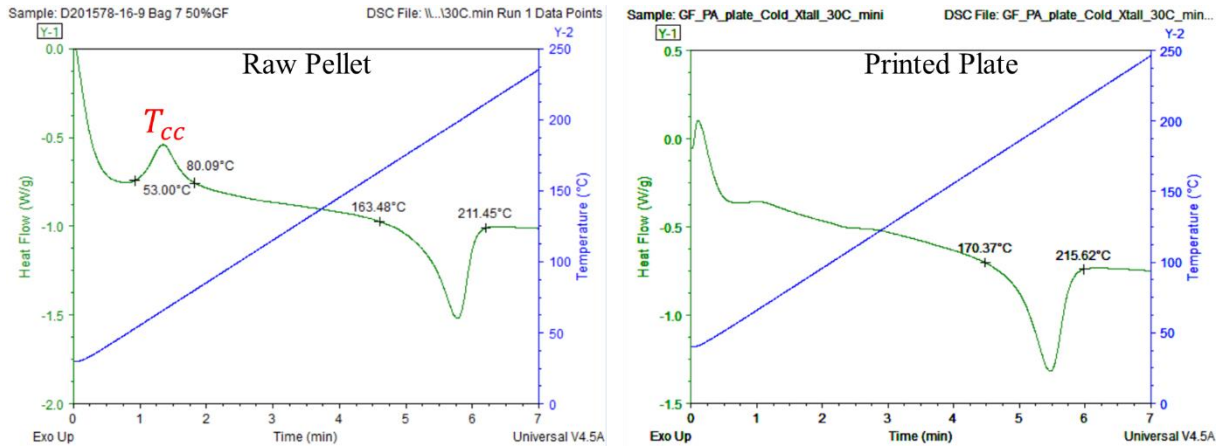

Figure 3.4-3: DSC experiment of a raw pellet and sample extracted from the flat plat showing no cold crystallization to validate predictions of crystallinity

A quantitative comparison of the deformation measured in the stacking direction was carried out for the plate. The displacement in the 3-direction was extracted along two profiles located in the middle of the plate and along with the two in-plane directions. Figure 3.4-4 shows the location of the profiles used to extract the deformation of the plate. Data points were extracted from the point cloud shown in Figure 3.2-5 along with the same two profiles. The plot in Figure 3.4-4 compares the deformation in the stacking direction measured experimentally against the deformation predicted with the simulations. The maximum deformation at the end of the plate in the x profile obtained from the experiment is 19.87 mm and the ones from FEA is 19.35 mm. A maximum difference of about 2.7% was observed between the experimental measurements and the numerical predictions along the X-profile. At the ends of the y-profile, the experimental deformation is 7.9 mm and the FEA deformation is 9.7 mm. The difference between the experimental and numerical predictions was below 2% for the most part of the Y-profile and increased to around 23% at the ends of the profile. In general, the simulation predictions are in good agreement with the experimental observations for the most part of the profiles.

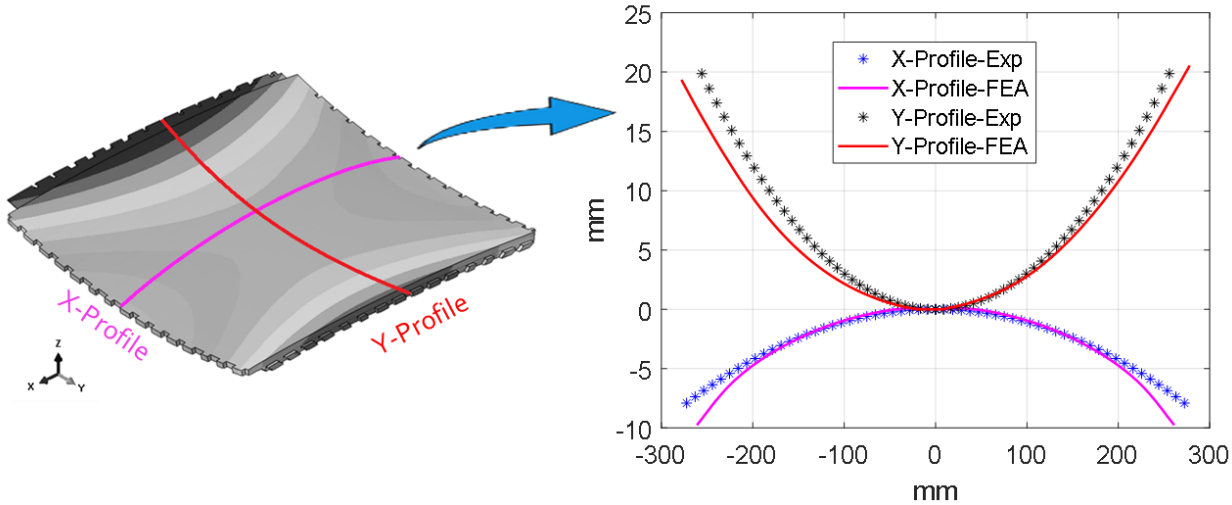

Figure 3.4-4: Comparison of deformation measured experimentally and predicted in process simulation.

3.4.2 Curved Wedge

Figure 3.4-5 shows a qualitative comparison between the temperature field captured with the thermal camera (left) and the temperature field predicted in the process simulations (right) after printing 20 layers, 40 layers, and 60 layers. Further, the scales in both temperature fields are in the same temperature range to be able to compare side-to-side the experimental and predicted temperature fields. Overall, a really close correspondence between the temperature fields characterized experimentally and predicted through the EDAM process simulations is observed.

One observation that should be noted is the simulation was constructed with voxel FE mesh. Therefore, the exposed surface in the curvature area is not as smooth as the experimental printed part which leads to an overexposure surface in the curvature area. The overexposed surface results in more heat loss, thus lower temperature, in the curvature region which can be observed around corner 2 on the right side of the curved wedge simulation. Looking at the same layer number, corner 2 region is colder than the corresponding layer in the straight wall region which is in the middle of the simulation screenshots. Meanwhile, the temperature of the experimental print does not vary from a straight or curved wall in the same layer.

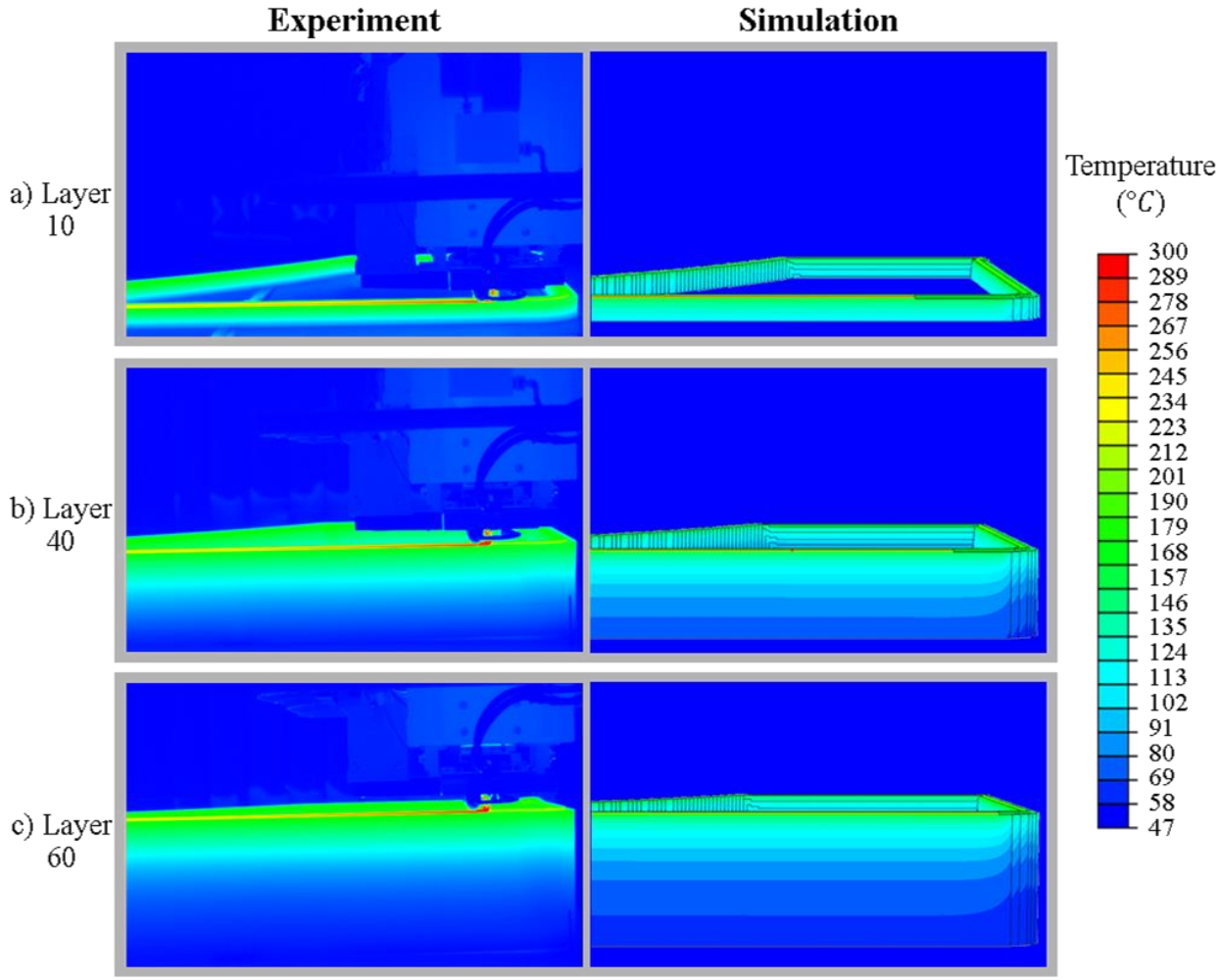

Figure 3.4-5: Validation of temperature fields characterized experimentally (left) and predicted (right) in the EDAM process simulation. A) Temperature field at layer 20. B) Temperature field at layer 40. C) Temperature field at layer 60

The transient temperature evolution during the printing process of the curved wedge was extracted at different layer locations from both the printing experiment and FEA. The goal is to provide a quantitative comparison of the temperature predictions and the experimental measurements. Seven layer locations were chosen starting at layer 10 and increasing in an interval of ten until layer 60, and in addition, the last layer number 65. Figure 3.4-6 shows approximately the layer locations from which transient temperature evolution was extracted for both experiment and simulation temperature history. The transient experimental temperature evolution was extracted at the middle of a printed bead right after the material deposited. The simulation temperature of a layer was

extracted at the top node of the elements. The temperature history of every 10 layers and the last layer was extracted and imported into Matlab© to plot for visualization.

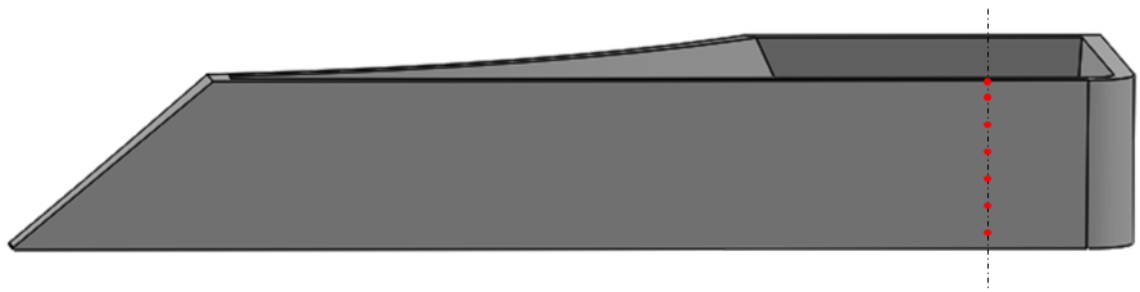

Figure 3.4-6: Layer locations in the curved wedge used for extracting time-temperature history

Figure 3.4-7 compares the experimental and predicted transient temperature evolution at the seven layer locations. The predictions of the transient temperature evolution are in good agreement with the experimental measurements, thereby demonstrating that the relevant heat transfer mechanisms are captured in the EDAM process simulation. The plot of the transient temperature evolution shows the relatively rapid cooling the material undergoes at the surface which is primarily due to heat losses through radiation and due to heat removed by the compression wheel. A local increase in temperature can be also noticed in the first six transient temperature curves as a new layer of material is deposited on top of the layer observed. Once the temperature decreased to about $150\ °C$, the polymer started to crystallize and thus to release heat of crystallization which is not noticeable in the plots of the transient temperature evolution. A more detailed analysis of the heat transfer mechanisms can be found in the study from Barocio [47].

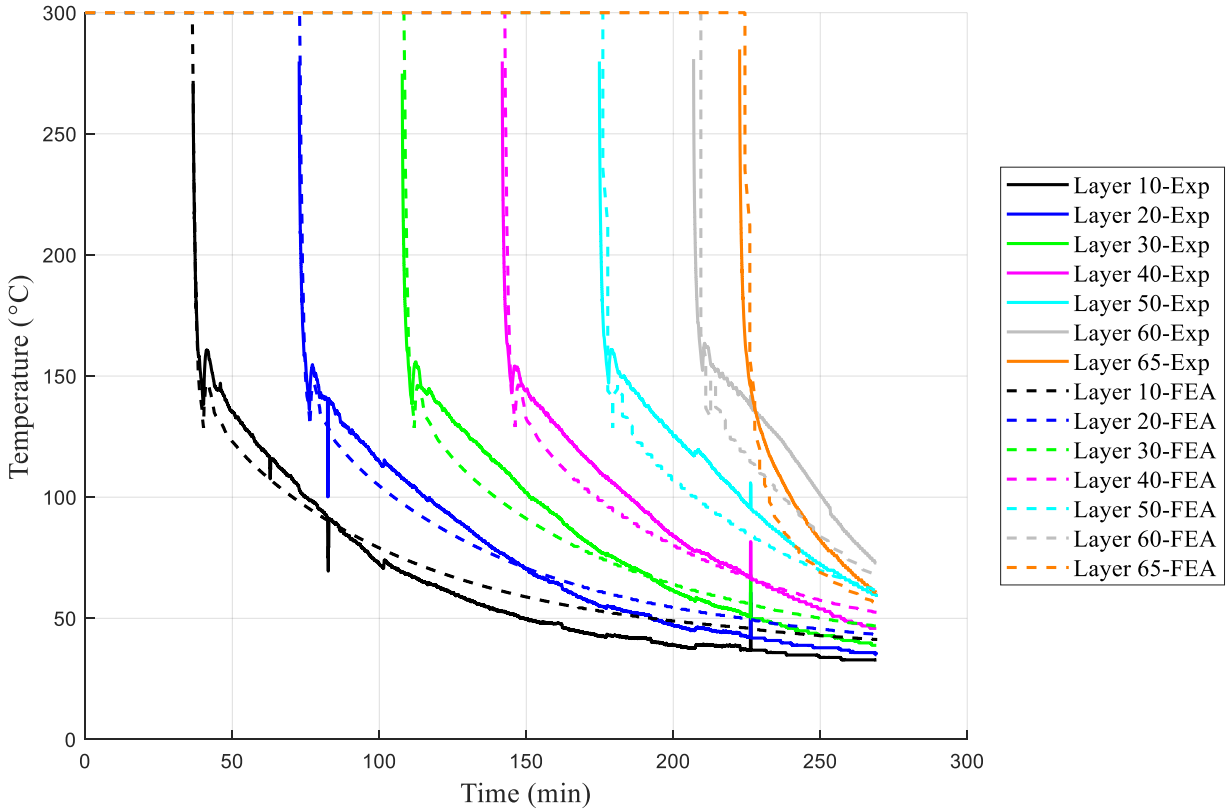

Figure 3.4-7: Comparison of time-temperature history measured experimentally and predicted with process simulation for different layers in the curved wedge

The development of temperature gradients along the height of the curved wedge caused the crystallinity to start developing at the bottom of the part and to progress in the vertical direction as the part was built layer-by-layer. Figure 3.4-8 shows the evolution of the degree of crystallinity X predicted in the EDAM process simulation of the curved wedge at layer 10, 40, 60, and after cooling for 5 minutes. Since the time between layers was at least three minutes for the curved wedge, the printed material had sufficient time to cool down and to partially crystallize. Thus, the crystallization front closely followed the layer deposition as shown for the 10th, 40th, and 60th layer in Figure 3.4-8. A degree of crystallinity of 0.25 was achieved in the entire part which corresponds to the maximum degree of crystallinity attained in this material. Achieving the maximum degree of crystallinity is important since it provides thermal stability to the printed material. Furthermore, the crystallinity also affects the thermoviscoelastic behavior of the printed material and the process of crystallization leads to shrinkage [27].

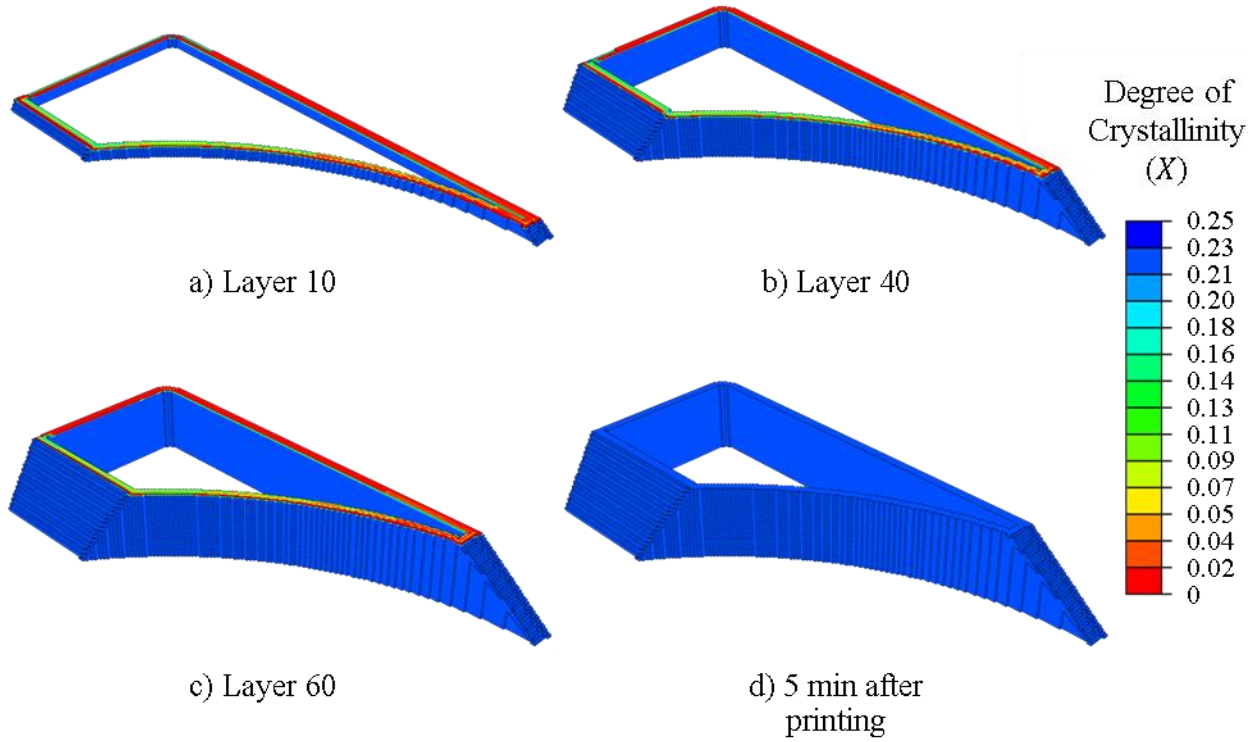

Figure 3.4-8: Evolution of the degree of crystallinity *X* predicted in the EDAM process simulation of the curved wedge

The deformation of the curved throughout the printing process and after cooling was also predicted in the process simulation. The curved wedge was initially bonded to the build sheet and gradually debonded from the build sheet as stresses develop in the part, thereby allowing the part to deform in the vertical direction. Figure 3.4-9 shows the evolution of the displacement in the layer stacking direction (3-direction) at different instants of the printing process of the curved wedge. The "Corner 1" of the curved wedge (indicated as C-1 in Figure 3.4-9) debonded from the substrate and started to curve up at around layer 40.

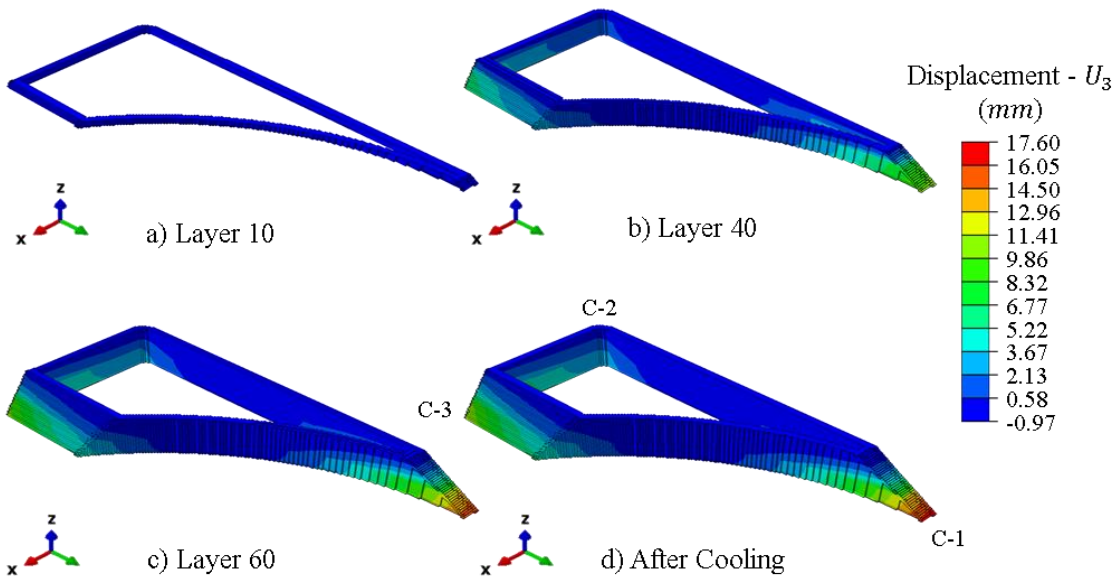

Figure 3.4-9: Deformation in the layer-stacking direction at different instants of the printing process of the curved wedge

The deformation measurements carried out at the three different corners of the curved wedge (Table 3.2-4) were also compared to the deformation extracted at the same locations in the process simulations. Table 3.4-1 shows the comparison between the maximum deformations measured experimentally and the maximum deformation predicted with the simulation of the EDAM process. The deformation predicted for corners 1 and 3 are in good agreement with the experimental observations whereas the deformation in corner 2 was underestimated in the simulations. The difference observed for corner 2 is attributed to the difference in the bonding behavior observed between the two pieces of build sheet used in the experiment (Refer to the section 3.2 Printing Experiment for further details).

Table 3.4-1: Comparison of deformation at three different corners in the curved wedge measured experimentally and predicted with simulations.

Location	Maximum deformation experiments (mm)	Maximum deformation predictions (mm)	Difference %
Curved wedge, corner 1	16.0	17.6	10.0
Curved wedge, corner 2	13.0	4.1	-68.5
Curved wedge, corner 3	13.0	12.1	-6.9

4. INVESTIGATION OF PROCESS-MICROSTRUCTURE-PROPERTY RELATIONSHIP IN THE EXTRUSION DEPOSITION ADDITIVE MANUFACTURING PROCESS

The properties of fiber-reinforced composites can be optimized in multiple ways both in terms of material selection and processing conditions. To do so, this chapter studies the relationship between the macroscopic and microscopic properties and the performance of the EDAM parts.

This chapter starts by presenting one possible way to change fiber orientation in the EDAM printed bead which is the adjustment of the bead aspect ratio through the bead compaction mechanism. Then the focus changes to the relationship of the orientation tensor to the macroscopic properties. Three fiber orientations are presented with two material systems; 30% by volume glass fiber-polyamide and 30% by volume carbon fiber-polyamide. The effective properties of all six cases obtained via virtual characterization, namely, elastic, thermophysical, and thermomechanical properties are also presented. Lastly, the chapter compares the effects of changing the properties of the fiber to temperature profile, stress history, and deformation of the final additive manufactured product.

4.1 Effects of Deposition Conditions on Fiber Orientation Distribution

This section investigates the effect of compaction mechanism on the fiber orientation which influences the effective properties. The compaction ratio or aspect ratio of the printed bead is defined as the ratio of the final width to the final height. Keeping the same print speed and extrudate volume, greater compaction results in more deformation on the initially circular bead cross-section. More compaction results in a thinner and wider bead, thus higher aspect ratio. Two printers, namely large-scale additive manufacturing (LSAM) system at Local Motors, and Composites Additive Manufacturing Research Instrument (CAMRI) at Purdue University were utilized. Those panels printed in LSAM and CAMRI were tensile tested to study the effect of the aspect ratio on the tensile modulus.

Sample preparation

Aspect ratios of 3, 4 and 5, were investigated in the LSAM at Local Motors as well as with the Composites Additive Manufacturing Research Instrument (CAMRI) at Purdue University [47]. A

constant bead-to-nozzle area ratio of 0.7712 was used in both cases. Thus, the combination of flow rate emerging from the nozzle to the speed of the print head was constant and the bead height was the only parameter changed. A bead-to-nozzle area ratio greater than one indicates that the flow emerging from the nozzle extends in the direction transverse to the print direction, whereas a bead-to-nozzle area ratio lower than one indicates that the extrudate is stretched as it emerges from the nozzle. In the former case, the flow developed transverse to the print direction will cause some of the fibers to flow and align transverse to the print direction. In the latter case, the fibers are more likely to flow and align along the print direction due to the extensional flow developed as the extrudate is stretched.

LSAM

Figure 4.1-1 shows a schematic representation of the beads printed in the LSAM with the three different aspect ratios and Table 4.1-1 listed the dimension of each aspect ratio. A numeric notation is adopted to indicate the local material orientation with the 1-direction corresponding to the print direction, the 2-direction corresponding to the direction transverse to the print, and the 3-direction corresponding to the stacking direction.

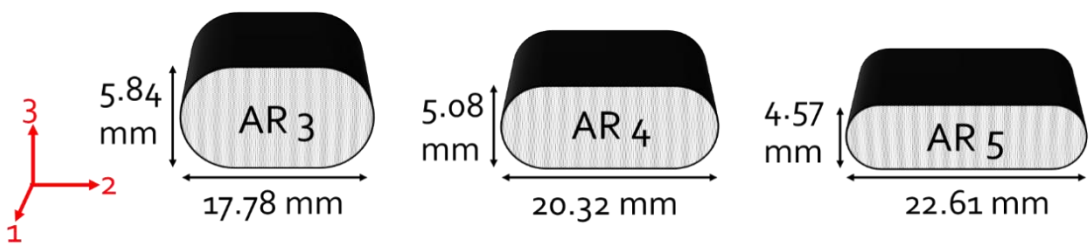

Figure 4.1-1: Dimensions and schematic representation of LSAM beads with different aspect ratios

Table 4.1-1: Dimensions of LSAM beads with aspect ratios

Aspect ratio	Bead to nozzle area ratio	Bead width (mm)	Bead Height (mm)
3	0.7712	17.78	5.84
4	0.7712	20.32	5.08
5	0.7712	22.61	4.57

The detailed description of LSAM sample preparation can be found in section 2.1 Specimen Preparation. In summary, hollow boxes were printed with the large-scale additive manufacturing (LSAM) system for each aspect ratio and tensile samples were cut in the print direction and planed to remove the curvature which is approximately 20% from both sides. A single bead was sectioned using the precision sectioning saw for fiber orientation measurements. Figure 4.1-2 depicted the extraction location of the fiber orientation measurements sample and tensile sample. Figure 4.1-3 shows the fiber orientation measurement sample ready for the computerized tomography (CT) scan.

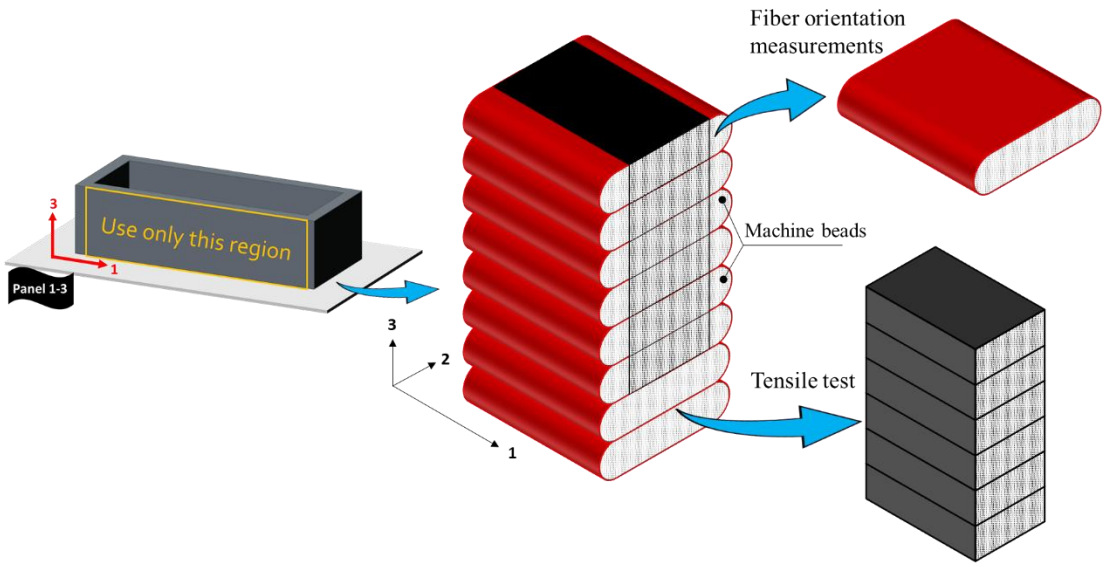

Figure 4.1-2: Illustration of the sequence followed for preparing specimens for tensile tests: printing box, extracting panels, machining of the panels.

Figure 4.1-3: Fiber orientation measurement sample

CAMRI

Figure 4.1-4 shows a schematic representation of the beads printed in the CAMRI with the three different aspect ratios. Table 4.1-2 listed the dimension and nozzle to the bead area ratio of CAMRI beads.

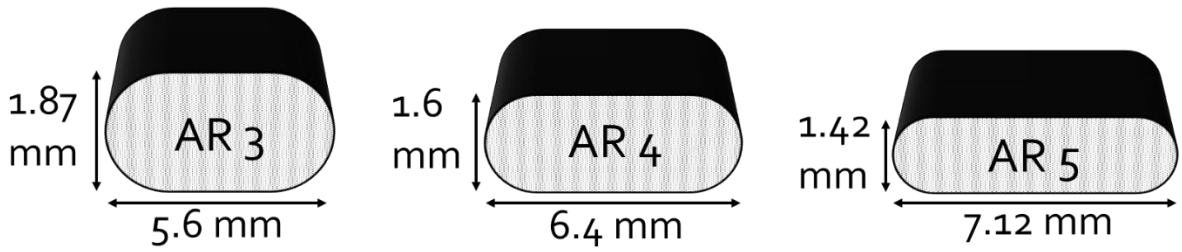

Figure 4.1-4: Dimensions and schematic representation of CAMRI beads with different aspect ratios

Table 4.1-2: Dimensions of CAMRI beads corresponding to each aspect ratio

Aspect ratio	Nozzle to bead area ratio	Bead width (mm)	Bead Height (mm)
3	0.7712	17.78	5.84
4	0.7712	20.32	5.08
5	0.7712	22.61	4.57

Figure 4.1-5 shows the key components in the CAMRI system. Table 4.1-3 listed the temperature set for each component in the extrusion process. Figure 4.1-6 shows the zones in the extruder. The temperature is set according to the manufacturer's recommendation and past experience printing with the CAMRI system.

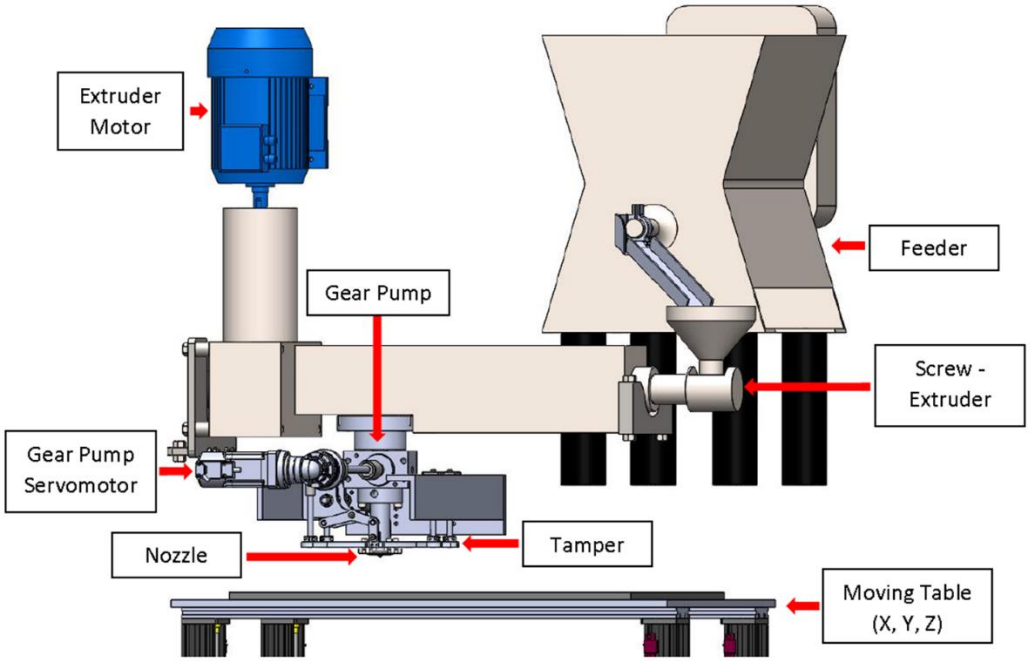

Figure 4.1-5: Key components in the CAMRI system

Table 4.1-3: Extrusion conditions used in the CAMRI

Extrusion Conditions	Values (°C)
Extruder hopper (zone 1):	260
Extruder zone 2	293
Extruder zone 3	293
Extruder-Pump connector	300
Extrusion Gear pump	300
Extrusion Nozzle	300
Extrusion temperature	285
Build plate temperature	180

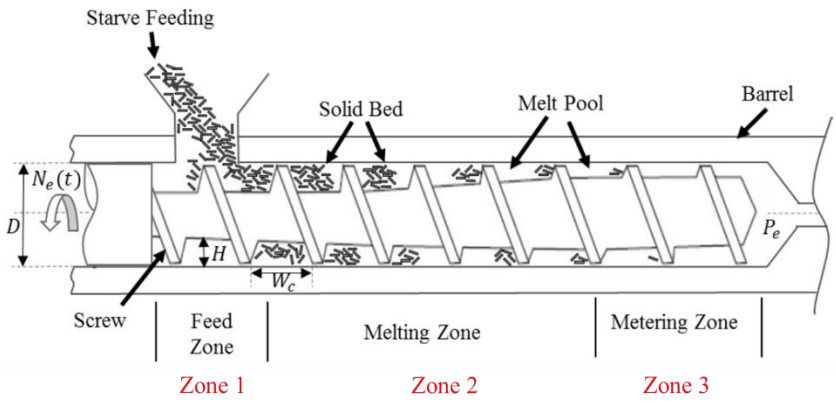

Figure 4.1-6: Extruder zones

A three-bead vertical wall was printed with the CAMRI system for each aspect ratio. The three aspect ratio walls were completed in a single print as shown in Figure 4.1-7.

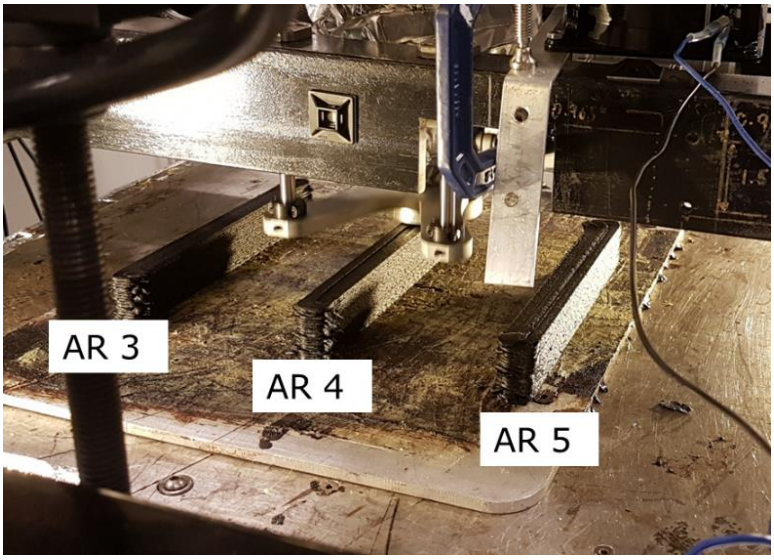

Figure 4.1-7: Printing of 3-bead-walls with three different aspect ratios in the CAMRI system.

The sample preparation step is slightly different from the LSAM tensile samples. As shown in Figure 4.1-8, two outer beads, one from each side were removed with a wood planar. Leaving only the middle bead for tensile specimen extraction.

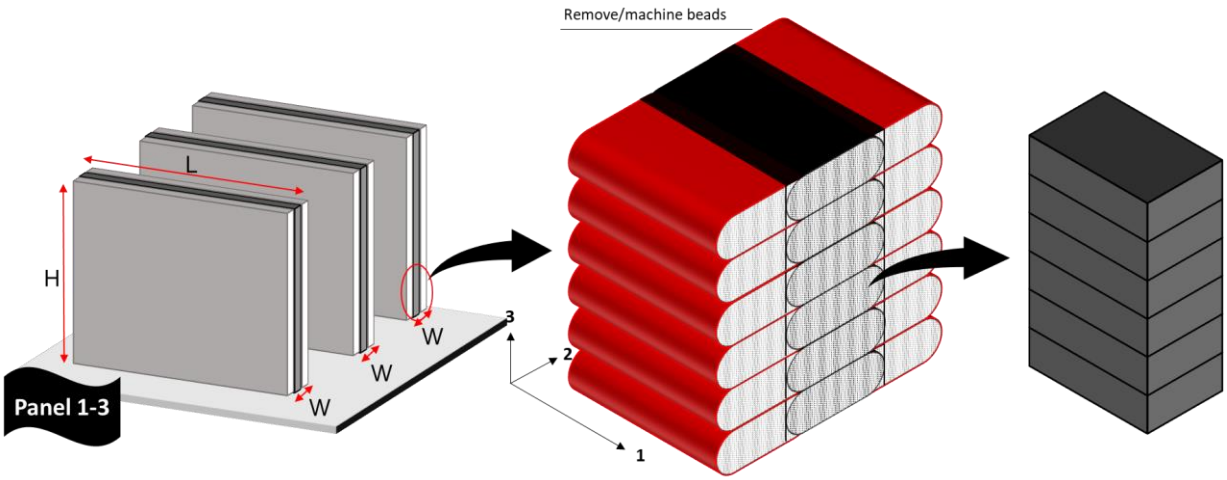

Figure 4.1-8: Extraction of a one- bead wall from a three-bead vertical wall.

For the fiber orientation measurement sample, a one bead wall was printed for each processing condition as shown in Figure 4.1-9. The sample for the CT scan was extracted from the middle of the wall lengthwise.

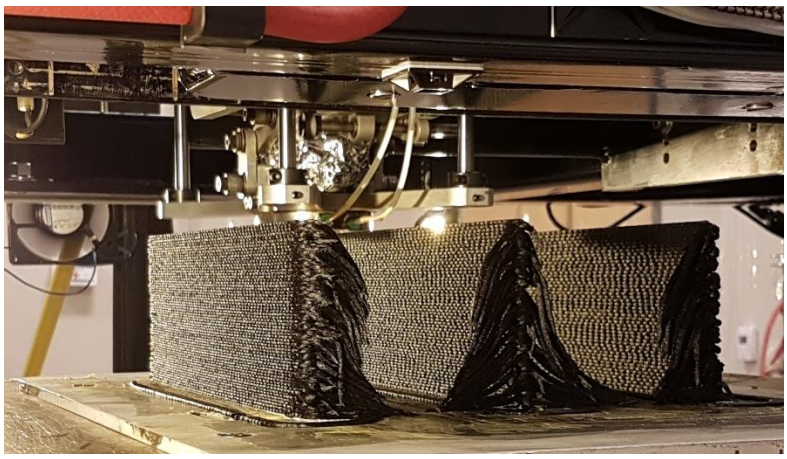

Figure 4.1-9: Printing of one-bead-walls with three different aspect ratios in the CAMRI system.

4.1.1 Experimental investigation of the effects of aspect ratio on fiber orientation distribution

The detailed description of CT scan and fiber orientation measurement can be found in section 2.2.1 Fiber Orientation. In summary, fiber orientation was obtained by using micro-Computerized Tomography (CT) technique scan-generated three-dimensional image of fibers. The micro-CT

scans were broken into finite rectangular sections as shown in the red sectioning lines in Figure 4.1-10. A_{11} is the orientation tensor in the 1 direction which is the print direction, pointing out of the page. A_{22} is the orientation tensor along the transverse direction which is to the left and right of the page. A_{33} is the orientation tensor along the stacking direction pointing upward. The table of the average fiber orientation of the 1-direction, 2-direction, and 3-direction can be found in Table A 2 and in the APPENDIX.

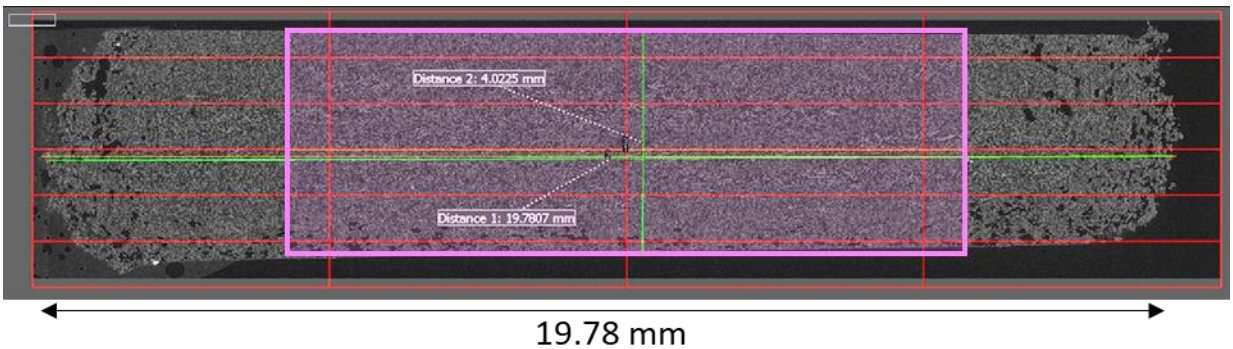

Figure 4.1-10: Micro CT scan of LSAM- AR 4

For the mechanical testing purpose, the outer part of the bead or the curvature part of the bead was removed by a wood planar. The region shown in pink is the remains for the tensile test. Table 4.1-4 summarizes the fiber orientation tensor of the area weight whole bead and area-weighted planed bead which will be utilized in the characterization section.

Table 4.1-4: Summary of the area-weighted average fiber orientation Tensor A_{ij} of LSAM- AR4 whole bead and planed bead.

Sample	**Whole bead**	**Planed bead**
LSAM – AR 4	$A_{ij} = \begin{bmatrix} 0.57 & 0 & 0 \\ 0 & 0.34 & 0 \\ 0 & 0 & 0.09 \end{bmatrix}$	$A_{ij} = \begin{bmatrix} 0.53 & 0 & 0 \\ 0 & 0.39 & 0 \\ 0 & 0 & 0.08 \end{bmatrix}$

Utilizing the same approach, the area-weighted average fiber orientation tensor of CAMRI beads of the aspect ratio of 3,4, and 5 are listed in Table 4.1-5 below. As an example, Figure 4.1-11 shows the Micro CT scan of CAMRI- AR 3 with the remainder of the bead after machining in pink.

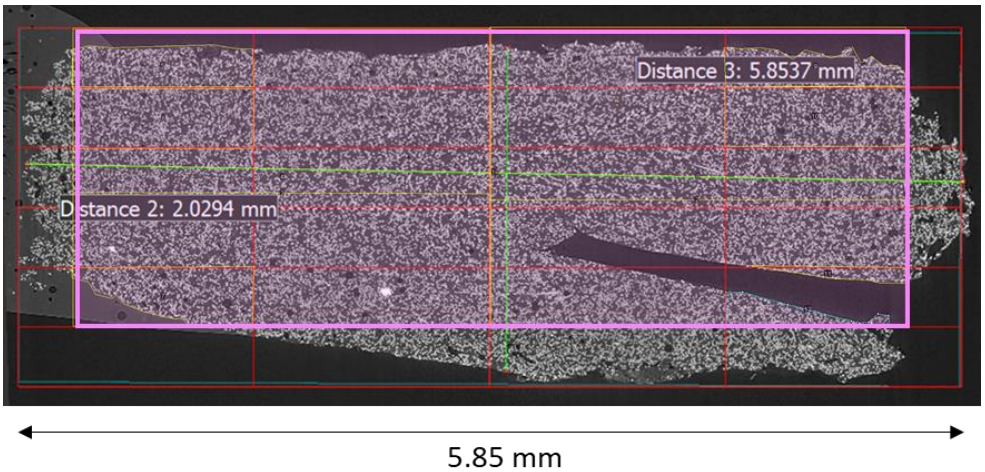

Figure 4.1-11: Micro CT scan of CAMRI- AR 3

Table 4.1-5: Summary of the area-weighted average fiber orientation Tensor A_{ij} of CAMRI-AR3, AR 4, and AR 5 whole bead and planed bead

Aspect Ratio	**Whole bead**	**Planed bead**
CAMRI -AR 3	$A_{ij} = \begin{bmatrix} 0.69 & 0 & 0 \\ 0 & 0.23 & 0 \\ 0 & 0 & 0.08 \end{bmatrix}$	$A_{ij} = \begin{bmatrix} 0.69 & 0 & 0 \\ 0 & 0.24 & 0 \\ 0 & 0 & 0.07 \end{bmatrix}$
CAMRI -AR 4	$A_{ij} = \begin{bmatrix} 0.72 & 0 & 0 \\ 0 & 0.2 & 0 \\ 0 & 0 & 0.07 \end{bmatrix}$	$A_{ij} = \begin{bmatrix} 0.73 & 0 & 0 \\ 0 & 0.2 & 0 \\ 0 & 0 & 0.07 \end{bmatrix}$
CAMRI -AR 5	$A_{ij} = \begin{bmatrix} 0.74 & 0 & 0 \\ 0 & 0.19 & 0 \\ 0 & 0 & 0.07 \end{bmatrix}$	$A_{ij} = \begin{bmatrix} 0.7 & 0 & 0 \\ 0 & 0.24 & 0 \\ 0 & 0 & 0.06 \end{bmatrix}$

4.2 Effects of Deposition Conditions on Mechanical Properties

4.2.1 Tensile properties experimentally characterized for three different aspect ratios printed in LSAM

The sample preparation for the LSAM was discussed in detail in section 2.1 Specimen Preparation. In summary, a hollow rectangular box was printed at Local Motors for each aspect ratio and was extracted into two useable long sides. Those sides were water jetted at Indiana Manufacturing Institute into tensile specimens by following the ASTM E638 guideline [29]. The specimens for

all aspect ratios were sent to DuPont for the tensile test. The details regarding the test setup was discussed in section 2.3.1 Tensile Properties ($\boldsymbol{E_1}, \boldsymbol{E_2}, \boldsymbol{E_3}$)

Figure 4.2-1 shows the stress vs strain plot provided by DuPont. Five samples were tested for each aspect ratio (AR). The green plots representing AR of 4 seems to have the highest tensile modulus. The blue plots, representing AR of 5, has less modulus than AR 4 samples. Lastly, the red plots, representing AR 3 has the least tensile modulus. However, all the plots are fairly close to each other. Table 2.1 5 summarizes the tensile test results as a function of the bead aspect ratio. As shown, the results for the AR 4 & AR 5 samples were both similar to each other, which suggests that the fiber orientation is not dramatically different among the ARs. Consideration of the fiber orientation created by the processing conditions used and the material removed during sample preparation is expected to elucidate an understanding of this trend with aspect ratio.

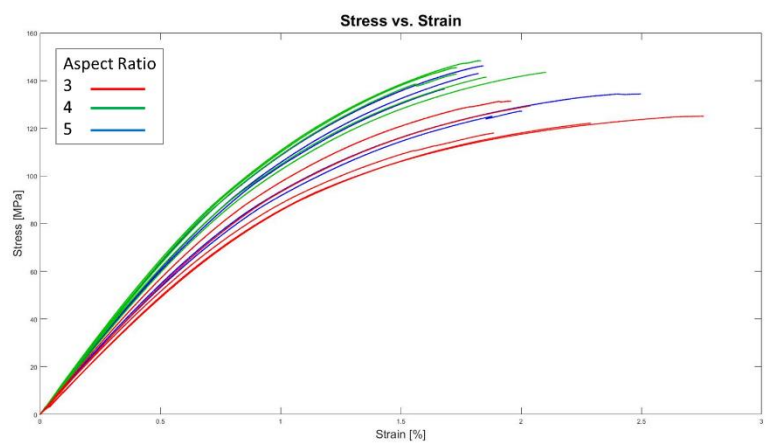

Figure 4.2-1: Stress-strain curves as a function of aspect ratio for the first five of seven tested samples

Table 4.2-1: Summary of tensile properties measured for different aspect ratios printed in the LSAM

AR	Avg E1 (GPa)	SD	Avg Ult. Strength (MPa)	SD	Avg. Failure Strain (%)	SD	Poison Ratio
3	11.2	1.0	126.7	7.7	2.12	0.33	0.319
4	13.0	0.9	141.2	7.1	1.86	0.14	0.336
5	12.6	0.9	138.9	6.6	1.91	0.28	0.325

4.2.2 Tensile properties experimentally characterized for three different aspect ratios printed in CAMRI

A mechanical test system (MTS) load frame with 22-kip capacity was used for load transfer. The full-filed strain field was acquired from the Digital Image Correlation (DIC) system. Figure 4.2-2 shows the stress vs strain plot of the CAMRI- AR 3, CAMRI- AR 4, and CAMRI- AR 5. Table 4.2-2 shows the average tensile modulus (E_1) and the average ultimate strength of all the aspect ratio.

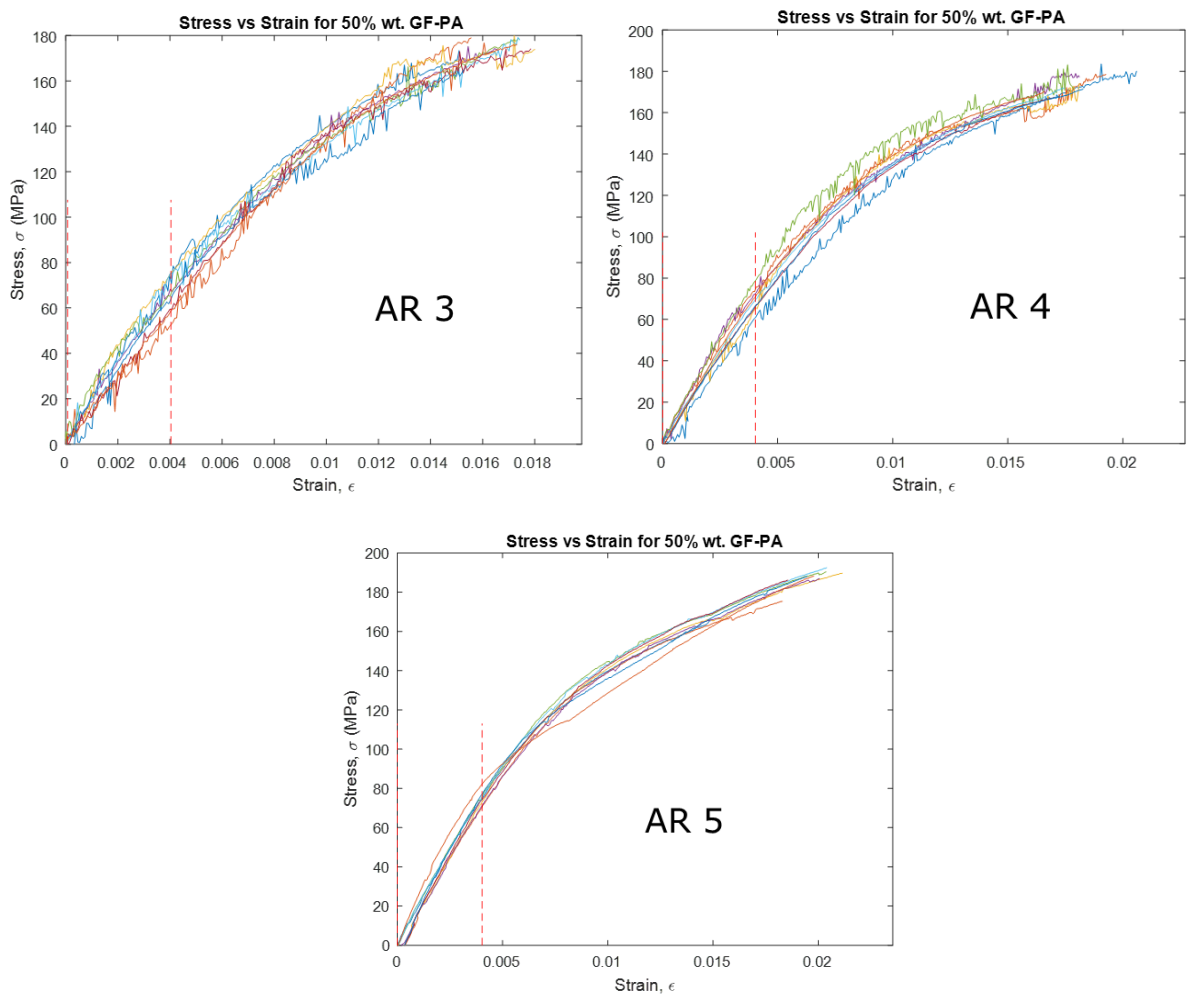

Figure 4.2-2: Stress vs strain plot of the tensile test in 1-direction of CAMRI- AR 3, CAMRI- AR 4 and CAMRI- AR 5

Table 4.2-2: Tensile modulus in 1-direction of CAMRI- AR 3, CAMRI- AR 4 and CAMRI- AR 5

CAMRI	Avg E1 (GPa)	SD	Avg Ult. Strength (MPa)	SD
AR 3	16.10	2.30	175.74	4.68
AR 4	17.43	1.17	175.94	6.37
AR 5	19.50	0.82	184.81	8.70

4.3 Virtual characterization of 50% wt. GF-PA different fiber orientation tensor

Additive manufactured 50% wt. GF-PA is a heterogeneous material consists of Polyamide as a matrix material and short glass fiber as a so-called "inclusion". The objective of virtual characterization is to predict the macroscopic or effective properties given the microstructure. Digimat Mean Field (MF) homogenization is the main tool in this process. In order to link between the micro (heterogeneous) and macro-scale (homogeneous), Digimat finds an equivalent homogeneous material that has the same effective macro stiffness as the real heterogeneous composite, under the same boundary conditions. There are two approaches in solving this problem; a direct finite element analysis of RVE at a micro scale which gives very accurate results but can be computationally expensive. The second approach, which was selected, is Mean-field homogenization (MFH) which computes estimates of the volume averages of the stress and strain field but is fast and less computationally expensive. The MFH approach uses in this study is the Mori-Tanaka model.

4.3.1 Overview of fiber orientation tensor investigated

Three orientation tensors (OT) selected to investigate are shown in Table 4.3-1. OT-2 is the fiber orientation measured from the 50% wt. GF-PA print with the CAMRI system. OT-1 and OT-3 were chosen as extreme cases and are not associated with any processing condition. The fiber orientation in the stacking direction (α_{33}) is kept constant as it is commonly seen in both LSAM and CAMRI prints.

Table 4.3-1: Orientation tensors

OT- 1	OT- 2	OT- 3
$\begin{bmatrix} \mathbf{0.5} & \mathbf{0} & \mathbf{0} \\ \mathbf{0} & \mathbf{0.43} & \mathbf{0} \\ \mathbf{0} & \mathbf{0} & \mathbf{0.07} \end{bmatrix}$	$\begin{bmatrix} 0.73 & 0 & 0 \\ 0 & 0.20 & 0 \\ 0 & 0 & 0.07 \end{bmatrix}$	$\begin{bmatrix} 0.9 & 0 & 0 \\ 0 & 0.03 & 0 \\ 0 & 0 & 0.07 \end{bmatrix}$

The constituent properties of glass fiber and polyamide are listed in Table 4.3-3. The values are from the manufacturer, literature, and reverse engineering in section 2.3.3 and section 2.4.3

Table 4.3-2: Constituent properties of polyamide and glass fiber

Constituent Properties	Polyamide	Glass fiber
Symmetry	Isotropic	Isotropic
E1 (GPa)	1.9	72
G12 (GPa)	1.9	30.4
v12	0.35	0.21
Density kg/m^3	1.09	2.54
CTE 1 (10^{-6})	88	2.5
Specific heat capacity $\frac{kJ}{kg \circ C}$	1.49	0.80
Thermal conductivity $\frac{W}{mK}$	0.19	1.58

4.3.2 Elastic properties

The process of virtual characterization is almost identical to section 2.3.3. The only change made is the fiber orientation tensor. Table 4.3-3 below shows the elastic properties of all three OTs.

Table 4.3-3: Elastic properties of GF-PA-OT1, GF-PA-OT2, and GF-PA-OT3

	GF-PA-OT1	GF-PA-OT2	GF-PA-OT3
E_{11} (GPa)	10.27	14.4	18.427
E_{22} (GPa)	9.30	6.82	5.99
E_{33} (GPa)	6.13	5.99	5.72
ν_{12}	0.32	0.37	0.35
ν_{13}	0.35	0.32	0.31
ν_{23}	0.36	0.41	0.44
G_{12} (GPa)	3.74	3.20	2.53
G_{13} (GPa)	2.35	2.45	2.24
G_{23} (GPa)	2.32	2.18	1.98

As expected, the modulus in each direction increases as the fiber alignment in that particular direction increases. The degree of anisotropy is highest in GF-PA-OT3 and lowest in GF-PA-OT1. The degree of anisotropy in the materials was represented by the ratio of the longitudinal and transverse Young's modulus. Figure 4.3-1 compares the elastic modulus of the GF-PA of different

OTs. E_1 varies the most among all the elastic properties due to fiber domination, while $E_{33}, G_{12}, G_{13}, and\ G_{23}$ doesn't show much variation due to matrix domination.

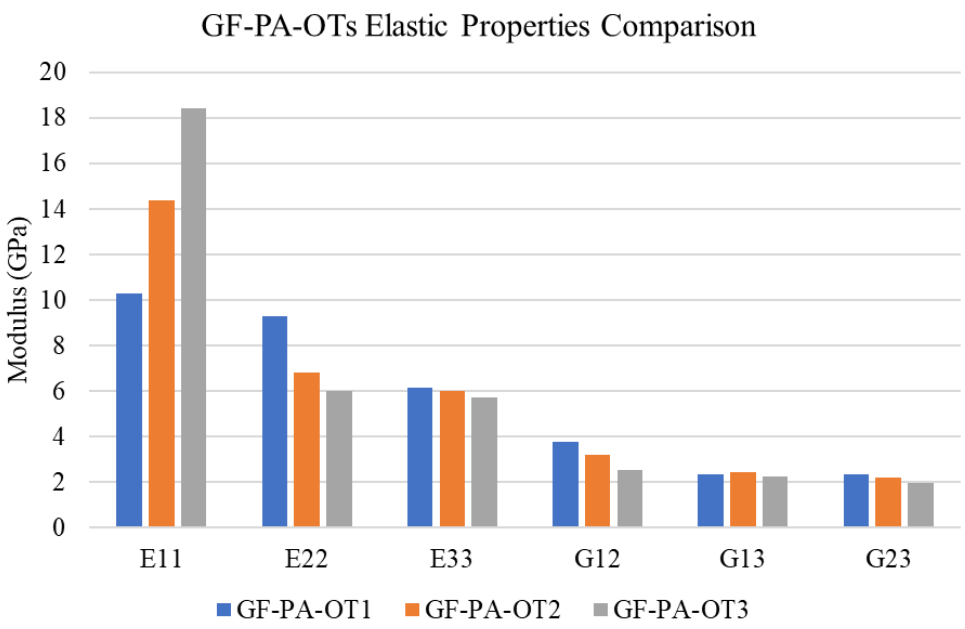

Figure 4.3-1: GF-PA-OTs Elastic Properties Comparison

4.3.3 Thermophysical Properties

Thermal gradients in the parts during manufacturing are caused by repeated deposition of hot material onto cooler material. Thermal gradients create internal residual stress and distort the part such as warp and curl. An increase in thermal conductivity of the material helps reduce thermal gradient throughout the part, thus improve geometry accuracy [8].

Thermal conductivities are fiber volume fraction and fiber orientation dependent in the printed material due to the presence of fibers with a relatively higher thermal conductivity than the surrounding polymer inside printed beads. Thermal conductivities are also temperature dependent due to changes in the conduction mechanisms occurring at the molecular level in the polymer. The contribution of fillers, such as fibers, to the thermal conductivity of a composite, was found to be less than that of the matrix because matrix polymer is almost continuous while fibers can only form a conductive chain as they are scattered in the dispersion system [50]. It should be noted that the size

and aspect ratio also influenced the composite's thermal conductivity [51]. However, those parameters are kept constant throughout this study.

Thermal conductivities of Polyamide as a function of temperature was reversed engineered in section 2.4.3 based on the experimental data by the thermophysical lab. The thermal diffusivity, the density, ρ, and the heat capacity, (T), are assumed to be constant for all OTs due to directional independence. Figure 4.3-2 compares the thermal conductivity of the 50% GF-PA with OT1, OT2, and OT3. GF-PA-OT3 has the highest K_{11} due to the most fiber collimation. From the graphs, anisotropic heat conduction is expected the most in OT3 due to the largest differences between K_{11} and K_{22}, and $K_{11}$and K_{33}. However, the K_{11} of all cases does not differ as significantly as their fiber orientation. Fu et al. [51] observed that the thermal conductivity of short-glass fiber-reinforced polymers decrease slowly with the decrease of fiber alignment. In other words, the change in glass fiber orientation does not change effective thermal conductivity significantly.

Note that the mean-field homogeneous predicted identical K_{33} for all OTs since the fiber orientation in the stacking direction is identical ($A_{33} = 0.07$). The thermal conductivities are tabulated in Appendix Table A 7.

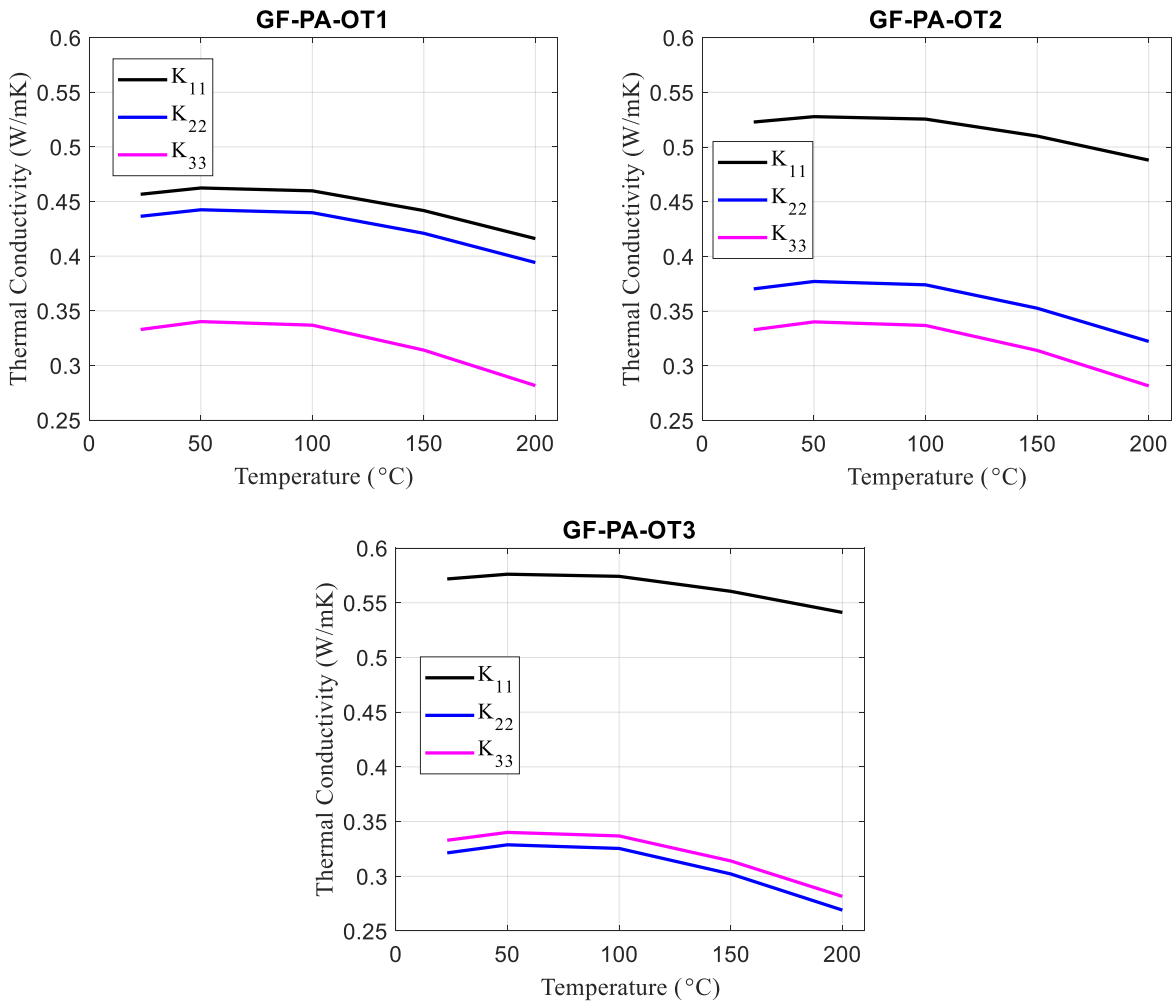

Figure 4.3-2: Thermal conductivity of 50% wt. GF-PA-OT1, OT2, and OT3

Figure 4.3-3 shows the comparison of effective thermal conductivity of GF-PA-OT3 in three principal directions with the neat Polyamide and glass fiber at 25℃. With the fiber orientation in the print direction of 90% ($A_{11} = 0.9$), the thermal conductivity in the print direction (K_{11}) is relatively low compared to the thermal conductivity of the glass fiber alone as expected.

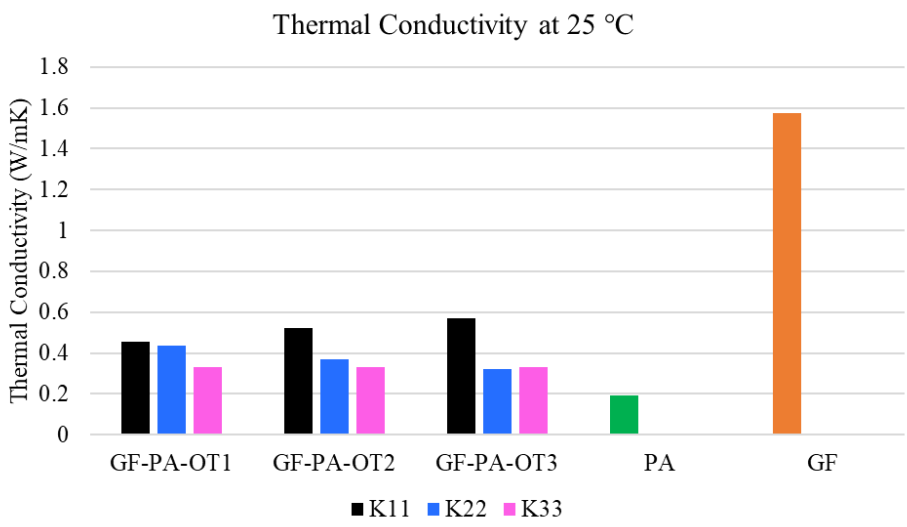

Figure 4.3-3: Comparison of effective thermal conductivity with constituent thermal conductivity

4.3.4 Thermomechanical Properties

The coefficient of thermal expansion (CTE) and crystallization shrinkage plays an important role in the stress and deformation of a part. It determines whether the part results in higher or lower residual stress. If the geometry involves circular region such as a ring, or turns, the CTE will determine the spring in or spring out effect.

The CTE prediction is coupled between the modulus and Poisson ratio of the glass fiber and the polyamide. Utilizing the constituent properties obtained in section 2.6.2, with the three OTs, the CTEs in the principal direction are listed in Table 4.3-4. Even though the fiber orientation in the 3-direction (A_{33}) is 0.07 for all the OTs, the CTE in the 3-direction (α_3) are different. Because the effective Poisson's ratio and effective modulus vary with fiber orientation.

Table 4.3-4: CTE of GF-PA-OT1, GF-PA-OT2, and GF-PA-OT3

CTE ($10^{-6} \cdot ℃^{-1}$)	**GF-PA-OT1**	**GF-PA-OT2**	**GF-PA-OT3**
$\boldsymbol{\alpha_1}$ **below** $\boldsymbol{T_g}$	18.55	8.85	8.05
$\boldsymbol{\alpha_2}$ **below** $\boldsymbol{T_g}$	22.96	55.50	75.89
$\boldsymbol{\alpha_3}$ **below** $\boldsymbol{T_g}$	84.99	76.62	63.97
$\boldsymbol{\alpha_1}$ **above** $\boldsymbol{T_g}$	18.55	8.85	8.05
$\boldsymbol{\alpha_2}$ **above** $\boldsymbol{T_g}$	23.46	60.40	95.21
$\boldsymbol{\alpha_3}$ **above** $\boldsymbol{T_g}$	106.82	90.27	76.58
$\boldsymbol{\alpha_1}$**above** $\boldsymbol{T_m}$	58.19	13.77	19.42
$\boldsymbol{\alpha_2}$ **above** $\boldsymbol{T_m}$	23.46	189.00	341.18
$\boldsymbol{\alpha_3}$ **above** $\boldsymbol{T_m}$	383.32	325.16	271.54

Experimental crystallization shrinkage experimental setup and data analysis were discussed earlier in section 2.6.3. As a summary, the experimental crystallization shrinkage was determined by the differences in the experimental strain and the fitted strain at the end of the crystallization temperature. The fitted strain above T_g and below T_m was extrapolated utilizing the same linear fitting coefficient to the end of crystallization temperature as shown in Figure 2.6-9 in section 2.6.3.

Following a similar process, the crystallization shrinkage of the three OTs was obtained by first reconstructing the strain vs temperature plot from the predicted CTEs. The CTE was experimentally characterized by the derivative with respect to the temperature of the fitted the strain vs temperature plot. The strain plot was divided into three parts based on the temperature; below T_g, between T_g and T_m, and above T_m. For GF-PA, the strain at all temperature range is best fitted with linear lines. Therefore, the CTE is simply the slope of the fitted lines as shown in Figure 4.3-4 for 50% wt. GF-PA.

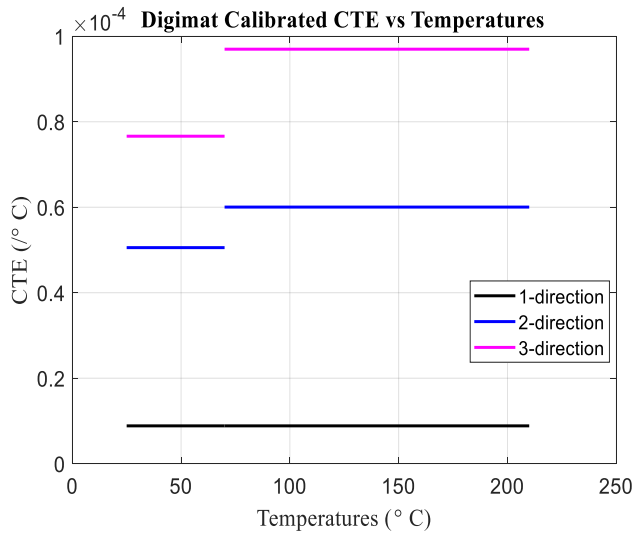

Figure 4.3-4: CTE as a function of temperature predicted for GF-PA-OT2

To reconstruct the strain vs temperature plot, the strain at room temperature (25℃) is set to be 0. From the temperature between 25℃ to 64 ℃ the slope of the strain plot is the CTE below T_g. The strain from 64 ℃ to 175 ℃ (T_m = 174.71℃) has CTE above T_g as the slope. However, it was plot up to 210 ℃. The strain from 175 ℃ to 210 ℃ has CTE above T_m as the slope. The crystallization shrinkage is approximated to be the differences between the dotted line and the solid line at 210 ℃ as shown in Figure 4.3-5. The crystallization shrinkage in the principal direction of all three OTs is summarized in Table 4.3-5.

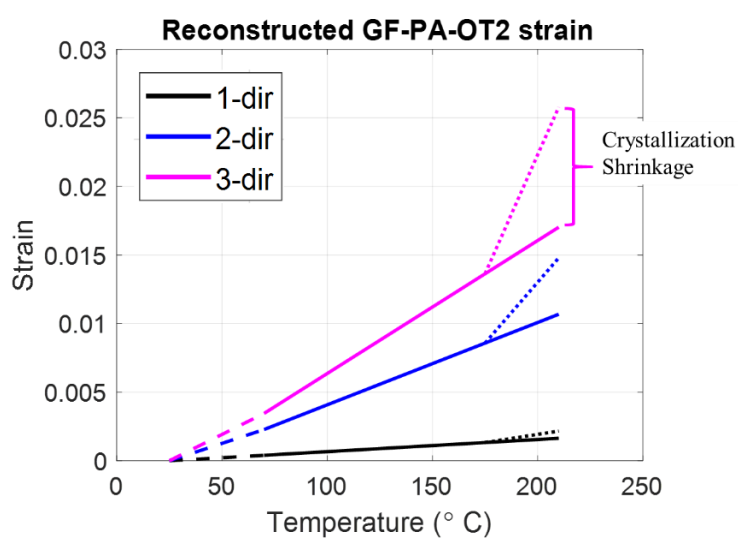

Figure 4.3-5: Reconstruction of strain as a function of temperature from CTE data

Table 4.3-5: Crystallization shrinkage obtained from the reconstruction of strain vs temperature plot

Crystallization shrinkage	GF-PA-OT1	GF-PA-OT2	GF-PA-OT3
1- direction	$1.40 \cdot 10^{-3}$	$0.53 \cdot 10^{-3}$	$0.4 \cdot 10^{-3}$
2- direction	$1.80 \cdot 10^{-3}$	$4.10 \cdot 10^{-3}$	$8.60 \cdot 10^{-3}$
3- direction	$9.7 \cdot 10^{-3}$	$8.8 \cdot 10^{-3}$	$6.80 \cdot 10^{-3}$

Figure 4.3-6 shows a comparison of the CTE at room temperature (25 °C) of GF-PA-OTs. The fiber alignment in the printing direction causes both a decrease of the coefficient of thermal expansion while also inhibit the crystallization shrinkage in this direction. Therefore, a larger amount of the material shrinkage takes place in the transverse directions and stacking direction whose has less fiber reinforcement. As expected, the CTE in the 1-direction is lowest in GF-PA-OT3 due to most fiber collimation in the print direction. However, the differences between GF-PA-OT1's CTE in the 1-direction and that of GF-PA-OT3 is very minimal relative to the changes in their CTE in the 2-direction. CTE is coupled with both the Poisson ratio and elastic properties of all directions. Even though, the fiber in the 3-direction is kept constant for all OTs ($A_{33} = 0.07$), the CTE in the 3-direction of the OTs are different.

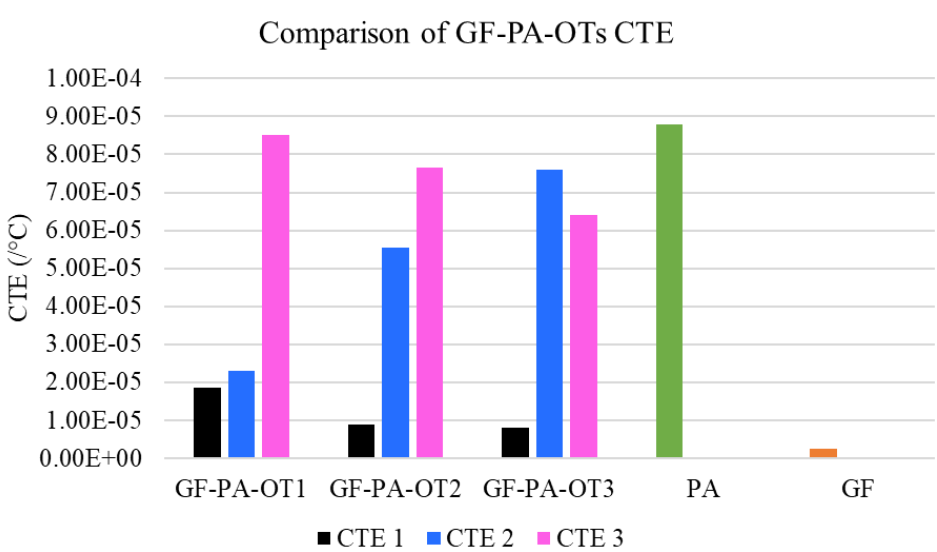

Figure 4.3-6: Comparison of GF-PA-OTs CTE

4.4 Effects of fiber orientation tensor on the residual stresses and deformation

Mechanical and thermomechanical properties of polymers, specifically the elastic moduli and coefficient of thermal expansion that governs the development of stresses and deformation in a printed part, are generally highly sensitive to temperature. Material utilized in the Extrusion deposition additive manufacturing (EDAM) process undergo large temperature changes from the melt temperature to room temperature. Hence, this chapter is structured to present thermal analysis prior to the mechanical analysis where the residual stresses and deformation are predicted.

4.4.1 Geometries investigated

The geometry selected to investigate differences in deformation of GF-PA-OTs needs to promote deformation, both in-plane and out-of-plane. Normally, if a printed geometry was measured, via 3D scanning, and compared to the predicted deformed shape, the actual deformation of the part would be hidden by the surface roughness and other imperfections that can occur during printing. Because of this, special geometries have to be designed so that it deforms in a specific way, based on their anisotropic structure. The design consideration is that the deformation should be conveniently measurable without 3D scanning and it should be sensitive enough for the differences to be noticeable.

For in-plane distortion, researchers have studied the spring in effect on the laminated composites structure with a curvature such as an angle bracket, L-bracket, rings, etc.[16][27][15] due to the anisotropy caused by differences between the in-plane and through-thickness properties of composites. Experimental results published recently by Radford and Rennick [15] showed that the larger the radius, the less distortion was measured. Several ideas of geometry incorporating the curvature are shown in Figure 4.4-1. The UU shape was selected because there are three features, to measure the deformation.

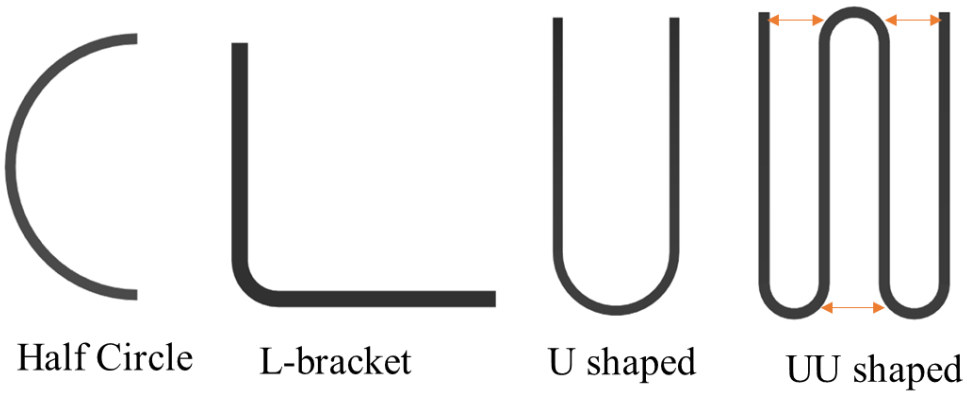

Figure 4.4-1: Geometries with curvature

Out of plane shape distortion, is also commonly observed in additive manufacturing. The distortion such as warpage, or for some cases, delamination is caused by the residual stresses arising from repeated deposition of hot material onto cooler material. The study by Compton et al. found that layer time, the temperature of the previously deposited bead, and the thickness of the section affects the out of plane distortion. Longer layer time, lower previous bead temperature, and thicker section lead to warpage and cracks. A potential geometry is a flat plate, Brenken et al.[45] observed an anticlastic bending occurring on an unsymmetrical four-layer flat plate with a raster angle of 0° and 90°. However, a 3D scanner is required to accurately measure that complex deformation.

Armillotta et al. [52] studied the warpage of FDM parts and concluded by experiments and analytic models that part geometry is most influential on the warpage. The warpage grows with increasing length and decreasing height. It is mostly influenced by length, less influenced by height, and the effect of width is almost negligible. When the height decreases, the bending stiffness decreases more rapidly than the bending moment increases, which results in a larger deflection. With this information, several geometries shown in Figure 4.4-2 were considered.

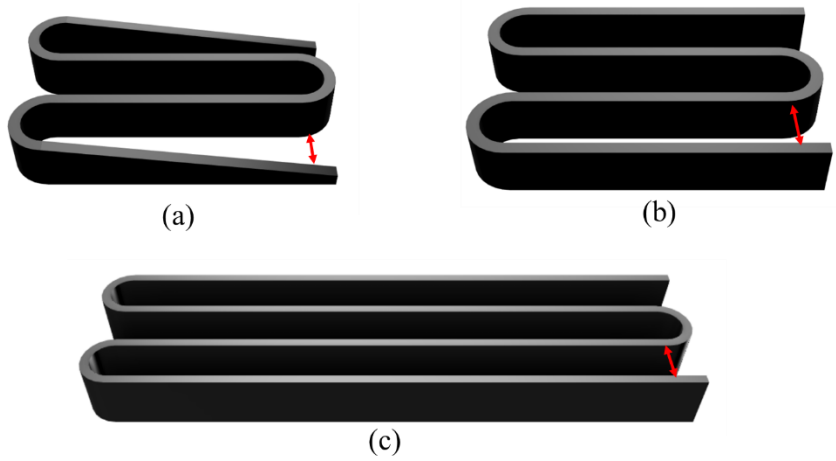

Figure 4.4-2: Geometries considered

The advantage of these geometries is the 'features' that can be easily measurable. The geometries above were designed to deform in a spring-in manner in which the distance shown in red arrow is measurable with scales. The height reduction with a slope as shown in Figure 4.4-2 (a) was originally thought to reduce the bending stiffness. The slope Geometry Figure 4.4-2 (a) was simulated and the reduction in bending stiff does not result in significant more deformation. The disadvantage is the geometry accuracy while shifting between the layers during experimental printing. Considering the tradeoffs, the height reduction idea was eliminated. Instead, a longer geometry was considered. Finally, the selected geometry named 'UU shape' is shown in Figure 4.4-3.

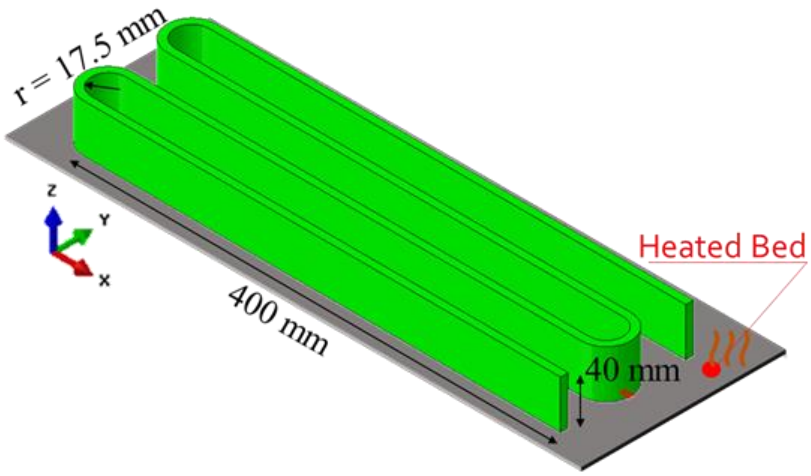

Figure 4.4-3: UU shape geometry

The UU shape was created for the CAMRI printer, which has a heated bed as shown in Figure 4.4-3. The bed of the CAMRI system is coated with the adhesive which prevents the part from dethatching. Figure 4.4-4 summarizes the steps of the UU shape process simulation. To model the CAMRI environment, the nodes of the bottom surface is fixed on the printed bed using the kinematic boundary condition during material deposition. Once the printing is completed, the part is left to cool down and fixed on the bed for 6 minutes. At the end of the cooling process, the part is crystallized and is taken off the bed which removes the constrain on the bottom surface. The part then is cooled down on the print bed for 10 minutes, then later cool to room temperature.

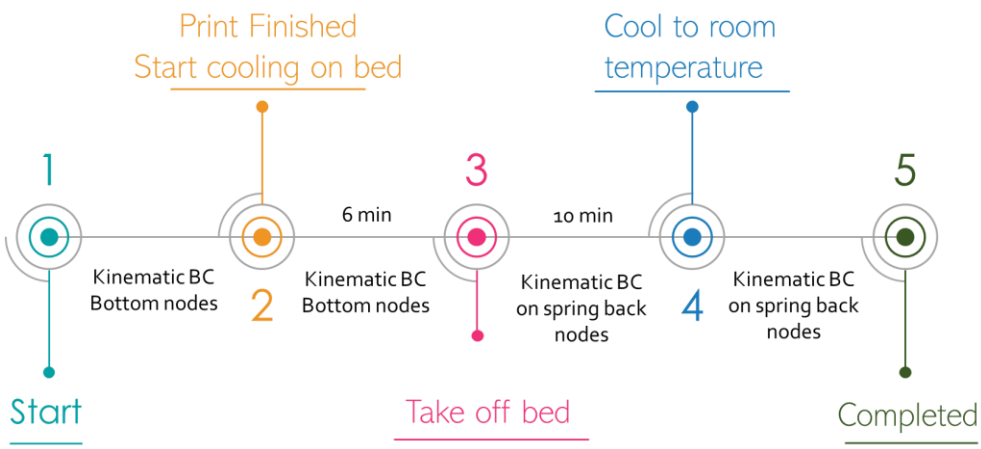

Figure 4.4-4: Steps in the UU shape process simulation

4.4.2 Thermal Analysis

Based on the bead's small size, a bead representation of 2 elements through the thickness and 2 beads through the width was chosen. Both the thermal and mechanical simulations were run to predict the deform shape of the UU geometry. The utilized parameters for the simulations were selected according to the printing conditions during the real print in CAMRI summarized in Table 4.4-1.

Table 4.4-1: Summary of the simulation parameter for UU shape thermal analysis

Parameter	Value
General Simulation Parameter	
Print speed	2500 mm/min
Elements per bead in width direction	2
Elements per bead in height direction	2
Total elements	54400
Length cooling step on bed	360 s
Length cooling step off bed	600 s
Time increment deposition	3 s
Time increment cooling steps	30 s
Heat Transfer Parameter	
Ambient temperature	25°C (298.15 K)
Printing bed temperature	120°C (393.15 K)
Material Extrusion Temperature	295°C (568.15 K)
Emissivity	0.92
Compactor	Tamper
Power remove by the compactor	36000 W

The temperature of the first few printed layers is strongly influenced by the temperature of the build plate. As the deposition front progresses in the stacking direction, the influence of the build plate rapidly decays due to the low thermal conductivity of the printed material in this direction and therefore, convection and radiation heat losses become dominant in the temperature evolution of the printed material [2]. Since thermal conductivity is the only thermal property that varies with fiber orientation tensor, it would be interesting to observe the influence of OTs at several layer locations. The temperature history of the part was probed at six locations at 6th, 13th, and 21st layer at the middle of the part lengthwise as shown in Figure 4.4-5.

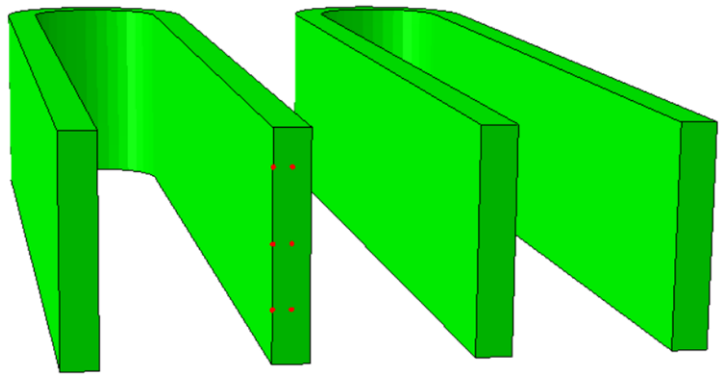

Figure 4.4-5: Locations for extracting temperature evolution

Figure 4.4-6 shows the temperature gradient at the cross-section at the exact half of the part lengthwise. The temperature gradient does not seem to differ noticeably with the change in OTs. Referring back to Figure 4.3-3, the thermal conductivity in the stacking direction is identical in all three GF-PA-OTs. Therefore, it is as expected for the temperature loss due to conduction in the 3 directions to not vary with OTs.

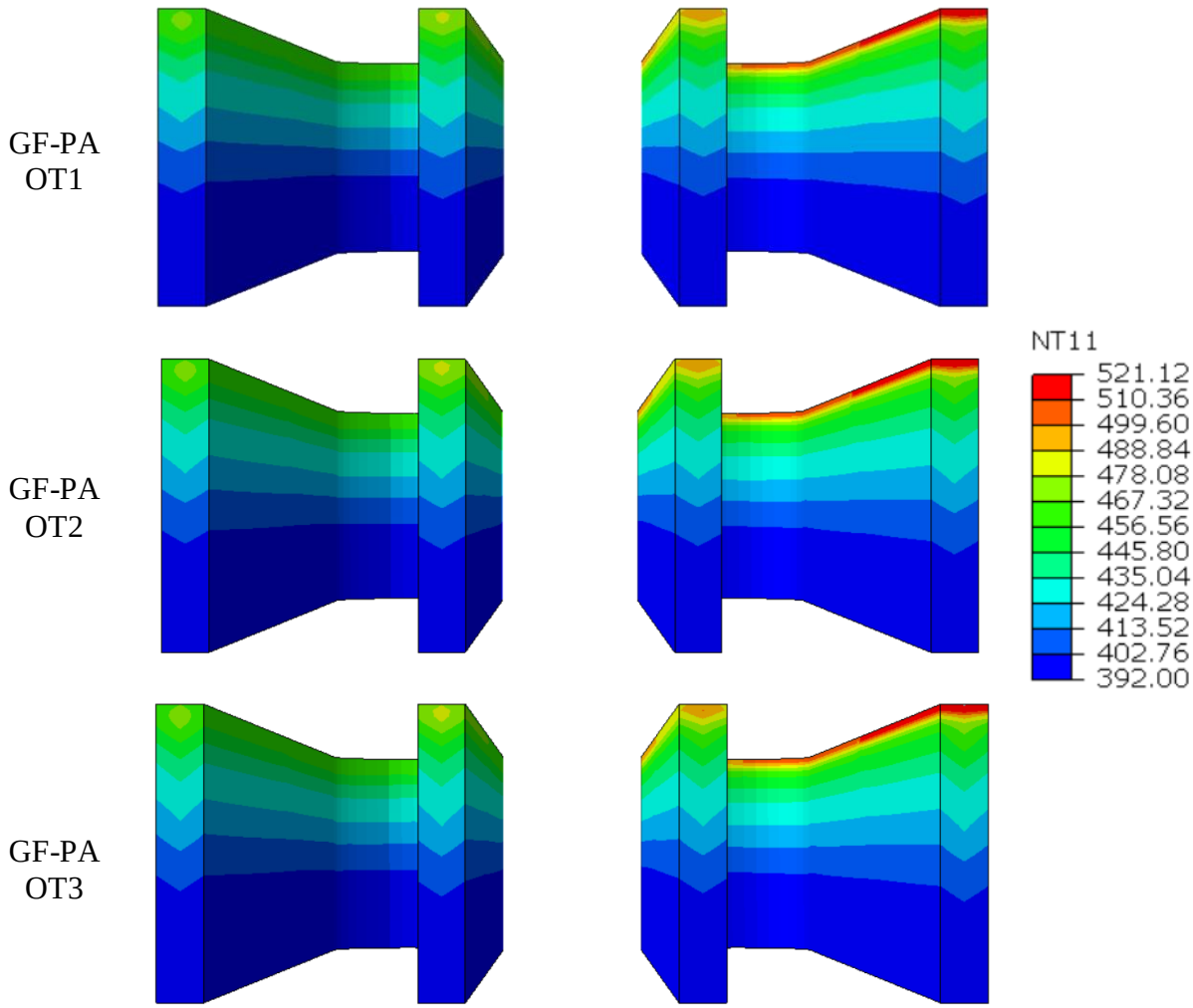

Figure 4.4-6: Comparison of the temperature gradient at the end of the deposition process

Layer 2 is expected to be most influenced by the thermal conductivity which is fiber orientation dependent. Even though K_{33} is constant for all GF-PA-OTs, there are some slight differences in temperature evolution during the part manufacturing predicted in the EDAM process simulation as shown in Figure 4.4-7. Heat transfer via conduction does not only occur in stacking direction but also in the print and transverse direction which is the cause of the very slight differences observed between OTs. The temperature history of Layer 13th and 21st, shown in APPENDIX Figure A 4, of the three OTs are almost identical.

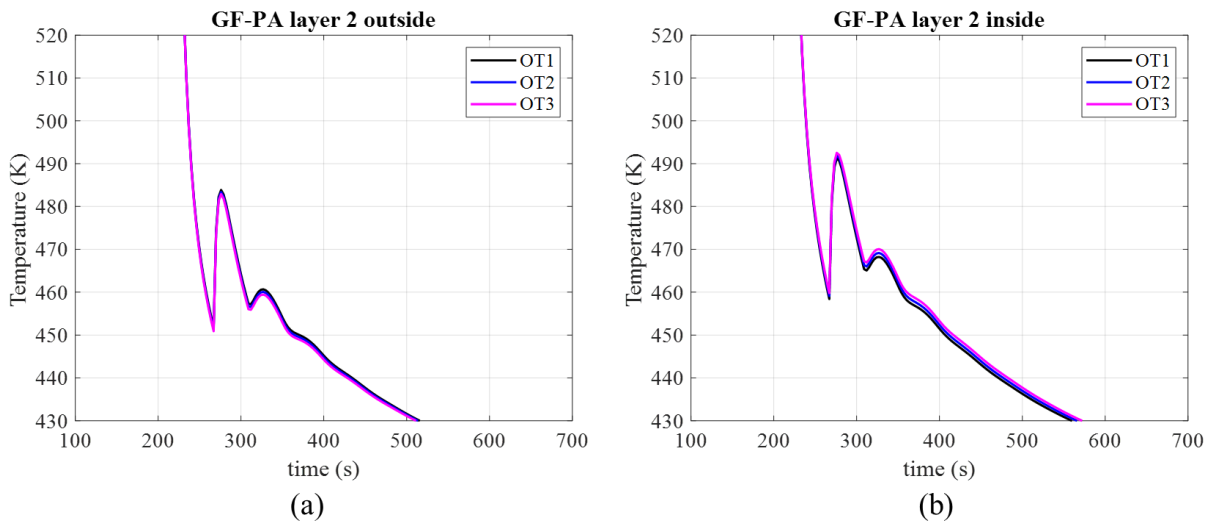

Figure 4.4-7: Comparison of different OT's transient evolution of the temperature of layer 2 during part manufacturing predicted in the EDAM process simulation

Figure 4.4-8 shows the predicted transient temperature evolution at the six locations of GF-PA-OT2.

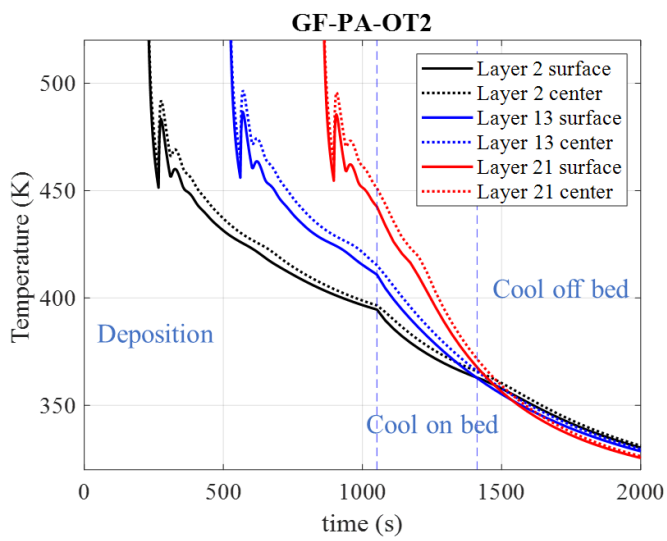

Figure 4.4-8: Transient evolution of temperature during part manufacturing at multiple layer locations predicted in the EDAM process simulation

4.4.3 Mechanical Analysis – Stress and Deformation

One of the most important problems in the EDAM process is the distortion of the part during the printing phase. The heating and rapid cooling cycles during the deposition of the material

accumulate residual stresses and strains [11]. Residual stresses are those that remain in a component or structure in the absence of an applied load. They generally formed as a result of a local mismatch in shape, such as thermal gradients or local deformation. This residual stress would lead to distortion and might lead to and delamination, which reduces the dimension accuracy of the final parts. In some cases, it can cause print failure due to part detaching from the print bed. Since residual stress leads to distortion, this section will first start with the discussion of the stress of GF-PA-OTs and follow by deformation comparison.

Residual stress

The stress evolution was obtained from Layer 13th of the third curve shown in Figure 4.4-9 where the layer starts at the corner marked with the red circle. The stress was taken at the first integration point of the element of the inner element and the outer element of layer 13th. The inner radius is 14.3 mm and the outer radius is 20.7 mm.

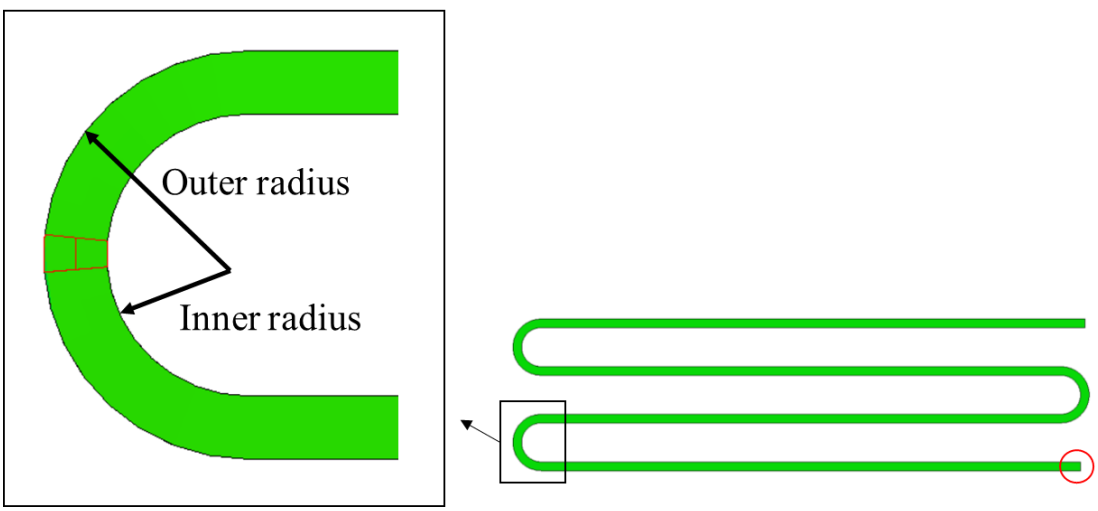

Figure 4.4-9: Stress evolution probe location

It is worthwhile to note that the stress in the curvature region, the half ring, is the main cause of in-plane deformation. The local orientation in the ring region is shown in Figure 4.4-10 with the black arrow as 1-direction, blue arrow as transverse direction, and pink pointing out the page as the 3-direction. The fiber orientation follows the path, in other words, the fiber orientation A_{11} follow along the black arrow, similarly for the A_{22} with blue arrow, and A_{33} with pink arrow.

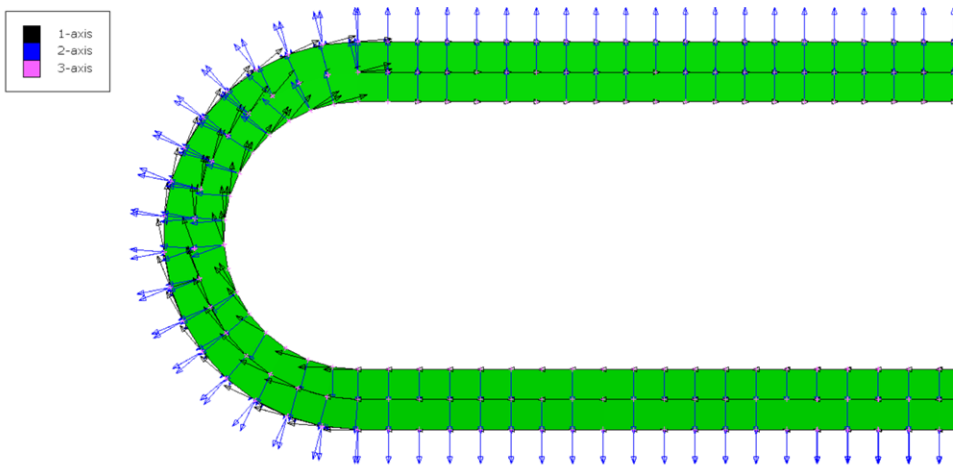

Figure 4.4-10: Local orientation of the ring

The stress in a cylinder consists of hoop stress, radial stress, and axial stress. The hoop stress (σ_θ), or circumferential stress, is the normal stress in the tangential direction to the cylinder. Axial stress (σ_a), or longitudinal stress is the normal stress parallel to the axis of cylindrical symmetry. Radial stress (σ_r), is acting in directions coplanar with but perpendicular to the symmetry axis. Figure 4.4-11 shows the hoop, radial, and axial stress in the curvature region of the UU geometry. The print direction, 1-direction, and hoop direction refer to the same direction because the EDAM process simulation uses a local coordinate as shown in Figure 4.4-10. Similarly, the transverse direction refers to the same direction as 2-direction, and radial direction.

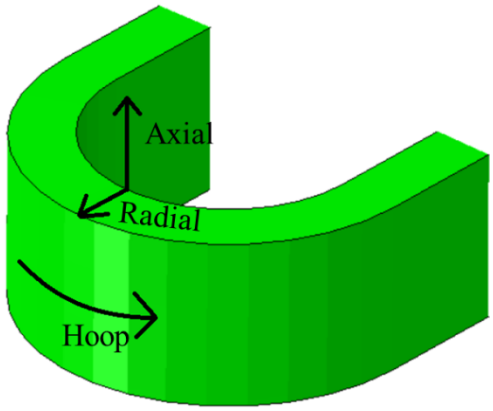

Figure 4.4-11: Hoop stress, radial stress, and axial stress

Stress in the hoop and radial direction has the most impact on the in-plane deformation. The axial stress is developed due to the thermal gradient and the difference in CTE of a different layer. The magnitude of axial stress not negligible, however, only a small influence on the hoop and radial stresses resulted from the Poisson effect [53]. Therefore, this section will only focus on the hoop and radial stress.

The CTE in the hoop direction (α_θ) is usually less than CTE in the radial direction (α_r), i.e. $\alpha_1 < \alpha_2$. For GF-PA-OT1 α_θ is only slightly lower than α_r. Meanwhile, α_θ is significantly lower than α_r for GF-PA-OT2 and GF-PA-OT3. When the material cools down from melt temperature to room temperature, the layer would shrink in both radial and circumferential directions. GF-PA-OT1 will shink similarily in the hoop and radial direction. In contrast, GF-PA-OT2 and OT3 will shink significantly more in the radial direction than the hoop direction. Thus, resulting in more stress.

Figure 4.4-12 shows the comparison of the stress evolution in the 1-direction of the GF-PA-OTs. Figure 4.4-13 shows the comparison of the stress evolution in the 1-direction of the GF-PA-OTs. The stress was probed from layer 13th which is in the middle of the part height-wise. This does not represent the entire cross-section of the curvature. First, the displacement of the bottom-most layer is constrained in all directions to mimic the contact of the part with the built plate. Secondly, the build plate is kept heated at 120 ℃. As shall see later, that the stress at the bottom layers is higher magnitude than the rest of the part.

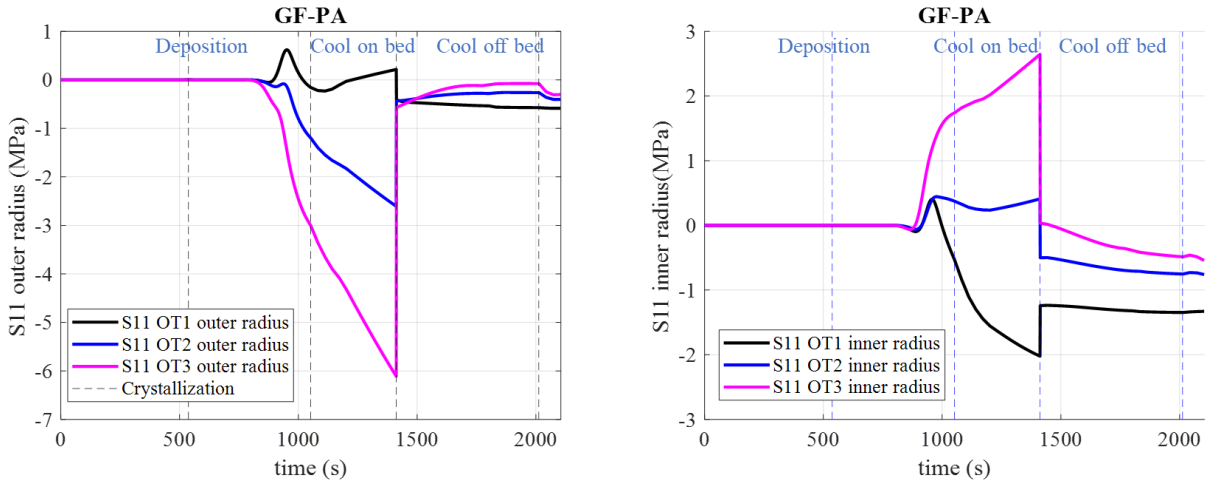

Figure 4.4-12: Comparison of the stress evolution in the 1-direction of GF-PA-OTs

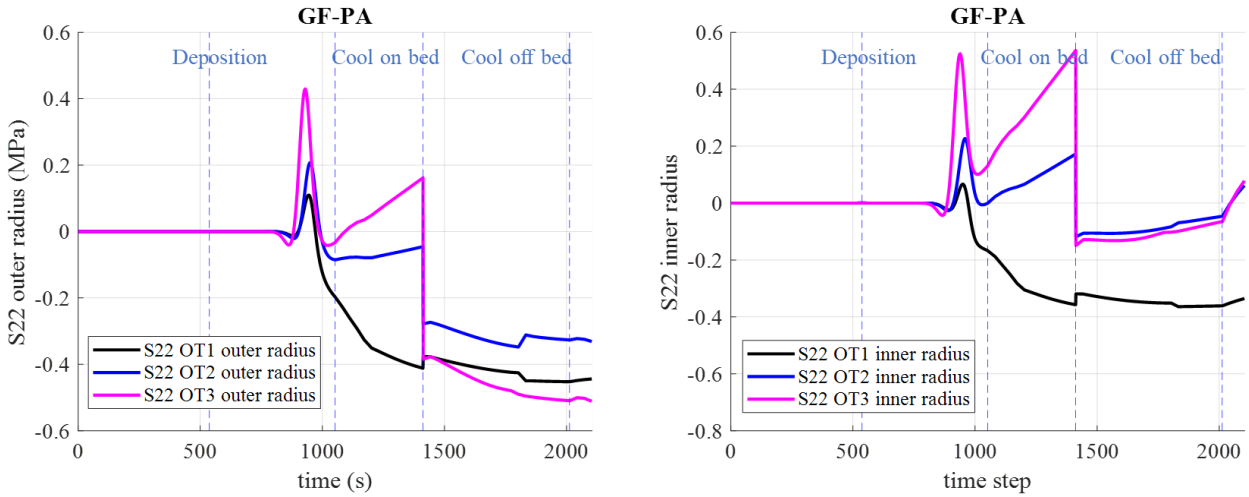

Figure 4.4-13: Comparison of the stress evolution in the 2-direction of GF-PA-OTs

Multiple mechanisms contribute to the stress evolution happening simultaneously. First, the mismatch of the thermal strain of the current layer and the layer below, and the mismatch of the current layer with the layer above. Secondly, the anisotropic crystallization shrinkage that developed as the material crystallizes down. Thirdly, as shown in Figure 4.4-6, the temperature is not uniform throughout the bead. There is a temperature gradient where the temperature is the highest at the center of the bead. Also, the inner radius has a higher temperature than the outer radius due to the smaller surface area for heat transfer via convection and radiation. Due to the viscoelastic properties of the polymer, the elastic and thermoelastic properties are dependent on

the temperature. The stress evolution can't be easily explained due to those factors. Therefore, the focus here is limited to only on the stress state just before the release of the constrain which is at 1412 seconds. It is the stress state that determines the spring-in or spring-out of the part.

The stress distribution was obtained from the cross-section shown in Figure 4.4-14. Figure 4.4-15 shows the stress distribution at the cross-section of the UU shape of the three GF-PA-OTs just before the release of the displacement constrain at the bottom surface. Red color indicates tensile stress, and blue means compressive stress. The stress distribution is uneven throughout the thickness as mentioned above. The top of the part is free to move, while the bottom-most layer's displacement is kept zero. Therefore, stress is higher at the bottom of the part.

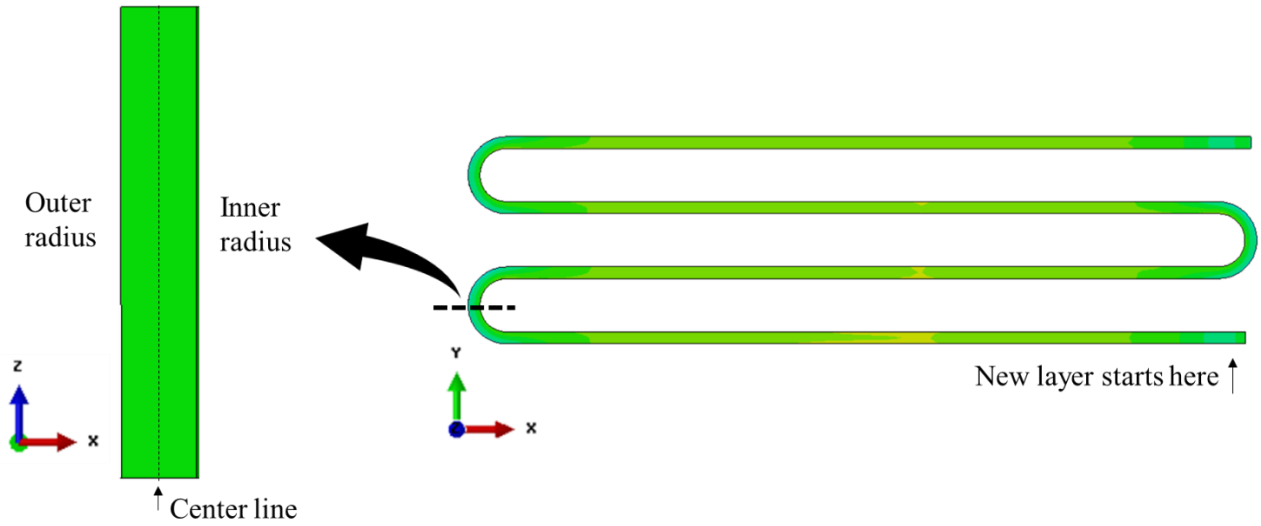

Figure 4.4-14: Location of the cross section cut

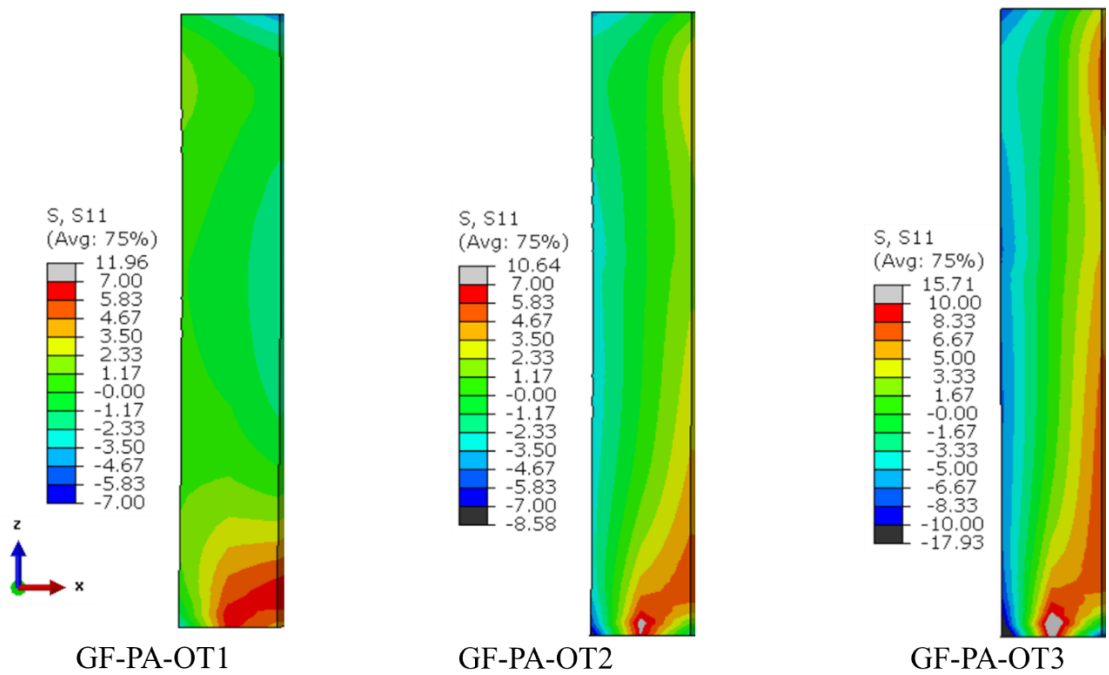

Figure 4.4-15: Stress distribution in the cross-sectional cut

As shown in Figure 4.4-15, the inner radius experiences tensile stress and the outer radius experiences compressive stress. The inner and outer radius can be split into two by the centerline/neutral axis. The force acting on the inner radius is simply the stress times the cross-sectional area on the right side of the centerline. The same goes for the force acting on the outer radius. Figure 4.4-16 summarizes the overall force acting on the inner and outer radius before the constrain is release and the bending moment can be visualized as shown in the dashed arrow. After strain removal, the part re-equilibrate and resulting in the equal and opposite moment as shown in the black solid arrow. The direction of this bending moment results in spring-in deformation where the half-circle closes inward.

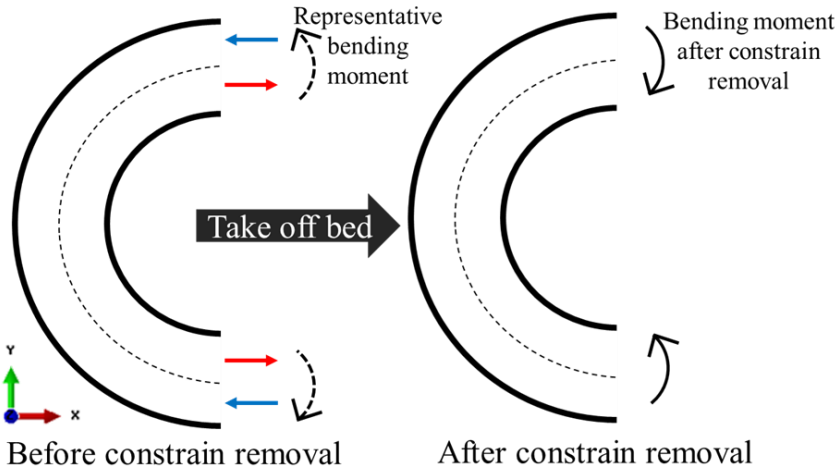

Figure 4.4-16: Compressive stress in the outer radius and tensile stress in the inner radius

Deformation

The advantage of the 'features' of this geometry is the ease to measure and compare the deformation of the printed part. Three deformed distances were measured to compare the in-plane deformation of GF-PA-OTs. Those measurements were taken after the part has cooled down on the bed for 6 min, cool down off bed for 10 min, and cool to room temperature. The distances are named 'A', 'B', and 'C' as shown in Figure 4.4-17.

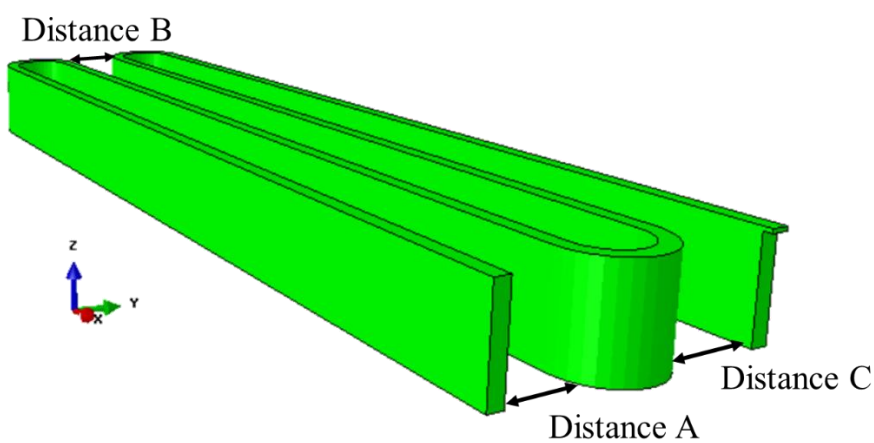

Figure 4.4-17: Locations of the in-plane deformation measurement

The warpage was measured at four locations to compare the out of plane deformation of GF-PA-OTs. The two locations are named ‘D’ and ‘E’ as shown in Figure 4.4-18.

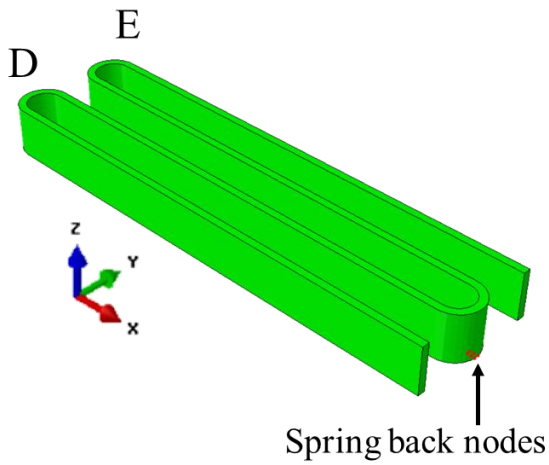

Figure 4.4-18: Locations of the out of plane deformation measurement

The top views of deformed UU geometry of GF-PA-OTs are shown in Figure 4.4-19 with the scale factor of 1. All OTs result in a spring-in type distortion, meaning the curvature closes inwards which was discussed in the Residual stress section. GF-PA-OT3 clearly deformed the most in the in-plane direction.

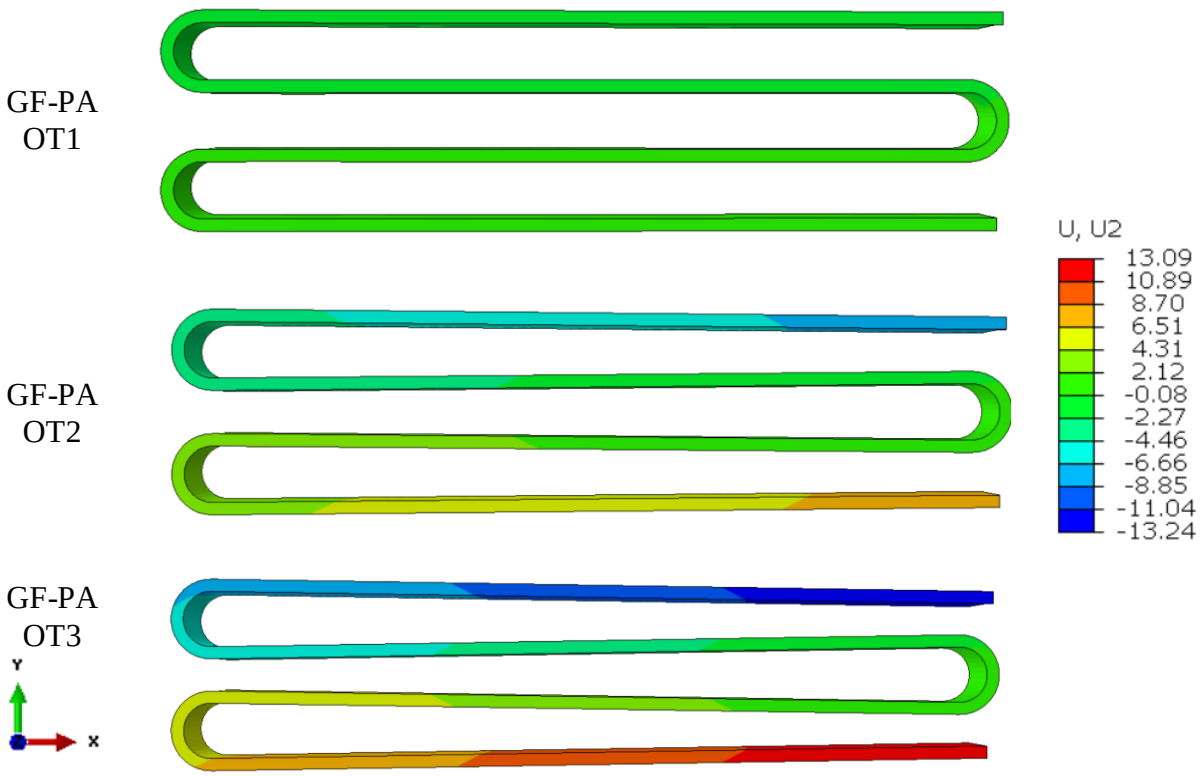

Figure 4.4-19: Deformation gradient in the 2-direction of GF-PA-OTs

The undeformed distance A and C is 28.59 mm, and undeformed distance B is 28.64 mm. The Deformed distance A, B, and C is the magnitude of the difference between their undeformed and deformed distance. The GF-PA-OT3 was found to deform the most in-plane with the maximum deformation of 12.55 mm. The maximum deformation of GF-PA-OT2 is 7.41 mm and that of GF-PA-OT1 is 1.26 mm.

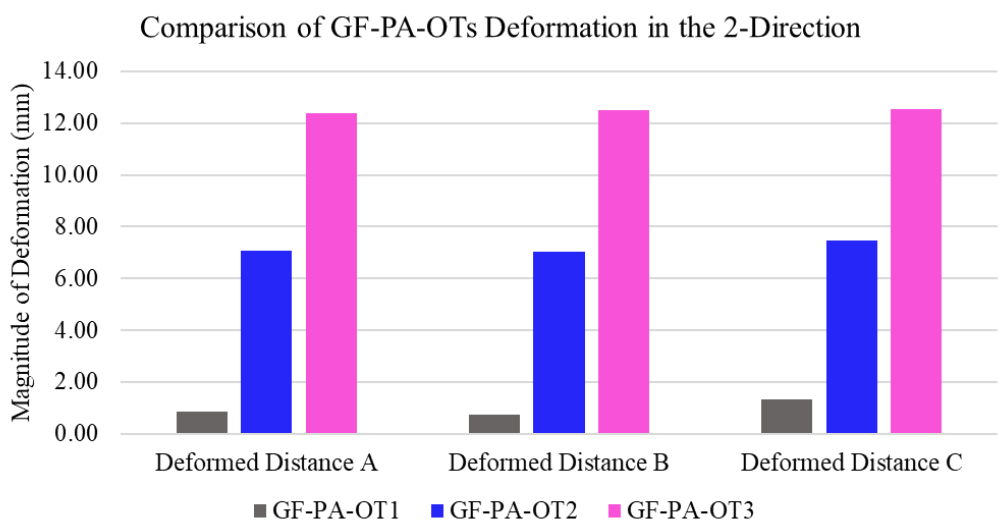

Figure 4.4-20: Comparison of the magnitude of deformation in the 2-direction of GF-PA-OTs

A kinematic boundary condition was specified during the deposition and cooling on bed process. In other words, all the nodes on the bottom surface of UU geometry are fixed and restrained in any movement. Then the material is set to cool off bed which the bottom of the surface is free to move except the spring back nodes which are restrained from any motion. The spring back nodes are shown in Figure 4.4-21. It was chosen there because they are in the middle of the geometry in the y-direction and it will not hinder the deformation in the 2-direction. However, it does bias the deformation in the 3-direction.

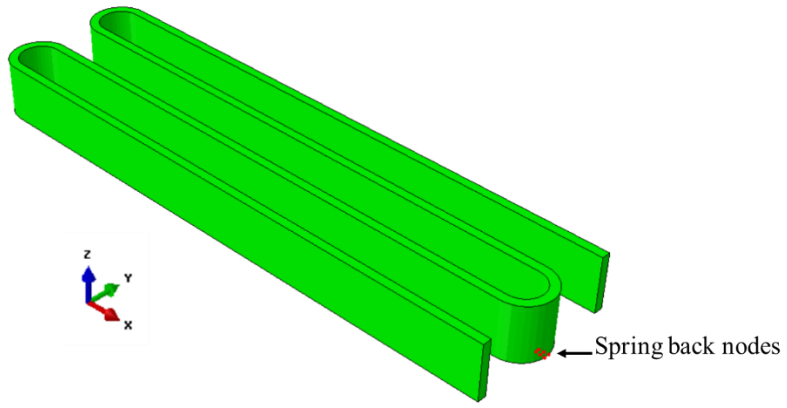

Figure 4.4-21: Spring back nodes of the UU geometry

Because of the restriction of the spring back nodes, only the deformation D and E are shown in Figure 4.4-22. GF-PA-OT1 deformed the most, however, the deformation of GF-PA-OT2 and GF-PA-OT3 are quite similar.

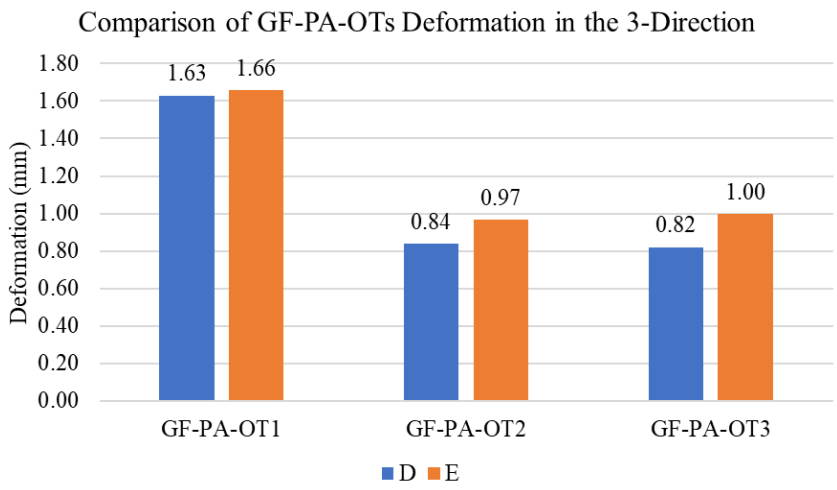

Figure 4.4-22: Comparison of out of plane deformation of GF-PA-OTs

4.5 Effects of Fiber Properties on the residual stress and deformation

This chapter studies the two types of commonly used fiber in reinforcing additive manufacturing thermoplastic pellets; carbon and glass fibers. Carbon fibers are known for their high stiffness-to-weight ratio but are expensive. On the other hand, glass fibers are relatively inexpensive and exhibit fairly good mechanical properties and are suitable for parts that are less stringent on weight and strength so that parts can be fabricated at a lower cost. Glass fiber weighs more than carbon fiber, and is not as stiff, but is more impact-resistant and has a greater elongation-to-break.

There have been several studies conducted to compare the mechanical properties of glass fiber and carbon fiber [54] [55] [56]. Goh et al. compared the mechanical properties such as tensile and flexural properties of Fused filament fabrication of continuous carbon (CFRTP) and glass fibers reinforced thermoplastics (GFRTP). CFRTP is found to have higher tensile strength, tensile modulus, flexural strength, and flexural modulus than GFRTP [55]. Another study by Wonderly et al. compared the strengths of the vacuum infusion of vinyl ester resin glass and carbon fiber

specimens. The carbon fiber laminates found to be mechanically superior under loading conditions where the strength is mainly fiber dominated such as under tensile loading while the glass fiber laminates were stronger under loading conditions where the strength is mainly resin dominated such as compressive loading [56].

The constituent properties of glass fiber, carbon fiber, and polyamide are shown in Table 4.5-1. The glass fiber properties were obtained from the reverse engineering of 50 % wt. GF-PA done in the earlier section. The properties of carbon fiber were obtained from a standard modulus carbon fiber T300 [57][58][59][60]. Carbon fiber is transversely isotropic while glass fiber is isotropic. While carbon fiber E_1 (233 GPa) is tripled of glass fiber E_1 (72 GPa), carbon fiber E_2 (23.1 GPa) is less than half of glass fiber's.

Table 4.5-1: Constitutive properties of carbon fiber and glass fiber

Constituent Properties	**Carbon fiber**	**Glass fiber**
Symmetry	Transverse Isotropic	Isotropic
$\boldsymbol{E_1}$ **(GPa)**	233	72
$\boldsymbol{E_2}$ **(GPa)**	23.1	72
$\boldsymbol{G_{12}}$ **(GPa)**	8.96	30.4
$\boldsymbol{G_{23}}$ **(GPa)**	8.27	30.4
$\boldsymbol{\nu_{12}}$	0.2	0.21
$\boldsymbol{\nu_{23}}$	0.4	0.21
Density	1.76	2.54
CTE 1, $\boldsymbol{\alpha_1}$ $\boldsymbol{(10^{-6})}$	0.54	2.5
CTE 2, $\boldsymbol{\alpha_2}$ $\boldsymbol{(10^{-6})}$	10.08	2.5
Specific heat capacity $\boldsymbol{C_p}$	0.777	0.8038
Thermal conductivity $\boldsymbol{K_{11}}$ **(W/mK)**	9.4	1.576
Thermal conductivity $\boldsymbol{K_{22}}$ **(W/mK)**	0.67	1.576

The study of this section focuses on the comparison of the temperature history, residual stress, and deformation of additive manufacture short carbon fiber reinforced polyamide (CF-PA) and glass fiber reinforced polyamide (GF-PA). In addition, the comparison of CF-PA-OT1, OT2, and OT3 was also studied along with the comparison of the influence of the fiber orientation tensor on GF-PA vs CF-PA.

4.5.1 Comparison of Carbon Fiber – Polyamide and Glass Fiber -Polyamide Properties

Elastic properties

Carbon fiber is lighter than glass fiber, with the same weight fraction, there is more volume fraction of CF than GF mixed with polymer. The 50% wt. GF-PA has a fiber volume fraction of 30%. The same fiber volume fraction with carbon fiber results in 40.8% by weight CF - PA. The effective properties are volume-based, which is essentially the amount of fiber. Therefore, 30% by volume CF-PA is chosen instead of 50% by weight CF-PA. The effective properties of CF-PA-OT1, CF-PA-OT2, and CF-PA-OT 3 are listed in Table 4.5-2. Figure 4.5-1 compares the elastic properties of all CF-PA-OTs.

Table 4.5-2: Effective elastic properties of CF-PA-OT1, CF-PA-OT2, and CF-PA-OT3

	CF-PA-OT1	**CF-PA-OT2**	**CF-PA-OT3**
Fiber Volume Fraction	30%	30%	30%
$\boldsymbol{E_{11}}$ **(GPa)**	18.84	30.18	41.50
$\boldsymbol{E_{22}}$ **(GPa)**	16.14	9.08	6.41
$\boldsymbol{E_{33}}$ **(GPa)**	6.57	6.39	5.71
$\boldsymbol{\nu_{12}}$	0.33	0.47	0.47
$\boldsymbol{\nu_{13}}$	0.40	0.38	0.37
$\boldsymbol{\nu_{23}}$	0.41	0.43	0.44
$\boldsymbol{G_{12}}$ **(GPa)**	8.48	6.44	3.94
$\boldsymbol{G_{13}}$ **(GPa)**	3.47	3.73	2.89
$\boldsymbol{G_{23}}$ **(GPa)**	3.37	2.99	2.32

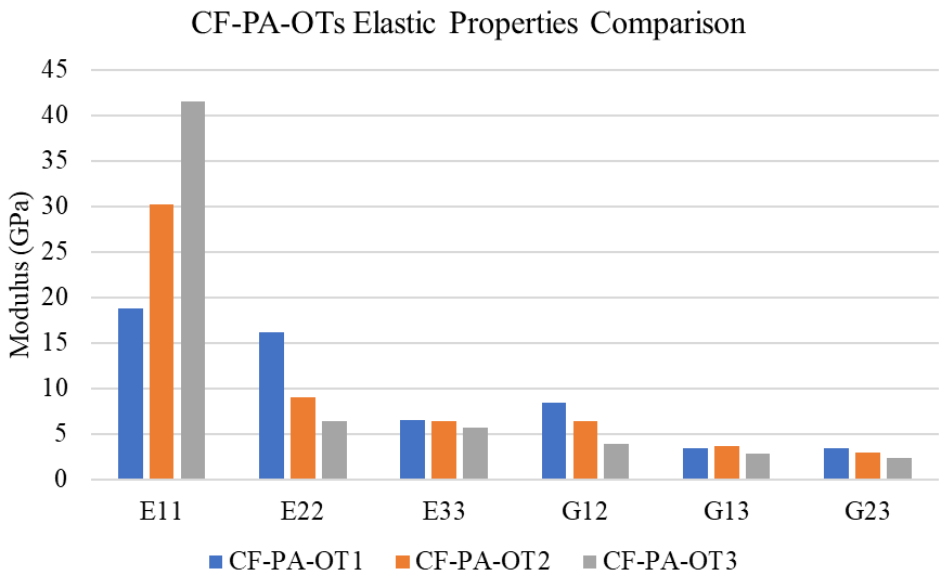

Figure 4.5-1: CF-PA-OTs Elastic Properties Comparison

All the modulus of CF-PA is higher than GF-PA. In the matrix dominated direction, such as 3-direction and 2-direction in OT3, the modulus of CF-PA is comparable to GF-PA as shown in Figure 4.5-2. Compare to GF-PA, CF-PA has a higher degree of anisotropy.

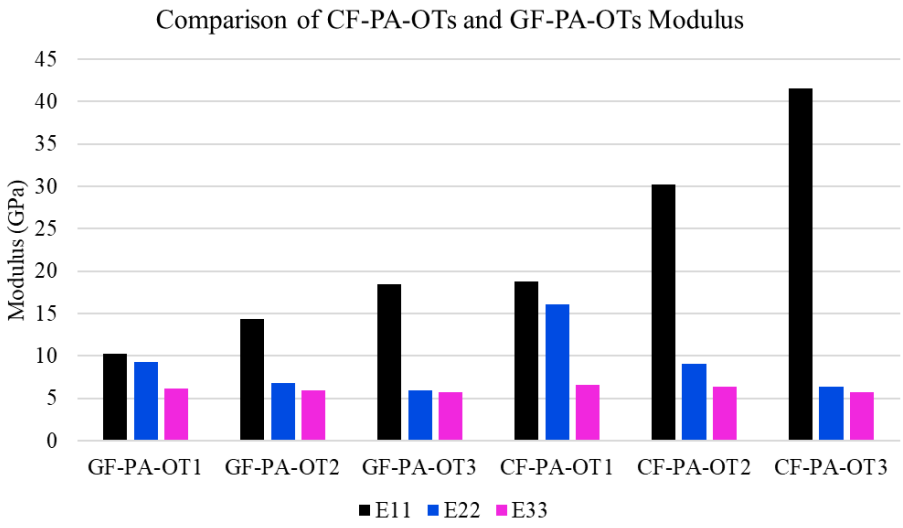

Figure 4.5-2: Comparison of CF-PA-OTs and GF-PA-OTs Modulus in the three principal directions

Thermophysical Properties

The thermal conductivity of carbon fiber T300 is much higher than that of glass fiber in the fiber axis direction ($K_{CF1}/K_{PA} = 48.53$, $K_{GF1}/K_{PA} = 8.14$). Hence, the thermal conductivity of the GF-PA will be much lower than that of the CF-PA at a similar fiber content. Although not very dramatic, the thermal conductivity of CF is lower than that of GF in the transverse direction ($K_{CF2}/K_{PA} = 3.46$, $K_{GF2}/K_{PA} = 8.14$). Figure 4.5-3 compares the thermal conductivity of the three cases of GF-PA and CF-PA along with the neat Polyamide (PA) and CF in the axis and transverse direction at 25 ℃.

In terms of the effects of fiber orientation tensor, Fu et al. studies found that thermal conductivity of the carbon-fiber-reinforced polymer composites is more sensitive to fiber orientation than the thermal conductivity of the short-glass fiber-reinforced polymer composites [51]. The explanation is that glass fiber is isotropic, while carbon fiber is transversely isotropic whose thermal conductivity is much higher than that of glass fiber in the fiber axis direction. Figure 4.5-3 agrees with Fu et al., K_{11} of CF-PA in all three OTs are 3-4 times higher than K_{11} of GF-PA of corresponding OTs. CF-PA's K_{22} has less dramatic change with OTs, however, it is still higher than that of GF-PA in all three cases. For K_{33}, CF-PA is only 1.3 times higher than that of GF-PA.

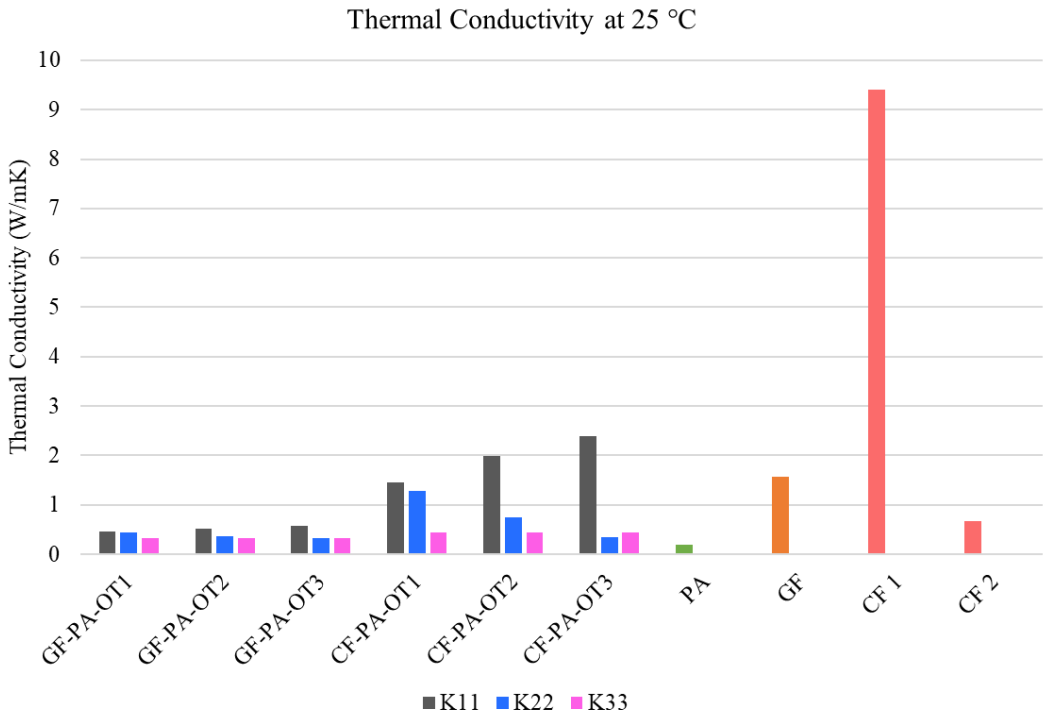

Figure 4.5-3: Comparison of thermal conductivity of GF-PA and CF-PA

Figure 4.5-4 shows the thermal conductivity as a function of the temperature of CF-PA. The values are tabulated in the APPENDIX Table A 7.

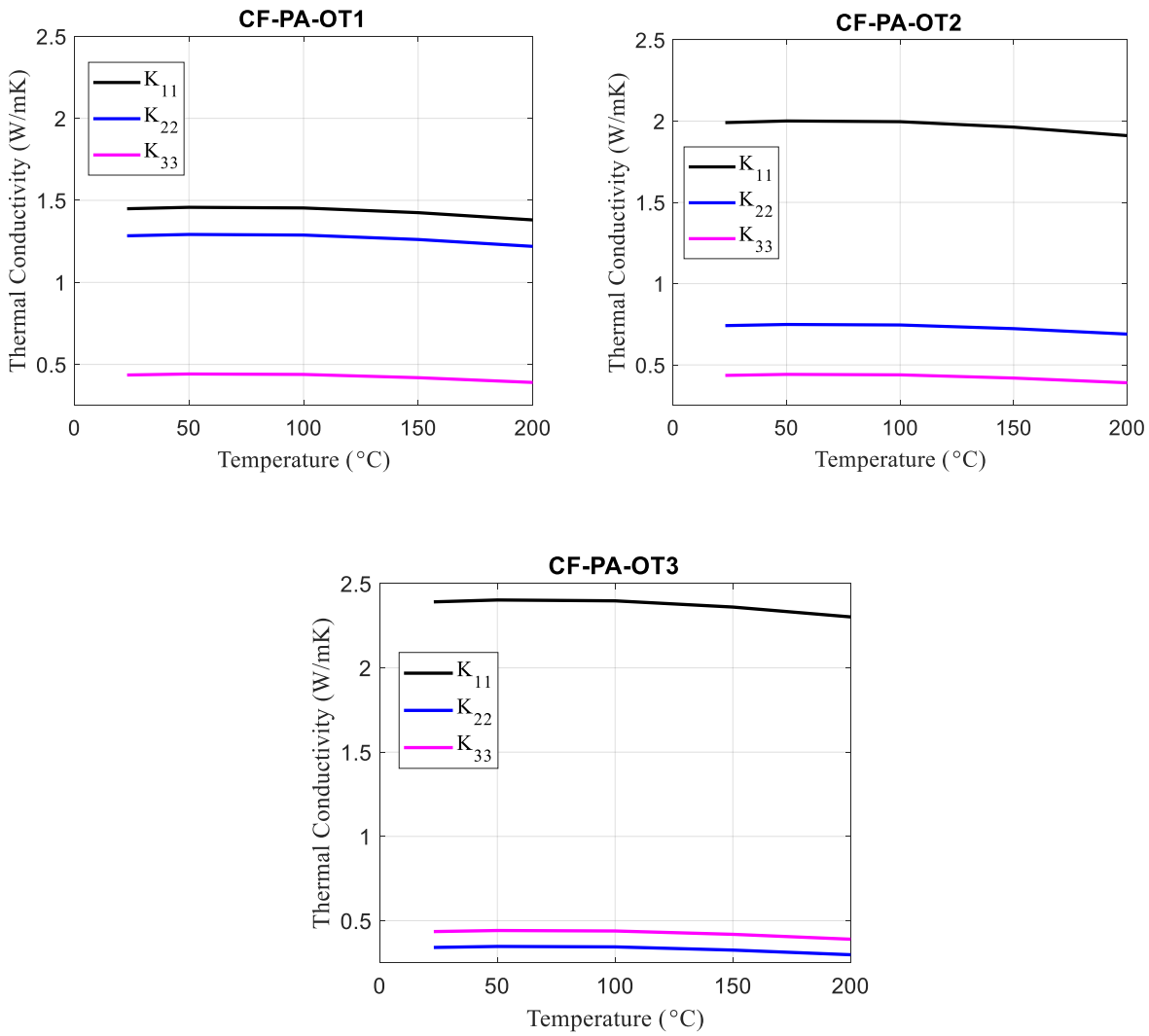

Figure 4.5-4: Thermal conductivity of 30% vol. CF-PA-OT1, OT2, and OT3

Thermoelastic Properties

The same pattern of CTE is observed in CF-PA as in GF-PA. CTE in the 2-direction (α_2) increases from OT1 to OT3 while the CTE in the 3-direction (α_3) and 1-direction (α_1) decreases. Figure 4.5-5 compares the CTE in the three principal directions with the CTE of PA and GF.

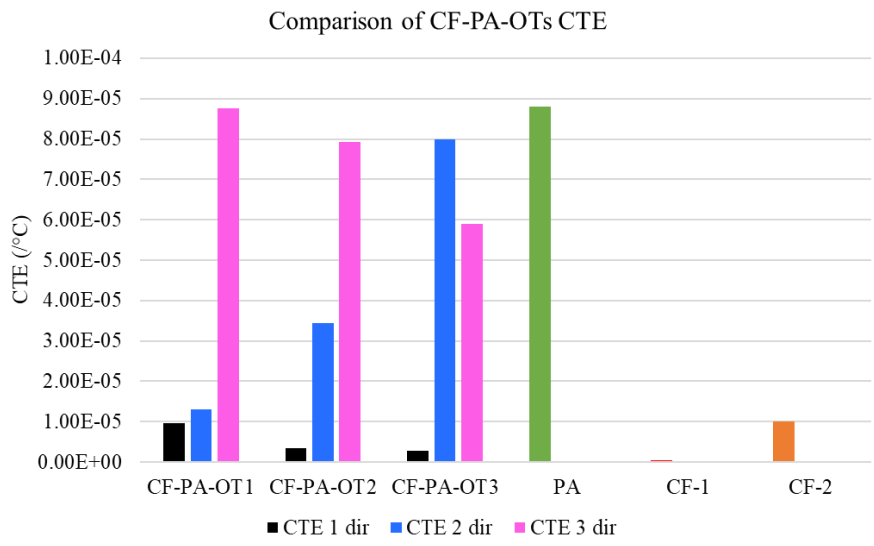

Figure 4.5-5: Comparison of GF-PA-OTs coefficient of thermal expansion

Figure 4.5-6 shows the CTE of CF-PA-OTs with the GF-PA-OTs. The pattern of changes in CTE with OTs is the same for both fiber types. In terms of magnitude, α_3 is comparable between CF-PA and GF-PA for each OTs.

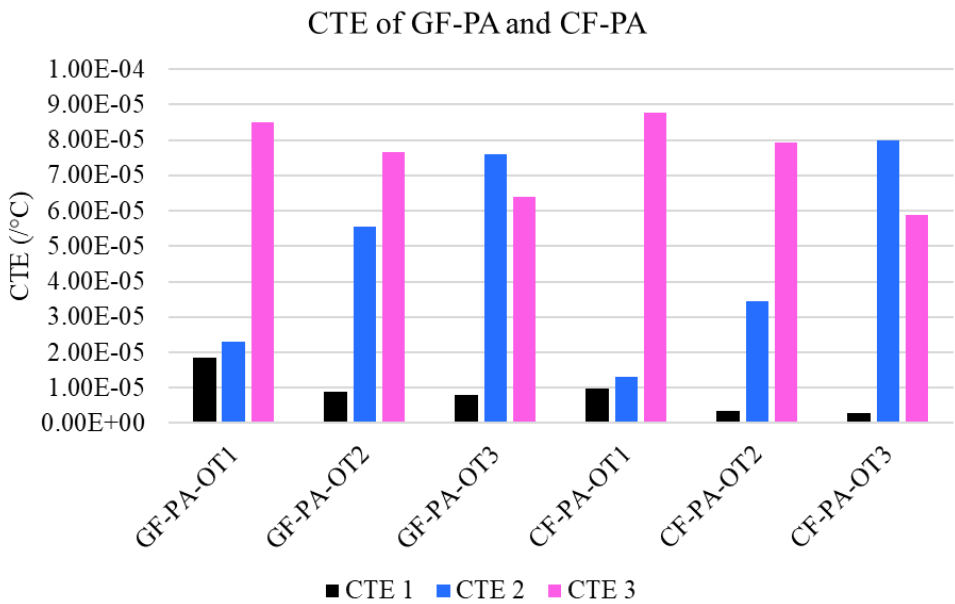

Figure 4.5-6: Comparison of the CTE of GF-PA and CF-PA

4.5.2 Thermal analysis results

The thermal properties that change with fiber type are thermal conductivity and heat capacity. Because the geometry and environment, namely the printer, is the same, convection and radiation are kept constant. The first heat conduction after the material leaves the nozzle is heat conduction through tamper. Simultaneously, heat anisotropic conduction through layers, and for the first few layers, heat conduction through build plate. An in-depth discussion of heat transfer mechanisms can be found in the dissertation from Eduardo Barocio [2].

The same conditions and procedures used for computing the thermal analysis of GF-PA were carried out for CF-PA. Figure 4.5-7 shows temperature distribution at the end of the deposition process predicted in the EDAM process simulation. CF-PA-OT2 as expected has a lower temperature than GF-PA-OT2 at every location of the UU geometry. The first noticeable difference is CF-PA has lower lay down bead temperature due to the heat lost during material compaction (tamping). In the CAMRI system, the tamper is cooled by circulating compressed air. Consequently, the heat loss due to material compaction was implemented in the EDAM process simulation. Further, the thermal conductivity of CF-PA is higher than GF-PA in all three principal directions. The anisotropic heat conduction of the printed material to the subsequent section is higher in CF-PA. In other words, heat in CF-PA can be transferred quicker from the middle of the bead to the surface to transfer to the environment through radiation and convection. Please note that this is an analysis of a thin wall geometry.

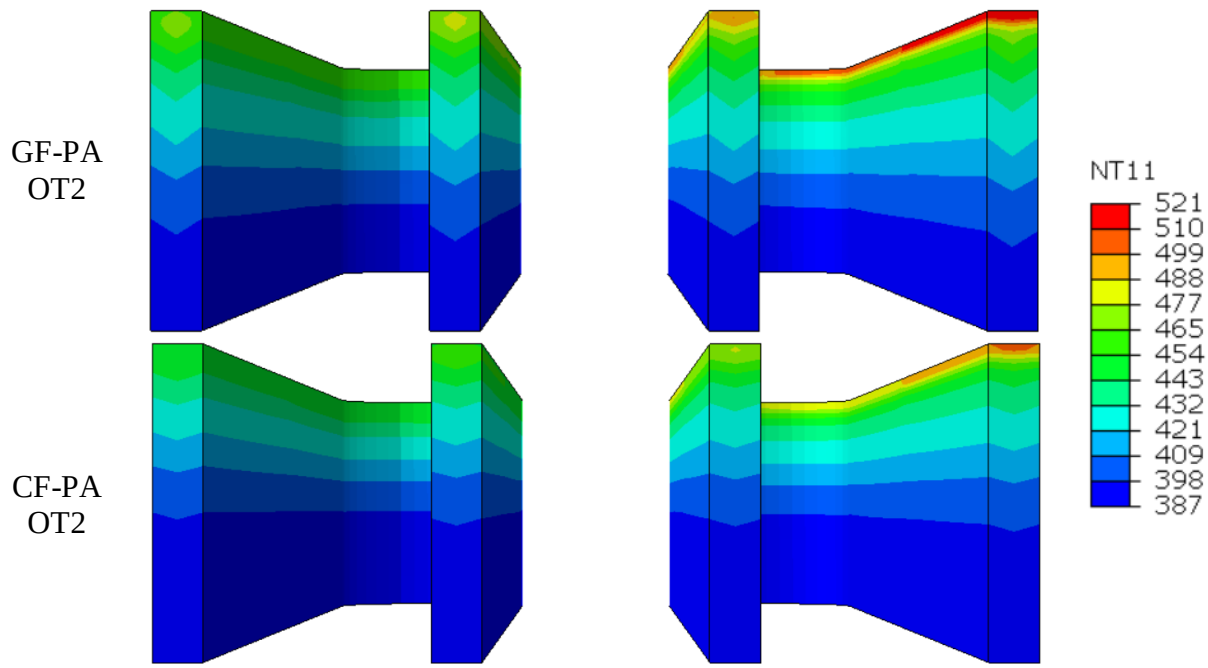

Figure 4.5-7: Comparison of the temperature profile at the end of the deposition process of GF-PA-OT2 and CF-PA-OT2

Figure 4.5-8 shows the comparison of the GF-PA-OT2 and CF-PA-OT2 temperature history of the surface of the wall on the left and at the interior of the wall on the right. The CF-PA-OT1 temperature is approximately 8 °C lower than GF-PA-OT2 difference at the surface of the wall, and approximately 12 °C at the wall interior.

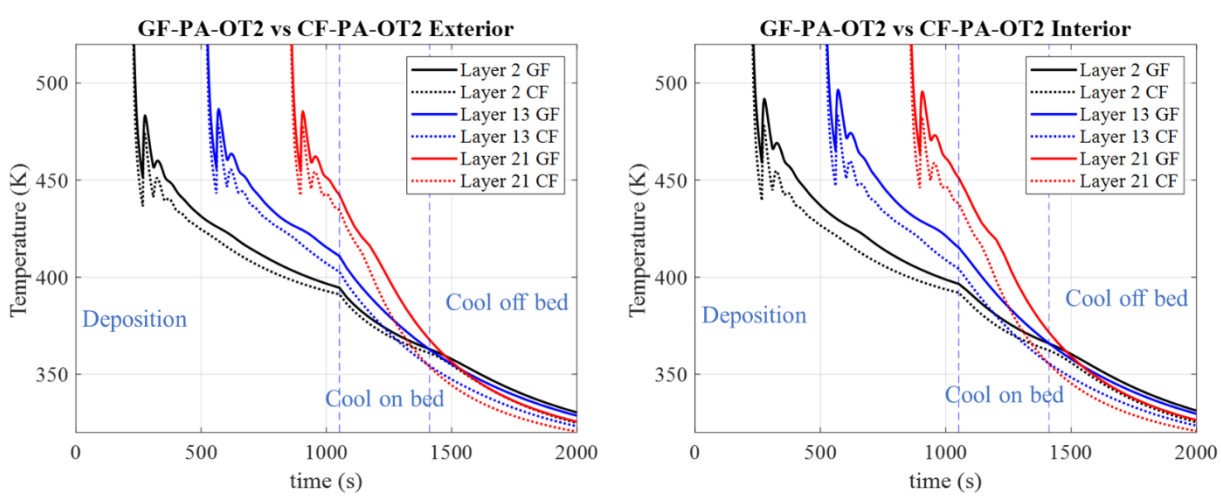

Figure 4.5-8: Comparison of GF-PA-OT2 and CF-PA-OT2 temperature evolution at several layer locations

In the earlier section, the temperature profiles of GF-PA-OTs are almost identical to one another. Figure 4.5-9 shows the temperature of CF-PA-OT1 vs CF-PA-OT2 vs CF-PA-OT3 at the cross-section at the middle of the part. There is a noticeable difference in temperature distribution in each layer. The temperature of each layer is most uniform in CF-PA-OT1 and the least uniform in CF-PA-OT3. Observing the at each layer, CF-PA-OT1 has the lowest temperature at the center of the bead while CF-PA-OT3 has the highest temperature at the same location. This indicates that heat is transferred from the center of the bead to the surface faster in CF-PA-OT1 than CF-PA-OT2, and slowest in CF-PA-OT3. The reason being CF-PA-OT1 has the highest thermal conductivity in the transverse direction (K_{22}) and CF-PA-OT3 has the least.

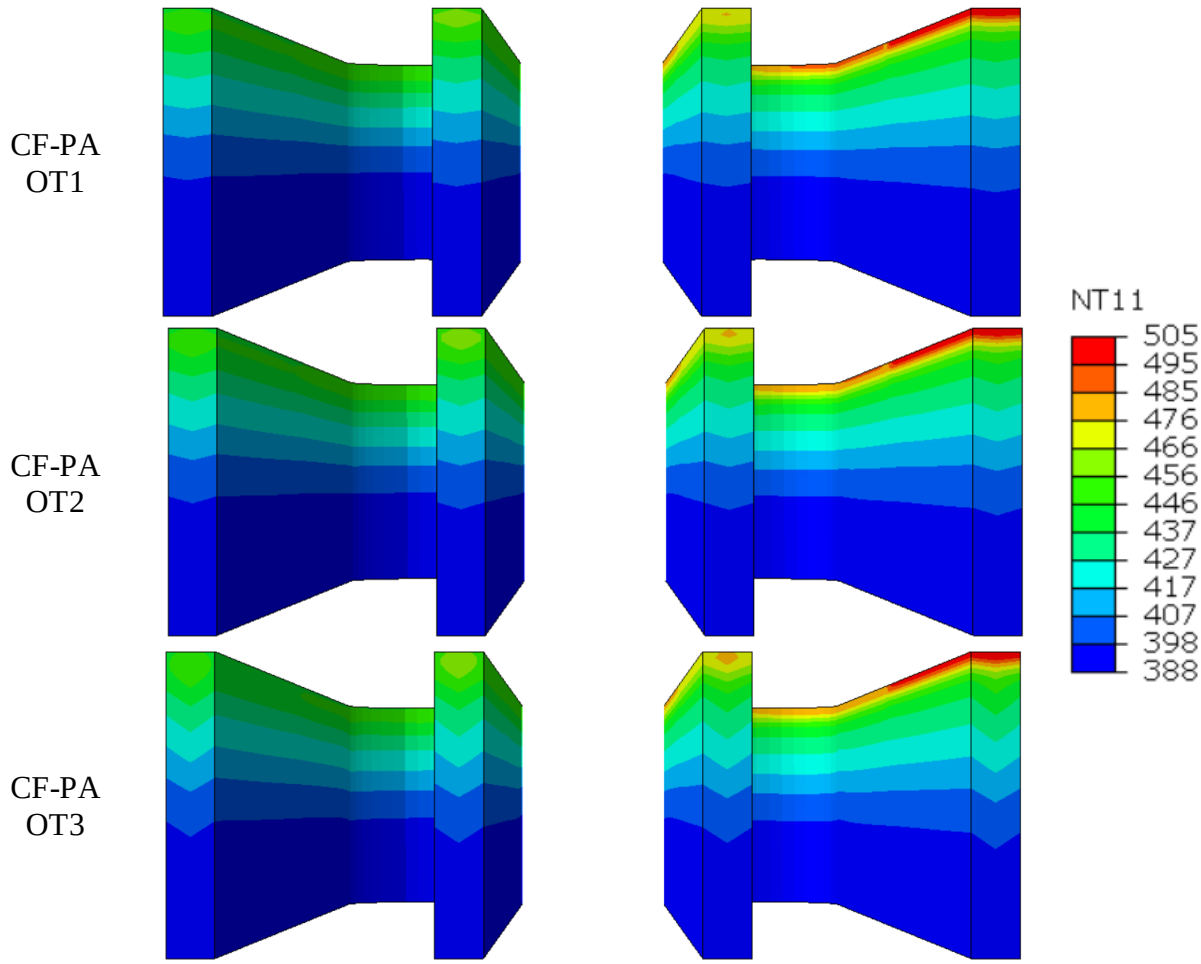

Figure 4.5-9: Comparison of the temperature gradient at the end of the deposition process of CF-PA-OT1, CF-PA-OT2, and CF-PA-OT3

Figure 4.5-10 shows the temperature evolution of layer 2 during part manufacturing predicted in the EDAM process simulation of the three CF-PA-OTs. The figure restates that temperature at the center of the bead is higher in CF-PA-OT1 than CF-PA-OT2 and lowest in CF-PA-OT3.

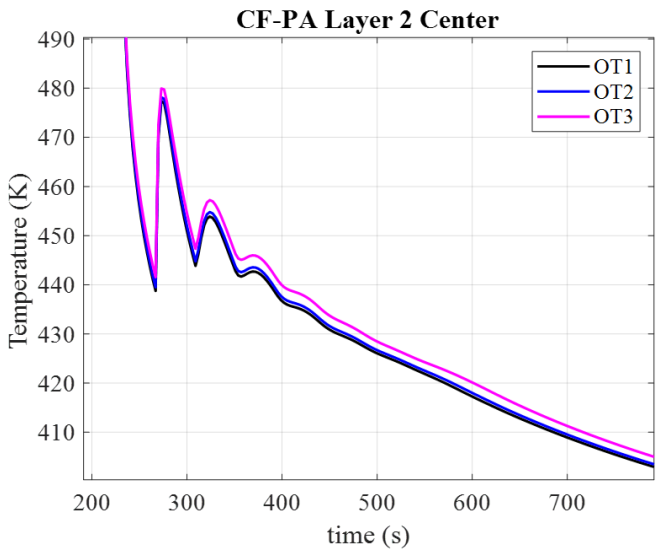

Figure 4.5-10: Temperature history of layer 2 of three OTs during part manufacturing predicted in the EDAM process simulation

Figure 4.5-11 compares the differences in the temperature at the center of the bead that at the surface of the bead. There are very slight differences, of approximately 1°C between the temperature at those locations for CF-PA-OT1. The differences in temperature are approximately 2.5 °C with CF-PA-OT2, and 5.6 °C with CF-PA-OT3.

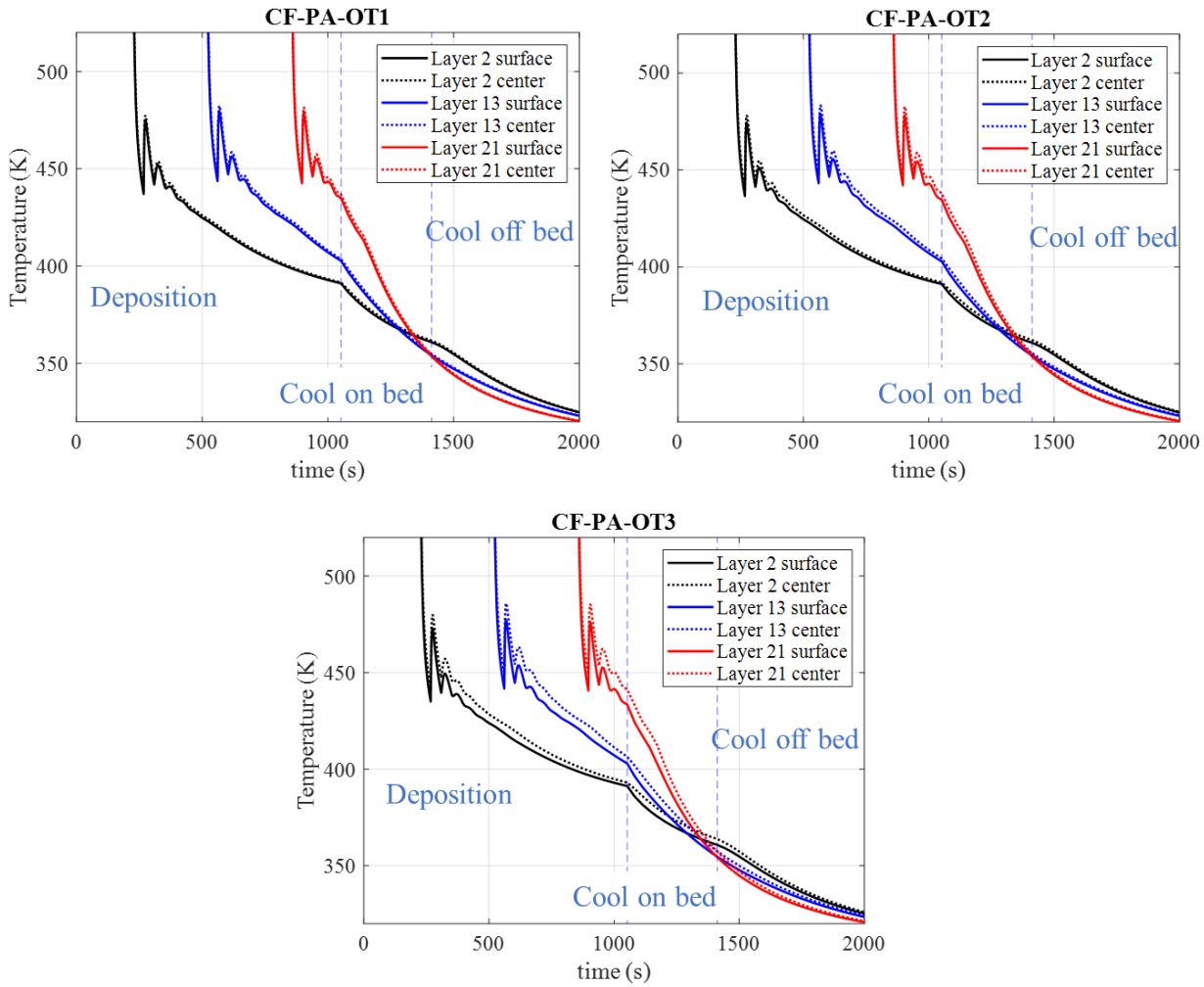

Figure 4.5-11: Comparison of temperature history at the center and surface of the bead of CF-PA-OTs

Lastly, the temperature gradient of all cases at the end of the deposition process taken at the same cross section as in Figure 4.4-5 is summarized in Figure 4.5-12. The Z position at the bottom surface is zero, and the Z at the top of the part is 40 mm. As mentioned before, the temperature gradients of the three OTs of GF-PA represented in solid lines are almost identical. The dotted line represents CF-PA-OTs which CF-PA-OT3 has the highest temperature, and CF-PA-OT2 has a lower temperature, and the lowest temperature is CF-PA-OT1. There are some differences for CF-PA, however, not very significant. This information will be helpful for the out-of-plane deformation comparison.

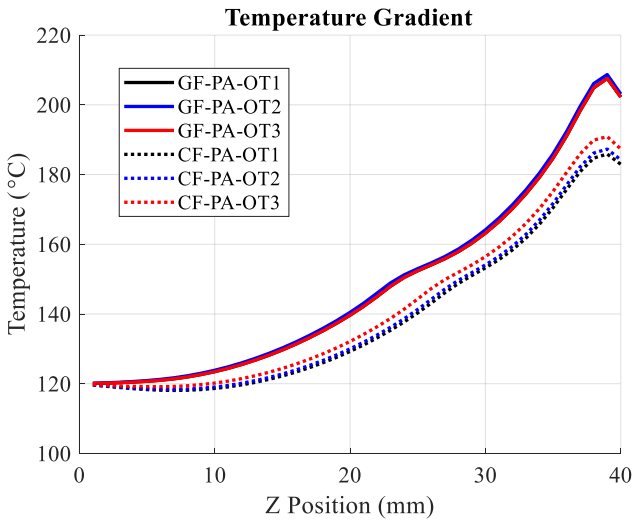

Figure 4.5-12: Comparison of the temperature gradient of all cases

4.5.3 Mechanical analysis results

Both the in-plane and out of plane deformation was measured at the same location as for the GF-PA-OTs. As expected, the in-plane deformation is highest in the CF-PA-OT3 as shown in Figure 4.5-13 due to the largest differences in the properties in the print direction and the transverse direction. As shown in the figure, the deformation in the 2-direction is comparable between the two materials. GF-PA-OT3 and CF-PA-OT3 are very similar. GF-PA-OT1 and GF-PA-OT2 have approximately 1.5 times more deformation than the CF-PA-OT1 and CF-PA-OT2 consecutively. The top view of GF-PA-OTs in-plane deformation can be found in Figure 4.4-19. The top view of CF-PA-OTs in-plane deformation can be found in Figure A 5.

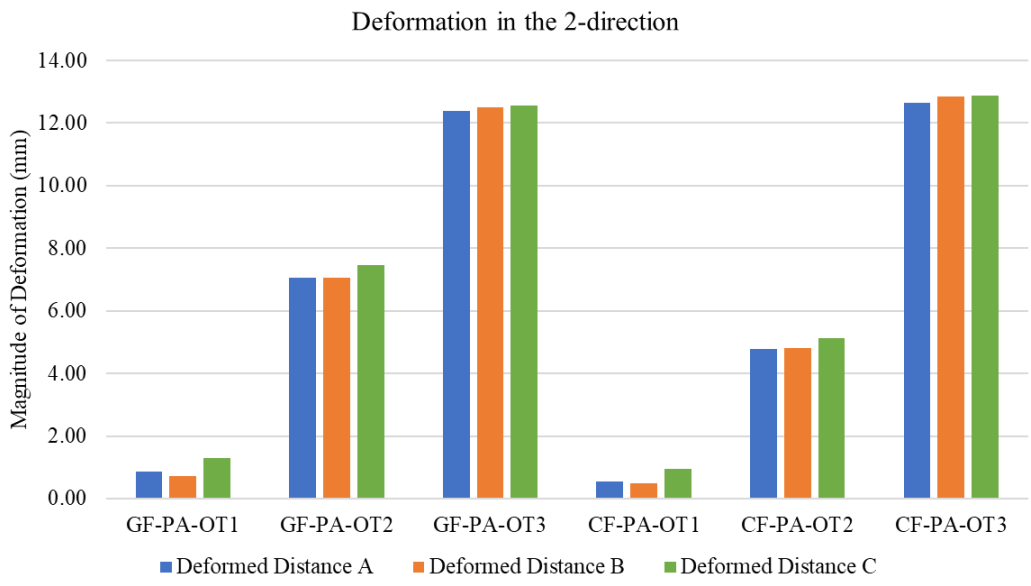

Figure 4.5-13: Comparison of the deformation in the 2-direction of GF-PA and CF-PA

Table 4.5-3 listed the numerical value for the in-plane deformation of all the GF-PA-OTs and CF-PA-OTs. The ratio of OT2/OT1, OT3/OT1, and OT3/OT2 of GF-PA and CF-PA are tabulated in Table 4.5-3. The changes in fiber orientation tensor in the UU geometry made a huge difference in geometry accuracy. The differences of in-plane deformation of OT3 is an order of magnitude larger than OT1. OT1 has A_{11} of 0.5, OT2 has A_{11} of 0.73, and OT3 has A_{11} of 0.9.

Table 4.5-3: Deformation in the 2-direction of all material

Unit: mm	**Deformed Distance A**	**Deformed Distance B**	**Deformed Distance C**	**Average**
GF-PA-OT1	0.86	0.73	1.30	0.96
GF-PA-OT2	7.07	7.04	7.45	7.19
GF-PA-OT3	12.39	12.51	12.55	12.48
CF-PA-OT1	0.54	0.49	0.95	0.66
CF-PA-OT2	4.79	4.81	5.13	4.91
CF-PA-OT3	12.65	12.84	12.87	12.79

Table 4.5-4: Ratio of the deformation of OT2/OT1, OT3/OT1, and OT3/OT2 of GF-PA and CF-PA

	GF-PA	CF-PA
OT2/OT1	7.47	7.44
OT3/OT1	12.97	19.39
OT3/OT2	1.74	2.61

Figure 4.5-14 shows the comparison of the out-of-plane (3-direction) deformation. The D and E locations can be found in Figure 4.4-18. As shown in Figure 4.5-12: Comparison of the temperature gradient of all cases, the temperature gradient is almost identical for all the GF-PA cases and all the CF-PA cases. Therefore, it suggests that the differences in the out-of-plane deformation between all three cases are a result of thermo-mechanical properties. The warpage resulted from the residual stress is caused by the mismatch in the thermal strain which is caused by thermal gradient and the differences in in-plane CTEs. Multiple phenomena occur simultaneously, for example, stress relaxation and crystallization shrinkage. The plot shows that changes in OTs influence the out-of-plane deformation. GF-PA-OT1 has the highest CTE in the 3-direction (α_3) of all GF-PA cases. Although, the deformation of OT2 and OT3 can't be simply rank. The most noticeable difference is that CF-PA-OTs has significantly less deformation than GF-PA-OTs because CF-PA has higher strength than GF-PA to oppose the distortion.

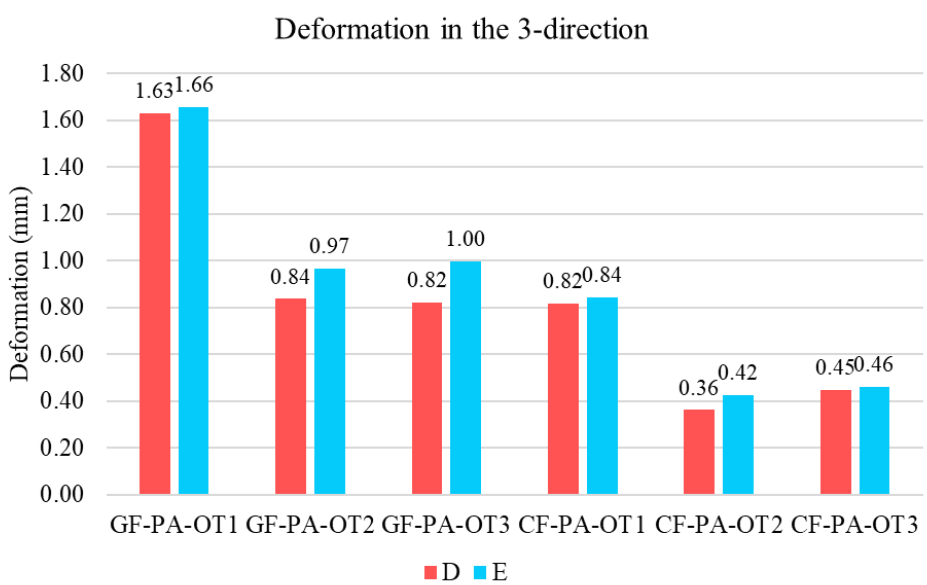

Figure 4.5-14: Comparison of the deformation in the 3-direction

5. CONCLUSIONS

This final chapter provides a brief overview of progress developed in each chapter to investigate the effect of fiber orientation on the final deformation of the part. General recommendations for future work and improvements to current work are provided at the end of this chapter.

The story starts with experimental characterization of 50% by weight GF-PA. The properties at the bead level are required to capture the properties of the part with any printing path. However, some experiments require specific sample dimensions that do not capture the entire printed bead. Therefore, a virtual characterization step is needed. Constituent properties of glass fiber and polyamide were reversed engineered using Mori-Tanaka homogenization available in Digimat mean-field homogenization (MF). Those properties were then used in virtual characterization in Digimat MF as well. Finally, all the material properties obtained were put together into a material card, ready for the EDAM process simulation.

To gain confidence, the material card and the EDAM process simulation was verified with two experimental prints. The printing experiment was conducted with the LSAM system at Local Motors. Those geometries are flat plate with two layers of 0°and two layers of 90° raster, and a curved wedge geometry. The predicted temperature history, degree of crystallinity, and deformation are in good agreement with the experimental print.

At this point, both the material model and EDAM process simulation are verified. Three orientation tensors (OT) were selected. OT1 being the extreme case of least fiber collimation system, OT2 is commonly observed in CAMRI prints, and OT3 being the extreme case of the high fiber collimation. The materials selected are 30% by volume glass fiber-polyamide (GF-PA) and 30% by volume carbon fiber-polyamide (CF-PA) because both glass fiber and carbon fiber are commonly used in the industry. A total of six material properties were obtained in Digimat MF, one per each case. The thermal conductivity of the GF-PA-OTs is not noticeably different among the three OTs. However, the thermal conductivity is noticeably different among CF-PA-OTs due to significant differences between the axial and transverse direction of CF. In terms of mechanical performance, OT3 was found to have the highest degree of anisotropy. Also, the degree of anisotropy is higher in CF-PA due to the significantly higher performance in the axial direction of carbon fiber than glass fiber.

In the end, the final EDAM part's geometry accuracy and performance are most important. The process simulation validated earlier was utilized to study the effect of the effective properties on the residual stress and deformation of an EDAM part. A geometry selected is named UU shaped, created for the CAMRI system, and is designed to promote deformation. Both thermal analysis and mechanical analysis was performed. The thermal analysis results suggest that the CF-PA parts are always at a lower temperature than GF-PA. However, the OT does not affect the temperature gradient noticeably. The mechanical analysis predicted that the OT3 has the highest in-plane deformation (1-2 plane) for both material systems, while OT1 has the highest out-of-plane deformation (3-direction). Both material system has similar in-plane deformation for the same OT. However, the out-of-plane deformation of CF-PA parts is significantly lower than GF-PA parts. This thermal and mechanical analysis was done on a medium-size, thin-wall geometry and the results may differ in thick wall geometry. This leads to future work discussions.

This study provides an idea of the relationship of the microstructure to the effective properties of the final geometry. It also serves as a good preliminary study to understand fiber orientation-induced deformations in EDAM. Only one geometry was investigated in this study which was designed for a medium-size part. More studies are needed on the investigation of more complex geometries commonly printed in the industry. More studies are also needed for the larger scale printer such as LSAM or BAAM printer. In a related topic, there is a knowledge gap between the processing conditions and the microstructure of the bead. Multiple factors can lead to changes in fiber alignment, such as nozzle shape and size, extrudate compaction mechanism, print speed, etc. Those relationships are important to implement the knowledge from this study into action.

APPENDIX

Tensile specimen dimensions

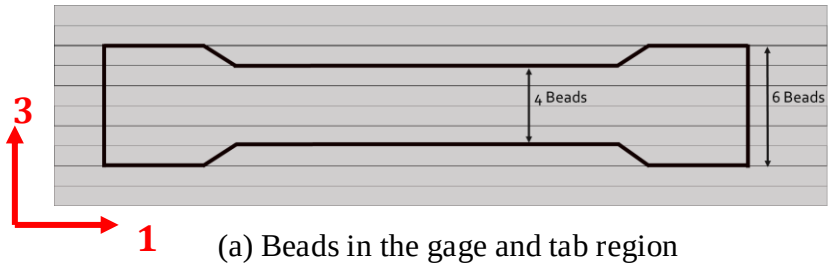

(a) Beads in the gage and tab region

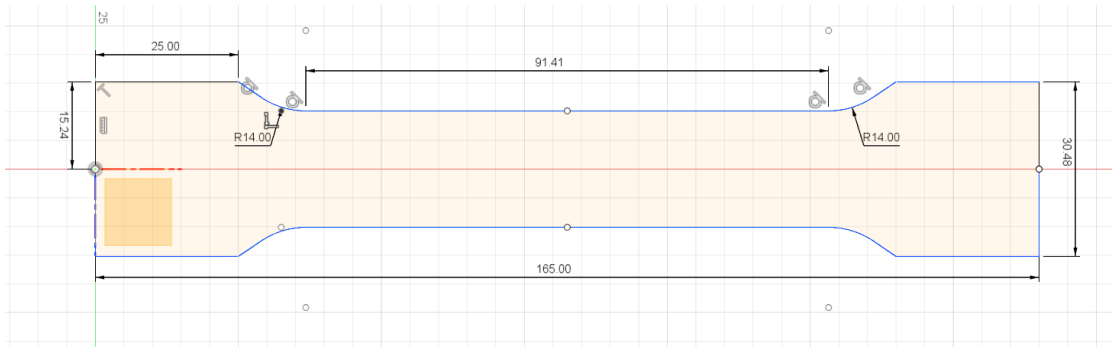

(b) Dimensions of the tensile specimen in mm

Figure A 1: Dimensions of specimens prepared for testing tensile properties in the 1-direction

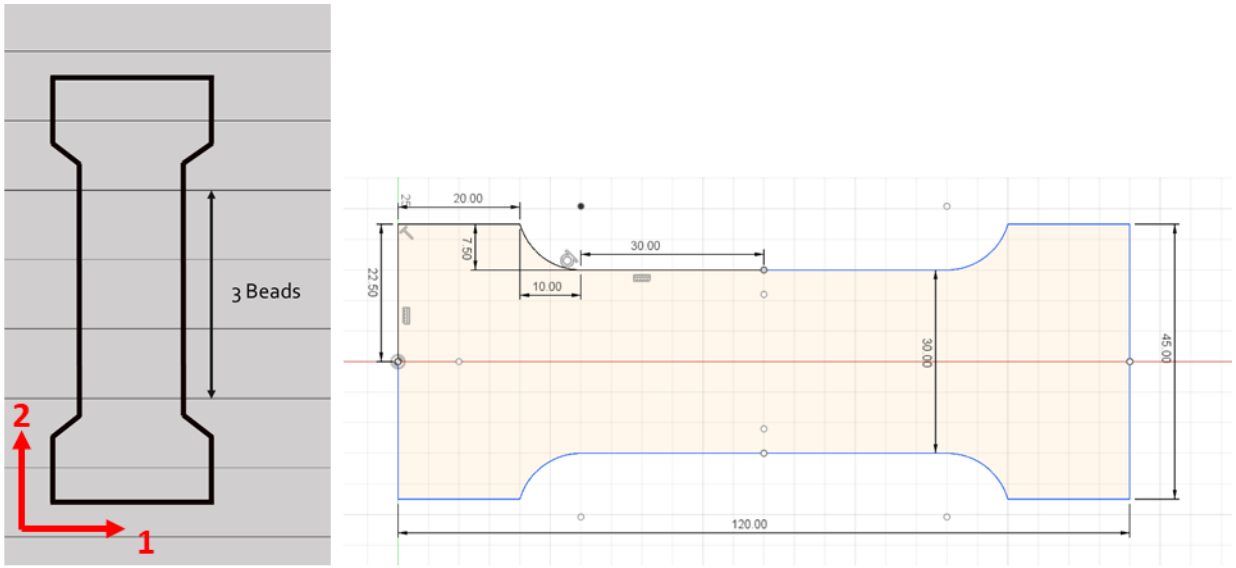

Figure A 2: Dimension of the Tensile Specimen in the 2 Direction

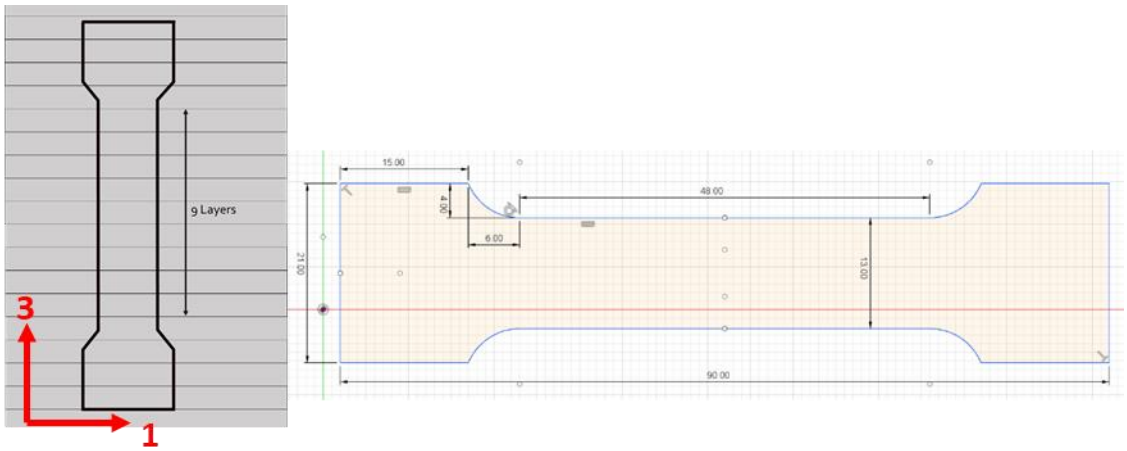

Figure A 3: Dimension of the Tensile Specimen in the 3 Direction

Table A 1: LSAM - AR 4 fiber orientation of each sections of the bead

A11 = 0.58	**1**	**2**	**3**	**4**
1	0.68	0.57	0.58	0.63
2	0.66	0.47	0.51	0.61
3	0.62	0.44	0.43	0.61
4	0.62	0.49	0.45	0.62
5	0.67	0.62	0.6	0.68
6	0.64	0.64	0.6	0.54

A22 = 0.32	**1**	**2**	**3**	**4**
1	0.2	0.31	0.31	0.22
2	0.23	0.45	0.4	0.25
3	0.29	0.5	0.5	0.29
4	0.3	0.44	0.49	0.3
5	0.23	0.29	0.31	0.23
6	0.24	0.26	0.3	0.35

A33 = 0.10	**1**	**2**	**3**	**4**
1	0.13	0.11	0.11	0.15
2	0.11	0.08	0.08	0.14
3	0.09	0.06	0.06	0.1
4	0.08	0.07	0.06	0.08
5	0.1	0.09	0.09	0.09
6	0.12	0.1	0.1	0.11

Table A 2: Area Weighted Fiber Orientation of Each Sections in the Bead

Weighted A11 = 0.57	**1**	**2**	**3**	**4**
1	0.32	0.33	0.31	0.27
2	0.58	0.47	0.51	0.49
3	0.60	0.44	0.43	0.52
4	0.59	0.49	0.45	0.52
5	0.60	0.62	0.60	0.52
6	0.26	0.20	0.12	0.04
Weighted A22 = 0.34	**1**	**2**	**3**	**4**
1	0.09	0.18	0.17	0.09
2	0.20	0.45	0.40	0.20
3	0.28	0.50	0.50	0.25
4	0.29	0.44	0.49	0.25
5	0.21	0.29	0.31	0.17
6	0.10	0.08	0.06	0.02
Weighted A33 = 0.09	**1**	**2**	**3**	**4**
1	0.06	0.06	0.06	0.06
2	0.10	0.08	0.08	0.11
3	0.09	0.06	0.06	0.09
4	0.08	0.07	0.06	0.07
5	0.09	0.09	0.09	0.07
6	0.05	0.03	0.02	0.01

Table A 3: Area Weighted Fiber Orientation for Tensile and Shear Specimens

Weighted A11 after Machining = 0.53	**1**	**2**	**3**	**4**
1	0.06	0.10	0.10	0.05
2	0.10	0.47	0.51	0.09
3	0.09	0.44	0.43	0.09
4	0.09	0.49	0.45	0.09
5	0.10	0.62	0.60	0.10
6	0.04	0.05	0.04	0.01
Weighted A22 after Machining = 0.39	**1**	**2**	**3**	**4**
1	0.02	0.05	0.05	0.02
2	0.03	0.45	0.40	0.04
3	0.04	0.50	0.50	0.04
4	0.04	0.44	0.49	0.04
5	0.03	0.29	0.31	0.03
6	0.01	0.02	0.02	0.01
Weighted A33 after Machining = 0.08	**1**	**2**	**3**	**4**
1	0.01	0.02	0.02	0.01
2	0.02	0.08	0.08	0.02
3	0.01	0.06	0.06	0.01
4	0.01	0.07	0.06	0.01
5	0.01	0.09	0.09	0.01
6	0.01	0.01	0.01	0.00

Table A 4: Heat Capacity as a Function of Temperature

Temperature (◦C)	Heat Capacity (W·sec/gm·K)
23	1.1459
25	1.1528
30	1.1702
35	1.1876
40	1.2051
45	1.2227
50	1.2404
55	1.2582
60	1.276
65	1.294
70	1.312
75	1.3301
80	1.3483
85	1.3666
90	1.3851
95	1.4034
100	1.4222
105	1.4442
110	1.4688
115	1.499
120	1.5316
125	1.5603
130	1.5866
135	1.6121
140	1.6346
145	1.6541
150	1.6686
155	1.6818
160	1.698

Temperature (◦C)	Heat Capacity (W·sec/gm·K)
165	1.7223
170	1.7584
175	1.8118
180	1.8895
185	2.0259
190	2.1986
195	2.3359
200	2.2758
205	1.9933
210	1.7797
215	1.7216
220	1.7113
225	1.7139
230	1.7196
235	1.7254
240	1.7322
245	1.7393
250	1.7462
255	1.7528
260	1.7595
265	1.7659
270	1.7723
275	1.7786
280	1.7856
285	1.7918
290	1.7978
295	1.8038
300	1.8058

Table A 5: Thermal Conductivity of 50% wt. GF-PA as a Function of Temperature in the Three Principal Direction

	Temperature (◦C)	Density (g/cm^3)	Specific Heat (W·sec/g·K)	Diffusivity (cm^2/sec)	Thermal Conductivity (W/cm·K)
1-Direction	23	1.4083	1.1459	0.00249	0.403
	50	1.4083	1.2404	0.00232	0.407
	100	1.4083	1.4222	0.00203	0.406
	150	1.4083	1.5686	0.0018	0.397
	200	1.4083	1.6815	0.00152	0.361
	250	1.4083	1.7462	0.00105	0.258
	300	1.4083	1.8058	0.0009	0.228
2- Direction	23	1.4931	1.1459	0.00279	0.478
	50	1.4931	1.2404	0.0026	0.481
	100	1.4931	1.4222	0.00225	0.477
	150	1.4931	1.5686	0.00192	0.449
	200	1.4931	1.6815	0.00162	0.408
	250	1.4931	1.7462	0.0001	0.28
	300	1.4931	1.8058	0.0001	0.27
3- Direction	23	1.4164	1.1459	0.00212	0.345
	50	1.4164	1.2404	0.00203	0.356
	100	1.4164	1.4222	0.00175	0.352
	150	1.4164	1.5686	0.00151	0.335
	200	1.4164	1.6815	0.00133	0.316

Table A 6: Summary of the Prony series descriptions of the TTS mater curves for the moduli E_1 and E_2

λ_w relaxation time (s)	E_{1w} (MPa)	E_{2w} (MPa)
-	229.84	20
$\mathbf{10^{-7}}$	3.0E-14	2.3E-14
$\mathbf{10^{-6}}$	2.2E-14	4.4E-14
$\mathbf{10^{-5}}$	2.2E-14	4.3E-14
$\mathbf{10^{-4}}$	2.2E-14	75.16
$\mathbf{10^{-3}}$	94.14	143.16
$\mathbf{10^{-2}}$	350.88	369.77
$\mathbf{10^{-1}}$	385.04	165.76
1	279.96	175.35
$\mathbf{10^{1}}$	136.53	91.10
$\mathbf{10^{2}}$	123.79	68.65
$\mathbf{10^{3}}$	229.57	82.54
$\mathbf{10^{4}}$	235.36	78.97
$\mathbf{10^{5}}$	129.41	38.84
$\mathbf{10^{6}}$	110.49	31.08
$\mathbf{10^{7}}$	118.27	25.92
$\mathbf{10^{8}}$	80.10	26.10
$\mathbf{10^{9}}$	94.37	24.23
$\mathbf{10^{10}}$	81.90	21.54
$\mathbf{10^{11}}$	113.55	34.16
$\mathbf{10^{12}}$	42.28	22.45
$\mathbf{10^{13}}$	172.15	22.72

Table A 7: Thermal conductivity of 50% wt. GF-PA

Thermal conductivity of 50% wt. GF-PA-OT1

Temp (℃)	K_{11} **(W/mK)**	K_{22} **(W/mK)**	K_{33} **(W/mK)**
23	0.457	0.436	0.333
50	0.462	0.442	0.340
100	0.460	0.440	0.337
150	0.442	0.421	0.314
200	0.416	0.394	0.282
250	0.291	0.265	0.128
300	0.271	0.244	0.106

Thermal conductivity of 50% wt. GF-PA-OT2

Temp (℃)	K_{11} **(W/mK)**	K_{22} **(W/mK)**	K_{33} **(W/mK)**
23	0.523	0.370	0.333
50	0.528	0.377	0.340
100	0.526	0.374	0.337
150	0.510	0.353	0.314
200	0.488	0.322	0.282
250	0.379	0.177	0.128
300	0.359	0.156	0.106

Thermal conductivity of 50% wt. GF-PA-OT3

Temp (℃)	K_{11} **(W/mK)**	K_{22} **(W/mK)**	K_{33} **(W/mK)**
23	0.572	0.321	0.333
50	0.576	0.329	0.340
100	0.574	0.325	0.337
150	0.560	0.302	0.314
200	0.541	0.269	0.282
250	0.443	0.113	0.128
300	0.424	0.091	0.106

Table A 8: Thermal conductivity of 30% vol. CF-PA

Thermal conductivity of 30% vol. CF-PA-OT1

Temp (℃)	K_{11} **(W/mK)**	K_{22} **(W/mK)**	K_{33} **(W/mK)**
23	1.449	1.284	0.436
50	1.458	1.292	0.442
100	1.454	1.289	0.439
150	1.425	1.261	0.419
200	1.381	1.220	0.390
250	1.033	0.901	0.227
300	0.935	0.814	0.196

Thermal conductivity of 30% vol. CF-PA-OT2

Temp (℃)	K_{11} **(W/mK)**	K_{22} **(W/mK)**	K_{33} **(W/mK)**
23	1.991	0.742	0.436
50	2.001	0.749	0.442
100	1.996	0.746	0.439
150	1.963	0.723	0.419
200	1.911	0.690	0.390
250	1.464	0.470	0.227
300	1.330	0.419	0.196

Thermal conductivity of 30% vol. CF-PA-OT3

Temp (℃)	K_{11} **(W/mK)**	K_{22} **(W/mK)**	K_{33} **(W/mK)**
23	2.391	0.341	0.436
50	2.403	0.347	0.442
100	2.398	0.345	0.439
150	2.361	0.326	0.419
200	2.302	0.298	0.390
250	1.782	0.152	0.227
300	1.622	0.127	0.196

Figure A 4: Evolution of temperature during part manufacturing at multiple layer locations predicted in the EDAM process simulation of the UU geometry

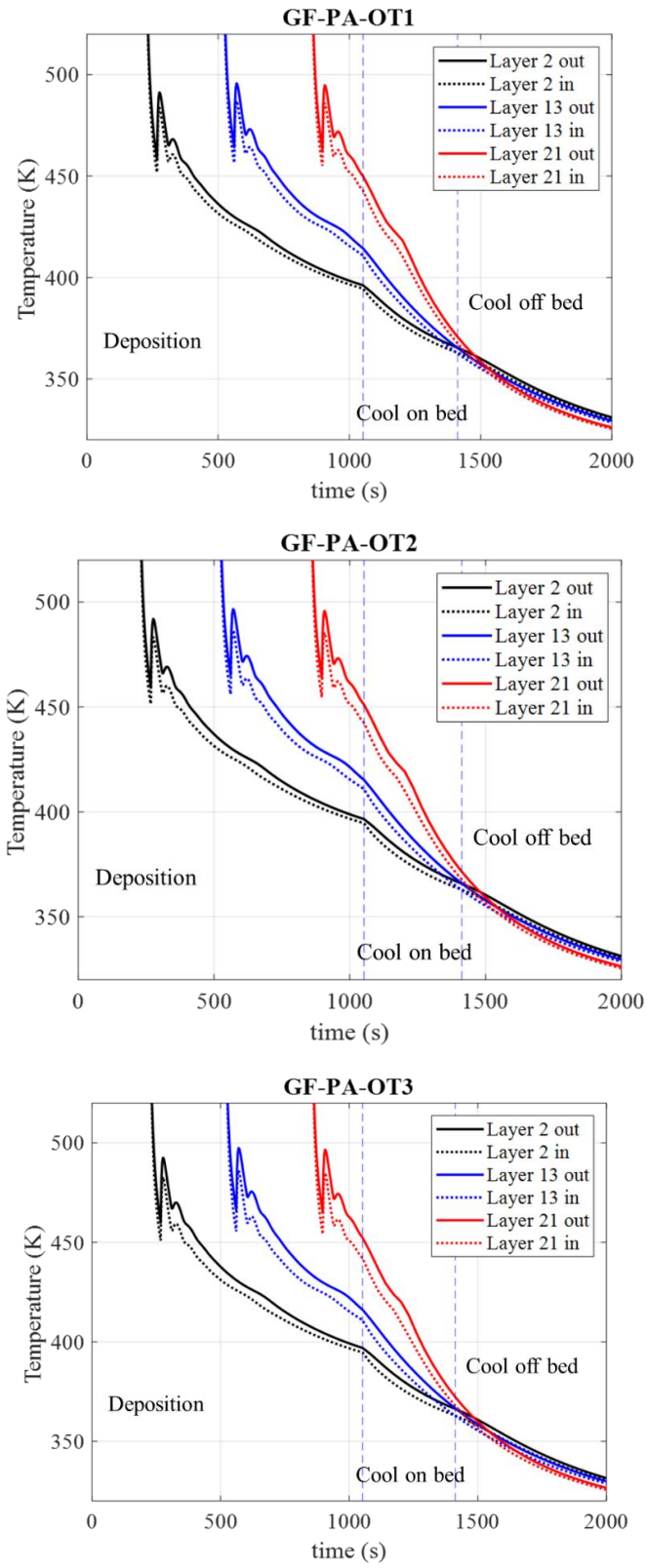

30% vol CF-PA In-Plane Deformation

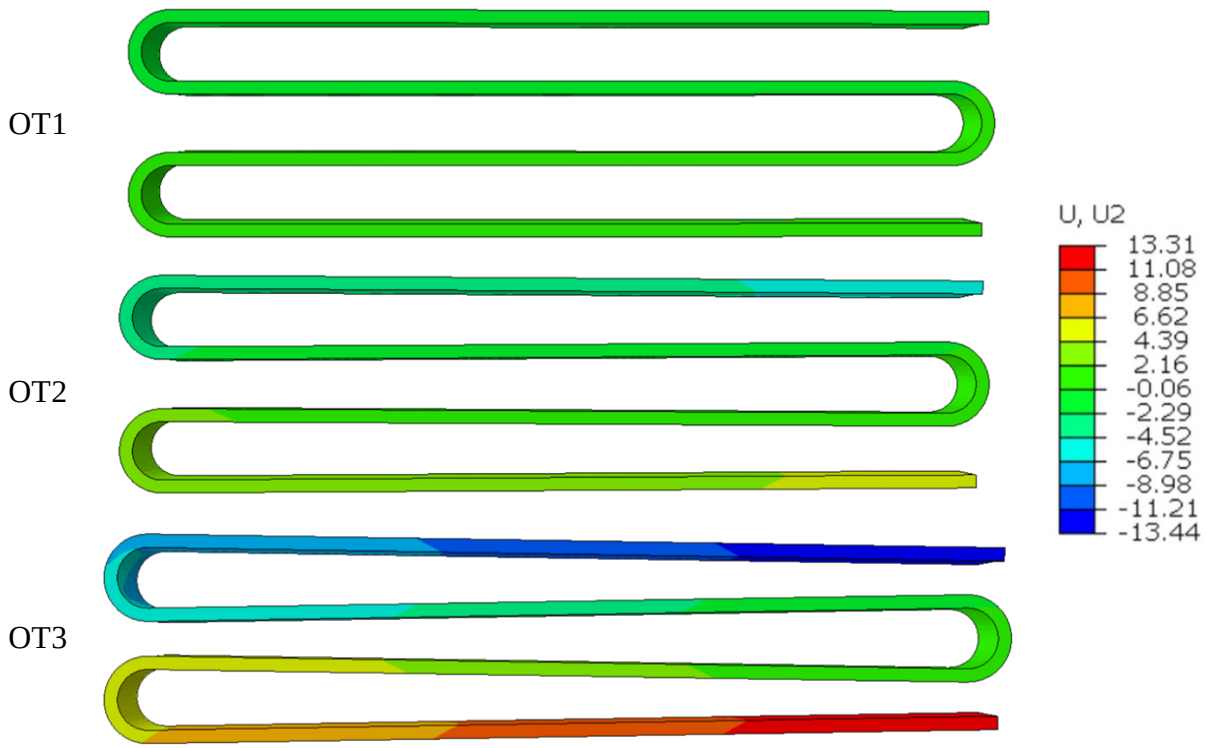

Figure A 5: Top view of the in-plane predicted deformation of 30% vol. CF-PA-OTs

REFERENCES

[1] C. E. D. C. Holshouser, C. Newell, S. Palas, L. J. Love, V. Kunc, R. F. Lind, P. D. Lloyd, J. C. Rowe, C. A. Blue, "Out of bounds additive manufacturing," *Advanced Materials and Processes*, 2013.

[2] E. Barocio, "Fusion Bonding of Fiber Reinforced Semi-Crystalline Polymers in Extrusion Deposition Additive Manufacturing," 2020.

[3] Thermwood, "LSAM - Large Scale Additive Manufacturing," 2019.

[4] B. Post and A. Roschli, "Wide and High Additive Manufacturing," no. March, 2017.

[5] K. Ramani, D. Bank, and N. Kraemer, "Effect of screw design on fiber damage in extrusion compounding and composite properties," *Polym. Compos.*, vol. 16, no. 3, pp. 258–266, 1995, doi: 10.1002/pc.750160310.

[6] H. J. Wolf, "Screw plasticating of discontinuous fiber filled thermoplastic: Mechanisms and prevention of fiber attrition," *Polym. Compos.*, vol. 15, no. 5, pp. 375–383, 1994, doi: 10.1002/pc.750150508.

[7] B. P. Heller, D. E. Smith, and D. A. Jack, "Effects of extrudate swell and nozzle geometry on fiber orientation in Fused Filament Fabrication nozzle flow," *Addit. Manuf.*, vol. 12, Part B, pp. 252–264, 2016, doi: http://dx.doi.org/10.1016/j.addma.2016.06.005.

[8] L. J. Love *et al.*, "The importance of carbon fiber to polymer additive manufacturing," *J. Mater. Res.*, vol. 29, no. 17, pp. 1893–1898, 2014, doi: 10.1557/jmr.2014.212.

[9] B. G. Compton, B. K. Post, C. E. Duty, L. Love, and V. Kunc, "Thermal analysis of additive manufacturing of large-scale thermoplastic polymer composites," *Addit. Manuf.*, vol. 17, pp. 77–86, 2017, doi: 10.1016/j.addma.2017.07.006.

[10] M. Li *et al.*, "Preparation and properties of polyamide 6 thermal conductive composites reinforced with fibers," *Mater. Des.*, vol. 51, pp. 257–261, 2013, doi: 10.1016/j.matdes.2013.03.076.

[11] A. Kantaros and D. Karalekas, "Fiber Bragg grating based investigation of residual strains in ABS parts fabricated by fused deposition modeling process," *Mater. Des.*, vol. 50, pp. 44–50, 2013, doi: 10.1016/j.matdes.2013.02.067.

[12] C. Casavola, A. Cazzato, V. Moramarco, and G. Pappalettera, "Preliminary study on residual stress in FDM parts," *Conf. Proc. Soc. Exp. Mech. Ser.*, vol. 9, no. Dmmm, pp. 91–96, 2017, doi: 10.1007/978-3-319-42255-8_12.

[13] C. Casavola, A. Cazzato, V. Moramarco, and G. Pappalettera, "Residual stress measurement in Fused Deposition Modelling parts," *Polym. Test.*, vol. 58, pp. 249–255, 2017, doi: 10.1016/j.polymertesting.2017.01.003.

[14] T. M. Wang, J. T. Xi, and Y. Jin, "A model research for prototype warp deformation in the FDM process," *Int. J. Adv. Manuf. Technol.*, vol. 33, no. 11–12, pp. 1087–1096, 2007, doi: 10.1007/s00170-006-0556-9.

[15] D. W. Radford and T. S. Rennick, "Separating sources of manufacturing distortion in laminated composites," *Journal of Reinforced Plastics and Composites*, vol. 19, no. 8. pp. 621–641, 2000, doi: 10.1106/CRMP-ARE5-GVPP-0Y7N.

[16] M. Cirino and R. Byron Pipes, "In-situ consolidation for the thermoplastic composite ring-residual stress state," *Compos. Manuf.*, vol. 2, no. 2, pp. 105–113, 1991, doi: 10.1016/0956-7143(91)90187-L.

[17] JD Eshelby, "The determination of the elastic field of an ellipsoidal inclusion, and related problems," *Proc. R. Soc. London*, no. A241, p. 376, 1957.

[18] R. Hill, "A self-consistent mechanics of composite materials," *J. Mech. Phys. Solids*, vol. 13, no. 4, pp. 213–222, 1965, doi: 10.1016/0022-5096(65)90010-4.

[19] T. Mori and K. Tanaka, "Average stress in matrix and average elastic energy of materials with misfitting inclusions," *Acta Metall.*, vol. 21, no. 5, pp. 571–574, 1973, doi: 10.1016/0001-6160(73)90064-3.

[20] T. T. Men, V. U. Ton, and A. Tuan, "Mean-field homogenization," 2011.

[21] E. Engineering, "Digimat User ' s Manual," no. October. pp. 1–8, 1999.

[22] T. Mura, "Micromechanics of Defects in Solids," *Martinus Nijhoff, The Hague*, 1982.

[23] Y. Benveniste, "A new approach to the application of Mori-Tanaka's theory in composite materials," *Mech. Mater.*, vol. 6, no. 2, pp. 147–157, 1987, doi: 10.1016/0167-6636(87)90005-6.

[24] T. Chen, G. J. Dvorak, and Y. Benveniste, "Mori-tanaka estimates of the overall elastic moduli of certain composite materials," *J. Appl. Mech. Trans. ASME*, vol. 59, no. 3, pp. 539–546, 1992, doi: 10.1115/1.2893757.

[25] O. Pierard, C. Friebel, and I. Doghri, “Mean-field homogenization of multi-phase thermo-elastic composites: A general framework and its validation,” *Compos. Sci. Technol.*, vol. 64, no. 10–11, pp. 1587–1603, 2004, doi: 10.1016/j.compscitech.2003.11.009.

[26] Y. Benveniste, G. J. Dvorak, and T. Chen, “On diagonal and elastic symmetry of the approximate effective stiffness tensor of heterogeneous media,” *J. Mech. Phys. Solids*, vol. 39, no. 7, pp. 927–946, 1991, doi: 10.1016/0022-5096(91)90012-D.

[27] B. Brenken, “Extrusion Deposition Additive Manufacturing of Fiber Reinforced Semi-crystalline Polymers,” Purdue University, 2017.

[28] A. Favaloro, B. Brenken, E. Barocio, and R. B. Pipes, “Simulation of Polymeric Composites Additive Manufacturing using Abaqus,” in *Science in the Age of Experience by Dassault Systemes*, 2017.

[29] ASTM, “D638 Standard Test Method for Tensile Properties of Plastics,” *ASTM Int.*, vol. 82, no. C, pp. 1–15, 2016, doi: 10.1520/D0638-14.1.

[30] S.-Y. Fu and B. Lauke, “Effects of fiber length and fiber orientation distributions on the tensile strength of short-fiber-reinforced polymers,” *Compos. Sci. Technol.*, vol. 56, no. 10, pp. 1179–1190, 1996, doi: http://dx.doi.org/10.1016/S0266-3538(96)00072-3.

[31] H. J. Wolf, “Screw plasticating of discontinuous fiber filled thermoplastic: Mechanisms and prevention of fiber attrition,” *Polym. Compos.*, vol. 15, no. 5, pp. 375–383, 1994, doi: 10.1002/pc.750150508.

[32] C. A. Schneider, W. S. Rasband, and K. W. Eliceiri, “NIH Image to ImageJ: 25 years of image analysis,” *Nat. Methods*, vol. 9, no. 7, pp. 671–675, 2012.

[33] N. M. Barkoula, B. Alcock, N. O. Cabrera, and T. Peijs, “Fatigue properties of highly oriented polypropylene tapes and all-polypropylene composites,” *Polym. Polym. Compos.*, vol. 16, no. 2, pp. 101–113, 2008, doi: 10.1177/096739110801600203.

[34] ASTM, “Astm D3039/D3039M,” *Annu. B. ASTM Stand.*, pp. 1–13, 2014, doi: 10.1520/D3039.

[35] ASTM, “Standard Test Method for Shear Properties of Composite Materials by the V-Notched,” *Annu. B. ASTM Stand.*, no. March, pp. 1–13, 2012, doi: 10.1520/D5379.

[36] American Society for Testing and Materials, “E1269-01 Standard Test Method for Determining Specific Heat Capacity by Differential Scanning Calorimetry,” *Astm*, vol. 14, no. Reapproved 2018, p. E 1269--01, 2001, doi: 10.1520/E1269-11R18.Copyright.

[37] ASTM, “Standard test method for thermal diffusivity of solids by the flash method (E1461-01),” *Am. Soc. Test. Mater.*, vol. 14, no. 2, pp. 1–13, 2001, doi: 10.1520/E1461-13.2.

[38] Y. Wang, H. L. Kang, R. Wang, R. G. Liu, and X. M. Hao, “Crystallization of polyamide 56/polyamide 66 blends: Non-isothermal crystallization kinetics,” *J. Appl. Polym. Sci.*, vol. 135, no. 26, pp. 1–13, 2018, doi: 10.1002/app.46409.

[39] E. Piorkowska and G. C. Rutledge, *Handbook of Polymer Crystallization*. John Wiley & Sons, Inc, 2013.

[40] C. N. Velisaris and J. C. Seferis, “Crystallization kinetics of polyetheretherketone (peek) matrices,” *Polym. Eng. Sci.*, vol. 26, no. 22, pp. 1574–1581, 1986, doi: 10.1002/pen.760262208.

[41] A. Greco and A. Maffezzoli, “Statistical and kinetic approaches for linear low-density polyethylene melting modeling,” *J. Appl. Polym. Sci.*, vol. 89, no. 2, pp. 289–295, 2003, doi: 10.1002/app.12079.

[42] E. A. Turi, *Thermal Characterization of Polymeric Materials*, Second Edi. Brooklyn: Academic Press, 1997.

[43] H. F. Brinson and L. C. Brinson, *Polymer engineering science and viscoelasticity: An introduction, Second edition*. 2015.

[44] P. Sunderland, W. Yu, and J.-A. MÃ¥nson, “A thermoviscoelastic analysis of process-induced internal stresses in thermoplastic matrix composites,” *Polym. Compos.*, vol. 22, no. 5, pp. 579–592, 2001, doi: 10.1002/pc.10561.

[45] B. Brenken, E. Barocio, A. Favaloro, V. Kunc, and R. B. Pipes, “Development and validation of extrusion deposition additive manufacturing process simulations,” *Addit. Manuf.*, vol. 25, 2019, doi: 10.1016/j.addma.2018.10.041.

[46] R. B. Pipes, E. Barocio, B. Brenken, A. Favaloro, and M. Bogdanor, “Extrusion Deposition Additive Manufacturing with Fiber-Reinforced Thermoplastic Polymers,” in *Structure and Properties of Additive Manufactured Polymer Components*, 1st ed., K. Friedrich and R. Walter, Eds. Woodhead Publishing, 2020, p. 450.

[47] E. Barocio, “Fusion Bonding of Fiber Reinforced Semi-Crystalline Polymers in Extrusion Deposition Additive Manufacturing,” Purdue University, 2018.

[48] Dassault Systèmes, “SIMULIA User Assistance 2019,” 2019. .

[49] E. Piorkowska and G. C. Rutledge, *Handbook of polymer crystallization*. John Wiley & Sons, 2013.

[50] Y. Agari, A. Ueda, and S. Nagai, "Thermal conductivity of a polyethylene filled with disoriented short-cut carbon fibers," *J. Appl. Polym. Sci.*, vol. 43, no. 6, pp. 1117–1124, 1991, doi: 10.1002/app.1991.070430612.

[51] S. Fu and Y. Mai, "Reinforced polymer composites," *Adv. Compos. Bull.*, vol. 2, no. 7, p. 19, 1989.

[52] A. Armillotta, M. Bellotti, and M. Cavallaro, "Warpage of FDM parts: Experimental tests and analytic model," *Robot. Comput. Integr. Manuf.*, vol. 50, no. August 2017, pp. 140–152, 2018, doi: 10.1016/j.rcim.2017.09.007.

[53] J. T. Tzeng and R. B. Pipes, "Thermal residual stress analysis for in situ and post-consolidated composite rings," *Compos. Manuf.*, vol. 3, no. 4, pp. 273–279, 1992, doi: 10.1016/0956-7143(92)90114-A.

[54] S. Y. Fu, B. Lauke, E. Mäder, C. Y. Yue, and X. Hu, "Tensile properties of short-glass-fiber- and short-carbon-fiber-reinforced polypropylene composites," *Compos. Part A Appl. Sci. Manuf.*, vol. 31, no. 10, pp. 1117–1125, 2000, doi: 10.1016/S1359-835X(00)00068-3.

[55] G. D. Goh *et al.*, "Characterization of mechanical properties and fracture mode of additively manufactured carbon fiber and glass fiber reinforced thermoplastics," *Mater. Des.*, vol. 137, pp. 79–89, 2018, doi: 10.1016/j.matdes.2017.10.021.

[56] C. Wonderly, J. Grenestedt, G. Fernlund, and E. Cĕpus, "Comparison of mechanical properties of glass fiber/vinyl ester and carbon fiber/vinyl ester composites," *Compos. Part B Eng.*, vol. 36, no. 5, pp. 417–426, 2005, doi: 10.1016/j.compositesb.2005.01.004.

[57] D. Bowles and S. Tompkins, "Prediction of coefficients of thermal expansion for unidirectional composites using homogenization method," *Fuhe Cailiao Xuebao/Acta Mater. Compos. Sin.*, vol. 14, no. 1, pp. 76–82, 1997.

[58] C. L. Choy, W. P. Leung, K. W. Kowk, and F. P. Lau, "Elastic moduli and thermal conductivity of injection-molded short-fiber–reinforced thermoplastics," *Polym. Compos.*, vol. 13, no. 2, pp. 69–80, 1992, doi: 10.1002/pc.750130202.

[59] Z. Ran, Y. Yan, J. Li, Z. Qi, and L. Yang, "Determination of thermal expansion coefficients for unidirectional fiber-reinforced composites," *Chinese J. Aeronaut.*, vol. 27, no. 5, pp. 1180–1187, 2014, doi: 10.1016/j.cja.2014.03.010.

[60] Toray, “T300 Standard modulus cabon fiber,” 2018.